Study of aerosol properties at local and global scale during extreme aerosol events, using ground-based and spaceborne remote sensing techniques

Christina – Anna Papanikolaou

Graduated from:

Physics Department, University of Crete, Heraklion

M.Sc Diploma in Environmental Physics, Physics Department

National and Kapodistrian University of Athens

A Ph.D. Thesis submitted in fulfillment of the requirements

for the Degree of Doctor of Philosophy

Laboratory of Optolectronics, Lasers and their Applications, Physics Department, School of Applied Mathematical & Physical Sciences, National Technical University of Athens (NTUA)

Supervisor: Prof. Alexandros Papayannis, NTUA

Co-Supervisor: Assist. Prof. Panagiotis Kokkalis, University of Kuwait, Kuwait

Athens, February 2023

This research project has been financed by the project “PANhellenic infrastructure for Atmospheric Composition and climatE change” (MIS 5021516), which is implemented under the Action “Reinforcement of the Research and Innovation Infrastructure”, funded by the Operational Programme “Competitiveness, Entrepreneurship and Innovation” (NSRF 2014–2020) and co-financed by Greece and the European Union (European Regional Development Fund).

Supervisor: Prof. Dr. Alexandros Papayannis

Physics Department
National Technical University of Athens, Greece

Co-Supervisor: Assist. Professor Dr. Panagiotis Kokkalis

Physics Department
University of Kuwait, Kuwait

Member of the Supervising Committee: Assist. Professor Dr. Eleni Giannakaki

Physics Department
National and Kapodistrian University of Athens, Greece

Examination Committee:

Professor Alexandros Papayannis (NTUA)

Assist. Professor Panagiotis Kokkalis (Univ. of Kuwait)

Assist. Professor Eleni Giannakaki (UOA)

Professor Vasilia Karathanasi (NTUA)

Professor Lucas-Alados Arboledas (Univ. of Granada)

Professor Emmanuella Remountaki (NTUA)

Professor Sotirios Karellas (NTUA)

ABSTRACT

The aim of this Ph.D. Thesis is to enrich the scientific knowledge in the field of natural phenomena and processes that take place in the Earth's atmosphere and affect the radiative equilibrium of the Earth. For this purpose, the main aspects studied in detail were the vertical profiles of the aerosol optical properties, from the lower troposphere up to the stratosphere, retrieved by ground-based and spaceborne, active and passive remote sensing techniques. The radiative impact of these extreme events was also estimated. Extreme events are usually very interesting and at the same time difficult to study, because of their low frequency of occurrence, and the lack of available data, where they occur. Therefore, there are still large uncertainties related to their climatic role in the Earth's system and energy budget, with impacts both at local and global scale concerning the human health and climate.

In Chapter 1 we present the structure and composition of the atmosphere and discuss the sources and different types of atmospheric aerosols, along with their role in Earth's radiative budget. In Chapter 2, at first, a theoretical background of remote sensing techniques for aerosol applications is provided. Since the aerosols interact with the incoming shortwave radiation and the longwave outgoing radiation, emphasis is given on the mechanisms of atmospheric aerosols and molecules interactions with light. Moreover, the operating principles of the atmospheric lidar technique are also presented, along with the corresponding lidar data processing procedures, for ground-based and spaceborne lidar systems.

Firstly, in Chapter 3, we present the results of four studies concerning extreme biomass burning events. The first paper deals with the spatio-temporal evolution of a long-lasting Canadian biomass burning event which affected Europe in August 2018. This large fire event produced several smoke layers in the troposphere, which were observed during their transport from Canada to Europe, using the lidar onboard Cloud-Aerosol Lidar and Infrared Pathfinder Satellite Observation (CALIPSO). The optical properties of pure smoke and mixtures of it, along their travel from Canada to Europe were thoroughly studied. The second paper refers to the vertical profiling of aerosol particles as obtained during the winter campaign of 2020, performed in the frame of the PANhellenic infrastructure for Atmospheric Composition and climatE chAnge (PANACEA) project over the city of Ioannina, Greece, a highly polluted area during wintertime due to domestic biomass burning (BB) heating activities. In this case the lidar technique was applied to monitor the spatio-temporal evolution of the vertical profiles of the optical properties of very fresh BB particles, such as the aerosol backscatter coefficient (b_{aer}) and the particle linear depolarization ratio (PLDR), at 532 nm. Additional measurements concerned the in-situ particulate matter ($PM_{2.5}$) and black carbon (BC) concentrations, were also performed. In the third paper we present the aerosol optical properties and atmospheric radiative forcing (RF) effect of the tropospheric and stratospheric smoke layers, observed by CALIPSO, during the extraordinary Australian BB event occurred during the period 25 December to 12 February, in summer 2019 - 2020. These BB aerosol layers were studied and analyzed within a large longitude

and latitude range, as they were transported from Australia to the South American continent, in the troposphere and the stratosphere. The last study of the chapter, concerns the long-range transport of aerosols over Athens, Greece during Autumn 2020. Three cases of intercontinental transport of aerosols reaching Athens were studied by the DEPOLarization lidar systEm (DEPOLE) of the National Technical University of Athens (NTUA). These aerosols originated from the North American continent during September 2020, while at the same time period an extreme wildfire event was taking place in the State of California.

In Chapter 4, we discuss the aerosol optical properties emitted by the Hunga Tonga-Ha'apai volcanic eruption in 2022, as observed by active and passive remote sensing techniques. The library of radiative transfer (LibRadtran) model has been applied to estimate the atmospheric radiative forcing effect of these volcanic particles. Finally, in Chapter 5, one of the most extreme Saharan dust events of the last years was studied by the elastic-Raman lidar system (aErosol and Ozone Lidar system-EOLE) and the DEPOLE, both located at NTUA. The retrieved vertical profiles of the aerosol optical properties, along with the very high values of the aerosol optical depth (AOD) observed by AErosol RObotic NETwork (AERONET) station located at NTUA, depicted an extremely strong Saharan dust transport event over our region. Finally, the radiative impact of this dust event was also estimated.

The main findings of this Ph.D. Thesis are summarized in Chapter 6, as following: (i) the smoke particles studied within the PBL showed extremely low PLDR values (0.01 - 0.03), indicating that their shape was almost spherical. (ii) In the free troposphere (FT) the fresh BB particles presented PLDR values, at 532 nm, of nearly spherical particles (< 0.10), with relatively small size ($Å_b$ for the pair 532/1064 nm ~ 1.00). (iii) The aged BB particles, in the troposphere, remained spherical throughout their transport, with a small variation in PLDR values, apart from the cases of mixing with desert dust, where PLDR values increased. Moreover, smoke particles appear to increase in size as they move away from their source. Saharan dust particles, despite their long-range transport, presented optical properties indicative of pure desert part particles (PLDR: 0.29 - 0.36 at 532 nm, $Å_{a,b}$: 0.16 ± 0.25 and 0.36 ± 0.19, LR: 53.22±38.76 sr at 532 nm). (iv) Stratospheric smoke particles show larger PLDR values (max. observed value 0.20) than the tropospheric ones, as well as smaller size ($Å_b$ ~ 1.40, max. value up to 3.00), while as they remain in the stratosphere and fend off the source, their size becomes slightly smaller. On the other hand, the particles of volcanic origin are less depolarizing (0.01 - 0.06), while their $Å_b$ (0.79 - 1.94) values indicate the co-existence of fine, and slightly larger particles. (v) Finally, based on their aerosol radiative effect at SRF-level, the extreme aerosol events studied can be arranged in descending order as: 1) Saharan dust (TOA: −70.11 W/m^2, SRF: −168.41 W/m^2), 2) tropospheric BB particles (Australia; TOA: −47.42 to +11.56 W/m^2, SRF: −87.10 to −4.53 W/m^2), 3) volcanic aerosols (Hunga Tonga; TOA: −46.76 W/m^2, SRF: −43.97 W/m^2), 4) stratospheric BB particles (Australia; TOA: −25.96 to +13.18 W/m^2, SRF: −42.79 to −3.80 W/m^2), 5) tropospheric BB particles (Athens, California origin; TOA: −1.33 W/m^2, SRF: –4.71 W/m^2).

ACKNOWLEDGEMENTS

This Doctoral Thesis is the result of a long-term effort and for this reason, I would like to express my appreciation to the people with whom I worked with, got inspired and supported during the years of its preparation.

First of all, I would like to thank from the bottom of my heart my supervisor Professor Alexandros Papayannis for giving me the opportunity to work on this Thesis, as Director of the *Laboratory of Optoelectronics, Laser and their Applications* of the National Technical University of Athens. I could not hope to find a better supervisor. I am feeling lucky that I met him, glad and thankful for his trust and support and for giving me the chance to make my own decisions and initiatives.

This Thesis would never be as it is without the contribution of my co-supervisor Assistant Professor Panagiotis Kokkalis; he was always willing to help me when I was confused and urged me to find in my own solutions under his guidance. His suggestions, ideas and scientific point of view were always innovative, so I will be always thankful to him.

I would also like to thank the Assistant Professor Elina Giannakaki, as she was the one to offer me the opportunity to perform research in atmospheric Physics, during my M.Sc. studies, by assigning me a Thesis to study a biomass burning event using the CALIPSO satellite observations; this was the trigger to the rest that followed.

Moreover, I personally thank my friend and colleague Maria Mylonaki; she was my co-traveler through these years and she will continue to be. My thanks go also, to my friend and colleague Dr. Ourania Soupiona, who I want to thank for the help and support. Last, but not least, I would like to thank Romanos Foskinis, Dimitra Anagnou, Marilena Gidarakou and Eleni Kralli with whom I became friend, apart from colleague, through all these years.

Lastly, I thank my parents, Christos and Zoi, for believing in me always and providing everything for me. I am also thankful to my sister Maria, for always encouraging me to proceed with my studies, as well to my sister Vaso and Margaritis for always having my back and believing in me. A simple thank is not enough to Giorgos; He was my motivator, my daily joy and my shoulder to cry on, when things where tough. My friends, Agapi and Maria, I thank you for always being there for me, listening to me talking about my research and complaining during the difficult periods. Last but not least, my special thanks go to my friend Vivi, that despite the distance, she was always a call away.

Christina -Anna Papanikolaou

Athens, February 2023

Μελέτη των οπτικών ιδιοτήτων των αιωρούμενων σωματιδίων σε τοπική και υπερτοπική κλίμακα κατά τη διάρκεια έντονων επεισοδίων σωματιδιακής ρύπανσης, με χρήση δεδομένων επίγειας και δορυφορικής τηλεπισκόπησης

Χριστίνα-Άννα Παπανικολάου

Απόφοιτη:

Τμήματος Φυσικής, του Πανεπιστημίου Κρήτης

Μεταπτυχιακό Δίπλωμα στην Φυσική Περιβάλλοντος, Εθνικό και Καποδιστριακό Πανεπιστήμιο Αθηνών

Η Διδακτορική αυτή Διατριβή παραδίδεται στα πλαίσια απόκτησης του Διδακτορικού Διπλώματος και εκπονήθηκε στην Εργαστήριο Οπτοηλεκτρονικής, Lasers και Εφαρμογών τους, του Τομέα Φυσικής, της Σχολής Εφαρμοσμένων Μαθηματικών και Φυσικών Επιστημών, του Εθνικού Μετσόβιου Πολυτεχνείου

Επιβλέπων: Καθ. Αλέξανδρος Παπαγιάννης

Συνεπιβλέπων: Επικ. Καθηγητής Παναγιώτης Κόκκαλης, University of Kuwait, Kuwait

Αθήνα, Φεβρουάριος 2023

ΠΕΡΙΛΗΨΗ

Σκοπός της παρούσας διδακτορικής διατριβής είναι η μελέτη των γεωμετρικών και οπτικών ιδιοτήτων των τροποσφαιρικών και στρατοσφαιρικών αιωρούμενων σωματιδίων τόσο σε τοπική όσο και σε παγκόσμια κλίμακα, κατά τη διάρκεια έντονων επεισοδίων σωματιδιακής ρύπανσης, χρησιμοποιώντας επίγειες και δορυφορικές μεθόδους τηλεπισκόπησης.

Στο Κεφάλαιο 1 παρουσιάζεται συνοπτικά η δομή και η σύνθεση της ατμόσφαιρας. Επίσης, γίνεται αναφορά στα ατμοσφαιρικά αιωρούμενα σωματίδια και στον ρόλο τους στο ενεργειακό ισοζύγιο της ατμόσφαιρας. Στο Κεφάλαιο 2, αρχικά παρουσιάζεται το θεωρητικό υπόβαθρο των μεθόδων με τηλεπισκόπησης με εφαρμογές στην ατμόσφαιρα. Δεδομένου ότι τα ατμοσφαιρικά αιωρούμενα σωματίδια αλληλοεπιδρούν με την εισερχόμενη ηλιακή ακτινοβολία, καθώς και την εξερχόμενη γήινη ακτινοβολία, έμφαση δίνεται στους μηχανισμούς των αλληλεπιδράσεων. Επιπλέον, παρουσιάζονται οι αρχές λειτουργίας της μεθόδου τηλεπισκόπησης lidar, με εφαρμογές στην ατμόσφαιρα. Τέλος, γίνεται εκτενής αναφορά στις μεθόδους επεξεργασίας δεδομένων lidar, τόσο από επίγεια όσο και δορυφορικά συστήματα, καθώς και στις οπτικές ιδιότητες των αιωρούμενων σωματιδίων που ανακτώνται από αυτά.

Αρχικά, στο Κεφάλαιο 3, παρουσιάζεται μια πλήρης ανάλυση τεσσάρων έντονων επεισοδίων σωματιδιακής ρύπανσης από καύση βιομάζα. Η πρώτη μελέτη σχετίζεται με τη χωροχρονική εξέλιξη ενός επεισοδίου πυρκαγιών στην περιοχή της Βρετανικής Κολομβίας (British Columbia), τον Αύγουστο του 2018. Αυτό το επεισόδιο παρήγαγε τεράστιες ποσότητες σωματιδίων καπνού στην τροπόσφαιρα, οι οπτικές ιδιότητες των οποίων, μελετήθηκαν διεξοδικά, κατά τη μεταφορά τους από τον Καναδά στην Ευρώπη, με δεδομένα από τον δορυφόρο Cloud-Aerosol Lidar and Infrared Pathfinder Satellite Observation (CALIPSO). Η δεύτερη δημοσίευση αφορά στην μελέτη της κατακόρυφης κατανομής των οπτικών ιδιοτήτων σωματιδίων καπνού, που πραγματοποιήθηκε κατά τη διάρκεια της χειμερινής εκστρατείας μετρήσεων της ΠΑΝελλΑδικής υποδομής για τη μΕλέτη της ατμοσφαιρικής σύστασης και κλΙματικής Αλλαγής (ΠΑΝΑΚΕΙΑ) το 2020 στην πόλη των Ιωαννίνων, η οποία υποφέρει κατά τους χειμερινούς μήνες από επεισόδια ατμοσφαιρικής ρύπανσης, λόγω δραστηριοτήτων οικιακών θέρμανσης. Η τεχνική lidar εφαρμόσθηκε για την ανάκτηση των οπτικών ιδιοτήτων των πολύ φρέσκων σωματιδίων καπνού, ενώ χρησιμοποιήθηκαν σωματιδιακές συγκεντρώσεις ($PM_{2.5}$) και συγκεντρώσεις Μαύρου Άνθρακα (BC), με στόχο την εκτίμηση της συμβολής της καύσης βιομάζας/ξύλου (BC_{wb}) στις συνολικές συγκεντρώσεις BC. Στην τρίτη μελέτη παρουσιάζονται οι οπτικές ιδιότητες σωματιδίων καπνού, τα οποία παράχθηκαν κατά τη διάρκεια ενός από τα πιο έντονα επεισόδια πυρκαγιών, παγκοσμίως, το οποίο έλαβε χώρα στην Αυστραλία και μελετήθηκε από τις 25 Δεκεμβρίου 2019 έως τις 12 Φεβρουαρίου 2020. Οι στρωματώσεις καπνού παρατηρήθηκαν στην τροπόσφαιρα και την στρατόσφαιρα του νότιου ημισφαιρίου, από τον δορυφόρο CALIPSO, και οι οπτικές τους ιδιότητες αναλύθηκαν σε μεγάλο εύρος γεωγραφικού μήκους και πλάτους, καθώς μεταφέρονταν σταδιακά από την Αυστραλία στην Νότια Αμερική, ενώ παρουσιάστηκε και η επίδραση τους στο ενεργειακό ισοζύγιο της ατμόσφαιρας. Η τελευταία μελέτη του κεφαλαίου αφορά στη μεγάλης εμβέλειας μεταφορά

αιωρούμενων σωματιδίων πάνω από την Αθήνα, στην Ελλάδα, το Φθινόπωρο 2020, κατά τη χρονική περίοδο που στην ευρύτερη περιοχή της Καλιφόρνια λάμβανε χώρα ένα ακραίο γεγονός δασικής πυρκαγιάς. Οι τρεις περιπτώσεις διηπειρωτικής μεταφοράς αιωρούμενων σωματιδίων πάνω από την Αθήνα μελετήθηκαν από το DEPOLarization lidar system (DEPOLE)) του Εθνικού Μετσόβιου Πολυτεχνείου (ΕΜΠ).

Στο Κεφάλαιο 4, παρουσιάζεται η μελέτη των αιωρούμενων σωματιδίων από την ηφαιστειακή έκρηξη Hunga Tonga-Ha'apai που έλαβε χώρα στις 15 Ιανουαρίου 2022. Τα στρατοσφαιρικά ηφαιστειακά αιωρούμενα σωματίδια μελετήθηκαν με τεχνικές ενεργητικής και παθητικής τηλεπισκόπησης, ενώ το μοντέλο μεταφοράς ακτινοβολίας libRadtran χρησιμοποιήθηκε προκειμένου να εκτιμηθεί η επίδραση των ηφαιστειακών σωματιδίων στο ενεργειακό ισοζύγιο της ατμόσφαιρας. Στο Κεφάλαιο 4, παρουσιάζεται το έντονο επεισόδιο ερημικής σκόνης από την έρημο Σαχάρα, όπως αυτό μετρήθηκε στην Αθήνα, στις 16-17 Μαρτίου 2022.

Τα κύρια ευρήματα αυτής της διδακτορικής διατριβής συνοψίζονται στο Κεφάλαιο 6, ως ακολούθως: (i) Τα σωματίδια καπνού που μελετήθηκαν μέσα στο Ατμοσφαιρικό Οριακό Στρώμα (ΑΟΣ) παρουσίασαν εξαιρετικά χαμηλές τιμές PLDR (0.01 - 0.03), υποδεικνύοντας ότι το σχήμα τους ήταν σχεδόν σφαιρικό. (ii) Στην FT τα φρέσκα σωματίδια BB, από τρία διαφορετικά επεισόδιά σωματιδιακής ρύπανσης, παρουσίασαν τιμές PLDR σχεδόν σφαιρικών σωματιδίων (< 0.10), ενώ το μέγεθος τους χαρακτηρίσθηκε σχετικά μικρό ($Å_b$ at 532/1064 nm~ 1.00). (iii) Τα γηρασμένα τροποσφαιρικά σωματίδια BB παρέμειναν σχεδόν σφαιρικά καθ' όλη τη διάρκεια της μεταφοράς τους, με μικρές διακυμάνσεις στις τιμές του PLDR, εκτός από περιπτώσεις πρόσμιξης με σωματίδια ερημικής σκόνης, που οι τιμές του PLDR παρουσίασαν μεγαλύτερη αύξηση. Τα σωματίδια καπνού φαίνεται να αυξάνονται σε μέγεθος, καθώς απομακρύνονται από την πηγή τους. Επίσης, τα σωματίδια ερημικής σκόνης, παρά την μεγάλης διάρκειας μεταφορά τους, παρουσίασαν τιμές ερημικής σκόνης χωρίς προσμίξεις (PLDR: 0.29 - 0.36 at 532 nm, $Å_{a,b}$: 0.16 ± 0.25 and 0.36 ± 0.19, LR: 53.22 ± 38.76 sr at 532 nm) (iv) Τα στρατοσφαιρικά σωματίδια καπνού παρουσιάζουν μεγαλύτερες τιμές PLDR (μέγιστη καταγεγραμμένη τιμή 0.20) από τα τροποσφαιρικά, καθώς και μικρότερο μέγεθος (Å~ 1.40, μέγιστη έως 3.00), ενώ όσο παραμένουν στην στρατόσφαιρα και απομακρύνονται από την πηγή, το μέγεθός τους γίνεται ελαφρώς μικρότερο. Επιπλέον, τα ηφαιστειακής προέλευσης σωματίδια, είναι λιγότερο αποπολωτικά (0.01 - 0.06), ενώ οι τιμές του $Å_b$ (0.79 - 1.94) υποδηλώνουν την ύπαρξη κυρίως μικρών σωματιδίων, και σε ορισμένες περιπτώσεις λίγο μεγαλύτερων. (v) Τέλος, με βάση την επίδραση που είχαν στο ισοζύγιο ακτινοβολίας της ατμόσφαιρας, μπορούμε να κατατάξουμε τα επεισόδια σωματιδιακής ρύπανσης που μελετήθηκαν με φθίνουσα σειρά 1) ερημική σκόνη (TOA: −70.11 W/m^2, SRF: −168.41 W/m^2), 2) τροποσφαιρικά σωματίδια BB (Αυστραλία; TOA: −47.42 to +11.56 W/m^2, SRF: −87.10 to −4.53 W/m^2), 3) ηφαιστειακά αιωρούμενα σωματίδια (TOA: −46.76 W/m^2, SRF: −43.97 W/m^2), 4) στρατοσφαιρικά σωματίδια BB (Αυστραλία; TOA: −25.96 to +13.18 W/m^2, SRF: −42.79 to −3.80 W/m^2), 5) τροποσφαιρικά σωματίδια BB (Αθήνα, με προέλευση Καλιφόρνια; TOA: −1.33 W/m^2, SRF: –4.71 W/m^2).

Table of Contents

ABSTRACT ..... **v**

ACKNOWLEDGEMENTS ..... **viii**

Μελέτη των οπτικών ιδιοτήτων των αιωρούμενων σωματιδίων σε τοπική και υπερτοπική κλίμακα κατά τη διάρκεια έντονων επεισοδίων σωματιδιακής ρύπανσης, με χρήση δεδομένων επίγειας και δορυφορικής τηλεπισκόπησης ..... **ix**

ΠΕΡΙΛΗΨΗ ..... **xi**

CHAPTER 1 ..... **1**

ATMOSPHERE AND ATMOSPHERIC AEROSOLS **1**

1.1 Atmospheric structure and composition **1**

1.2 Atmospheric aerosols **3**

1.3 Atmospheric aerosol types **5**

1.3.1 Mineral Dust aerosols 6

1.3.2 Biomass Burning (smoke) aerosols 6

1.3.3 Marine (or sea spray) aerosols 7

1.3.5 Clean and polluted continental aerosols 8

1.3.6 Volcanic aerosols 9

1.3.7 Bioaerosols 11

1.3.8 Aerosol mixtures 11

1.4 Aerosol climate effects **11**

CHAPTER 2 ..... **14**

REMOTE SENSING OF THE ATMOSPHERE **14**

2.1 Light and matter interaction **14**

2.2 Atmospheric lidar and operating principles **18**

2.3 Lidar Signals Processing **19**

2.4 Aerosol optical properties measured by lidar **21**

2.5 Processing of the Cloud-Aerosol Lidar with Orthogonal Polarization (CALIOP) profile data **24**

2.5.1 Cloud-Aerosol Lidar with Orthogonal Polarization (CALIOP) system 24

2.5.2 CALIOP data 24

2.5.3 Level 2 Aerosol Profile products 25

2.5.4 CALIPSO algorithm 28

CHAPTER 3 ..... **29**

EXTREME BIOMASS BURNING EVENTS **29**

3.1 Canadian Biomass Burning Aerosol Properties Modification during a Long-Ranged Event on August 2018 29
3.1.1 Introduction 29
3.1.2 Methodology and data 30
3.1.3 Results and Discussion 35
3.1.4 Conclusions 45
3.2 Vertical Profiling of Fresh Biomass Burning Aerosol Optical Properties over the Greek Urban City of Ioannina, during the PANACEA Winter Campaign 46
3.2.1 Introduction 46
3.2.2 Lidar Location and Methodology 48
3.2.3 Results and Discussion 53
3.2.4 Conclusions 65
3.3 Australian Bushfires (2019–2020): Aerosol Optical Properties and Radiative Forcing 66
3.3.1 Introduction 66
3.3.2 Methods and Tools 68
3.3.3 Results 74
3.3.4 Conclusions 84
3.4 Long-range transported aerosols over Athens, Greece during Autumn 2020 85
3.4.1 Introduction 85
3.4.2 Methodology 86
3.4.3 Results 87
3.4.4 Conclusions 90
CHAPTER 4 92
EXTREME VOLCANIC AEROSOL EVENT 92
4.1 Optical properties and radiative forcing of the Hunga Tonga-Ha'apai volcanic eruption in 2022 92
4.1.1 Introduction 92
4.1.2 Methodology 93
4.1.3 Results 95
4.1.4 Conclusions 100
CHAPTER 5 102
EXTREME SAHARAN DUST EVENT 102
5.1 Extreme Saharan dust event over Athens, Greece (March 2022): aerosol optical properties and radiative impact 102
5.1.1 Introduction 102

1.1.2 Methodology 102
5.1.3 Results 104
5.1.4 Conclusions 109
CHAPTER 6 110
CONCUSIONS 110
ΕΚΤΕΤΑΜΕΝΗ ΠΕΡΙΛΗΨΗ 114
BIBLIOGRAPHY 126
APPENDICES 150
APPENDIX A: Paper I 150
APPENDIX B: Paper II 154
Appendix C: Paper III 159
Appendix D 162
LIST OF ABBREVIATIONS 165
LIST OF FIGURES 167
LIST OF TABLES 173
CURICULUM VITAE 176
DATA SOURCE ACKNOWLEDGEMENTS 182

To my family…

CHAPTER 1
ATMOSPHERE AND ATMOSPHERIC AEROSOLS

1.1 Atmospheric structure and composition

The Earth's atmosphere (considering dry air conditions) contains nitrogen (78.09%), oxygen (20.95%), argon (0.93%), carbon dioxide (0.04%), and small amounts of other gases. The atmosphere can be divided into five main layers based on the vertical distribution of temperature (Figures 1.11a): (i) the *troposphere* is characterized by a negative temperature gradient. Its height varies with latitude, lowest over the poles (~7-9 km) and highest at the equator (~18-20 km) and by season (lower in winter and higher in summer). (ii) the *stratosphere* spans from the *tropopause* to 60 km above the Earth's surface. The troposphere is characterized by the lowest humidity and aerosols and highest ozone concentrations and a positive temperature gradient, (ii) the *mesosphere* extends up to 85 kilometers and is characterized by a negative temperature gradient, (iv) the *thermosphere* extends from 90 km up to 500 - 1,000 km, and (v) the *exosphere* which is the uppermost region of Earth's atmosphere that gradually fades into the outer vacuum space (Speight, 2020).

Approximately 75-80% of the mass of the atmosphere resides within the troposphere, while the lower boundary of the troposphere is the so-called *Planetary Boundary Layer* (*PBL*). In contrast to the free atmosphere above it, the presence of the underlying Earth's surface has a measurable direct influence on the PBL, which responds to surface forcing within a timescale of about an hour or less, thus the PBL height is not constant and exhibits a diurnal variation (Stull, 1988; Emeis, 2010; Speight, 2020).

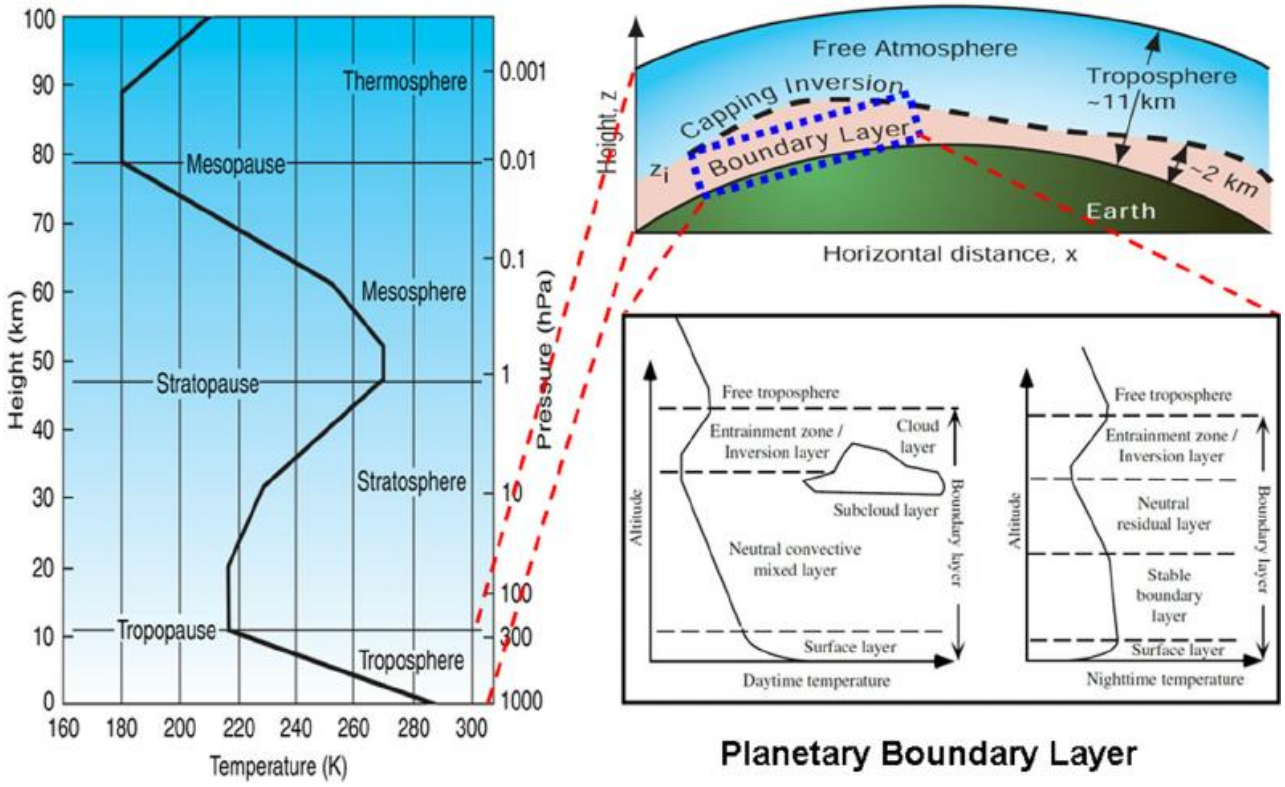

Figure 1. 1: (left) The vertical structure of the atmosphere, (right) including the planetary boundary layer (Figures from Wallace and Hobbs (2006), modified by Lin *et al.* (2015).

The PBL has a well-defined structure, as seen in Figures 1. 1b and 1. 2, which evolves during the Earth's diurnal cycle. The three main components of its structure are (i) *the mixed layer*, (ii) *the residual layer*, and (iii) *the stable boundary layer*. If clouds are present in the mixed layer, then it is also divided into a *cloud layer* and a *subcloud layer,* above and below the cloud, respectively. The mixed layer (ML) appears during daytime and reaches its maximum depth in late afternoon due to the solar heating of the Earth's surface. The turbulence within the mixed layer is usually convectively driven. Most pollutant sources are near the earth's surface; thus, increased pollutant concentrations can accumulate within the ML. The free troposphere is clearly separated from the ML by the so-called *entrainment zone* (EZ). Half an hour before sunset, the *stable boundary layer* (SBL) forms under the *residual layer* (RL). The RL contains the pollutants and moisture from the already developed ML. As the night progresses, the bottom portion of the residual layer is transformed, by its contact with the ground, into a stable boundary layer. This is characterized by statically stable air with weaker, sporadic turbulence. During nighttime, the turbulence decreases in the EZ, but a nonturbulent layer, the so-called capping inversion, remains, and leads to the separation of the free troposphere (FT) from the RL. Finally, the region at the bottom of the PBL is the so-called surface layer (SL), where turbulent fluxes and stress vary by less than 10% of their magnitude (Stull, 1988).

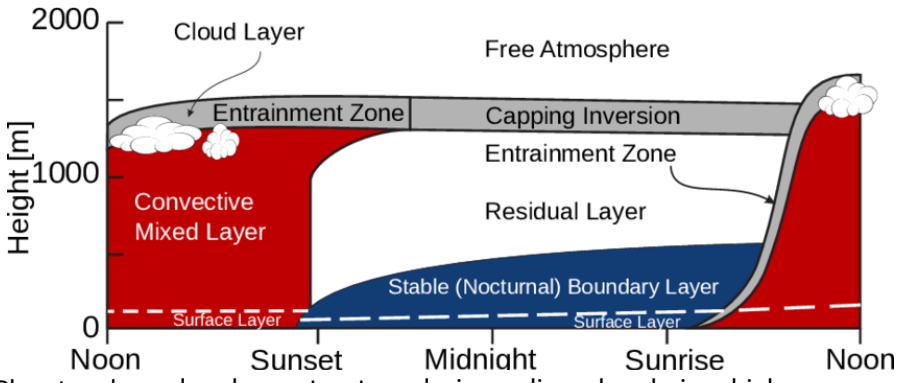

Figure 1. 2: Planetary boundary layer structure during a diurnal cycle in a high-pressure region over land. Adapted with permission of Springer, from "An introduction to Boundary Layer Meteorology", Stull (1988). modified by Allaerts et al. (2016).

1.2 Atmospheric aerosols

The term "aerosol" was first used to describe a stable liquid suspension of solid particles more than 80 years ago (Hinds, 1998). The simplest definition of an aerosol is a suspension of solid or liquid particles in a gas, and it encompasses a wide variety of phenomena including dust, fume, smoke, mist, fog, haze, and smog (Seinfeld and Pandis, 1998). Particles can either be created in the atmosphere by the oxidation of precursor gases or by condensing on already existing ones, or they can be directly released into it, by primary natural or anthropogenic sources. The first two processes produce particles that are referred to as primary particles and secondary particles, respectively (Finlayson-Pitts and Pitts, 1997; Seinfeld and Pandis, 1998). Both anthropogenic activities and natural sources produce particles that end up in the atmospheric circulation.

Atmospheric particles may come through four main activities: fuel combustion, industrial processes, non-industrial fugitive sources, and transportation activities. Their natural sources include arid areas, oceans, volcanic eruptions, forest fires and pollen. On a global scale, the natural aerosols are likely 4 to 5 times larger than the anthropogenic ones, but regional differences in man-made pollution may significantly alter this ratio in some areas, especially in the industrialized Northern Hemisphere (Seinfeld and Pandis, 1998). Aerosol sources can be used to classify the atmospheric aerosols into different categories. Atmospheric aerosols can be generated from both natural and anthropogenic sources, on a global basis, as can be seen in Figures 1.3.

(a)

(b)

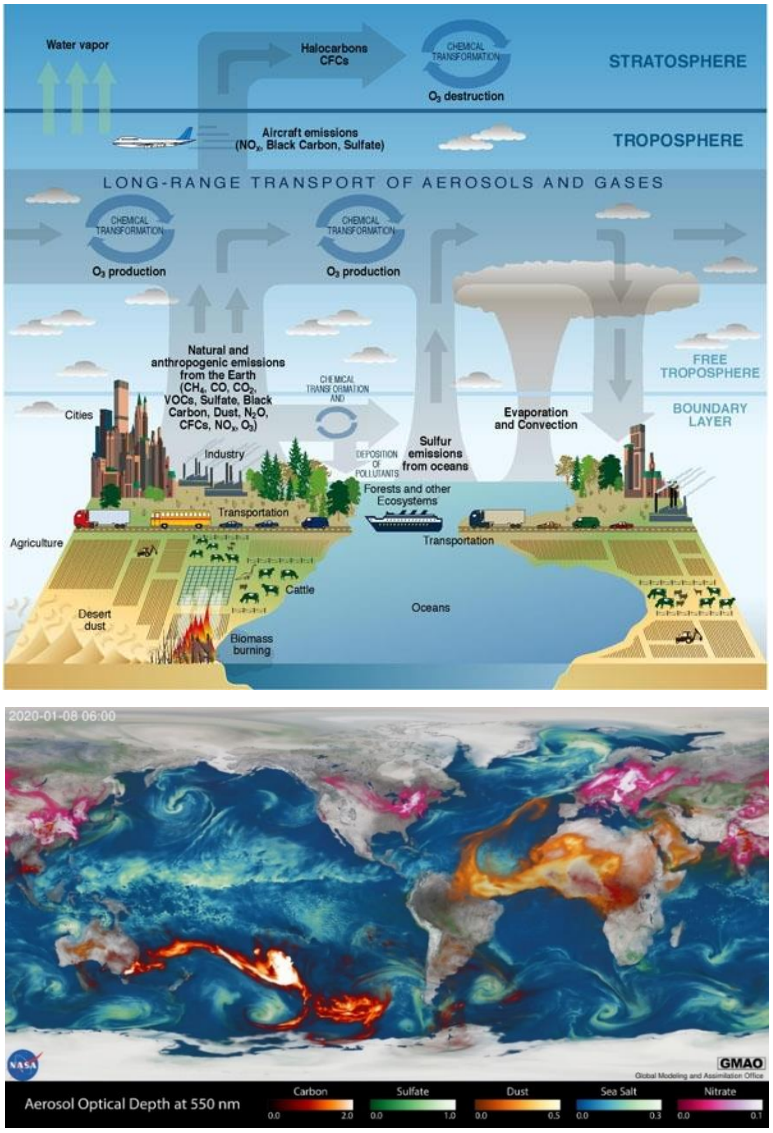

Figure 1. 3: (a) Sources of aerosol, both of anthropogenic and natural origin. Credit: CCSP Strategic Plan (illustrated by P. Rekacewicz), (b) main aerosol sources observed in a global scale (https://svs.gsfc.nasa.gov).

Atmospheric particles range in size from a few tens of Å to several hundred of µm. Particles with a diameter of less than or equal to 2.5 µm ($PM_{2.5}$) are generally referred to as "fine", while those with a diameter greater than 2.5 µm are referred to as "coarse" (Figure 1. 4). As a result, any discussion about aerosols' physical and chemical properties and health effects implies their distinction between fine and coarse. The fine and coarse particle modes, in general, are transformed separately, and are removed from the atmosphere by different mechanisms. They present different chemical compositions, optical properties, and differ significantly in their deposition patterns in the human respiratory system (Bui et al., 2020; Chalvatzaki et al., 2018).

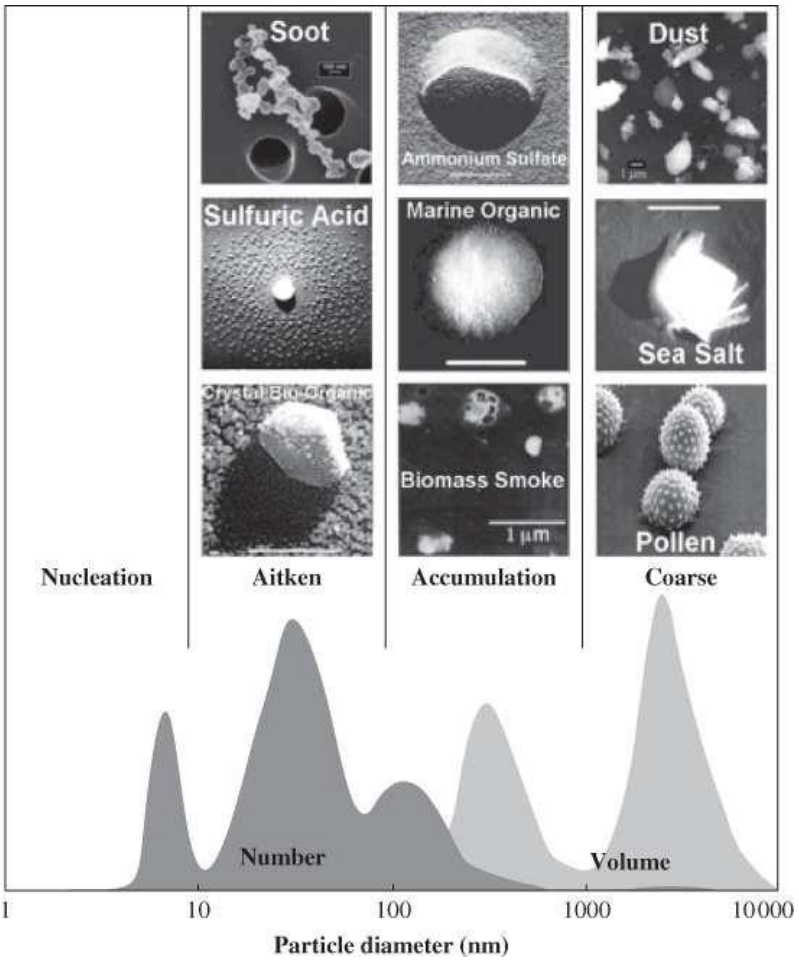

Figure 1. 4: Aerosol size distribution and morphology of various aerosol types (Colbeck and Lazaridis, 2014).

Particles in the atmosphere can change in size and composition through evaporation, condensation of certain vapor species, coagulation with other particles, chemical reactions, or activation in the presence of water supersaturation to form fog and cloud droplets. Both dry deposition at the Earth's surface and incorporation into cloud droplets during the formation of precipitation are methods by which particles are eventually removed from the atmosphere (wet deposition). Furthermore, aerosols vary in concentration and composition over the Earth, with their residence time in the troposphere varying from a few days to a few weeks, depending on deposition process and the uneven geographical distribution of particle sources (Seinfeld and Pandis, 1998).

1.3 Atmospheric aerosol types

The seven major categories of atmospheric aerosol types presented in this section are the following: *mineral dust, biomass burning (smoke), marine, continental clean and polluted and volcanic aerosols and bioaerosols*. However, according to each location of observation, atmospheric aerosols can be observed as *mixtures of different aerosol types* (e.g. polluted dust, as the mixture of dust and biomass burning aerosols).

1.3.1 Mineral Dust aerosols

Mineral dust is entrained into the atmosphere by the action of wind stress on the land surface. Most of the dust sources are arid or semiarid areas with low vegetation cover and easily erodible soils or fine-grained loose surface deposits (Prospero et al., 2002; Albani et al., 2014). Often, dust aerosols can be transported at distances of several thousand kilometers away from their origin, depending on the dynamic processes taking place in the production area (Ansmann et al., 2003; Mahowald et al., 2014). Mineral dust's interaction with the climate system is both *direct*, by absorbing and scattering short (SW) and long-wave (LW) radiation, and *indirect*, through aerosol-cloud interactions (Perlwitz and Miller, 2010). The arid regions of North Africa are estimated to emit about 800 Tg yr^{-1} of mineral dust, which is 70% of the global total and six times bigger than the second largest mineral dust source, Asia (Murayama et al., 2004).

Saharan dust storms significantly affect the European continent, during strong and regular events (Soupiona et al., 2019a; Kokkalis et al., 2021; Mylonaki et al., 2021c). However, even more distant regions are affected by these events, such as the Barbados Islands (Groß *et al.*, 2015), which have the longest continuous record of in situ atmospheric desert dust measurements, Puerto Rico (Gioda et al., 2013) and Miami (Prospero, 1999).

Figure 1. 5: Desert dust storm (left) and Saharan Dust Outbreak over Northwestern Africa (right) (earthobservatory.nasa.gov).

1.3.2 Biomass Burning (smoke) aerosols

Biomass burning (BB) aerosols can be produced by both natural (e.g., forest fires) and anthropogenic sources (e.g., anthropogenic wood and crop burning). BB emissions include elemental carbon (EC) and organic carbon (OC), as well as other particulate substances, along with gases such as CO_2, CO, NO_x, CH_4, and nonmethane hydrocarbons (NMHCs), while Black Carbon (BC) is produced from the incomplete combustion of both fuels and biomass.

BB aerosols play an important role in the Earth's climate system, as they scatter and absorb shortwave radiation (direct effect), while influencing the cloud processes as cloud condensation nuclei (CCN) or ice nuclei (IN) (indirect effect) (IPCC, 2014; Ortiz-Amezcua et al., 2017; McKendry et al., 2011; Torres et al., 2020). The kind of burning influences the size of the

smoke particles and the released amount of soot and, thus, the aerosols' chemical and optical properties. Flaming fires emit smaller and highly absorbing particles, whereas larger and less-absorbing particles are produced in smoldering fires. Smoke particles can experience medium- to long-range (intercontinental) transport, which can also affect the particles chemical and optical properties (Amiridis et al., 2008; Alados-Arboledas et al., 2011; Nicolae et al., 2013; Vakkari, 2014). It has been shown that smoke plumes from large forest fires can be injected into the free troposphere and stratosphere, and then easily be transported by air masses along the Earth (Ortiz-Amezcua et al., 2017; Hu et al., 2019; Ohneiser et al., 2020b; Papanikolaou et al., 2020, 2022a; Ansmann et al., 2020).

In Figure 1.6 we present satellite images (in the visible channel) of the record-breaking bushfires in Southeast Australia in the summer of 2019–2020, considered to be the most devastating in the history of the country (Ohneiser et al., 2020a; Khaykin et al., 2020; Papanikolaou et al., 2022a).

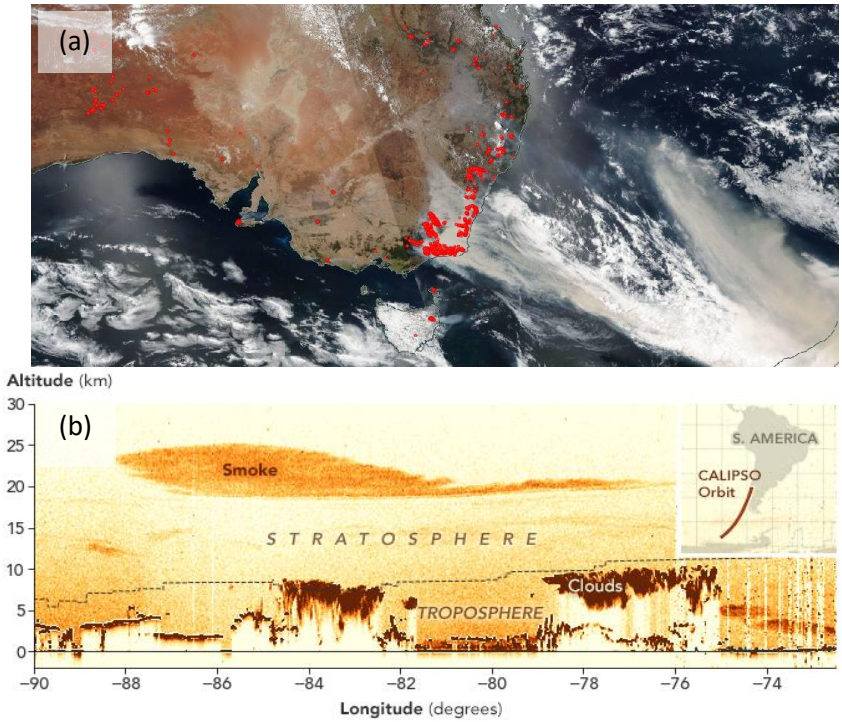

Figure 1. 6: (a) Wildfires burning across Australia, along with the smoke cascading off the edge of Australia on 01 January 2020, as captured by NOAA-NASA's Suomi NPP (https://www.nasa.gov), (b) smoke between 15 and 19 km in the stratosphere on 06 January 2020, as measured by CALIPSO, after the most explosive fire activity in Australia (https://earthobservatory.nasa.gov).

1.3.3 Marine (or sea spray) aerosols

The aerosols over the oceans play an important role in the Earth's atmosphere and climate system. Marine aerosols are generated mechanically, as well as chemically, from the atmospheric reactions of gases emitted from the sea surface (Saltzman, 2013). They mainly consist of sea salt hydro-genes or dimethylsulfide (DMS) from phytoplankton (Hoppel and Frick, 1990; Heintzenberg et al., 2000; Smirnov et al., 2003; Saltzman, 2013). Specifically, marine

aerosols feature a predominant coarse mode; dry marine aerosols (pristine sodium chloride crystals that form under ideal conditions) have cubic shape. However, marine aerosols are emitted as sea-spray in the atmosphere and depending on the relative humidity, the water in the emitted droplets can partly or completely evaporate, while the solid salt can partially or completely dissolve in the liquid coating (Kahnert and Kanngießer, 2023).

In continental areas it is difficult to find pure marine particles; nevertheless, they can be measured, either by stations located at the shorelines, under specific meteorological conditions or by shipborne platforms (Figure 1.7). Consequently, the observations of pure marine aerosols are rare, however, the high population in coastal European regions combined with the intense maritime traffic, create mixed marine aerosols (Preißler et al., 2013b; Papagiannopoulos et al., 2016, 2018).

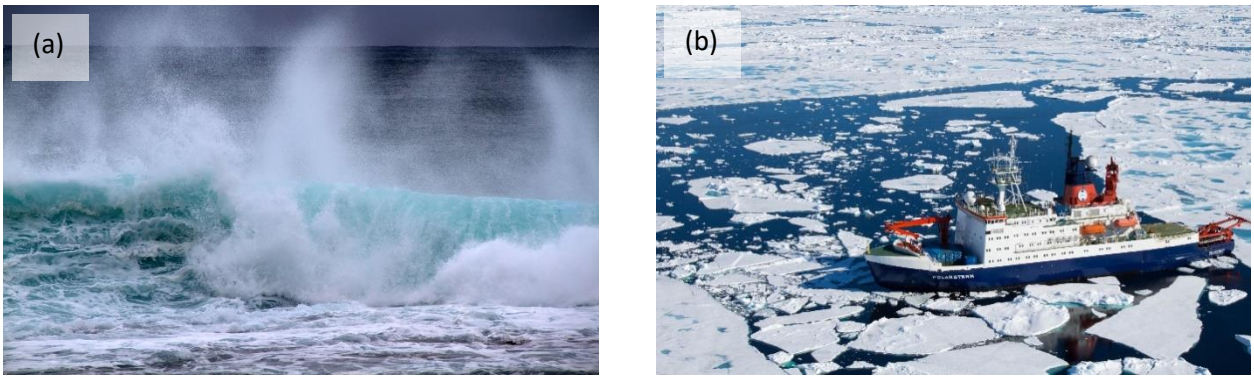

Figure 1. 7: (a) Sea-spray aerosols (https://source.colostate.edu/) and (b) shipborne aerosol measurements in Arctic (https://www.meteorologicaltechnologyinternational.com).

1.3.5 Clean and polluted continental aerosols

Clean continental aerosols, also called continental background or rural aerosols, represent a mixture of urban components with particles from agricultural activity and natural sources without or with very low anthropogenic contribution (less than 0.1 μg/m^3 soot). This type of aerosols can usually be observed after precipitation events, when particulate pollution has been removed from the atmosphere, or when clean air masses arrive from remote, less-polluted areas (e.g., from Northern or Northeastern Europe). Typically, no specific sources can be related to such aerosols. The clean continental particles are less light absorbing than the anthropogenic influenced.

Polluted continental aerosols, or urban aerosols, originate in highly industrialized regions, from fossil fuel combustion and traffic (Figure 1.8). Sulfate particles dominate in this aerosol type, while soot, nitrates, ammonium, and organic carbon are present as well. Since polluted air masses contains mainly water-soluble substances, the hygroscopic growth plays an important role on the aerosols' sizes (Chen et al., 2018). It should be noted that different stages of industrial development and environmental conditions lead to significant differences in the chemical and optical properties of polluted continental aerosols. Small continental polluted particles are

usually dominant in Europe and the United States, while in Southeast Asia larger particles can be found

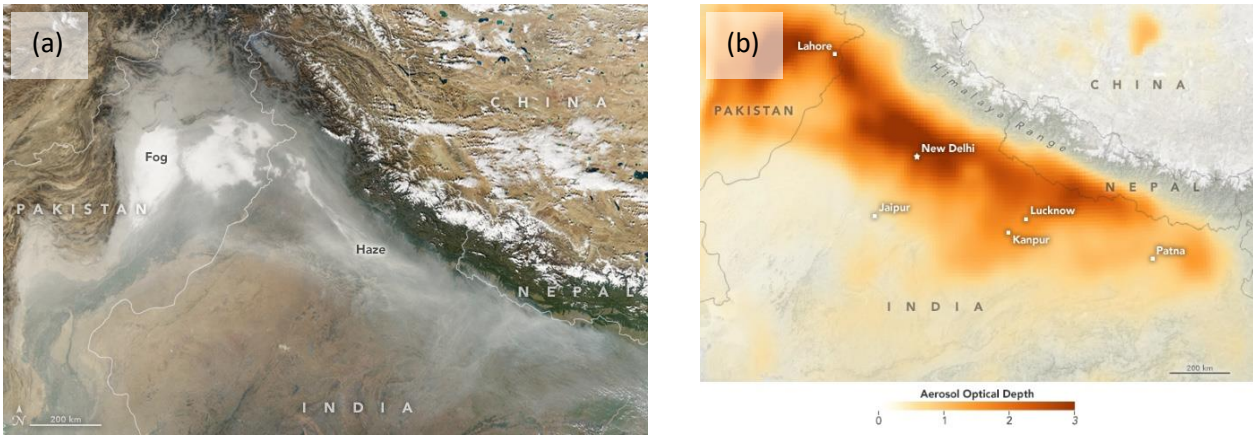

Figure 1. 8: (a) India obscured by air pollution in 2017 image and (b) the corresponding aerosol optical depth map, both acquired by MODIS (nasa.org).

1.3.6 Volcanic aerosols

Volcanic eruptions can emit aloft large amounts of aerosols and gases into the troposphere, and in some cases into the stratosphere. The emitted gases include CO_2, SO_2, along with HCl and other trace gases. SO_2 reacts with H_2O and OH to form sulfate aerosols (Millán et al., 2022). The sulfate aerosols produced by volcanic eruptions reside for 1–3 years in the stratosphere where they scatter sunlight, resulting in a net negative radiative forcing at the top-of-the-atmosphere and cooling at the surface (Aubry et al., 2021). For example, the eruption of Pinatubo volcano in Philippines in 1991 emitted millions of tons of sulfur dioxide and caused a global cooling of about 0.5°C (Minnis et al., 1993). On the other hand, on 14 April 2010 the eruption from ice-covered volcano Eyjafjallajökull, in Southern Iceland, released ash debris that due to prevailing meteorological conditions in the free troposphere, were advected to Europe within less than two days (Harris et al., 2012; Kokkalis et al., 2013. Papayannis et al., 2012). The event caused an almost complete disruption of the air traffic over Europe between 15 and 20 April, for the first time since the second world war. Volcanic aerosols that have been detected by lidar stations in Central and Southern Europe in the past, originated from eruptions of Mount Etna and other volcanoes on the Aleutian Islands, Kamchatka, Alaska, and on the Kuril Islands (Pappalardo et al., 2004; Zerefos et al., 2006; Wang et al., 2008; Mattis et al., 2010; Boselli et al., 2018). Among the most recent and most popular volcanic eruptions is the Hunga Tonga-Hunga Ha'apai eruption (January 15th 2022; Figure 1.9), off the coast of the Tonga island in the South Pacific Ocean that was characterized as one of the most explosive volcanic eruptions of the 21st century and has attracted global attention (Gui et al., 2022; Adam, 2022; Zhao et al., 2022; Zhang et al., 2022; Zuo et al., 2022; Rakesh et al., 2022; Proud et al., 2022).

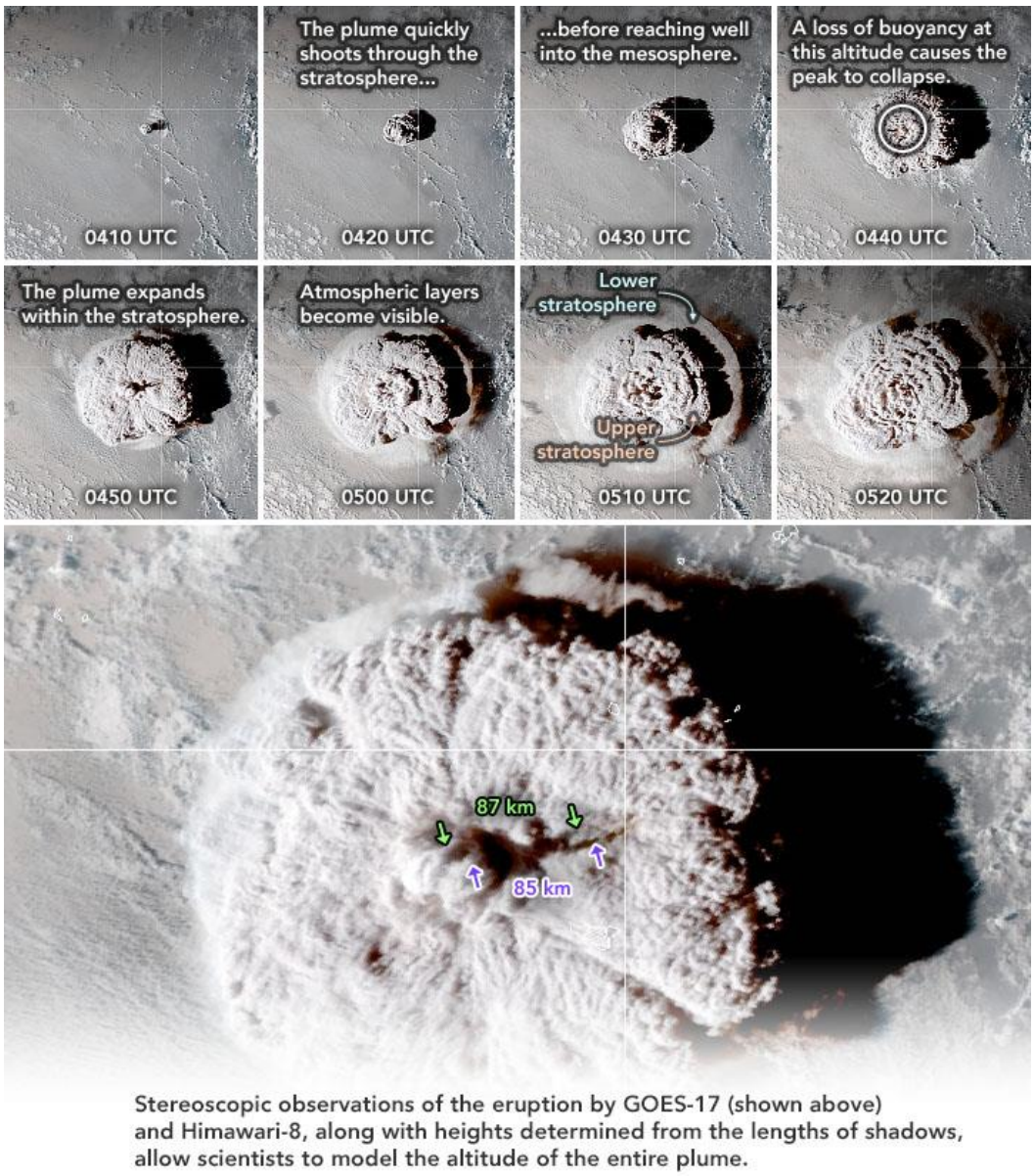

Figure 1. 9: Eruption of the under-sea volcano Hunga Tonga-Hunga Ha'apai as observed by GOES-17 and Himawari-8 (earthobservatory. nasa.gov).

1.3.7 Bioaerosols

The bioaerosols are airborne particles with a biological origin, such as bacteria, viruses, fungi, and fungal spores, which are various components or byproducts of living substances, such as pollen (Figure 1. 10). They are classified as coarse mode aerosols because of their diameters, which range from 10 nm to 100 µm. Bioaerosols have been the focus of much research over the past few decades because of their impact on human health (diseases, allergies, etc.) and their role in climate (acting as CCN or IN) (Fröhlich-Nowoisky et al., 2016; Richardson et al., 2019; Kim et al., 2018a; Lazaridis, 2019).

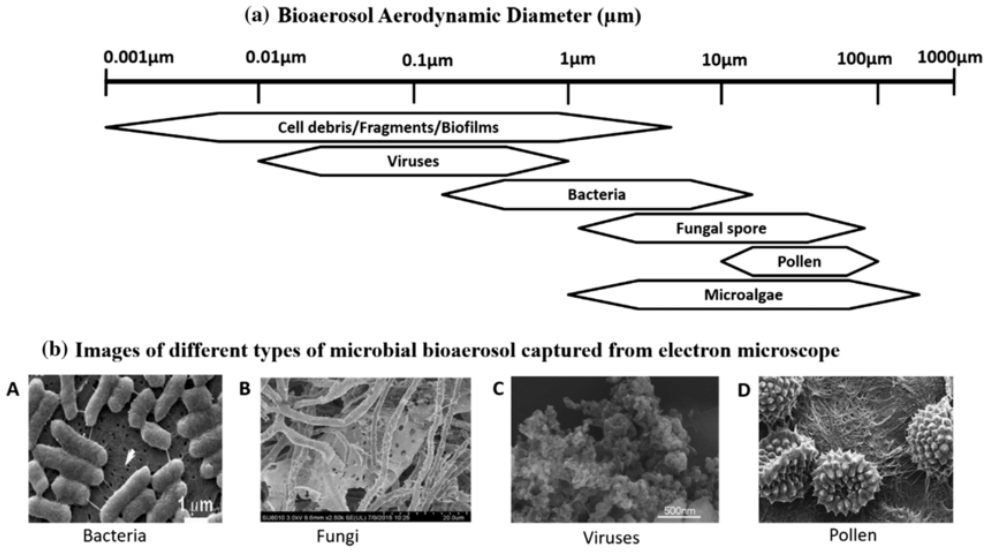

Figure 1. 10: Major bioaerosol components present in the atmosphere, (a) bioaerosol aerodynamic diameter and (b) images of different types of bioaerosol microorganisms view from an electron microscope. (Sharma Ghimire et al., 2019).

1.3.8 Aerosol mixtures

Different types of aerosols can be mixed, either during long pathways of air masse travelling across various aerosol sources, or when different aerosol sources are located close to each other, and, thus, mixing occurs directly after the aerosol emission. For instance, marine aerosols are large and non-absorbing, whereas BB aerosols show a considerable absorption and consist of relatively small particles. Thus, mixing of different aerosol types may result in quite different optical properties (Groß *et al.*, 2011a, 2013; Burton *et al.*, 2013; Zhu and Sartelet, 2016).

1.4 Aerosol climate effects

Atmospheric aerosols can affect the climate in various ways, as they interact with shortwave radiation, through scattering and/or absorption, disturbing the Earth's radiative balance i.e. the balance between the incoming shortwave radiation and the emitted Earth's radiation. As a result, when present in high quantities in atmosphere, they have a tendency to scatter sunlight, preventing the direct solar beams from reaching the Earth's surface, causing that way cooling at the surface. On the other hand, some of the aerosols are strongly absorbing (e.g.,

BC) and thus they produce a warming effect, locally. The aforementioned aerosol-light interaction is the so called “direct effect” of aerosols in the Earth’s climate. The degree to which suspended particles affect the climate depends on their shape, size and chemical composition (IPCC, 2014)

The *indirect effect* of atmospheric aerosols, is related to the aerosol-clouds interaction, that can change the clouds’ formation and characteristics. By serving as IN or cloud condensation nuclei, atmospheric aerosols can increase the clouds’ albedo and consequently the radiation scattered by them. Furthermore, the increased concentration of CCNs leads to cloud formation with higher concentration of water droplets, smaller effective radius of the droplets, which, consequently leads to a decrease in the probability of precipitation (Seinfeld and Pandis, 2006). Moreover, absorbing aerosols (like BC), lead to rapid adjustments, and the corresponding perturbation to the atmospheric temperature structure alters the cloud distribution, also known as semi-direct effect. The level of scientific understanding of semi-direct effect is considered low, with models indicating a likely negative (−0.44 to +0.1 W/m^2) forcing (Allen et al., 2019).

To measure the possible aerosol impact on the Earth’s radiative balance, the term of Radiative Forcing (RF) is utilized. RF is defined as an energy imbalance imposed on the Earth’s climate system, either naturally (e.g., changes in solar energy output, volcanic eruptions, etc.) or by human activities (e.g., emissions of greenhouse gases, aerosols, etc.). It is usually expressed in W/m^2, averaged over a particular period of time. In Figure 1.11, we present the global average effective RF estimations in 2019 compared to 1750, as well as the uncertainties for the main drivers of the Earth's climate, as obtained from IPCC AR6 (IPCC, 2022). Current growth in forcings is dominated by CO_2 with 2.16 (1.90 to 2.41) W/m^2. The forcing from well-mixed greenhouse gases, is 0.54 (0.43 to 0.65) W/m^2 for methane (CH_4), 0.21 (0.18 to 0.24) W/m^2 for nitrous oxide emissions (N_2O) and 0.41 (0.33 to 0.49) W/m^2 for halogens. In general, aerosols contribute negatively to the forcing with –0.22 (–0.47 to 0.04) W/m^2 for aerosol-radiation and –0.84 (–1.45 to –0.25) W/m^2 for aerosol-cloud interactions (Figure 1.11). The total anthropogenic forcing is 2.72 (1.96 to 3.48) W/m^2 and most of the uncertainty is still related to aerosol effects (IPCC, 2022).

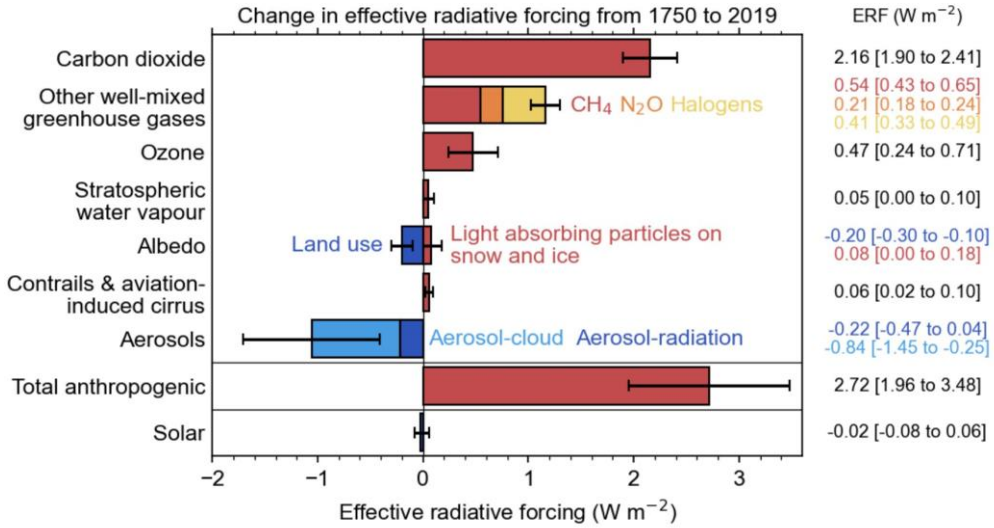

Figure 1. 11: The change in effective radiative forcing from 1750 to 2019 (IPCC, 2022).

CHAPTER 2
REMOTE SENSING OF THE ATMOSPHERE

2.1 Light and matter interaction

When light is transmitted through a medium, it suffers extinction, as a result of two main extinction processes: absorption and scattering. *Transmition* is the propagation of light within a medium, in our case the atmosphere. For an initial intensity I_o and I, the intensity of the radiation that has passed through the atmosphere, the transmittance is given by:

$$T = I/I_o \tag{2.1}$$

And Beer–Lambert law (citation) is commonly expressed as:

$$A = \log_{10}(I_o/I\,) \;=\; \varepsilon c l \tag{2.2}$$

Where, A is the absorbance (no units), $\log_{10}(I_o/I\,)$ can be recognized as $1/T$, the quantity ε is a constant called ε is the molar absorptivity (l mol^{-1} m^{-1}), c is the concentration (mol l^{-1}) and l is the length of the light path (m).

Absorption is one of the possible results during the interaction of light and matter. Absorption occurs when the wavelength coincides with the absorption band of the corresponding molecule and for a photon to be absorbed, it has to be of a specific wavelength (λ). Because of the principle of conservation of energy, the absorption of light induces a change in the energy state of the atom (or molecule) by either an electronic, vibrational, or rotational transition.

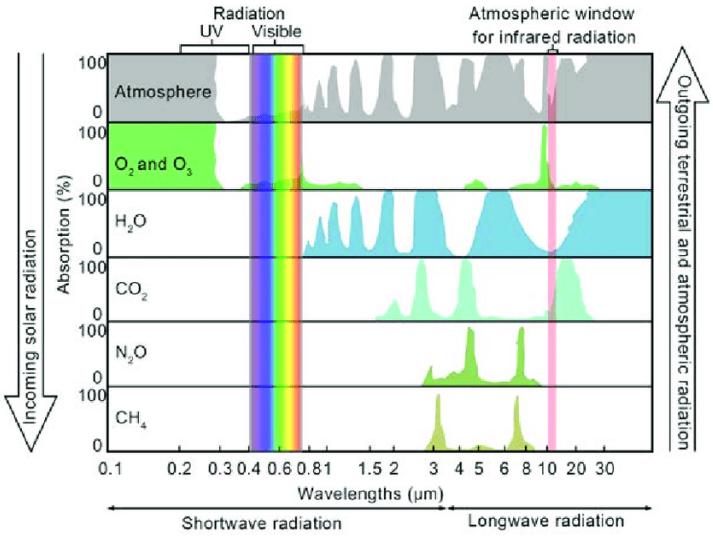

Figure 2. 1: Absorption spectra of the most important trace gases in the atmosphere (Takle, 2015).

Extinction of light is the sum of the absorption and scattering processes; thus, it represents the total effect of light attenuation passing through a medium. The key parameters ruling the scattering and absorption processes are: the value of the incident radiation λ, the size and the complex refractive index (CRI) of the scatterer.

Scattering occurs when particles or large molecules present in the atmosphere, interact with and cause the electromagnetic radiation to be redirected from its original path (Figure 2.2). The amount scattered in any direction is described by the single scattering phase function P(θ), where θ is the scattering angle, that is the angle between the scattered light and the forward direction (e.g. backscatter corresponds to θ = 180°).

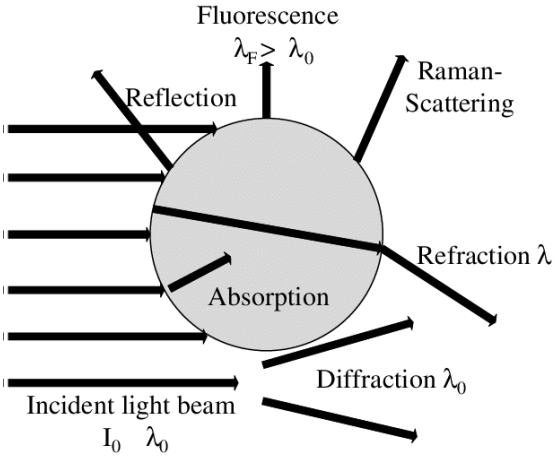

Figure 2. 2: Potential interaction between an incident light beam and a spherical particle (Glasse et al., 2014).

Elastic scattering occurs when there is no loss of the incident photon's energy, keeping the λ of the scattered light unaltered. The two elastic scattering processes are *Rayleigh* and *Mie* scattering. The first one occurs when the scatterers are much smaller (radius less than ~ 1/10) than the λ of the radiation, while the second one occurs when the scatterers have a similar size as the λ of the incident light.

Rayleigh scattering is used as a synonym of scattering by the molecules of the atmosphere. The Earth's Atmosphere is composed of 99% of nitrogen and oxygen and for this reason we consider these two gases as the source of Rayleigh scattering. The intensity of the Rayleigh scattered radiation is inversely proportional to the fourth power of wavelength ($\sim\lambda^{-4}$).

Mie scattering is not limited to a particular scatterer size, as it even includes Rayleigh scattering. Scattering from greater particles does not depend on the wavelength of the radiation. The spectral dependence of the intensity of scattered radiation varies in the region where particle size and wavelength of radiation are of comparable magnitude. For this reason, information on the size and other properties of air components for particles may be derived using the spectrum dependence of scattered light. The small, compared to the wavelength, particles interact with radiation, without their shape playing an important role in the scattering processes. On the other

hand, the theory of Mie scattering cannot be applied to the large and non-spherical particles (e.g., ice crystals, desert dust) (Kovalev and Eichinger, 2004). The atmospheric scattering as a function of the scatterers radius and incident radiation wavelength is presented in Figure 2.3.

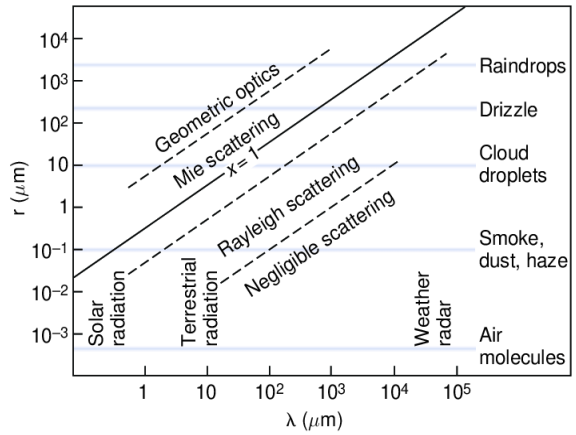

Figure 2. 3: Atmospheric scattering as a function of particle radius and incident radiation wavelength (Wallace and Hobbs, 2006).

Fluorescence of light is based on the fact that in elastic scattering, apart from the photons of the incident beam that are redirected from their original path, without a change in photon energy, absorption of light by the particle can also occur. In the latter case, the absorbed energy may be released as a thermal emission or fluorescence. The former is believed to be the dominant process, yet certain aerosol particles containing bio-agents have been found to be fluorescent (Veselovskii et al., 2022; Union et al., 2005; Pan et al., 2007; Richardson et al., 2019).

A typical example of an inelastic scattering is the Raman scattering, which occurs in molecules when the kinetic energy of the incident photon is increased (Stokes Raman scattering) or reduced (anti-Stokes Raman scattering) during the molecular interaction (Figure 2.4a). By measuring the energy difference between the incident electromagnetic radiation and the scattered electromagnetic radiation, important information about the vibrational energy and frequencies can be obtained. The energy difference between a molecule's starting and final state determines the frequency change of scattered radiation, which is unique for each molecule. Changing the energy level of the molecule oscillation results in a frequency change that ranges from a few hundred to a few thousand cm^{-1} depending on the Raman scattering molecule (Kovalev and Eichinger, 2004).

The air molecules of nitrogen (N_2) oxygen (O_2) water vapor (H_2O) have a sufficient concentration to produce Raman signals detectable with a lidar. The rotational-vibrational Raman spectra, with an incident light at 355 nm excites the atmospheric N_2 molecules, which emit light at the 1st Stokes line at 387 nm, while the Raman lines of the water vapor are at 407 nm (Figure 2.4b). When the incident beam is at 532 nm, the Raman scattered photon is detected at 607 nm.

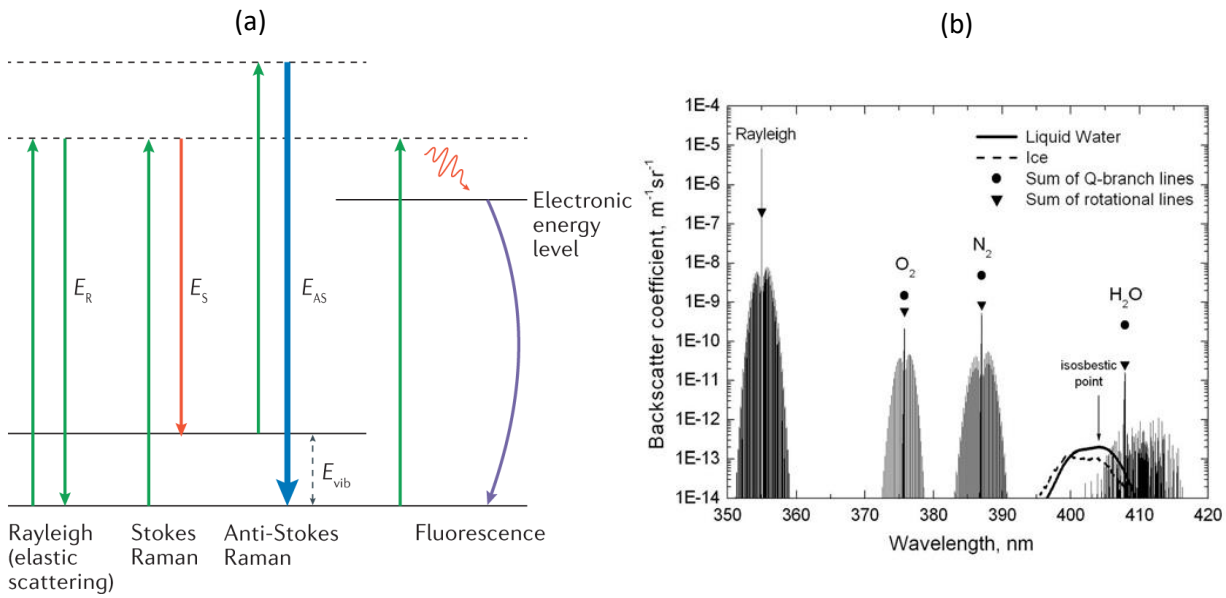

Figure 2. 4: (a) Energy level diagram of Rayleigh scattering, Raman scattering and fluorescence (Mosca et al., 2021), (b) Atmospheric Raman backscatter spectrum for a stimulation wavelength of 355 nm (Wandinger, 2005).

Finally, the *light depolarization* effect provides information about the shape of the scattering particles. Spherical scatterers do not change the polarization state of an incident laser beam when it is linearly polarized, whereas non-spherical scatterers lead to a depolarization of the backscattered radiation. As a result, polarization-sensitive light detection is especially valuable in the study of cirrus clouds and dust layers (Freudenthaler et al., 2009). When the polarization state of the laser radiation emitted is well known, it is possible to measure how much radiation is backscattered in the same polarization and how much at the perpendicular (Figure 2.5).

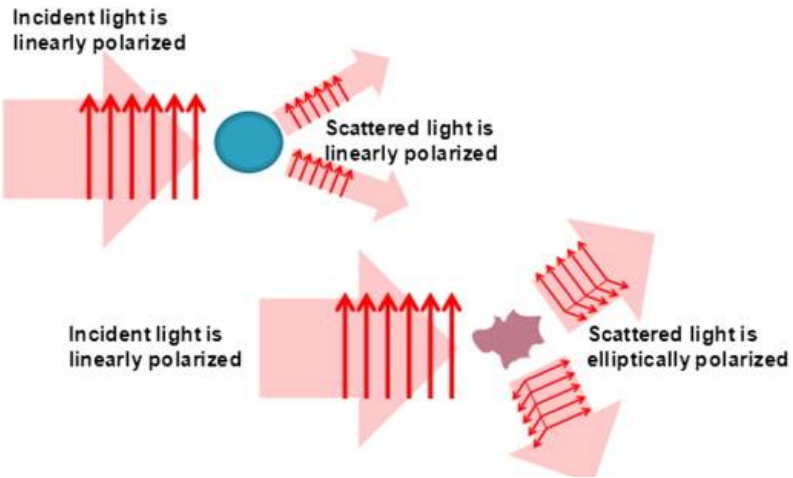

Figure 2. 5: Diagram illustrating the interaction between linearly polarized light with spherical and non-spherical particles (Baumgardner et al., 2014).

2.2 Atmospheric lidar and operating principles

The term “lidar” stands for “Light Detection and Ranging” and is an active remote sensing system that measures the effect of light interaction with the atmospheric components. Lidars are based on the emission of monochromatic electromagnetic radiation, the detection of the backscattered radiation from particles, atoms and molecules, and the recording of the time elapsing between emission and reception, which corresponds to the distance the target has from the laser source. Based on the optical characteristics of its constituent parts, this operation produces a “snap shot” of the vertical profile of the air components measured by the instrument. Due to their high spatial and temporal resolution, lidar systems have a wide range of uses in atmospheric research, as they are used to measure various atmospheric properties, such as the atmospheric humidity and temperature, the wind speed and the ozone in the atmosphere, as well as the atmospheric aerosols. This Ph.D. Thesis is focused on the use of lidars to measure the vertical distribution of the aerosol optical properties.

The emission and transmission of light pulses into the atmosphere, the interaction of the radiation with the atmospheric components, through scattering, absorption, depolarization and fluorescence, and eventually, the detection of the backscattered laser radiation from the lidar system are the basic physical mechanisms occurring during the lidar operation. A receiving telescope detects all backscattered laser light and then the detected lidar signals are spectrally separated and fed to photomultiplier tubes (PMTs) or Avalanche Photodiodes (APDs). The output signal pulses from the PMTs and APDs are processed to obtain information about the type of scatterer, its composition, its distance from the instrument, as well as its spatial and temporal distribution in the atmosphere.

A typical lidar system layout (Figure 2.5) consists of laser transmitter, an optical receiver and a data acquisition sub-system. The laser generates short light pulses with a pulse duration from a few fs to a few tens of ns, within a certain range of wavelength (250 nm to 11 μm), depending on the application. The light pulses have sufficient energy, moderate repetition rate, and low divergence. Beam expanders are commonly used in lidar systems to decrease the emitted laser beam's divergence. The backscattered photons are collected by the telescope within the receiving part. Important parameter of this part of the lidar system is the primary mirror and its reflectance. Following the telescope's collection of backscattered photons, the optical signal from each photon is transformed into an electrical signal by the detector. Several optical filters spectrally filter the collected lidar signals before sending them to the photomultipliers and avalanche photodiodes, depending on the working wavelengths (Papayannis et al., 1990).

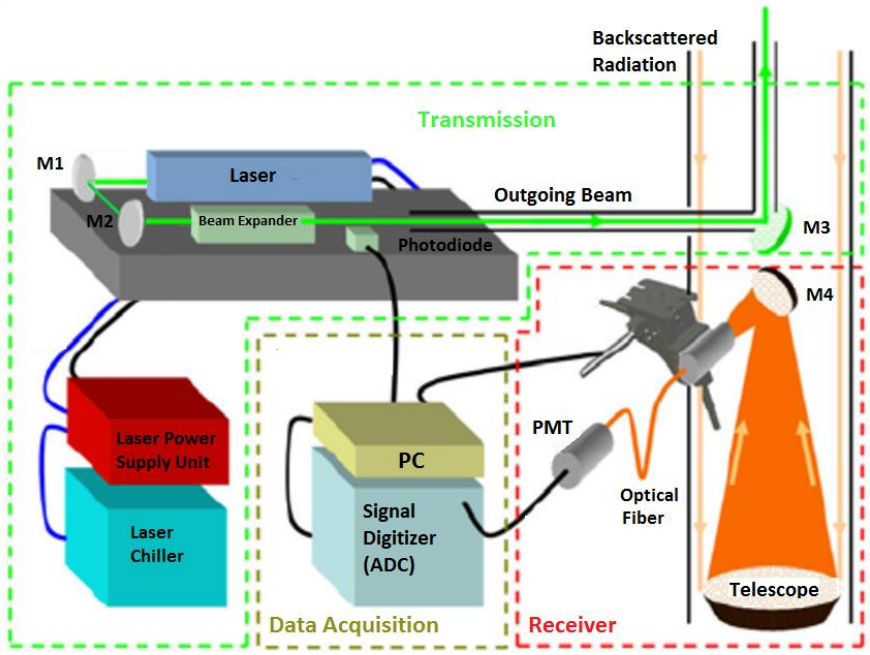

Figure 2. 6: Typical lidar system layout showing the transmission, receiver and data acquisition sub-systems (Sharma et al., 2009).

2.3 Lidar Signals Processing

The lidar data processing is performed on the raw lidar signals. Before extracting the aerosol optical characteristics, it is important to make the following measurements and adjustments as part of the data "pre-processing".

First and foremost, here are two techniques of measuring the detected backscattered lidar signal: the *Analog mode,* with high linearity, which is efficient in measuring strong signals at low altitudes and the *Photon-counting mode*, that has the capability to measure weak signals from high altitudes (D 'amico et al., 2015).

The fist detection mode, Analog Detection (AD), is based on an analog-to-digital converter (ADC), which samples and digitizes the lidar signals. Depending on the type of the Transient Recorder (TR-XX-YYY) the sampling rate (XX) ranges from 20 MHz (7.5 m range resolution) to 40 MHz (3.75 m range resolution). The memory length (YYY) defines the maximum signal length and repetition rate and ranges from 80 (8192 databins) to 160 (16384 databins). Lidar signals are usually averaged over time intervals of a few minutes (~1.5 min.) to reduce the amount of data that must be stored and decrease the noise level.

The Photon-counting detection mode (PC) is used to measure flux levels as low as a few tens of photons per second. In the photon counting mode, cathode emits only single electrons, while the individual anode charges are integrated to produce proportional voltage pulses, which are passed through a discriminator to a pulse counter.

So, in order to avoid the saturation of the signal in short distances and maintain the system's sensitivity in far distances, we perform the "gluing" of both signals measured by each mode, which gives the advantage of generating one single lidar signal with high linearity, due to the AD signals in near range and the PC mode in far range. Gluing algorithms solve the fitting coefficients by matching both AD and PC data over a predefined spatial range (D'Amico et al., 2016).

Moreover, *a trigger delay correction* is applied to the lidar data. Trigger delay is a delay between the actual time of the outgoing laser pulse and the time at which the acquisition system starts to record the lidar signal. This delay implies a systematic shift on the atmospheric range gates which finally causes a systematic error in the range-correction of the lidar signal, which can propagate to the calculation of the final aerosol properties (D'Amico et al., 2016).

When retrieving lidar profiles, it is necessary to take extra precautions to carefully remove not only outliers, spikes, and electronic contamination from each profile in the signal useful regions, but also in the background region. Any contamination of the signal in the background region has the same order of magnitude as the true signal and, thus, produces a disproportionate effect on the lidar profile. The atmospheric background noise including sunlight and cosmic noise is not range-dependent. Thus, it should be determined at the very far range of the lidar profile, where the transmitted laser beam has been totally attenuated and hence only atmospheric background and cosmic noise might be present.

One of the main hardware limitations of the PC mode is that this acquisition mode presents a *dead time*, which corresponds to a period of insensitivity after a photon detection during which arriving photons cannot be registered. When the backscatter lidar signal is strong the number of uncounted photons is significant and can lead the detector to saturation.

Finally, the overlap correction refers to the incapability of the laser beam to totally enter the telescope's field-of-view. The effect of the overlap function on the backscattered lidar signal is eliminated above a certain altitude, called overlap height. This is the minimum distance of full overlap where the overlap function $O(R)$ equals 1. To minimize the distance of full overlap, the laser beam is transmitted to the atmosphere with a small tilted angle. Above that range, the backscattered light beam is totally captured by the receiver telescope. However, at any lower altitude from ground to this full overlap range, the backscattered signal is affected by the incomplete overlap function (i.e., $O(R) < 1$; Wandinger, 2005).

2.4 Aerosol optical properties measured by lidar

The determination of the optical properties of the suspended particles is based on the solution of the two following lidar equations:

$$\mathrm{P}(\lambda, r) = P_0 \cdot \frac{c\tau}{2} \cdot \mathrm{A} \cdot \eta \cdot \frac{\mathrm{O}(r)}{r^2} \cdot \mathrm{b}(\lambda,\ r) \cdot \exp\left[-2 \int_0^{\mathrm{r}} \mathrm{a}(\mathrm{R}, \lambda)\mathrm{d}R\right] +\ P_{bg} \tag{2.3}$$

$$\mathrm{P}(\lambda_{\mathrm{Ra}}, \mathrm{r}) = P_0(\lambda_0) \cdot \frac{c\tau}{2} \cdot \mathrm{A} \cdot \eta \cdot \frac{\mathrm{O}(r)}{r^2} \cdot \mathrm{b}_{mol}(\lambda_{Ra},\ r) \cdot \exp\left[-\int_0^{\mathrm{r}} (\mathrm{a}(\lambda_0, R) + \mathrm{a}\ (\lambda_{Ra}, R)\mathrm{d}R\right] \tag{2.4}$$

Equation (2.1) describes the elastically backscattered lidar signal from a range r while the Raman signal equation is described by equation (2.2) (Weitkamp, 2005). The term P is the measured signal power due to the elastic and the Raman scattering, while the λ_0 and λ_{Ra} are the emitted wavelength and the Raman wavelength that occurs due to inelastic scattering, respectively. P_0 is the average power of a single laser pulse emitted, c is the speed of light, τ is the temporal pulse length, A is the area of the primary receiver optics (telescope), η is the overall system efficiency and O(r) describes the overlap between the outgoing laser beam and the receiver field of view (overlap function). The term b is the atmospheric (total) backscatter coefficient:

$$\mathrm{b}(\lambda,\ r) = b_{mol}(\lambda,\ r) +\ b_{aer}(\lambda,\ r) \tag{2.5}$$

that expresses the elastic backscatter from the molecules and aerosols of the atmosphere. The term a is the atmospheric (total) extinction coefficient, that is related to scattering and absorption of light by molecules and aerosols:

$$\mathrm{a}(\lambda,\ r) = \mathrm{a}_{mol}(\lambda,\ r) +\ \mathrm{a}_{aer}(\lambda,\ r) \tag{2.6}$$

The last term, P_{bg}, includes the atmospheric background light and any electronic (thermal noise and the dark current noise of the detectors used) background noise signal.

In the case where the total backscattered radiation is known without distinction between the contribution of molecules and particles we apply the method by Klett (Klett, 1981). The molecular atmosphere scattering properties, $\mathrm{b}_{mol}(\lambda, r)$ and $\mathrm{a}_{mol}(\lambda, r)$ are considered known and determined from the best available nearby meteorological radiosonde data or approximated from a standard atmospheric model. The most critical parameter in the Klett method is the correct assumption of the extinction-to-backscatter ratio, i.e. the lidar ratio (LR). The LR has to remain constant with range, meaning that the size distribution and composition of the aerosol scatterers are not changing with range and that the variations in the aerosol backscattering are only due to changes in their number density.

Following the assumption of the, constant with altitude, LR for aerosols:

$$\mathrm{LR}(\lambda) = \frac{\mathrm{a}_{aer}(\lambda,r)}{\mathrm{b}_{aer}(\lambda,r)} \tag{2.7}$$

while LR_{mol} (λ) is considered constant and for the full-beam area of the laser beam with the telescope's field of view, the lidar equation can be solved as follows:

$$S(\lambda,r) = \mathrm{P}(\lambda,r) - P_{bg} \tag{2.8}$$

So that the background signal P_{bg} to be subtracted from the detected lidar signal P (λ, r). Then, the Range Corrected Signal (RCS) using the equation (2.3) will be:

$$RCS(\lambda,r) = S(\lambda,r) \cdot r^2 \tag{2.9}$$

$$RCS(\lambda,r) = \eta \cdot P_0 \cdot O(r) \cdot [b_{mol}(r,\lambda) + b_{aer}(r,\lambda)] \cdot exp\left[-2\int_0^r \left(\mathrm{a}_{mol}(\lambda,R) + \mathrm{a}_{aer}(\lambda,R)\right)dR\right] \tag{2.10}$$

Thus, the backscatter coefficient will be calculated as follows:

$$\mathrm{b}(\lambda,r) = \frac{RCS(\lambda,r)\cdot\exp\left[2(LR(\lambda)-LR_{mol})\int_r^{r_{ref}} b_{mol}(\lambda,R)dR\right]}{\frac{RCS(\lambda,r_{ref})}{C\cdot b_{mol}(\lambda,r_{ref})} + 2LR(\lambda)\int_r^{r_{ref}} RCS(\lambda,R)\cdot\exp[2(LR(\lambda)-LR_{mol})\cdot\int_R^{r_{ref}} b_{mol}(\lambda,r')dr']\,dR} \tag{2.11}$$

where

$$C = \frac{b_{mol}(\lambda,r_{ref}) + b_{aer}(\lambda,r_{ref})}{b_{mol}(\lambda,r_{ref})} \tag{2.12}$$

In eq. 2.11, r_{ref} is the reference height and by making the assumption that in r_{ref} there is an aerosol free region, we can assume that b_{aer} (λ, r_{ref}) = 0, and thus, C=1. Then, the a_{aer}(λ, r) can be estimated from equation (2.7).

The privilege of the Raman technique is that the only unknowns are the aerosol extinction coefficients at the two wavelengths, λ_0 and λ_{Ra}. However, the *Ångström exponent* ($\mathring{A}_a$) is considered known for the two wavelengths, λ_0 and λ_{Ra}, so the aerosol extinction coefficients can be retrieved from (2.13) without the assumption of a constant LR (Ansmann et al., 1992):

$$\mathrm{a}_{aer}(\lambda,r) = \frac{\frac{d}{dr}\left(ln\frac{N_{Ra}}{P\cdot r^2}\right) - \mathrm{a}_{mol}(\lambda,r) - \mathrm{a}_{mol}(\lambda_{Ra},r)}{1+\left(\frac{\lambda}{\lambda_{Ra}}\right)\mathring{A}_a} \tag{2.13}$$

Thus, the Raman backscatter coefficient and accordingly the lidar ratio vertical profile can be independently calculated, using the backscattered signal from the atmospheric molecules. The error introduced by the estimation of the $\mathring{A}_a$ can lead to an uncertainty of less than 10% (Ferrare and Feltz, 1999). The lidar ratio can be derived from the profiles of $a_{aer}(\lambda,r)$ and $b_{aer}(\lambda,r)$ determined in an independent way and with the same time and height resolutions. This can be obtained, either by using the Raman technique or it can also be estimated using the combination of co-located elastic lidar and sun photometer measurements (Mattis et al., 2004).

The $\mathring{A}_a$ indicates the aerosol extinction coefficient dependence on the wavelength, and it is defined by Angström (1929) as:

$$\mathring{A}_a = \frac{\ln\left[\frac{a_{aer}(\lambda_{1,r})}{a_{aer}(\lambda_{2,r})}\right]}{ln\frac{\lambda_1}{\lambda_2}} \tag{2.14}$$

As the lidar ratio, the $\mathring{A}_a$ is not dependent on the aerosol concentration, but on the aerosol properties. In general, the coefficient value rises as the aerosol size decreases and is affected by the complex refractive index of the particles.

Moreover, as it is well documented that atmospheric aerosols vary in shape, the depolarization factor based on the phenomenon of the depolarization of light is used to define the shape of the aerosols. The volume linear depolarization ratio (VLDR) is defined as the ratio of the perpendicular to the parallel component of the total backscatter coefficient and is given by the equation:

$$\mathrm{VLDR} = \frac{b_{\perp}}{b_{\parallel}} \tag{2.15}$$

Particle linear depolarization ratio (PLDR) is defined as the ratio of the perpendicular polarization component to the parallel component of aerosol backscatter coefficient (without molecular part):

$$\mathrm{PLDR} = \frac{b_{aer_{\perp}}}{b_{aer_{\parallel}}} = \frac{(1+LDR_{mol})\cdot VLDR\cdot R-(1+VLDR)LDR_{mol}}{(1+LDR_{mol})\cdot R-(1+VLDR)} \tag{2.16}$$

where R the ratio of the aerosol to the molecular backscatter coefficient, also known as the scattering ratio and can be retrieved from the total lidar signal P (Freudenthaler et al., 2009), while LDR_{mol} is the depolarization factor of the molecules in the atmosphere and can be easily calculated (Murayama et al., 1999).

To measure the depolarization of the radiation due to the non-spherical aerosols, a calibration method is necessary to be performed. The “±45° calibration technique” is one of the

widely used calibration technique (Freudenthaler *et al.*, 2009). The process requires the recording of the backscattered lidar signals, $b_{\perp}$ and $b_{\parallel}$, by rotating the depolarization analyzer at ±45° with respect to the default measuring position (Belegante et al., 2018).

Finally, the aerosol optical depth (AOD), can also be obtained by a lidar measurement, using the total aerosol extinction, that represents the aerosol load in an air column (Liou, 2002). AOD is frequently used to measure the concentration of aerosol particles in the atmosphere. AOD can be calculated by integrating the aerosol extinction coefficient over height:

$$AOD = \int_0^r a_{aer}(\lambda, r)\, dR \tag{2.17}$$

2.5 Processing of the Cloud-Aerosol Lidar with Orthogonal Polarization (CALIOP) profile data

2.5.1 Cloud-Aerosol Lidar with Orthogonal Polarization (CALIOP) system

The Cloud-Aerosol Lidar with Orthogonal Polarization (CALIOP) system, on board the Cloud-Aerosol Lidar and Infrared Pathfinder Satellite Observation (CALIPSO) satellite, was launched on April 28, 2006 (Winker et al., 2009). It consists of the emission and the signal acquisition subsystem. The laser emission subsystem includes two Q-switched Nd: YAG lasers. Each laser emits 110 mJ/pulse at 532 nm and 1064 nm, simultaneously with a pulse repetition frequency of 20.16 Hz, and a 20 ns pulse duration. The emitted beams exit with a high degree of linear polarization. To reduce the angular deflection of the laser beam emitted, two beam expanders are used to finally produce a beam of 70 m in diameter on the surface of the earth. The backscattered lidar signal is received by a 1-m-diameter telescope and separated into three channels: the 1064nm where the signal is detected by an avalanche photodiode (APD), and two channels where the two orthogonal (parallel and perpendicular) polarizations at 532 nm, where the signals are detected by photomultipliers (PMTs). Each laser is placed in a sealed metal can, filled with dry air at a pressure slightly higher than the atmospheric pressure. Inside this box there are also laser pulses energy counter (Winker et al., 2009).

2.5.2 CALIOP data

The CALIPSO data are accessible via the National Aeronautics and Space Administration (NASA) Langley Research Center Atmospheric Science Data Center (LaRC ASDC). The information is stored in Hierarchical Data Format (HDF), the standard data format for all NASA Earth Observing System (EOS) data products. The CALIPSO lidar data (also referred to as CALIOP lidar data) are stored for day- and night-time conditions (day and night orbit) and are available in various ‘‘levels’’ that, according to NASA Earth Observing System (EOS) standards, reflect the degree of processing involved for different levels:

- Level 1B data contain calibrated and geo-located profiles (half orbit, night and day).

- Level 2 data sets provide geophysical products subdivided in aerosol or cloud information reported for layers as well as for profiles. They also contain information on the vertical feature mask (aerosol particle properties, cloud type, cloud particle phase) and of polar stratospheric clouds.
- Level 3 data are globally gridded and monthly averaged Aerosol Profile data and ancillary data.

2.5.3 Level 2 Aerosol Profile products

The most detailed analysis of feature optical properties is provided by the range-resolved cloud and aerosol profile products. Included in the standard output are profiles of total, parallel, and perpendicular backscatter at 532 nm, extinction coefficients and particulate depolarization ratios at 532 nm. The nighttime profiles from the 532 nm channels are calibrated by the standard lidar technique of normalizing the high-altitude return signal to a molecular model, while daytime calibrations are interpolated from adjacent nighttime calibrations. The 1064 nm profile is calibrated relative to the 532 nm backscatter intensity using returns from cirrus clouds (Winker et al., 2009). The CALIPSO polarization gain ratio is used to quantify the differences in the responsivity and gain of the two 532-nm detection channels and calculates the ratio of the nearly equal optical fluxes incident on the parallel- and perpendicular-channel detectors as a spatial pseudodepolarizer is inserted into the 532-nm receiver optical path (Powell et al., 2009).

The ancillary scalar-valued information reported with each set of profiles includes time and position data (latitude, longitude), surface elevation statistics, and a set of quality assurance flags. The meteorological context is provided by accompanying profiles of temperature and atmospheric pressure and number density, obtained from the Global Modeling and Assimilation Office (GMAO) and interpolated to the CALIPSO orbit track. The aerosol profile products are similar in format. However, because the spatial scale of aerosol variability is considerably greater than that for clouds, and because the weaker scattering from aerosols requires more averaging in order to obtain accurate results, the aerosol profile products are reported on a coarser spatial grid of 40-km horizontally and by 120-m vertically.

Discriminating clouds from aerosols

Intensive scattering properties are those that depend only on the type of particulate being measured, and are independent of the amount or concentration. *Extensive* properties on the other hand depend directly on particulate amount within the scattering volume. To differentiate between clouds and aerosols, the CALIPSO cloud-aerosol discrimination (CAD) algorithm relies on the statistical differences in both the intensive and extensive scattering characteristics exhibited by the two types of features. The particulate backscatter ratio (or color ratio) is plotted as a function of particulate backscatter coefficients at 532 nm, for several feature types defined by the Optical Properties of Aerosols and Clouds (OPAC) software package. Because clouds generally consist of particles which are quite large with respect to the CALIPSO wavelengths, the aerosol backscatter and extinction coefficients are not expected to show any substantial spectral

variation. Therefore, both the backscatter and extinction color ratios should be approximately equal to 1. Conversely, the particle sizes for most aerosols (with the possible exception of some dust layers) are much smaller, and thus, should exhibit a spectrally dependent scattering efficiency. The expectation is that b_{aer} will be smaller at 1064 nm than at 532 nm, so that in general, the backscatter color ratio will be less than 1 (Vaughan et al., 2004).

Aerosol subtyping and lidar ratio selection

The most difficult task among the scene classification algorithms is to determine the appropriate lidar ratio to be used in the optical analyses of the probed aerosol layers. According to Kim *et al.* (2018), the CALIPSO aerosol-typing scheme is mainly based on the layer-integrated particle linear depolarization ratio at 532 nm, and the layer-integrated attenuated backscatter (γ') coefficients at 532 and 1064 nm. Information about aerosol layer base and top height, as well as of tropopause and temperature (from atmospheric models) is available and used in addition. In the first step, PSCs are identified by using information on latitude, month, temperature, and tropopause height. Aerosol typing is then performed in several follow-on steps: If $\gamma' < 0.001$ sr^{-1}, which is equivalent to an AOD of < 0.04–0.08 at 532 nm (for lidar ratios of 40–80 sr), the aerosol layer is automatically classified as sulfate layer. The PLDR at 532 nm is not used.

However, according to Ansmann et al. (2021a) this step can lead to a misclassification of the optically thin smoke layers. If $\gamma' > 0.001$ sr^{-1}, which means an AOD at 532 nm > 0.04–0.08, then the depolarization ratio comes into play. If the depolarization ratio PLDR > 0.15, the aerosol is classified as volcanic ash. If the PLDR is in the range from 0.075 to 0.015, the aerosol is categorized as smoke, and if PLDR < 0.075, the aerosol is classified as sulfate aerosol. Studies of stratospheric BB aerosol layers (Ohneiser et al., 2020a; Haarig et al., 2018; Hu et al., 2019; Papanikolaou et al., 2022a) showed that smoke layers can frequently produce depolarization ratios greater than 0.15 at 532 nm. So, stratospheric smoke usually presents a variety in PLDR values, that can lead to misclassification.

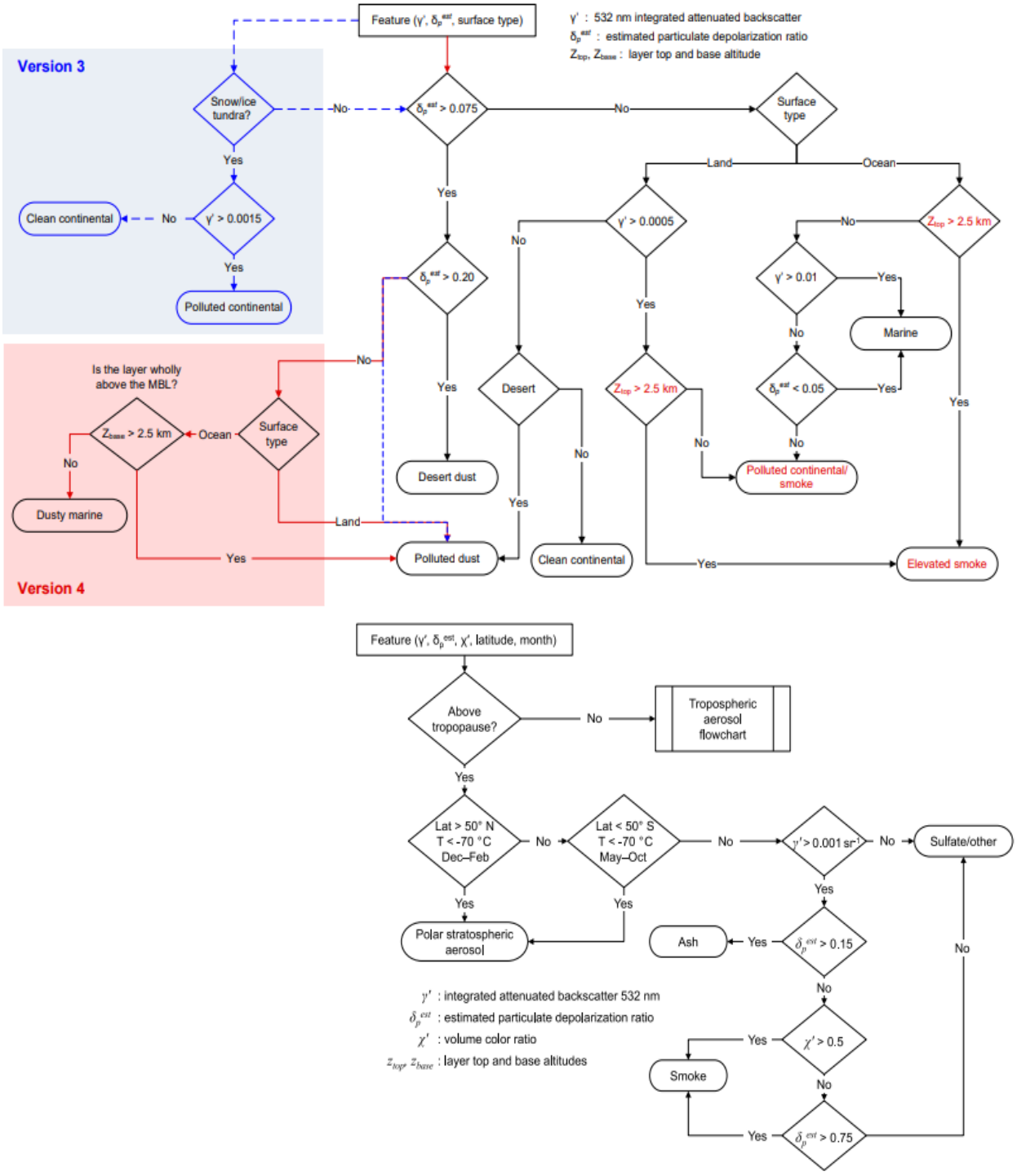

Figure 2. 7: Flowchart of the CALIPSO aerosol subtype selection scheme for tropospheric and stratospheric aerosols, in V3 and V4 of CALIPSO products (Kim et al., 2018b).

2.5.4 CALIPSO algorithm

In order to process the CALIOP data and apply the proper quality assurance controls, an algorithm was developed in MATLAB environment. The interface of the algorithm, along with some output figures can be seen in Figure 2.5. The algorithm uses as inputs the Level 2 Aerosol profile data (from v3.01 and on) and the corresponding VFM products. Initially, the user has to define the coordinates, upon which the retrieval of the profile data will take place. The data can also be averaged for a radius (in km) around the specified coordinates. The Atmospheric Volume Description (AVD) value, indicative of the features: aerosol, cloud and stratosphere, also has to be determined, along with the corresponding CAD values (Liu et al., 2019). The standard CAD score, reported in the CALIPSO products range between −100 and 100. The sign of the CAD score indicates the feature type: positive values signify clouds, while negative values signify aerosols. The absolute value of the CAD score provides a confidence level for the classification. For the tropospheric layers the CAD score was set between −80 and −100. However, as the altitude of the stratospheric layers increases above the tropopause, the signal-to-noise ratio decreases and leads to low CAD score magnitudes within the layers (Liu et al., 2019).

The CALIPSO orbit, and the minimum distance of the chosen coordinates and the orbit are visualized initially. Finally, the retrieved aerosol optical properties are:

- b_{aer} at 532 and 1064 nm
- a_{aer} at 532 and 1064 nm
- PLDR at 532 nm
- $Å_b$ for the pair of 532/1064 nm
- LR 532 and 1064 nm,

along with the aerosol subtype for each aerosol layer.

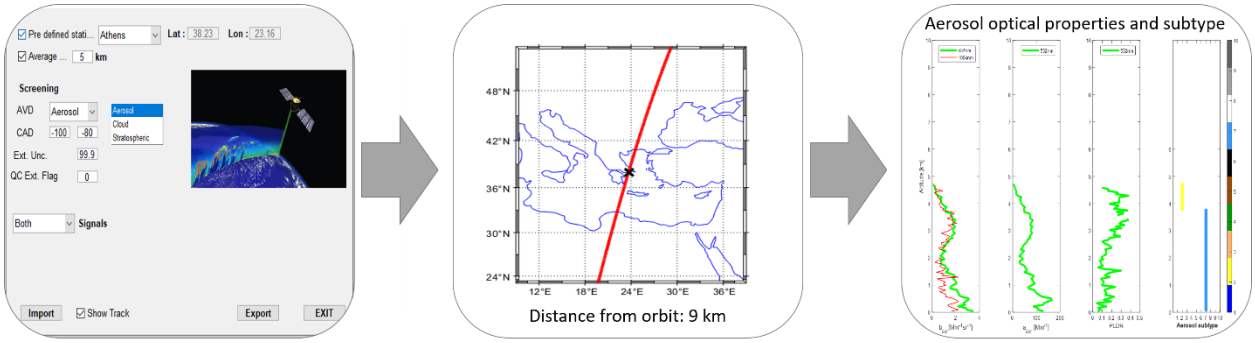

Figure 2. 8: CALIPSO algorithm used in processing the Level 2 APro data, from version 3.01 and on, developed in MATLAB environment.

CHAPTER 3
EXTREME BIOMASS BURNING EVENTS

In Chapter 3 a full discussion, interpretation and evaluation of the results concerning four extreme BB events are contained, with reference to other literature findings (Papanikolaou *et al.*, 2020, Papanikolaou *et al.*, 2022a; Papanikolaou *et al.*, 2022b; cf. Appendix A—Paper I, Appendix B —Paper II, Appendix C —Paper III, Appendix D—Poster I).

3.1 Canadian Biomass Burning Aerosol Properties Modification during a Long-Ranged Event on August 2018

3.1.1 Introduction

Atmospheric aerosols play a fundamental role on the Earth's atmosphere having a significant impact on climate, as they can interact with radiation and clouds (Groß et al., 2015b; Shin et al., 2019; Liu et al., 2020). Atmospheric aerosols are difficult to characterize due to their highly variable spatio-temporal distribution and their production mechanisms. Moreover, natural and anthropogenic aerosols can be mixed or aged during their transport, which furthermore influences their properties (Shin et al., 2019; Liu et al., 2020; Groß et al., 2015b).

Wildfires, agricultural burnings and increased use of wood as fuel for heating are the major sources of atmospheric aerosols related to biomass burning (Nepomuceno Pereira et al., 2014a). Biomass burning aerosols (BBs) can directly scatter and absorb shortwave radiation. Depending on their chemical composition. For instance, BB particles contain a mixture of organic carbon (EC), elemental carbon (EC), and black carbon (BC).

Furthermore, increased attention is drawn to the fact that a great number of health effects on humans are related with increased concentrations of BB particles. BBs can be produced by natural sources and/or anthropogenic processes. On a global scale, the Central and Southern Africa, North America, Canada and Siberia (Russian Federation), the Midwest and the Amazon in Brazil, are the largest sources of biomass burning aerosols on Earth, mostly during the dry seasons (Generoso et al., 2003; Freitas et al., 2005; Kim et al., 2020).

It is well known that the kind of vegetation burning influences the released amount of soot in the form of BC and the size of the emitted smoke aerosols and, thus, their optical and physico-chemical properties (Ortiz-Amezcua et al., 2017; Generoso et al., 2003; Freitas et al., 2005; Kim et al., 2020; Bougiatioti et al., 2016). BBs are one of the key aerosol types in climate research and due to the scarcity of relevant data in the literature, the vertical stratification of their optical, microphysical and chemical properties in free tropospheric layers is urgently needed (Nepomuceno Pereira et al., 2014a).

Moreover, smoke plumes from forest fires can be injected directly into the PBL and the FT (Giannakaki et al., 2010; Labonne et al., 2007), or even to the lower stratosphere (Baars et al.,

2019; Hu et al., 2019). Long-range transport mechanisms, found in the free troposphere and lower stratosphere can distribute these smoke aerosols hemispherically (Ortiz-Amezcua et al., 2017; Amiridis et al., 2010; Ancellet et al., 2016). This fact leads to an important issue regarding the transformation processes undertaken by the smoke aerosols, such as coagulation, condensation, and gas-to-particle conversion frequent during long-range transport leading to changes in their size and therefore to their optical properties (Nepomuceno Pereira et al., 2014a).

In recent years, an increasing number of investigations focusing on the retrieval of the vertical profiling of the BBs' geometrical and physico-chemical properties in the case of large fires all over the world is based on ground-based and spaceborne lidar systems (Ortiz-Amezcua et al., 2017; Baars et al., 2019; Wandinger et al., 2002; Groß et al., 2011b; Tesche et al., 2011a, 2013; Nicolae et al., 2013; Vaughan et al., 2018; Floutsi et al., 2020).

In this Thesis, we investigate the modification of the vertical profiles of the BBs' geometrical and optical properties during a long-range biomass burning event which occurred over Canada from the 16 to 26 August 2018, as observed by the CALIPSO satellite. following the BBs from their source along their pathway towards Europe. The mean values of smoke plumes' altitude, and the relevant values of BBs' b_{aer}, the PLDR at 532 nm, as well as the backscatter-related $Å_b$ at 532/1064 nm are presented and discussed during this intercontinental transport.

3.1.2 Methodology and data

Smoke Event Description

In 2018, the Canadian region of British Columbia experienced its worst fire season on record since 2115 fires burned over 1.35 million hectares. This large fire event surpassed the 2017 fire season—previously the largest burned area—in which over 1.22 million ha were burned (British Columbia's forest fires, 2018). The fires of 2018 in British Columbia accounted for about 60% of the total burned area in Canada in 2018, compared to an average of 7% over the 1990 to 2018 period (Remer et al., 2005). Smoke emitted from these fires largely contributed to the poor air quality measured in the province during the fire period of April to September. All air quality measuring stations had at least one day where the Air Quality Health Index (AQHI) reached 7 or even higher values. Furthermore, most of these stations preserved these high values for more than seven days, while three of them for almost a month (British Columbia's forest fires, 2018). On 16 August 2018 in British Columbia 559 wildfires were active, leading the local BC. government to declare this province at the state of emergency. These smoke aerosol plumes travelled across the Atlantic Ocean and affected the western coasts of Europe on the 25 and 26 August.

This intercontinental transport event was studied by (Papanikolaou et al., 2020)with the synergy of satellite observations and models: data from the CALIOP lidar system on board the CALIPSO satellite, the Moderate Resolution Imaging Spectroradiometer (MODIS), instrument on board the Terra and Aqua satellites, the HYSPLIT trajectory model and the NASA's tool Giovanni

will be used to study the source, the transportation and the modification of the geometrical and physical properties of the detected BBs.

Satellites, Models and Tools

MODIS is flying on two satellites (Terra and Aqua) in orbits that complement each other and provides the diurnal variation of the rapidly varying atmospheric parameters for climate and global change studies with almost complete global coverage in one day (Berrick et al., 2009). In this study active fire data from MODIS Terra and Aqua, distributed through the Fire Information for Resource Management System (FIRMS), were used to analyze the distribution of fires in Canada during the studied period. In Figure 3.1b we present with a red dot the location where MODIS detected at least one fire event during the compositing time period, with confidence greater that 80% (The fire maps are available from NASA's Earth Observing System Data and Information System (EOSDIS) (https://firms.modaps.eosdis.nasa.gov). The period covered by the fire map shown was set to 8 days, from 8 to 16 August 2018 coinciding with the period of intense wildfires in Canada.

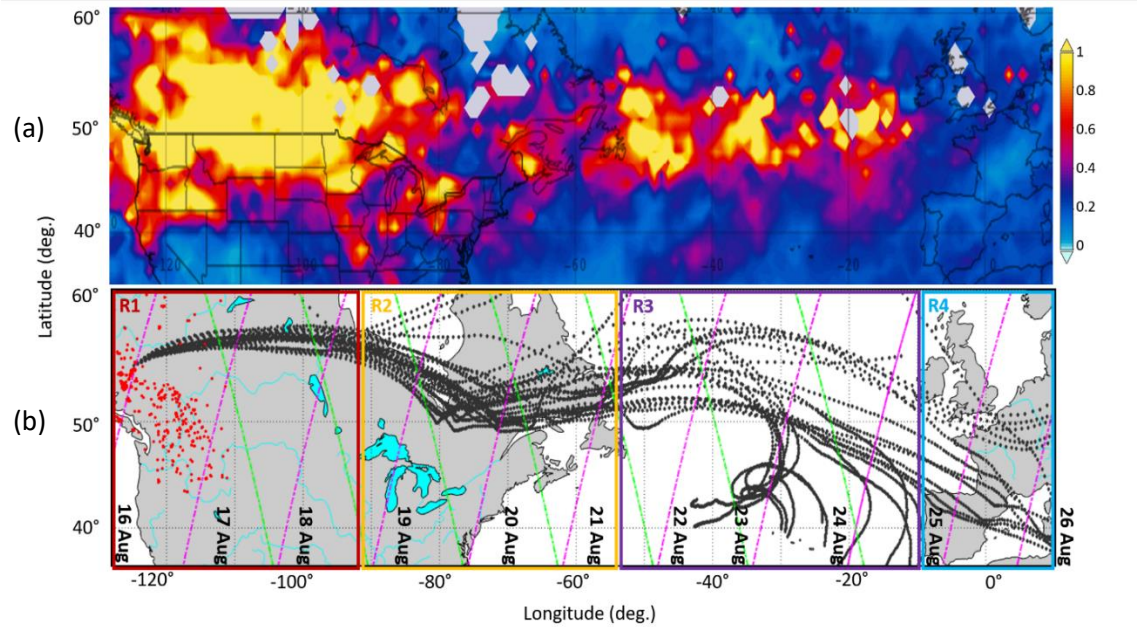

Figure 3. 1: (a) Time Averaged Map of Combined Dark Target and Deep Blue AOD at 550 nm for land and ocean: Mean daily 1° (MODIS-Aqua MYD08_D3 v6.1) from 16 August 2018 and for a 10-day period. (b) The 10-day forward HYSPLIT trajectories starting on 16 August and ending on 10 August. The red dots correspond to active fires observed in BC, Canada, by MODIS with confidence greater than 80%. Magenta and green lines correspond to nighttime and daytime CALIPSO orbits, respectively. Red, yellow, purple and cyan boxes correspond to the four subregions (R1–R4) of the smoke motion (Papanikolaou et al., 2020).

Aerosol observations from several space-borne instruments can be accessed through the Giovanni tool, which is a data exploration system for visualization, and analysis of NASA Earth Science data (https://giovanni.gsfc.nasa.gov/giovanni/) (Berrick et al., 2009). The Giovanni tool was used to verify the path of smoke plume motion and visualize the AOD at 550 nm (based on

MODIS (Aqua) data, with a temporal resolution of 24 h and spatial resolution of 1° (Figure 3.1a). In this figure we see that AOD values at 550 nm were greater than 0.825 close to the burning areas, while at the time smoke was reaching the European continent these values were still increased (>0.413).

The HYSPLIT model "ensembles" has been an attractive approach to study an atmospheric transport (Rolph et al., 2017). The "ensemble" method, that was used for the analysis of the forward air mass trajectories, is created by slightly offsetting the meteorological data to test the sensitivity of the advection calculation to the gradients in the meteorological data fields. Multiple trajectories start from the selected starting point, and each member of the trajectory ensemble is calculated by offsetting the meteorological data by a fixed grid factor. As a result, 27 members occur for all-possible offsets in longitude, latitude and altitude. This can work as an approximation of the true flow field (Rolph et al., 2017; Winker et al., 2009).

One indicative forward air mass trajectory is shown in Figures 3.1 and 3.2. The coordinates and altitudes of the smoke plumes were observed over Canada and categorized as smoke aerosols by the CALIPSO algorithm. These coordinates and altitudes were used as initial values for the model. The air mass starting point was placed at 52.6° N and 123.7° W, for this indicative trajectory, and the height was at 4500 above mean sea level (amsl.). The vertical motion calculation method used was the model vertical velocity along with the meteorological data GDAS1 (Global Data Analysis System). The duration of the trajectory was 240 h forward. The trajectory analysis showed the path that the smoke followed to reach Europe.

Methods and Data Analysis

Since the active fires in the Canadian region were detected by MODIS, the CALIPSO orbits were used, at first, to observe the smoke layers in this region, near the wildfires area. The night and day orbits were used in order to track the transport of the smoke plume towards Europe, from 16 to 26 August. The plume was observed initially over the BC on the 16 August (11:00 UTC) between 45-56° N and 123-127° W, within the height region 2-5 km amsl. In Figure 3.2 (b1–b4), we present the orbits of CALIPSO, along with the forward ensemble air mass trajectory. The CALIPSO "curtains" shown in the background represent the vertical distribution of the total attenuated backscatter coefficient at 532 nm, while in the foreground, the forward air mass trajectories show the path that the smoke plume followed, from Canada to Europe in a 10-day period.

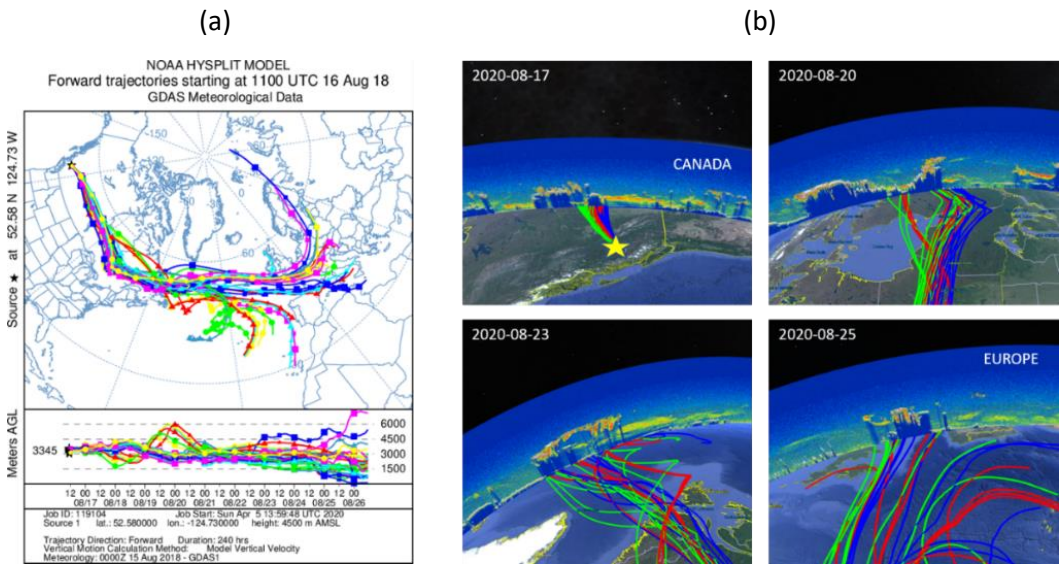

Figure 3. 2: (a) 10-day forward ensemble air mass trajectories starting on 16 August (11:00 UTC), as provided by HYSPLIT. Different color-lines of the forward trajectories correspond to trajectories for all-possible offsets in longitude, latitude and altitude according to the ensemble analysis). (b) 10-day-forward ensemble air mass trajectories, along with selected CALIPSO curtains (Papanikolaou et al., 2020).

The observations of CALIOP were used to track the biomass burning plumes throughout their transport from Canada to Europe. In order to study the geometrical and optical properties of the smoke layers, the main region of smoke's spatial distribution was limited from 38° N to 58° N and from 125° W to 10° E. The nighttime and daytime CALIPSO orbits where used to follow the smoke aerosol layers. The horizontal averaging applied to the CALIOP data was 105 km, in order to enhance the detection of the aerosol layers. For the data analysis, we used AVD to screen out any other scatterer apart from aerosols.

The vertically resolved particle optical properties (b_{aer} and PLDR at 532 nm and $Å_b$ 532/1064 nm) were retrieved by the CALIPSO nighttime and daytime orbits. The retrievals were made per 2° latitude and longitude, along the CALIPSO orbits. The dates of the orbits used are presented in Figure 3.1b. Magenta and green lines correspond to nighttime and daytime CALIPSO orbits, respectively. The retrievals were made per 2° latitude and longitude, along each one of the CALIPSO orbits used. Profiles not containing any smoke layers were excluded. However, most of them, usually, included more than one smoke layer, in different heights. As mentioned before, the minimum spatial averaging of the CALIPSO product is 5 km and the average we used was 105 km. While the average can be applied in intensive aerosol parameters (b_{aer} and PLDR at 532 nm

and $Å_b$ at 532/1064 nm) it cannot be applied in the typing product. Thus, more than one aerosol type was attributed in each layer, as can be seen in Figure 3.3d.

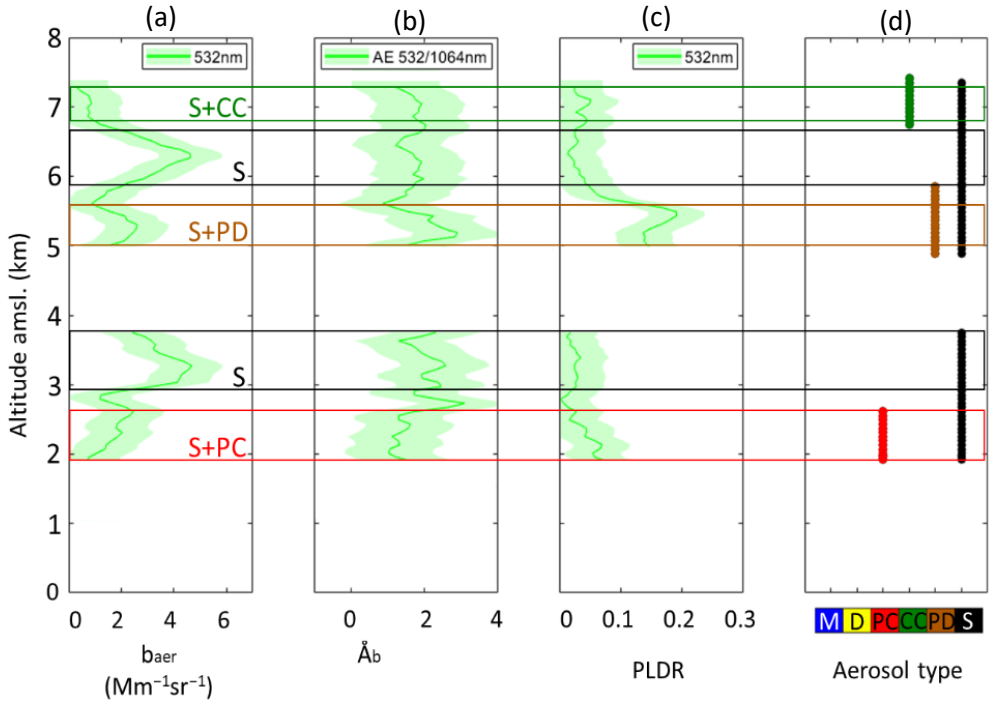

Figure 3. 3: Vertically resolved aerosol optical properties: (a) b_{aer} 532 nm, (b) $Å_b$ 532/1064 nm, (c) PLDR at 532 nm and (d) aerosol typing according to the CALIPSO algorithm (M: marine, D: Dust, PC: Polluted Continental, CC: Clean Continental, PD: Polluted Dust, S: Smoke), as retrieved from the nighttime CALIOP orbit on 20 August. The coordinates used to derive these properties were 42.5° N and 73.8° W. Green shadowed lines correspond to the standard deviation for each aerosol property (Papanikolaou et al., 2020).

As an example of the aforementioned retrievals, the vertically resolved aerosol optical properties and the corresponding subtypes are presented in Figure 3.3 as derived from the nighttime CALIPSO orbit on 20 August 2018, 07:03, 42.5° N and 73.8° W. As it is shown in this figure, at least 5 aerosol layers were observed (Figure 3.3d). Two of them were categorized as pure smoke (S), while 3 as smoke mixed with clean continental aerosols (S+CC), smoke with polluted dust (S+PD) and smoke with polluted continental (S+PC).

Initially, all aerosol layers containing smoke, according to CALIPSO typing algorithm, were isolated and analyzed. However, as all the studied layers contained, either pure smoke, or smoke mixed with other aerosols, 6 new categories were added in this work: pure smoke (1), smoke mixed with polluted dust (2), with desert dust (3), with clean continental (4), with polluted continental (5) and with marine aerosols (6). In that way, two aerosol categories containing smoke mixed with dust have emerged, the first containing smoke mixed with polluted dust and the second containing smoke mixed with dessert dust. In the first category the smoke is mixed with dust that is already mixed with smoke or other continental polluted aerosols, while the

second category is a mixture of two pure aerosol types: smoke and dessert dust. Differences between these categories occurred, mostly, based on their PLDR and LR values.

The analysis applied on the data sets was the box plot. The box plot analysis is useful for analyzing data sets as large as those studied here, as they provide a visual summary of the data and an easy identification of the median and mean values, the dispersion of the data set, and signs of skewness. The minimum and maximum values are found at the end of the whiskers and are useful for providing a visual indicator regarding the range of the data. The 75^{th} percentile and 25^{th} percentile values indicate the values at which 75% of the data are above it and 25% below.

The box plot analysis was first applied on the whole dataset of the event, then on the four subregions that the smoke region was divided and finally, only on the pure smoke aerosol layers which were identified. Regarding the four subregions (R1 to R4), the first subregion (R1) contains all the smoke layers located over the active fires and up to two days eastward travel from the fire source. The second subregion (R2) is the one containing all the smoke layers eastward of the first region and up to the Eastern Canadian coasts. The third subregion (R3) contains the smoke layers which cross the Atlantic Ocean and finally the fourth subregion (R4) contains the smoke layers that reached the western coasts of Europe (in Figure 3.1 the four subregions are presented with the corresponding colors).

3.1.3 Results and Discussion

Mixed Smoke Layers Analysis

The total attenuated aerosol backscatter coefficient at 532 nm for each day of the tracked smoke plume, in the time period 16–26 August 2018, are presented in Figure 3.4, where the corresponding color bar on the right of the figure indicates the intensity of the aerosol load (e.g., the atmospheric aerosol layers are delineated by the yellow, orange and light-red colors). These aerosol layers were identified as smoke, pure or mixed with other aerosol types, by the CALIPSO algorithm. The corresponding aerosol types, according to CALIPSO's algorithm, are presented in Figure 3.5. With black color are represented the smoke layers, with brown and yellow colors the polluted dust and desert dust, respectively, with green and red colors the clean and polluted continental and, finally, with blue color the marine layers.

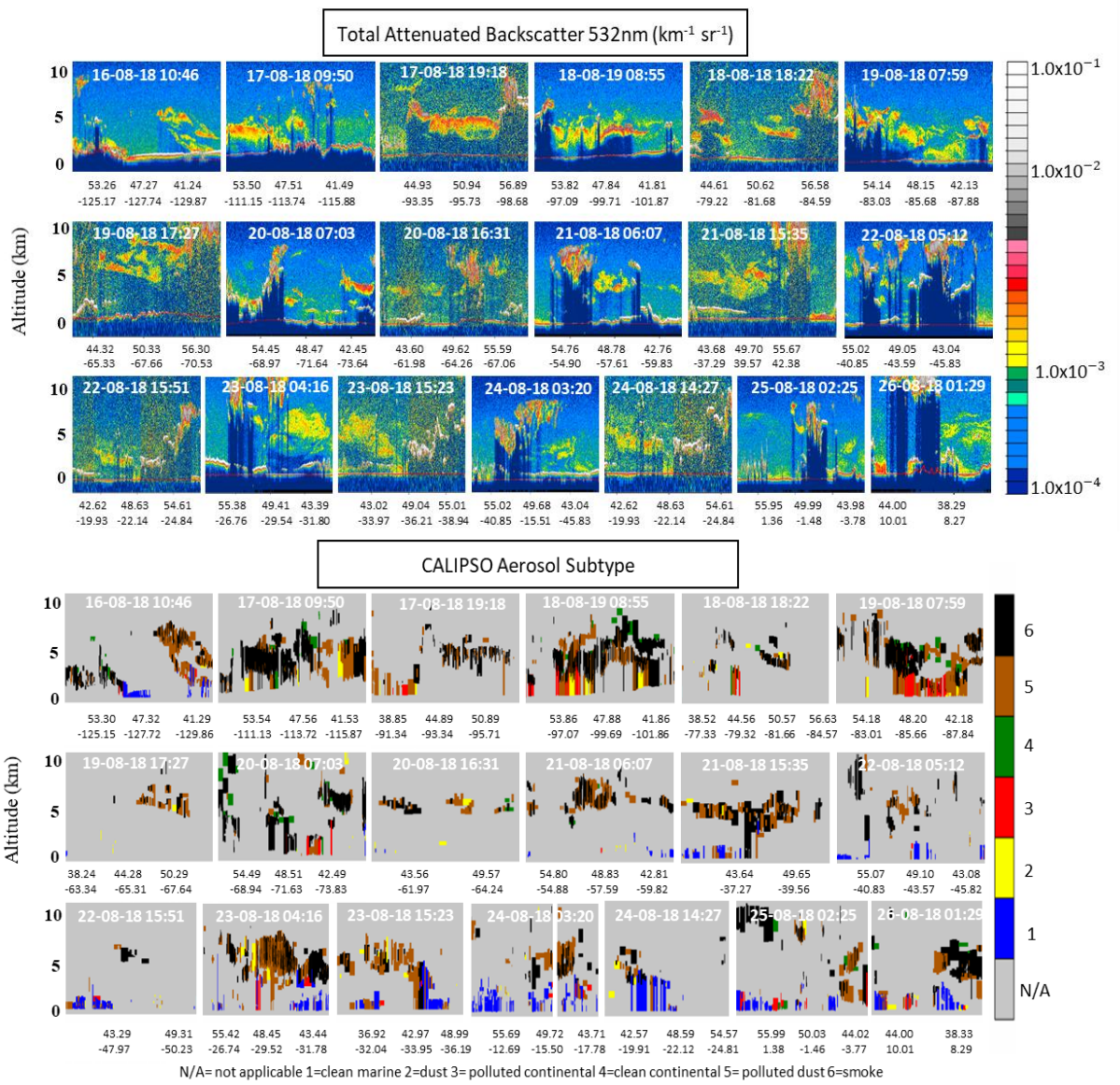

Figure 3. 4: CALIPSO total attenuated backscatter coefficient at 532 nm and aerosol subtypes versus altitude, latitude and longitude for nighttime and daytime orbits (16th-26th of August 2018) (Papanikolaou et al., 2020).

The total number of the corresponding profiles obtained was 715. We then focused on the aerosol layers of pure smoke or mixtures of smoke aerosols as categorized by CALIPSO. In total, we found 745 layers of smoke: 312 of them were identified as pure smoke, 257 as smoke mixed with polluted dust, 74 as smoke mixed with clean continental aerosols, 35 as smoke mixed with polluted continental, 41 as smoke mixed with dessert dust and, finally, 26 as smoke mixed with marine aerosols, the percentages are extensively shown in Figure 3.5.

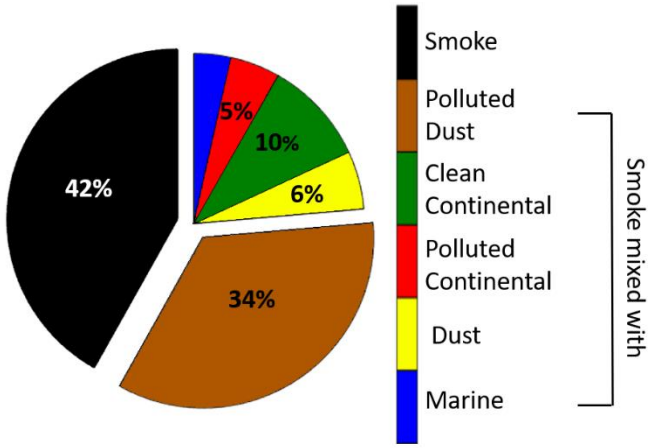

Figure 3. 6: Percentages of aerosol layers mixing types for the total event, types found in percentages less than 3%, are not presented with numbers in the figure (Papanikolaou et al., 2020).

Furthermore, we proceeded with the box-plot analysis of the aerosol layers' properties concerning their geometrical height properties (amsl.), the values of b_{aer} and PLDR at 532 nm, as well as the $Å_b$ at 532/1064 nm. This analysis was performed using all available biomass burning layers and their mixtures to obtain representative values of aerosol properties during a large-scale biomass burning event. The results are presented in Figure 3.6 containing the box plot analysis that represents the distribution of the values of the aerosol properties mentioned before for all aerosol layers studied within this event. Each color of the boxes corresponds to the aerosol type of pure smoke and different smoke mixtures. Green rhombus corresponds to the mean values. The horizontal line inside the box represents the median values, while the smallest and largest values are put at the end of the whiskers. The box limits (up and down) correspond to the 75th percentile and 25th percentile values that indicate the values at which 75% of the data are above it and 25% below. The number of layers for all mixing types are presented above the altitude box.

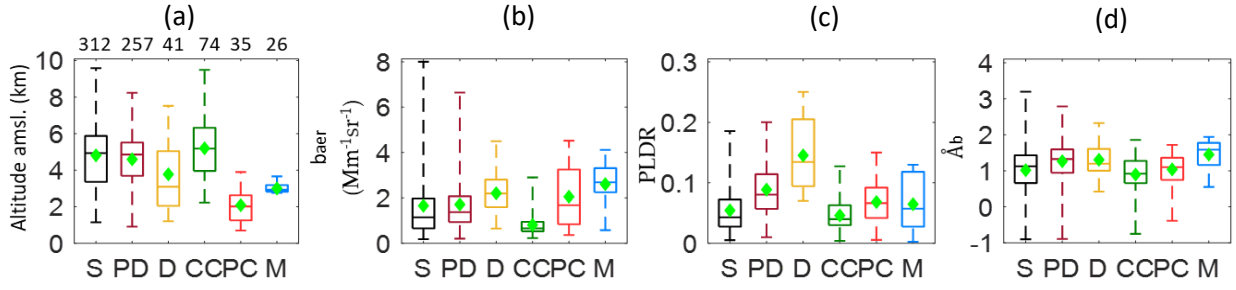

Figure 3. 5: Aerosol layers mixtures according to (a) their altitude (amsl.), (b) b_{aer} at 532 nm, (c) PLDR at 532 nm, (d) $Å_b$ at 532/1064 nm, for the total event (S: pure smoke layers, PD: smoke mixed with polluted dust layers, CC: smoke mixed with clean continental layers, PC: smoke mixed with polluted continental layers, D: smoke mixed with dust layers and M: smoke mixed with marine layers) (Papanikolaou et al., 2020).

From the analysis of Figure 3.6a, it was found that mean values of the layers' altitude ranged between 2.1 ± 0.9 km (smoke mixed with polluted continental aerosols) and 5.2 ± 1.5 km (smoke mixed with clean continental aerosols). The 75% of the smoke mixed with polluted continental aerosol layers was found at altitudes greater than 2.6 km and 25% at altitudes lower than 1.3 km amsl. Specifically, the smoke layers containing polluted continental aerosols were probed at lower altitudes. Smoke mixed with clean continental aerosol layers were found at altitudes greater than 6.3 km in 75% and only 25% were found at altitudes lower than 4 km amsl. This could be explained by the fact that the sources of the polluted continental aerosols are, mostly, at near ground levels. Moreover, the pure smoke aerosol layers were found mostly above 5.9 km amsl. (75%).

Concerning the mixtures of smoke with marine aerosols the mean altitude of these layers was found at about 2.9 ± 0.3 km amsl. (2.8 to 3.7 km amsl.), which seems quite improbable, as typically, the marine boundary layer (MBL) does not exceed 1.5 km height (Ho et al., 2015; Amiridis et al., 2008). Therefore, this could be due to a possible aerosol misclassification by the CALIPSO algorithm. In our case, layers of pure smoke, smoke mixed with polluted dust or with clean continental aerosols were observed at, approximately, the same altitude ranges, is in agreement with studies related to smoke injection height (Labonne, Bréon and Chevallier, 2007; Amiridis *et al.*, 2010)

In general, the mean b_{aer} values at 532 nm (Figure 3.6b) retrieved from each of the corresponding smoke layers, ranged from 0.8 to 2.6 $Mm^{-1}sr^{-1}$. On the other hand, layers including smoke aerosols mixed with dust, pure or polluted showed mean b_{aer} values at 2.2 ± 0.9 and 1.7 ± 0.6 $Mm^{-1}sr^{-1}$, respectively. More precisely, for these smoke mixtures 75% of the b_{aer} values were greater than 2.9 and 2.1 $Mm^{-1}sr^{-1}$. The b_{aer} values of pure smoke layers appeared to be mainly (75%) greater than 2.0 $Mm^{-1}sr^{-1}$, with some values reaching even 8 $Mm^{-1}sr^{-1}$. The smoke mixed with clean continental aerosol layers showed the smallest b_{aer} values (0.8 ± 0.5 $Mm^{-1}sr^{-1}$).

The mean values of the PLDR and AE (Figure 3.6c, d) indicate changes in the shape and size of the aerosols due to the transforming processes that smoke aerosols went through, during their long-range transport, as mentioned before. The PLDR values, that ranged between 0.04 to 0.15 and those of AE greater than 1 (not exceeding 1.9), are representative for smoke aerosols (Giannakaki et al., 2015; Nisantzi et al., 2014). On the other hand, PLDR values, greater than 0.20 and $Å_b$ values close to zero, indicate the presence of dust aerosols (Groß et al., 2015b, 2011b). We further found that 75% of the pure smoke aerosols PLDR and $Å_b$ values were greater than 0.07 and 1.4, respectively. The corresponding PLDR and $Å_b$ values for the smoke aerosols mixed with polluted dust were 0.11 and 1.6, respectively. For the layers containing smoke mixed with clean and polluted continentals the PLDR and $Å_b$ values were 0.06, 0.09 and 1.3, 1.4, respectively. In Table 3.1 are presented extensively all values obtained by the analysis of the data in Figure 3.6. An Appendix A is also found at the end of a paper containing all the information of the box plot analysis from the following sections as well (Tables A1-A5).

Table 3. 1: Descriptive statistics of the altitude, b_{aer}, PLDR and $Å_b$ values for different aerosol types for the total event: mean, standard deviation (std), median, maximum value (max), minimum value (min), 75th and 25th percentile for all variables.

	Type	Parameter	Mean	Std	Median	Max	Min	75th perc	25th perc
Pure	**S**	Alt (km)	4.81	2.02	4.93	9.59	1.15	5.88	3.36
		b_{aer} ($Mm^{-1}sr^{-1}$)	1.65	1.60	1.14	8.01	0.18	1.97	0.66
		PLDR	0.05	0.04	0.05	0.19	0.01	0.07	0.03
		$Å_b$	1.05	0.74	1.12	3.20	-1.00	1.43	0.66
Smoke mixed with	**PD**	Alt (km)	4.59	1.43	4.86	8.24	0.91	5.52	3.69
		b_{aer} ($Mm^{-1}sr^{-1}$)	1.71	0.61	1.37	6.64	0.20	2.07	0.93
		PLDR	0.09	0.05	0.08	0.20	0.01	0.11	0.06
		$Å_b$	1.26	0.59	1.33	2.79	-0.89	1.60	0.95
	D	Alt (km)	3.87	1.80	3.09	7.52	1.21	5.04	2.04
		b_{aer} ($Mm^{-1}sr^{-1}$)	2.24	0.93	2.25	4.50	0.65	2.88	1.59
		PLDR	0.15	0.06	0.13	0.25	0.07	0.21	0.09
		$Å_b$	1.31	0.45	1.20	2.33	0.42	1.61	1.00
	CC	Alt (km)	5.19	1.59	5.19	9.50	2.22	6.32	3.96
		b_{aer} ($Mm^{-1}sr^{-1}$)	0.80	0.50	0.65	2.90	0.23	0.94	0.53
		PLDR	0.05	0.03	0.04	0.13	0.00	0.06	0.03
		$Å_b$	0.89	0.55	0.92	1.86	-0.75	1.28	0.66
	CP	Alt (km)	2.08	0.96	2.01	3.90	0.70	2.63	1.25
		b_{aer} ($Mm^{-1}sr^{-1}$)	2.05	1.35	1.67	4.52	0.36	3.25	0.83
		PLDR	0.07	0.04	0.07	0.15	0.00	0.09	0.03
		$Å_b$	1.04	0.44	1.72	1.72	-0.39	1.36	0.75
	M	Alt (km)	2.99	0.25	2.93	3.66	2.76	3.18	2.82
		b_{aer} ($Mm^{-1}sr^{-1}$)	2.60	1.00	2.69	4.12	0.57	3.31	2.25
		PLDR	0.06	0.04	0.13	0.13	0.00	0.12	0.03
		$Å_b$	1.45	0.42	1.59	1.94	0.55	1.78	1.16

In conclusion, the smoke layers mixed with clean continental aerosol differentiated compared to the other aerosol categories, regarding the low value of b_{aer}. This fact might explain the reason why CALIPSO algorithm classified these layers as clean continental ones. Furthermore, the smoke layers mixed with desert dust were those that seem to pole apart from the other types. The mean altitude of these layers was 3.9 ± 1.8 km amsl., and the $Å_b$ 532/1064 nm mean value was similar to that of the other types, although it presented the smallest variation. However, the PLDR values of this category were the only ones which were greater than 0.20. Compared to the smoke mixed with polluted dust category, aerosol layers of smoke mixed with dessert dust were found in lower altitudes and were more depolarized (PLDR equal to 0.15 ± 0.06), but with the same $Å_b$ mean values of the order of 1.3 ± 0.4.

Smoke Transportation Analysis per Region

For each one of these four subregions that the study region was divided, the studied layers were also analyzed to percentages per mixing type and per region. In R1, 263 aerosol layers were detected, from them 40% of which were identified as pure smoke and the rest 60% as smoke mixed with polluted dust, clean and polluted continental and dust. The R2 contained a 51% of pure smoke layers. In R3, 33% was categorized as pure smoke layers, 38% as smoke mixed with polluted dust and 12% as smoke mixed with aerosols. Finally, in R4, 48% of the layers were categorized as pure smoke and 36% as smoke mixed with polluted dust. The exact percentages are shown in Figure 3.7.

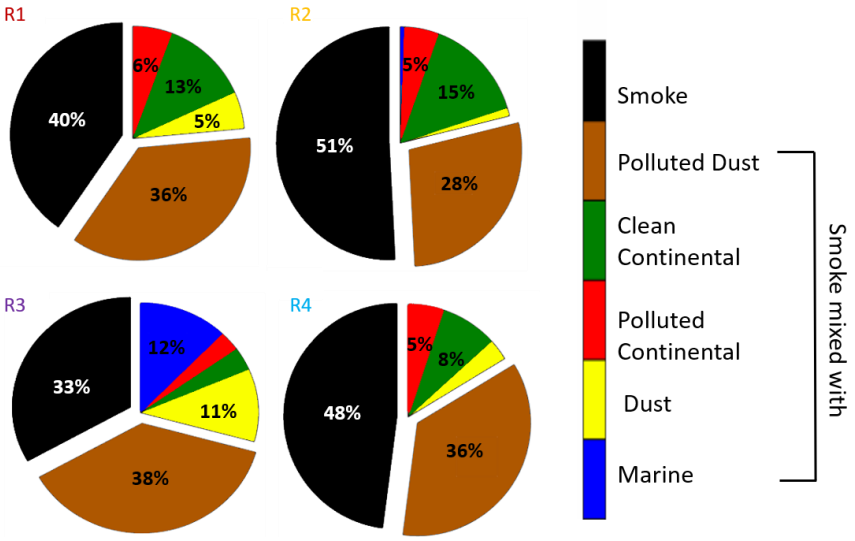

Figure 3. 7: Percentages of the aerosol layers mixing types for the subregions (R1–R4). Aerosol types found in percentages less than 3%, are not presented with numbers in the figure (Papanikolaou et al., 2020).

As discussed previously, the majority of the identified smoke layers were either pure or mixed with polluted dust. However, we have to note that the percentages of pure smoke layers are larger in the subregions R2 and R4 compared to R1, which is the active fire area. This could be explained by the fact that the first CALIPSO trajectory may have passed over the fires but did

not pass at the exact time or place that the smoke layers were more intense. It could also be related to smoke layers from the same event or even layers originating from other fires, which may have contributed to already existing smoke layers in subregion R2. The thriving percentages of smoke mixed with polluted dust, in subregions R1 to R4, is something worth to be mentioned. This could be related to the mechanisms which are responsible for the mixing of dust with smoke during BB events. It has been shown that flaming fires may be efficient enough to mobilize the surface soil dust (Burton et al., 2013) and so dust can be elevated and thus mixed with the smoke. This could also lead to the conclusion that some of the layers were misclassified by the automated CALIPSO classification (Tesche et al., 2009).

In contrast to the smoke layers mixed with polluted dust, smoke layers mixed with marine aerosols are observed only in subregions R2 and R3 in almost insignificant percentages (26 layers in total). This is quite expected and related to the injection of the marine aerosols into the lowermost part of the atmosphere, with a maximum of MBL height up to 1.5 km height (Ho et al., 2015; Amiridis et al., 2008) thus not mixing with smoke aerosols present, mostly, in the free troposphere. The percentages of clean and polluted continental aerosols mixed with smoke were found between 5–15% in each subregion, indicating insignificant contribution of the aerosol types to the smoke layers, as they were transported towards Europe.

In Figure 3.8 we present the box-plot analysis for the four subregions over which smoke was observed. Each colored box corresponds to the aerosol type of pure smoke and smoke mixtures. The mean, median, min, max values and 75th, 25th percentiles for all variables (altitude, b_{aer}, PLDR and $\mathring{A}_b$ (532/1064 nm) are presented as mentioned before. The number of layers for all mixing types are presented above the altitude boxes within each subregion (R1 to R4: left to right).

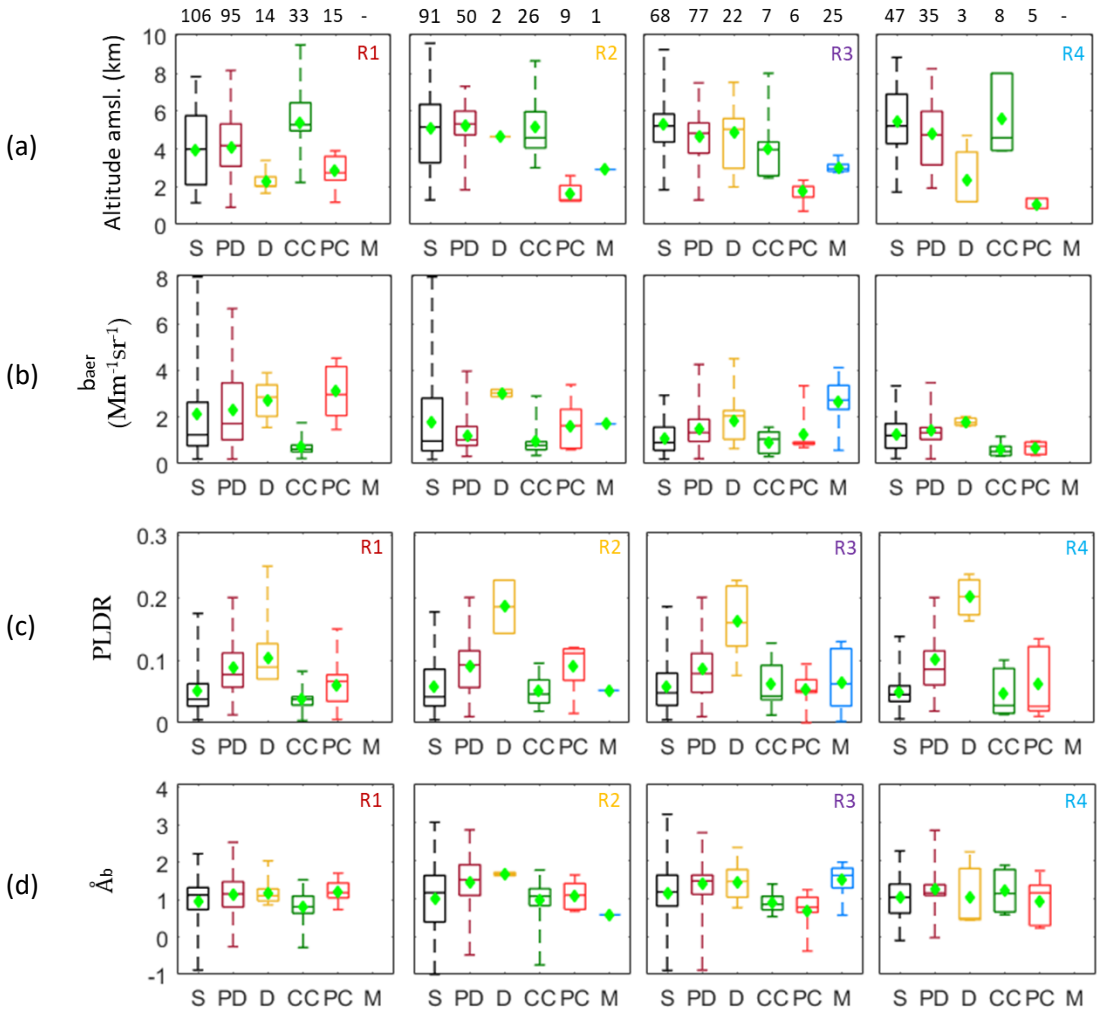

Figure 3. 8: Aerosol layers mixtures according to (a) their altitude (amsl.), (b) b_{aer} at 532 nm, (c) PLDR at 532 nm, (d) Å$_b$ (532/1064 nm). R1–R4 (left to right) correspond to the four subregions (S: pure smoke layers, PD: smoke mixed with polluted dust layers, CC: smoke mixed with clean continental layers, PC: smoke mixed with polluted continental layers, D: smoke mixed with dust layers and M: smoke mixed with marine layers) (Papanikolaou et al., 2020).

Thus, in the R1 region (Figure 3.8) all aerosol subtypes (smoke and smoke mixtures) were found, except the marine aerosol mixtures. We found 106 pure smoke layers, 95 smoke mixtures with polluted dust, 33 mixed with clean continental, 15 mixed with polluted continental and 14 mixed with desert dust. The smoke layers and those mixed with polluted dust were found at mean altitudes of 4.0 ± 1.9 km and 4.1 ± 1.4 km, respectively. The clean continental layers were observed at mean altitude of 5.4 ± 1.5 km and the layers containing polluted continental and dust aerosols were found at 2.8 ± 0.9 km and 2.3 ± 0.5 km, respectively. The corresponding aerosol b_{aer} mean values for all subtypes ranged between 0.7–3.1 $Mm^{-1}sr^{-1}$, while the mean PLDR ranged from 0.04 ± 0.02 (for smoke with clean continental aerosols) to 0.10 ± 0.05 (for smoke mixed with dessert dust). Finally, the mean Å$_b$ values ranged from 0.9 to 1.2.

In the R2 region all aerosol subtypes of smoke and smoke mixtures were observed. We found 91 pure smoke layers, 50 polluted dust smoke mixtures, 26 clean continental smoke mixtures, nine polluted continental smoke mixtures, two layers of smoke mixed with dust and one with marine aerosols. Smoke and polluted dust were detected at 5.1 ± 2.2 and 5.2 ± 1.1 km altitude, respectively, while smoke mixed with clean continental aerosols at 5.2 ± 1.5 km. Layers of smoke mixed with dust had a mean altitude of 4.7 ± 0.1 km, while smoke mixed with polluted continental and marine aerosols were found at 1.6 ± 0.6 and 2.9 km, respectively. The corresponding values of ± ranged from 1.0 to 3.0 $Mm^{-1}sr^{-1}$. The PLDR values ranged from 0.05 to 0.18, while the AE mean values were found equal to 0.6 for smoke mixed with marine aerosol layers and 1.6 ± 0.1 for smoke mixed with dust aerosols.

In the R3 region all aerosol subtypes of smoke and smoke mixtures were, also, observed. We found 68 pure smoke layers, 77 polluted dust smoke mixtures, 22 layers of smoke mixed with desert dust, seven clean continental smoke mixtures, six polluted continental smoke mixtures and 25 layers of smoke mixed with marine aerosols. Pure smoke layers and those mixed with polluted and dessert dust were detected at 5.3 ± 1.5, 4.7 ± 1.2 and 4.9 ± 1.6 km, respectively. Clean continental layers were found at 4.0 ± 1.9 km, while the layers containing polluted continental and marine smoke mixtures were found at 1.8 ± 0.6 and 3.0 ± 0.3 km, respectively. The values of b_{aer} ranged from 0.9 to 2.6 $Mm^{-1}sr^{-1}$, while the PLDR means ranged from 0.05 to 0.16. The $Å_b$ mean values ranged from 0.7 to 1.5.

In the R4 region, over Western Europe, all aerosol subtypes (smoke and smoke mixtures) were found except the marine aerosol mixtures. We found 47 pure smoke layers, 35 polluted dust smoke mixtures, eight clean continental smoke mixtures, five polluted continental and three smoke layers mixed with dessert dust. Smoke and polluted dust mixed layers were detected at 5.5 ± 2.0 and 4.8 ± 1.8 km altitude, respectively. The smoke mixed with clean continental aerosol layers and polluted continental were found at 5.6 ± 2.0 and 1.1 ± 0.3 km, respectively, while the desert dust smoke mixtures were detected at 2.4 ± 2.2 km. The corresponding b_{aer} values ranged from 0.7 to 1.8 $Mm^{-1}sr^{-1}$. The mean PLDR values ranged from 0.05 to 0.20 (for pure smoke and smoke mixed with dessert dust, respectively), while those of $Å_b$ ranged from 0.9 to 1.2.

According to Figure 3.6a and Figure 3.8a, we observe a large variability in the layers' height. This could be explained by the fact that the BB injection heights can differ according to the intensity of the BB event. Studies based on CALIPSO data obtained over the mid and high latitudes, showed that BB plumes can be equally injected within the mixing layer (50%) and the free troposphere (50%) (Labonne et al., 2007; Amiridis et al., 2010). On the other hand, the PLDR values Figure 3.9c) for the smoke mixtures with dust ranged from 0.10 ± 0.05 to 0.20 ± 0.04, in all subregions, which is in accordance with values previously found in the literature (Groß et al., 2011b; Tesche et al., 2013, 2009, 2011b; Soupiona et al., 2019b). The relevant values for the pure smoke aerosols were found equal to 0.05 ± 0.04, again in agreement with literature findings (Ortiz-Amezcua et al., 2017; Ancellet et al., 2016; Müller et al., 2005). As for the polluted dust smoke mixtures, the mean PLDR value was quite stable and equal to 0.09 ± 0.05, in all subregions.

The rest of the smoke mixtures showed PLDR values (in all subregions) ranging from 0.04 ± 0.02 to 0.09 ± 0.04.

In general, the Å_b (532/1064 nm) values regarding the biomass burning aerosols from different sources, pure or mixed, presented a large variability (from 0.8 to 2.2). The Å_b mean values obtained in this paper ranged from 0.8 to 1.2 for smoke mixed with other types of aerosols in R1. In R2, the Å_b mean values were found equal to 0.6 for smoke mixed with marine aerosol layers, and to 1.6 ± 0.1 for smoke mixed with dust aerosols. In R3 and R4 subregions, the values of Å_b ranged from 0.7 to 1.5 and 0.9 to 1.2, respectively, again in agreement with values found in the literature for pure smoke and smoke mixtures (Müller et al., 2007a; Nicolae et al., 2013; Müller et al., 2005; Soupiona et al., 2019a).

Pure Smoke Layers Properties

In the following section we will focus on the study of the modification of the pure smoke aerosol layers and the relevant optical properties during their travel from Canada to Europe. We found 312 pure smoke layers of which the mean altitudes are presented in Figure 3.9a. The relevant optical properties of pure smoke aerosols (b_{aer} and PLDR at 532 nm, and the Å_b (532/1064 nm)), are also presented in Figure 3.9b–d, respectively for each subregion. The four colors of the boxplots correspond to the four subregions (R1 to R4). Each colored box corresponds to the aerosol type of pure smoke and smoke mixtures. The mean, median, min, max values and 75th, 25th percentiles for all variables (altitude, b_{aer}, PLDR and Å_b) are presented as mentioned before. The number of the pure smoke layers for each subregion is presented above the altitude box.

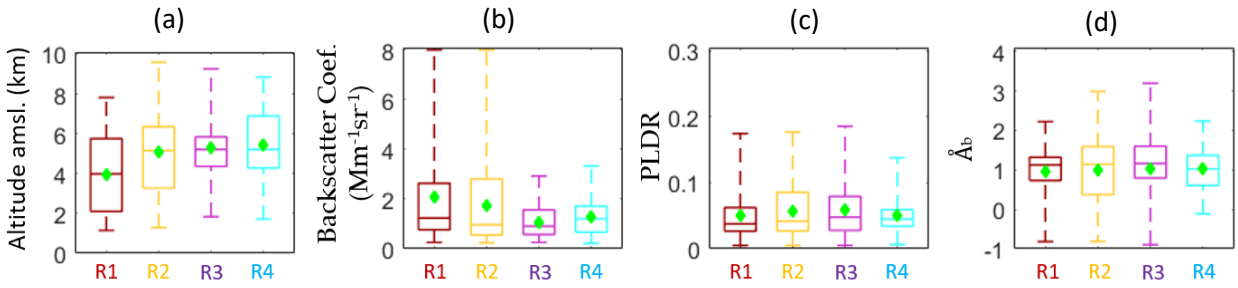

Figure 3. 9: Pure smoke aerosol layers according to (a) their altitude (amsl.) and relevant optical properties: (b) b_{aer} at 532 nm, (**c**) PLDR at 532 nm, (d) AE related to β (532/1064 nm). R1–R4 correspond to the four subregions (Papanikolaou et al., 2020).

According to Figure 3.9, the aerosol layers identified as pure smoke were found to be 106 in R1, 91 in R2, 68 in R3 and 47 in R4 subregions. As expected, the number of pure smoke layers during the air mass transport from R1 to R4 diminishes, as we move away from the BB area. We also observe that the smoke layers' height is increasing during its motion towards Europe, with mean values starting at 4.0 ± 1.9 km and reaching 5.5 ± 2.0 km height amsl. On the other hand, the mean value of b_{aer} at 532 nm, is decreasing as expected from 2.1 to 1.1 $Mm^{-1}sr^{-1}$, while the

PLDR and $Å_b$ mean values, seem to keep a steady value in all subregions, around 0.05 ± 0.04 and 1.0 ± 0.6, respectively.

The optical properties of the pure smoke layers in all regions seem to agree well with values found in the literature for Canadian and North American (tropospheric) biomass burning events (Table 2). The mean PLDR value of 0.05 ± 0.04 is within the limits originated by literature values, indicating PLDR values lower than 0.05 (Dubovik et al., 2002) that can reach up to 0.14 (McKendry et al., 2011). According to Groß et al., 2015, the PLDR at 532 nm for the Canadian Biomass Burning measurements was found at 0.07 ± 0.02. Ancellet *et al.*, 2016 showed values that ranged from 0.02 to 0.08, while (Ortiz-Amezcua et al., 2017) presented values ranging from 0.05 to 0.10. The mean $Å_b$ value obtained by this study is among the lowest found in the literature (1.0 ± 0.6), regarding tropospheric Canadian and North American BB events (Müller et al., 2007b; Dubovik et al., 2002; Preißler et al., 2013a; Veselovskii et al., 2015).

Table 3. 2: Optical properties of smoke aerosols measured during Canadian and North American biomass burning events, as cited in the relevant literature (2002–today).

Reference	**PLDR (532 nm)**	**$Å_b$ (532/1064 nm)**
Wandinger *et al.* (2002)	0.06-0.11	-
Dubovik *et al.* (2002)	-	1.0-2.3
Müller *et al.* (2005)	-	0-2.1
Müller *et al.* (2007)	≤0.05	1.0
McKendry *et al.* (2011)	0.07-0.14	-
Preißler *et al.* (2013)	-	2.2
Groß *et al.* (2015)	0.07±0.02	-
Veselovskii et al. (2015)	-	-
Ancellet *et al.* (2016)	0.02-0.08	-
Ortiz-Amezcua *et al.* (2017)	0.05-0.10	-
Vaughan *et al.* (2018)	≤0.06	-
This study (Papanikolaou et al., 2020)	**0.05±0.04**	**1.0±0.6**

3.1.4 Conclusions

In this paper a long-range transport event of biomass burning aerosols was studied, where aerosol layers of pure biomass burning, and mixed smoke aerosols were detected and analyzed in a region spanning from the wildfire sources up to the European continent. Forward trajectory analysis and satellite fire observations were the main tools used in order to analyze the evolution of this biomass burning event. The CALIOP lidar on board the CALIPSO satellite was used to track the transport of the smoke layers. The altitude of the observed layers, the values b_{aer} and PLDR at 532 nm, as well as those of the $Å_b$ (532/1064 nm) were fully studied.

From the 745 aerosol layers detected, 42% of them were identified as pure biomass burning aerosols. The remaining 58% were attributed to smoke mixed with: polluted dust (34%),

clean continental (10%), polluted continental (5%), Saharan dust (6%) or marine aerosols (3%). The smoke layers observed by the CALIPSO satellite were found within a wide range of altitudes from 0.8 km up to 10 km height. Most of the layers' altitude was found between 2.1 and 5.2 km amsl. The mean value of b_{aer} at 532 nm, for every smoke mixing type ranged from 0.8 to 2.6 $Mm^{-1}sr^{-1}$, while the mean value of PLDR at 532 nm, ranged from 0.04 ± 0.02 (smoke mixed with clean continental aerosols in R1), indicating nearly spherical aerosols, to 0.20 ± 0.04 (for smoke mixed with desert dust in R4). The mean PLDR value at 532 nm concerning pure biomass burning aerosols was found equal to 0.05 ± 0.04. The mean value of the ±-related $\mathring{A}_b$ (532/1064 nm) ranged for all smoke mixed layers between 0.8 to 1.6, while for pure biomass burning aerosols stayed constant at 1.0 ± 0.6, within each subregion.

The majority of the identified smoke layers were either pure or mixed with polluted dust. However, for the smoke mixed with polluted dust layers we found mean values of PLDR and $\mathring{A}_b$, equal to 0.09 ± 0.05 and 1.3 ± 0.6, respectively, in all subregions. These values do not seem to be indicative of dust aerosols (even polluted), thus this kind of layering could be possibly misclassified by the CALIPSO algorithm. The percentages of the clean and polluted continental aerosols were found between 5–15%, in each subregion, with no significant contribution in the aerosol optical properties. We, also, found that the smoke layers mixed with desert dust was the aerosol type showing the most observable changes, mostly in the PLDR values. Another result of our study was that the marine aerosols were not found to be significantly mixed with smoke aerosols as they were, mostly, confined within the MBL. The altitudes where the marine smoke mixtures were found (3.0 ± 0.2 km), along with the values of $\mathring{A}_b$ (0.6 to 1.9), could also lead to a possible aerosol misclassification by the CALISPO algorithm. Additionally, we found that the shape and the size (as they result from the PLDR and $\mathring{A}_b$ values) of pure smoke aerosols are not significantly changing during this smoke aerosol transportation. Finally, the mixing of smoke with other aerosol types played the major role for the changes observed in the aerosol optical properties.

3.2 Vertical Profiling of Fresh Biomass Burning Aerosol Optical Properties over the Greek Urban City of Ioannina, during the PANACEA Winter Campaign

3.2.1 Introduction

Wildfires, agricultural fires, and the use of wood as fuel for domestic heating during the winter season, are the major sources of the BB particles (Nepomuceno Pereira et al., 2014b; Diapouli et al., 2017; Liakakou et al., 2020). Biomass combustion is considered one of the main global sources of air pollution, especially when they are related to residential heating; it is calculated to contribute more than 50% of BC and OC and approximately 45% of $PM_{2.5}$ (Klimont et al., 2017). In urban environments, BC is mainly emitted from traffic and residential heating as a result of incomplete combustion of fossil and/or biomass fuel (Liakakou et al., 2020).

During the last decade, Greece has faced a severe financial crisis. Many households contributed to the already existing problem of air particle pollution by using wood as heating

material (Sarigiannis et al., 2014; Fameli and Assimakopoulos, 2016; Fourtziou et al., 2017; Gratsea et al., 2017). Thus, the local emissions of BB related particles may have led to a sharp increase in the intensity of air pollution episodes during cold winter periods, especially under specific meteorological conditions (e.g., stagnant air masses under temperature inversions) within a shallow PBL as discussed by Kassomenos et al. (2003) and Sindosi et al. (2003, 2019, 2021) (Kassomenos et al., 2003; Sindosi et al., 2003, 2019; Sindosi and Hatzianastassiou, 2021).

Several middle- and large-sized Greek cities are suffering from high particulate matter (PM) concentrations, either locally produced or transported long distances. The PANhellenic infrastructure for Atmospheric Composition and climatE chAnge (PANACEA) gives the opportunity to study the atmospheric composition in these cities, focusing on the anthropogenic sources (e.g., industrial, transportation, and domestic heating activities). Within the PANACEA context, simultaneous measurements of aerosols have been performed in several Greek urban and regional background stations during different seasons, using a synergy of in situ and remote sensing instrumentation (https://panacea-ri.gr) (Mylonaki et al., 2021c) to assess the emission sources, the physicochemical properties, as well as the climate and health impacts.

The middle-sized city of Ioannina (~112,486 inhabitants) is situated in the Epirus mountainous region in Northwestern Greece. Ioannina frequently suffers from wintertime air pollution episodes due to BB domestic heating activities (Sindosi et al., 2019; Kaskaoutis et al., 2020), mainly due to its local topography leading to the formation of stagnant air masses over the city. The high levels of particulate matter concentrations, at ground level, exceed the current annual limit value of 25 $\mu g/m^3$ (Sindosi and Hatzianastassiou, 2021) as set by the European 2008/50/EC Air Quality Directive regarding $PM_{2.5}$ mass concentrations. Despite the severity of these air particulate pollution episodes occurring during winter-time, there has been a lack of knowledge of the spatio-temporal evolution of the vertical mixing of the particles over the Ioannina basin; this information would be extremely valuable to forecast air pollution episodes and provide tools to policy makers to reduce air pollution in the area and the relevant mortality and morbidity issues attributed to PM exposure.

To fulfill this lack of information, the lidar technique was applied during the PANACEA winter campaign (10 January 2020–7 February 2020) at Ioannina, as it is an ideal tool to monitor the spatio-temporal evolution of the atmospheric structure and the PM distribution with increased temporal (30–60 s) and spatial (7.5 m) resolution. Therefore, in this work we present, for the first time, the evolution of the vertical distribution of aerosol optical properties, the aerosol backscatter coefficient (b_{aer}), and the particle linear depolarization ratio (PLDR), during 13-day measurements as retrieved from the mobile single-wavelength (532 nm) depolarization Aerosol lIdAr System (AIAS), within the PBL and the lower free troposphere (LFT), up to 4 km height amsl. The lidar measurements were complemented by in situ fine aerosol ($PM_{2.5}$) mass concentration and BC measurements, as well as meteorological data (temperature (T), relative humidity (RH), wind speed, and direction) obtained at the lidar site.

3.2.2 Lidar Location and Methodology

Location and Description of the NTUA mobile Lidar System

The city of Ioannina is the capital of the region of Epirus, in Northwestern Greece (Figure 3.10a). It is located near Lake Pamvotis (coverage 19 km^2) inside a basin surrounded by high mountains (Figure 3.10b): the Pindos mountains on the east, and other mountains on the south and the southwest side of the city. Figure B1 depicts the mountains' names and the corresponding summits' height. The location of the city plays a major role in the air mass circulation over the studied area, which during the winter period usually remains constraint within a shallow PBL accompanied by stagnant air masses due to strong temperature inversions occurring from evening to late morning hours, especially during cold winter nights. In this context, all emissions from the city's anthropogenic activities (transport and domestic heating) are trapped inside a shallow PBL, leading to the formation of intense smog events and very poor air quality levels (Sindosi et al., 2019; Sindosi and Hatzianastassiou, 2021; Kaskaoutis et al., 2020).

During the campaign, the AIAS elastic depolarization lidar system, operated by the National and Technical University of Athens (NTUA) in cooperation with the Biomedical Research Foundation Academy of Athens (BRFAA), was located 1–1.5 km from the city center and Lake Pamvotis (39.65° N, 20.85° E, 500 m amsl.). AIAS emits a linearly polarized laser beam at 532 nm to the atmosphere and detects the parallel and vertical components of the elastically backscattered lidar signal at 532 nm using a combination of analogue and photon-counting signal digitizers. The spatial vertical resolution is equal to 7.5 m and the temporal resolution of the acquired lidar signals is 1.5 min. The full overlap height of AIAS is reached at 250 m above ground level (agl.). The technical characteristics of the AIAS lidar system are provided by Papayannis et *al.* (2020) and Mylonaki *et al.* (2021).

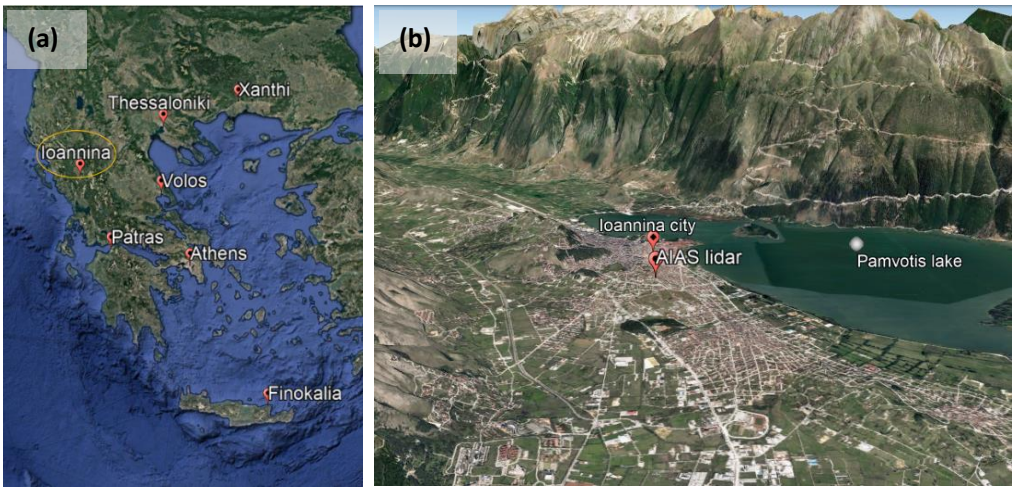

Figure 3. 10: (a) PANACEA sites during the winter campaign 2020; (b) AIAS mobile lidar system location (39.65° N, 20.85° E) inside the Ioannina basin. The map shows the Ioannina city, the Pamvotis lake and the surrounding area (Google Earth Pro v7.1.5. Epirus Region, Greece) (Papanikolaou et al., 2022b).

Methods, Models and Tools

The AIAS lidar system was operated almost in a continuous mode from early morning hours (~06:30 UTC) until the late evening ones (~19:30 UTC), with one-hour break in the afternoon, to retrieve the vertical profiles of the b_{aer} and the PLDR at 532 nm. In total, 42 measurements were performed during morning, noon, and evening hours. Special emphasis was given to the analysis of the vertical profiles of b_{aer} and PLDR during the late afternoon and evening hours, when the BB activity for domestic heating purposes was more intense and very fresh (~hours) BB particles were produced. By excluding the cloudy days and the measurements that were not useable due to unfavorable meteorological conditions (e.g., most of the morning measurements were under fog conditions), in total 17 aerosol profiles of the optical properties were analyzed and presented in this study, showing the vertical mixing of the particles occurring during winter-time in Ioannina city. The late afternoon and evening measurements, along with the one morning measurement that were used in this study, can be seen in Figure 3.11.

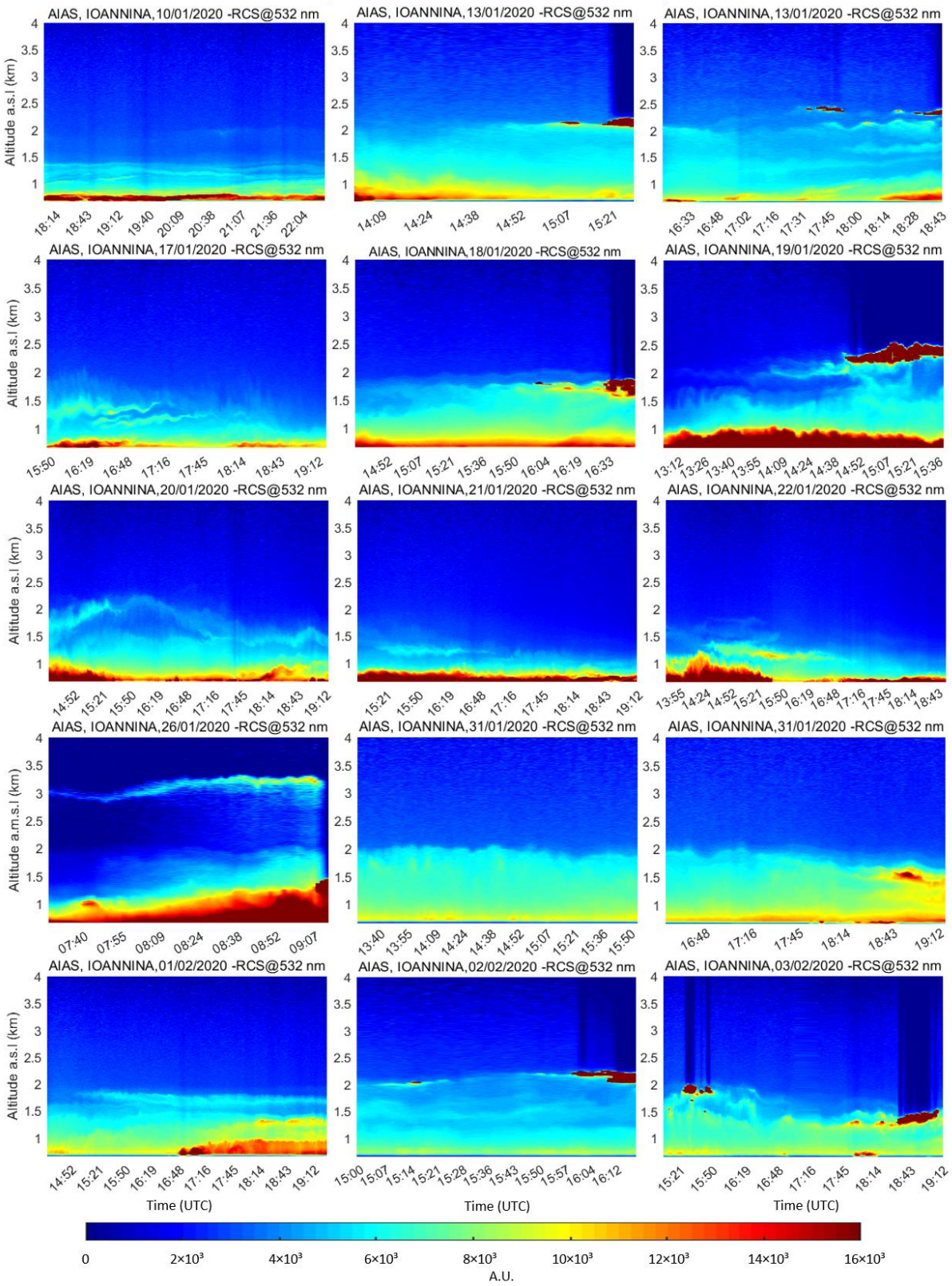

Figure 3. 11: Spatio-temporal evolution of the range-corrected lidar signal at 532 nm, for the days used in this study, during the PANACEA campaign, in Ioannina city (Papanikolaou et al., 2022b).

Lidar Data Processing

The acquired lidar data were processed, in a near real-time lidar mode, using the Single Calculus Chain (SCC) as described by D'Amico *et al.* (2015) and Mattis *et al.* (2016), to retrieve the vertical profiles of the b_{aer} and the PLDR at 532 nm. Since AIAS is a depolarization lidar system, a calibration constant was needed for the PLDR value to be calculated. The calibration method used for AIAS was the "±45° calibration", which uses two measurements taken by rotating the depolarization analyzer at ±45° (Belegante et al., 2018; Freudenthaler, 2016). The calculation of PLDR by the SCC is fully described by D'Amico et al. (2015, 2016), and Mattis et al. (2016).

In order to retrieve the profiles of b_{aer} an assumption of a constant LR has to be made (Klett, 1981, 1985), regarding the specific aerosol type (Papayannis et al., 2009). In this study, two aerosol types were identified: (i) the majority of the studied cases referred to locally produced BB aerosols, while one case (ii) was identified as long-range transport of dust aerosols in the free troposphere. Concerning the BB aerosols, as their LR values may vary in the range 43 to 98 sr (Groß et al., 2013; Burton et al., 2013; Murayama et al., 2004; Balis et al., 2003; Müller, 2003; Burton et al., 2012; Nicolae et al., 2013) the LR assumed for the studied BB cases in this study was equal to 70 ± 20 sr, as mostly observed in this kind of aerosols. On the other hand, the LR value used for the dust case was equal to 50 ± 15 sr according to Groß *et al.* (2011), Sicard *et al.* (2016), Soupiona *et al.* (2020) and Mylonaki et al. (2021). The corresponding systematic errors of the retrieved b_{aer} and PLDR values using the SCC processing chain can be found in (D'Amico 2016; Mattis *et al.*, 2016). In our case the corresponding uncertainty of b_{aer} and PLDR is of the order of ~11 ± 8% and 16 ± 11%, respectively (Mylonaki *et al.*, 2021).

Planetary Boundary Layer Height Calculation

It is well established that the variability of the PBL height (PBLH) over ground depends mainly on the topographical characteristics of the area under study, as well as on the prevailing synoptic and micrometeorological conditions site, taking into account the season of the measurements (Papanastasiou and Melas, 2009; Stull, 1988). On the other hand, the PBLH variation is mostly related to the vertical mixing and thus, it can directly control the dispersion of air pollutants inside the PBL (Emeis and Schäfer, 2006; Su et al., 2018). Thus, the PBLH remains a crucial input parameter to atmospheric models, enabling a realistic description of the lower atmospheric dynamics and providing accurate and real-time air-pollution dispersion forecasts.

The role of the PBLH becomes more important during the cold winter periods, when low-altitude temperature inversions form, which play a major role in the confinement of local emissions inside a shallow PBL, leading to increased air pollutants loadings near ground. In our study, the PBLH variation was estimated by applying the extended-Kalman filtering (EKF) technique to the range-corrected and background-subtracted (RCS) lidar signals (Kokkalis et al., 2020).

Hybrid Single Particle Langrangian Integrated Trajectory Model (HYSPLIT)

The air mass trajectories arriving over the Ioannina city from long ranges (greater than several km distances) were calculated using the HYSPLIT, in the backward mode, described by Stein *et al.* (2015). This enabled us to identify the origin of the air masses observed by the lidar in the LFT and consequently the associated aerosols' source region. For the backward air mass trajectory analysis, the "normal" method was used, based on the GDAS1 (Global Data Analysis System) meteorological data. The vertical motion used to calculate the air mass trajectories was taken from the model's vertical velocity. As initial values for the model, we used the geographical coordinates of the AIAS lidar system (39.65° N, 20.85° E) and the altitude (amsl.) of the observed aerosol layers. The duration of the air mass trajectories calculation was set to 144 h in order to obtain representative results of the PM source regions.

Moderate Resolution Imaging Spectroradiometer (MODIS)

In this study active fire data from MODIS, distributed through the Fire Information for Resource Management System (FIRMS) (https://firms.modaps.eosdis.nasa.gov/map/). In order to have a better estimation of the active fires during the studied period, the confidence of the fire data was selected to be higher than 70%. The active fire data were used in order to ensure that the BB aerosols observed with the AIAS mobile lidar system over the Ioannina city were locally originated and there was no other contribution from other relevant sources in Greece, Balkans, and Europe during this time period. However, since these data were only used for a specific reason (i.e., to confirm the local origin of the emitted BB aerosols) no further results related to the active fires are presented here.

Low-Cost Sensors

The Purple Air PA-II sensor (PurpleAir Inc., Draper, UT, USA) is a low-cost PM monitoring device, based on an optical particle counter (OPC), PMS5003, Plantower Ltd., Beijing, China), which provides mass concentrations (PM_1, $PM_{2.5}$, and PM_{10} fractions), along with the T, RH, and barometric pressure (P) data at a 2-min resolution. The sampled air mass is guided throw a built-in fan to the laser detector after two 90° turns. As an output the sensor provides PM_1, $PM_{2.5}$, and PM_{10} mass concentrations, as well as the cumulative particle size distribution in six size ranges (lower than 0.3 μm, 0.5 μm, 1 μm, 2.5 μm, 5 μm, and 10 μm) among other parameters (Stavroulas et al., 2020; Kosmopoulos et al., 2020).

In this study we used the $PM_{2.5}$ mass concentration, as well as T and RH data derived from the sensor PANACEA- 013 located at Anatoli in the south suburbs of Ioannina city after applying a quadratic regression model correction derived during an extensive characterization campaign held at Ioannina during winter and spring time 2019–2020, using as reference a 32 channel HORIBA APDA-372 (Horiba Ltd., Kyoto, Japan) optical particle counter, an instrument that is a reference-equivalent method for determining $PM_{2.5}$ and PM_{10} according to EN 14,907 and EN 12,341 standards. The correction, when applied, was found to yield significant decrease in the normalized Root Mean Squared Error (nRMSE) as well as an almost 10-fold decrease in the Mean

Absolute Error (MAE). A detailed description on the PA-II correction, specific for the Ioannina environment can be found in Stavroulas *et al.* (2020).

Aethalometer

BC measurements were obtained using a seven-wavelength dual spot aethalometer (AE-33, Magee Scientific, Berkeley, CA, USA in the same sampling site as the lidar system. The AE-33 was sampling total suspended particles at 2 L/min, through short conductive tubing, on a PTFE-coated glass-fiber filter tape (Part No, 8060). BC concentration was determined using the 880 nm aethalometer channel using an AE provided by the manufacturer. The AE-33 compensates for the filter loading effect in real-time utilizing the Dual Spot technology while a correction specific to the filter material used; it also applied regarding the multiple scattering artefact (Drinovec et al., 2015). The 1-min resolution BC measurements were averaged on an hourly basis. Source specific BC fractions, namely those related to wood burning (BC_{wb}) and fossil fuel combustion (BC_{ff}) were calculated by the instrument, applying the "Aethalometer Model" at the 470 and 950 nm wavelength pair, assuming a fixed Absorption Ångström Exponent (AAE) for wood burning (AAE_{wb} = 2) and fossil fuel combustion (AAE_{ff} = 1) (Sandradewi et al., 2008).

3.2.3 Results and Discussion

Figure 3.12 presents the vertical distribution of b_{aer} and PLDR at 532 nm, as observed by the AIAS mobile depolarization lidar during the winter PANACEA campaign over the city of Ioannina. The under-study cases are presented with a different color for each day and time. The PBLH along with its standard deviation (std) is also shown by the black solid and dashed lines, respectively. lidar during the winter PANACEA campaign over the city of Ioannina. Each case shown is presented with different color. The PBLH along with its standard deviation is presented with the black solid and dashed lines, respectively.

The majority of the cases presented here show low altitude aerosol layers (from near ground up to 2.40 km amsl.) with quite low PLDR values (lower than 0.11), except for the case of the 26 January 2020, when dust aerosol layers (Figure 3.12; purple solid line) 7 of 23 were observed from 2.71 up to 3.48 km altitude, showing increased PLDR values reaching up to 0.34. The mean value of PBLH of all the under-study cases was found equal to 1.13 ± 0.07 km amsl. The mean values of the aerosol optical properties (b_{aer} and PLDR) were calculated within the PBL and inside each one of the aerosol layers observed above it.

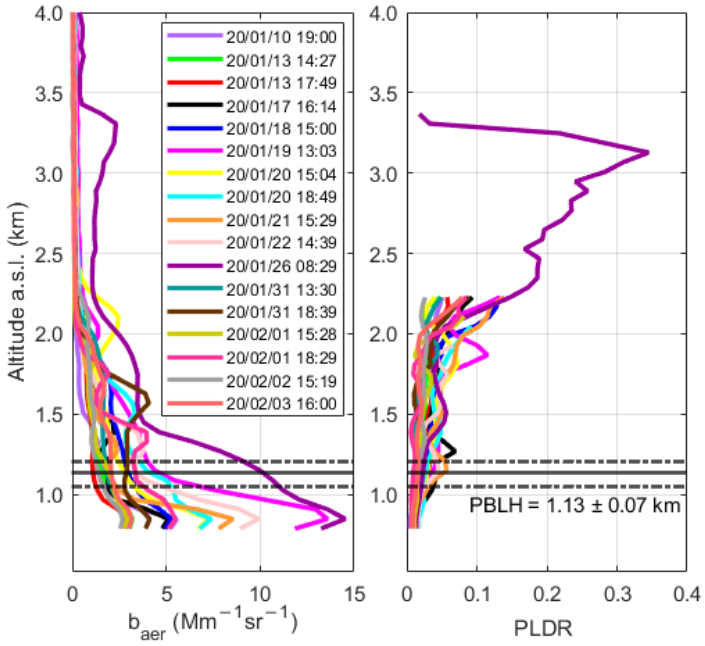

Figure 3. 12: Vertical distribution of b_{aer} ($Mm^{-1}sr^{-1}$) and PLDR at 532 nm, as observed by the AIAS mobile depolarization system (Papanikolaou et al., 2022b).

In Figure 3.13, we present the geometrical and optical properties observed over Ioannina during this campaign. The black rhombus denotes the PBLH values, while the different colored-bars denote the top and bottom of the aerosol layers (AL) above it (Figure 3.13a). The mean values of b_{aer} and PLDR at 532 nm, along with their standard deviation (std) as they were calculated inside the PBL (black rhombus) and the AL (different-colored-squares), are also presented (Figure 3.13b, c). In the same graph can also be found, the wind speed and direction (Figure 3.13d), the PM2.5 mass concentrations, with the T and RH (Figure 3.13), and the $BC_{(wb,\ ff)}$ mass concentrations (Figure 3.13f), as obtained during the available days of the winter PANACEA campaign. The results presented in Figure 3.13 and the corresponding meteorological data are extensively presented in Tables B.1 and B.2, while the timeseries analysis of the BC, along with the BC_{wb}, BC_{ff} and $PM_{2.5}$ mass concentrations during the campaign are also presented in Figure B. 2.

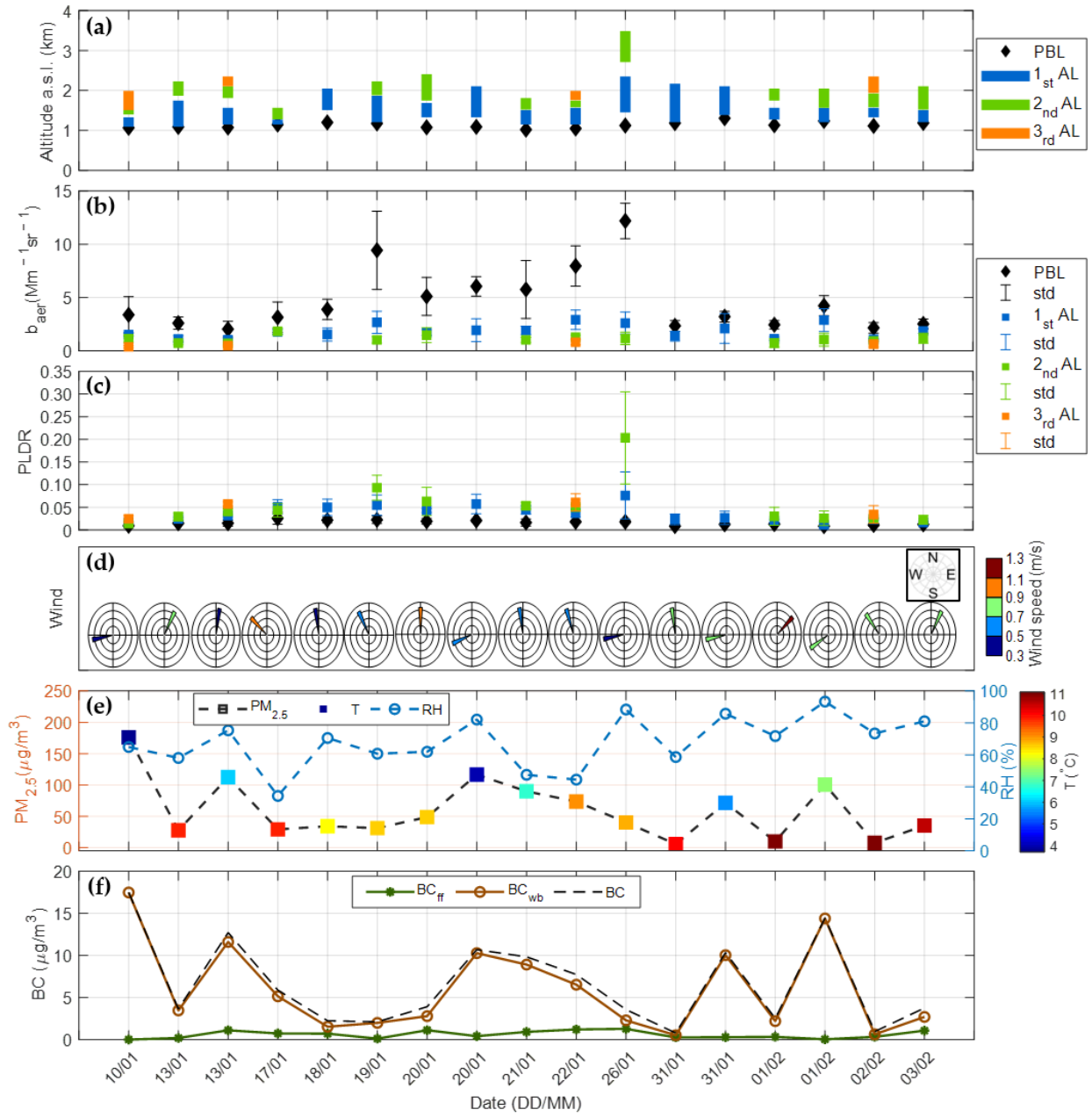

Figure 3. 13: Temporal variation of (a) the PBL altitude (amsl.; black rhombus) along with the base and top of each aerosol layer (AL; colored bars) (km) and the corresponding mean values of (b) b_{aer} and std ($Mm^{-1}sr^{-1}$) and (c) PLDR and std at 532 nm, as obtained by the AIAS mobile depolarization lidar, along with the (d) wind speed (m/s) and direction (°), (e) $PM_{2.5}$ mass concentrations (μg/m³), T (°C), RH (%), (f) the BC mass concentrations (μg/m³) along with the contribution of the fossil fuel and wood burning to the total BC mass concentrations, during the PANACEA winter campaign in Ioannina. All data presented are averaged for the same time periods during which the lidar profiles were retrieved (Papanikolaou et al., 2022b).

From the analysis of the data presented in Figure 3.13a, we found that the PBLH ranged from 1.02 to 1.31 km amsl. during the afternoon and evening hours of the campaign. The mean

altitude of the AL found in the FT was equal to 1.21 ± 0.06 km for the BB smoke particles, and of 3.16 ± 0.27 km for the dust aerosol layer on 26 January. Specifically, the BB aerosols were initially emitted in the PBL during daytime, and were later convected into the LFT due to the prevailing unstable conditions which are connected to thermals of warm air rising from ground up to the top of the PBL, in the form of updrafts (Solomos et al., 2019; Zeng et al., 2021). Thus, BB smoke layers were found during the campaign in the LFT (1.21 to 2.23 km), while the long-range transported dust layer was detected at higher altitudes (3.16 km). This could also be related to the fact that the sources of the BB aerosols (fireplaces and wood stoves) are local ones at near ground levels, typically smoldering fires with low injection heights (Huang et al., 2013; Eloranta and Piironen, 1994), in contrast to the dust and mixed dust aerosols, which are generally found in higher heights, typically between 3–6 km amsl. (She, 2001).

The mean value of b_{aer} at 532 nm within the PBL during the campaign (Figure 3.13b) was found equal to 4.61 ± 2.88 $Mm^{-1}sr^{-1}$. However, in some days of measurements (i.e., 19, 22 and 26 January) the mean b_{aer} was greater than 7.96 $Mm^{-1}sr^{-1}$ reaching up to the value of 12.19 $Mm^{-1}sr^{-1}$, while in the rest of the days it ranged from 2.03 ± 0.74 to 6.05 ± 0.91 $Mm^{-1}sr^{-1}$. The FT BB aerosol layers showed a mean b_{aer} of 1.45 ± 0.43 $Mm^{-1}sr^{-1}$, ranging between 0.37 ± 0.11 and 2.91 ± 0.91 $Mm^{-1}sr^{-1}$. The mixed dust aerosol layer showed a value of b_{aer} equal to 1.50 ± 0.59 $Mm^{-1}sr^{-1}$. The mean values of the PLDR (Figure 3.13c), indicative of the aerosols' shape, were found to be extremely low inside the PBL and ranged between 0.01 ± 0.01 and 0.03 ± 0.01. Regarding the FT aerosol layers, the mean PLDR values were found equal to 0.04 ± 0.02 and reached values up to 0.09 ± 0.03, which are typical for BB aerosol and BB mixtures (Table 3.3) (Yang et al., 2021b; Akagi et al., 2013; Li et al., 2021; Giglio et al., 2018, 2016; Behrendt and Nakamura, 2002; Emde et al., 2016; Anderson et al., 1986; Soupiona et al., 2020b).

On the other hand, the mean PLDR value of the aerosol layer on 26 January 2020, was equal 0.20 ± 0.10, indicating the presence of dust aerosols (Akagi et al., 2013; Flemming et al., 2017; Soupiona et al., 2020b; Kokkalis et al., 2021; Mona et al., 2006).

Table 3. 3: PLDR (532 nm) values of fresh BB aerosols as cited in the relevant literature (2012–today).

Reference	**PLDR**
Burton et al. (2012)	0.02-0.05
Nicolae et al. (2013)	<0.05 (0.02-0.04)
Burton et al. (s2013)	0.03-0.06
Nepomuceno et al. (2014)	≤0.05
Burton et al. (2015)	0.02-0.03
Stachlewska et al. (2018)	≤0.065
Papanikolaou et al. (2020)	0.05±0.04
This study (Papanikolaou et al. 2022b)	**0.02±0.01 (PBL) 0.04±0.02 (FT)**

At ground level, the average wind speed during the period of measurements was extremely low (0.7 ± 0.2 m/s) with values ranging from 0.3 to 1.2 m/s, with a mean North-Northwest direction (Figure 3.13d). At the same level, the $PM_{2.5}$ mass concentrations ranged from 5.6 to 175.7 μg/m^3, while the T and RH did not vary significantly during the campaign time period ranged from 3.7 to 11.1 °C and 34 to 93%, respectively (Figure 3.13e, Table B2). The BC concentrations presented a mean value of 6.6 ± 5.1 μg/m^3 (0.8 to 17.5 μg/m^3) and exhibit a similar trend to the $PM_{2.5}$ concentrations. It is evident, that the increase in the BC consternations at the surface, especially during evening hours, can be attributed mostly to wood burning activities. There is no clear linkage between the wind direction-intensity (Figure 3.13d) and the recorded hourly BC values (Figure 3.13f), at least for the cases examined and presented in this study, which are characterized by small wind intensities (0.3–1.3 m/s) and limited direction range (90° range covering from W to NNE), even though the aforementioned meteorological properties (along with temperature) are playing an important role in the development of the PBLH, which may affect also the distribution of particles at the lowest atmospheric height. The reason behind this can be the amount of wood burning, that is higher than any other anthropogenic-industrial activity that take place in the area.

According to a previous study (Zielinski et al., 2020) related to wood burning, the BC concentrations seem to also increase with the absence of precipitation, along with wind speeds lower than 3 m/s and a shallow PBL, it should be noted that the period of measurements was very dry, essentially there was no rain except for the 26 January (0.6 mm). The participation of the fossil fuel in the BC mass concentrations values was nearly negligible throughout most of the period (0.1 to 35.8%), with extremely low values ranging from 0 to 1.3 μg/m^3, while the wood burning BC_{wb} mass concentrations (0.5 to 17.5 μg/m^3), at most times, were almost largely dominated by the BC, with contribution that for two cases (i.e., 10 January and 1 February) reached the extreme value of 100% (64.1–100%). According to Stavroulas *et al.* (2020), during the period 15 December 2019 to 13 January 2020, an average BC concentration of 5.02 μg/m^3 was measured in Ioannina reaching up to 31 μg/m^3 (hourly max), with an extremely high BC_{wb} contribution of 75%, that during night-time was reaching up to 88%.

Relevant studies related to BC measurements showed that in Athens (Greece), during the last few years, the BC concentrations reached values up to 32.7 μg/m^3, while the BC_{wb} contribution ranged from 20–25% up to 40% of the BC, during the night (Liakakou et al., 2020; Fourtziou et al., 2017; Gratsea et al., 2017; Kalogridis et al., 2018). In other European cities (e.g., Granada, Lisbon, London, Madrid, Paris, Porto, Rome, or Zurich) measurements during the winter period showed mean BC concentrations lower than 13.1 μg/m^3 with a BC_{wb} contribution that did not exceed 47 ± 6% of the BC (Herich et al., 2011; Titos et al., 2017; Fuller et al., 2014, 2013; Costabile et al., 2017; Borrego et al., 2010) apart from the BC_{wb} contribution of 88% in rural area of Spain, during the winter of 2014–2015, as described by Becerril-valle *et al.* (2017). It is of interest to mention that BC concentrations emitted in a middle-sized urban city such as Ioannina (~280 inhabitants/km^2) during winter is of the same order, and in some cases even greater, than

the BC emissions in some of the biggest European cities and capitals (~3000–20,000 inhabitants/km^2). This is the result of a decrease in consumption of conventional fuel for residential heating (e.g., oil) in Ioannina and the strengthened use of cheaper wood or pellet burning during the times of austerity in Greece.

In most of the studied cases, the $PM_{2.5}$ and BC_{wb} concentrations were lower during early afternoon hours, than during night-time. These quantities were also decreasing as T increased. Temperature plays a very important role in the development of the PBLH, which may affect also the distribution of aerosols inside the PBL. Decreased shortwave radiation and thus temperature can prevent the vertical mixing of aerosols. Especially during the cold winter periods, when low-altitude temperature inversions can be formed and thus the local emissions can be trapped inside a shallow PBL, leading to increased particle concentrations near ground. Based on the relatively similar behavior of the $PM_{2.5}$ and the BC_{wb} concentrations and the inversely proportional between $PM_{2.5}$, BC, BC_{wb}, and T, an analysis was applied to find the correlation between the aforementioned quantities. In Figure 5 we present the linear fits, along with the coefficients of determination and the linear regression equations, as obtained for the following quantities: (a) BC and $PM_{2.5}$, (b) BC_{wb} and BC, (c) BC_{wb} and $PM_{2.5}$, (d) BC and T, (e) BC_{wb} and T, and, finally, (f) $PM_{2.5}$ and T, respectively. The correlation plots between the BC_{ff} and the quantities BC, $PM_{2.5}$, and T can be found in Figure B3 in the Appendix B.

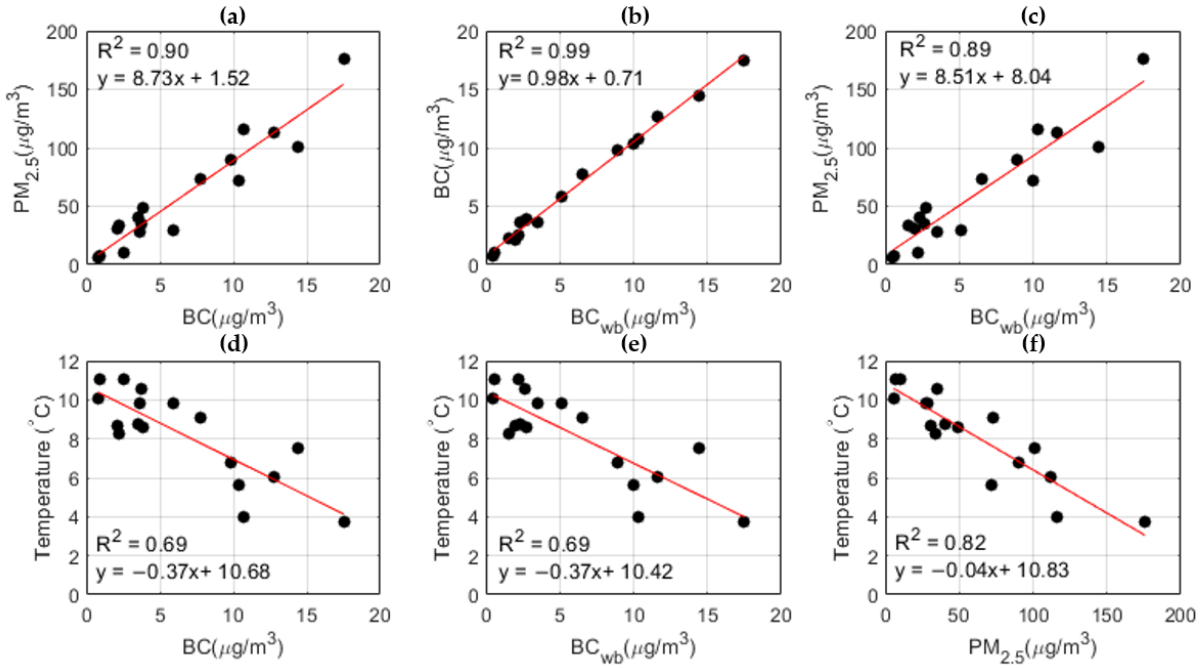

Figure 3. 14: Correlation graphs between: (a) BC_{wb} and $PM_{2.5}$, (b) BC_{wb} and T and finally, (c) $PM_{2.5}$ and T, along with the linear fit (red solid line) and the corresponding coefficients of determination R^2 (Papanikolaou et al., 2022b).

The coefficients of determination along with the linear regression equations for each plot are revealing a significant correlation between the parameters presented in the correlation plots in Figure 3.14. These results highlight the strong correlation between BC, BC_{wb}, and $PM_{2.5}$ ((a) R2 = 0.90, (b) R^2 = 0.99, (c) R^2 = 0.89), along with the almost complete composition of BC aerosols by biomass (wood) burning particles and the very important contribution of wood burning. The inverse relationship between both BC_{wb} and $PM_{2.5}$ with T ((d) R^2 = 0.69, (e) R^2 = 0.69, and (f) R^2 = 0.82) is also pointed out. In addition, the trends in BC concentrations appeared to be almost similar to those of $PM_{2.5}$ concentrations (Figures 3.14 and B2). These similar trends, along with the highly correlated BC, BC_{wb}, and $PM_{2.5}$ concentrations, suggesting that the $PM_{2.5}$ may contain a significant proportion of BC, and hence BC_{wb} concentrations in the study area for the studied period.

Case Studies

Moreover, we selected to analyze three cases of typical interest. The first two were related to local BB aerosols emitted from local sources namely wood burning for heating purposes, during afternoon and early night-time hours. The third case was related to the long-range transport event of dust aerosols over the city.

Local Biomass Burning Aerosol: Case I

Figure 3.15a illustrates the spatio-temporal evolution of the range-corrected lidar signals obtained by AIAS at 532 nm, from 0.52 up to 4 km height amsl., over the city of Ioannina, on 22 January 2020 between 13:54 and 19:09 UTC. The color scale on the right side of the figure indicates the range -corrected signal in arbitrary units (A.U.). Furthermore, in the same figure we present the PBLH (black dots). What is easily observed is an intense confinement of aerosols from ground up to 1.05 km height, which indicates the presence of locally emitted aerosols. Increased aerosol backscattering is also observed near ground during the lidar measurements that day 13:56–19:09 UTC). The green-colored rectangle indicates the time window (14:39–15:41 UTC), in which the retrieval of the vertical profile of the aerosol optical properties b_{aer} and PLDR took place.

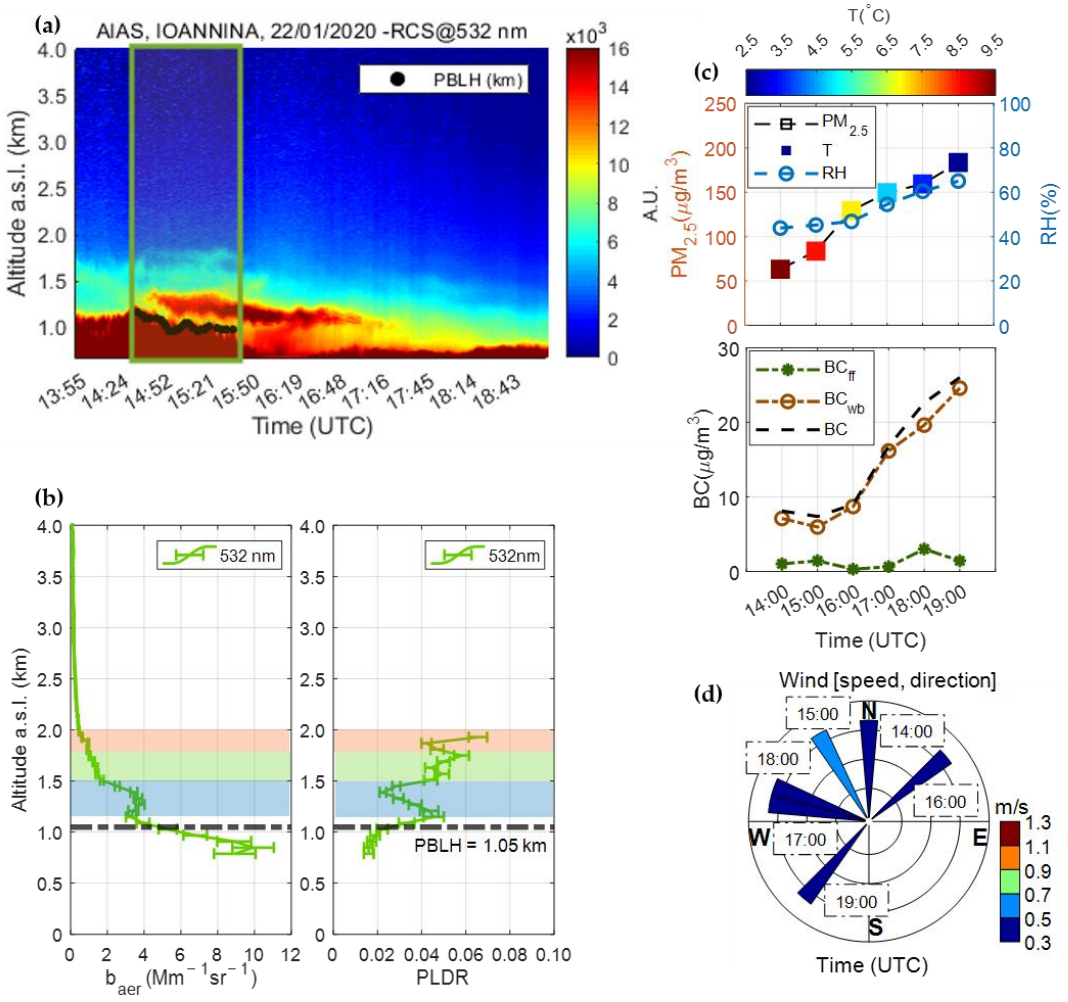

Figure 3. 15: (a) Spatio-temporal evolution of the range-corrected lidar signal at 532 nm, and (b) the vertical distribution of b_{aer} ($Mm^{-1}sr^{-1}$) and PLDR at 532 nm, as observed by the AIAS mobile lidar on 22 January 2020 between 14:39 – 15:41 UTC over the city of Ioannina. The 3-colored-shadowed rectangles represent the geometrical boundaries of the studied aerosol layers. The black dashed line represents the mean PBLH. (c) upper graph: Temporal evolution of the $PM_{2.5}$ mass concentration (μg/m³), versus T (°C) and RH (%); lower graph: BC mass concentrations (μg/m³) at ground level, along with the contribution of the fossil fuel (BC_{ff}) and wood burning (BC_{wb}) to the total BC concentrations. (d) the wind speed and direction (hourly mean), during the measurement time (Papanikolaou et al., 2022b).

In Figure 3.15b the 3-colored horizontal shadowed rectangles represent the geometrical boundaries of the studied aerosol layers, while the black dashed line delineates the mean value of the PBLH inside the temporal window. Finally, in Figure 3.15c we present (upper graph) the hourly variation of the $PM_{2.5}$ mass concentration (μg/m³), the T (°C), the RH (%), given by the Purple Air sensor, while in the same figure (lower graph) we show the BC mass concentration levels) (μg/m³) along with the contribution of the fossil fuel (BC_{ff}) and wood burning (BC_{wb}) to the total BC mass concentrations measured by the aethalometer.

On 22 January (Figure 3.15a, b) we observed three aerosol layers over the PBL that is situated at 1.05 km amsl. The first layer (denoted by the blue shadowed rectangle) was found between 1.15 and 1.57 km. The second one (green shadowed rectangle) was found from 1.58 to 1.75 km and the last and higher one (orange shadowed rectangle) between 1.76 and 1.99 km. On that day the mean b_{aer} value inside the PBL was found equal to 7.96 ± 1.88 $Mm^{-1}sr^{-1}$. Regarding the three aerosol layers mentioned above (from the lower to the higher one), their mean b_{aer} values were found equal to 2.91 ± 0.91, 1.29 ± 0.18 and 0.80 ± 0.25 $Mm^{-1}sr^{-1}$, respectively. The mean PLDR value was 0.02 ± 0.01 inside the PBL, while the mean PLDR values at the three layers were equal to 0.04 ± 0.01, 0.05 ± 0.01 and 0.06 ± 0.02, respectively, which are in accordance with values found in the literature indicating the presence of fresh BB aerosols.

During the lidar measurement time, the ground level $PM_{2.5}$ mass concentrations were very high ranging from 63.3 to 183.3 $\mu g/m^3$, in line with the decrease in temperature during late afternoon and night-time hours (from 9.6 °C at 14:00 UTC down to 2.5 °C at 19:00 UTC). In the same period the RH increased from 44 to 65%, while the wind speed was extremely low (0.3 to 0.5 m/s) with the North (Northeast, Northwest) direction during early afternoon (14:00–16:00), changed to the West (Northwest, Southwest) direction during night-time (17:00–19:00). The BC concentration levels, during the same time period, showed an increase from 7.4 to 26.0 $\mu g/m^3$, with the contribution of the BC_{wb} concentrations (80.7 to 96.7%) being almost equal to the total BC concentrations (6.0–24.6 $\mu g/m^3$). The corresponding BC_{ff} concentrations showed a very low variability, being always lower than 3.0 $\mu g/m^3$.

Local Biomass Burning Aerosol: Case II

The second case of local BB emissions is shown in Figure 3.16, where we present the spatio-temporal evolution of the range-corrected lidar signals at 532 nm (as in Figure 3.15a) from 0.52 up to 4 km height amsl., on 1 February 2020, between 14:32 to 19:31 UTC. In this Figure we can observe the spatio-temporal evolution of the PBLH denoted by the black dots, showing a shallow PBL confined from ground up to 1.24 km amsl. with a high aerosol load. Over the PBL a distinct aerosol layer (with yellow-brownish color topped by a light blue-yellowish thin layer) centered at ~1.39 km height extending up to 2 km height. We selected to further analyze the lidar data obtained from 18:29 to 19:31 UTC (within the green-colored rectangle, Figure 3.16a).

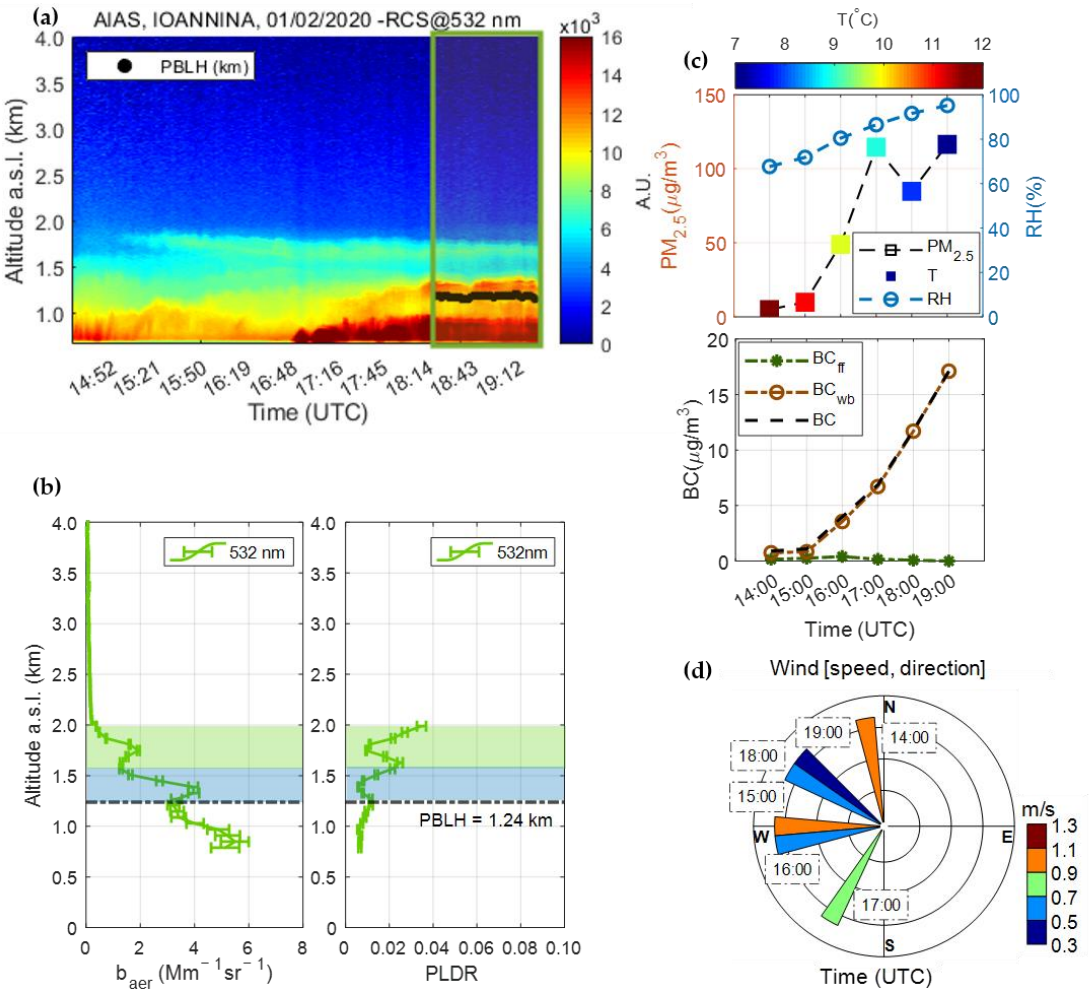

Figure 3. 16: (a) Spatio-temporal evolution of the range-corrected signal at 532 nm, (b) the vertical distribution of b_{aer} ($Mm^{-1}sr^{-1}$) and PLDR at 532 nm, as observed by the AIAS mobile lidar on 01 February 2020 between 14:32 and 19:31 UTC over the city of Ioannina. The 2-colored-shadowed rectangle represent the geometrical boundaries of the studied aerosol layers. The black dashed line represents the mean PBLH. (c) upper graph: Temporal evolution of the $PM_{2.5}$ mass concentration (μg/m³), versus T (°C) and RH (%); lower graph: BC mass concentrations (μg/m³) at ground level, along with the contribution of the fossil fuel (BC_{ff}) and wood burning (BC_{wb}) activities to the total BC concentrations. (d) the wind speed and direction (hourly mean), during the measurement time (Papanikolaou et al., 2022b).

The corresponding aerosol optical properties within the selected time-range were retrieved again by the SCC and are shown in Figure 3.16b; for two FT layers: the first between 1.24 and 1.57 km height amsl. (light blue shadowed rectangle) and the second (green shadowed rectangle) from 1.57 to 2.04 km height amsl. and inside the PBL. In the FT region the mean b_{aer} was found equal to 2.87 ± 1.06 and 0.80 ± 0.25 $Mm^{-1}sr^{-1}$, for the light blue and green layer, while the relevant mean PLDR values were 0.01 ± 0.01 and 0.03 ± 0.02, respectively. Inside the PBL the mean value of b_{aer} was found equal to 4.23 ± 0.94 $Mm^{-1}sr^{-1}$, and the corresponding mean PLDR

value was very low again, equal to 0.01 ± 0.01. All values of PLDR measured inside the PBL and the FT.

During the lidar measurement time on that day the $PM_{2.5}$ concentrations ranged from 4.9 to 116.4 μg/m^3 inside the PBL, showing again the presence of local aerosol emissions, especially during the cold (~8°C) evening hours (17:00–19:00 UTC) with high (~91%) RH values (Figure 7c-upper graph) and wind speed ranging from 0.3 to 0.9 m/s, while its direction changed from South to North-Northwest. During these evening hours, the total BC concentrations increased from 0.9 to 17.1 μg/m3 and the corresponding BC_{wb} concentrations showed a very similar growth rate and contribution reaching up to 100% of the total BC, thus proving that the aerosol source is again the local BB activities. During the whole measurement period the BC_{ff} remained extremely low (0.1–0.4 μg/m^3), showing no contribution from other local aerosol sources than the BB ones. During same hours, the $PM_{2.5}$ concentrations were found ranging from 5.0 to 116.4 μg/m^3.

Dust Aerosol Mixtures

The third case concerns a long-range transport of dust aerosols over the measuring site. In Figure 3.17a we present the spatio-temporal evolution of the range-corrected lidar signals at 532 nm from 0.52 up to 4 km height amsl., on 26 January 2020 (07:28–09:07 UTC). The PBLH (denoted by the black dots) at ~1.12 km amsl. can also be seen in Figure 3.17a, and over it we clearly see an aerosol layer extending from the top of the PBL up to ~2.34 km height and a filamented one at ~3.10 km height. We selected to analyze the aerosol data obtained in the time period from 08:29 to 09:04 UTC, (green rectangle; Figure 3.17a). The vertical profile of the aerosol optical properties (b_{aer}, PLDR) retrieved by the SCC is shown in Figure 3.17b. In this figure we have selected two different layer stratifications over the PBL (mean PBLH equal to 1.12 km amsl.) denoted by two colors: the first one (blue shadowed rectangle) located between 1.45 and 2.34 km and the second one (green shadowed rectangle) from 2.71 to 3.49 km amsl.

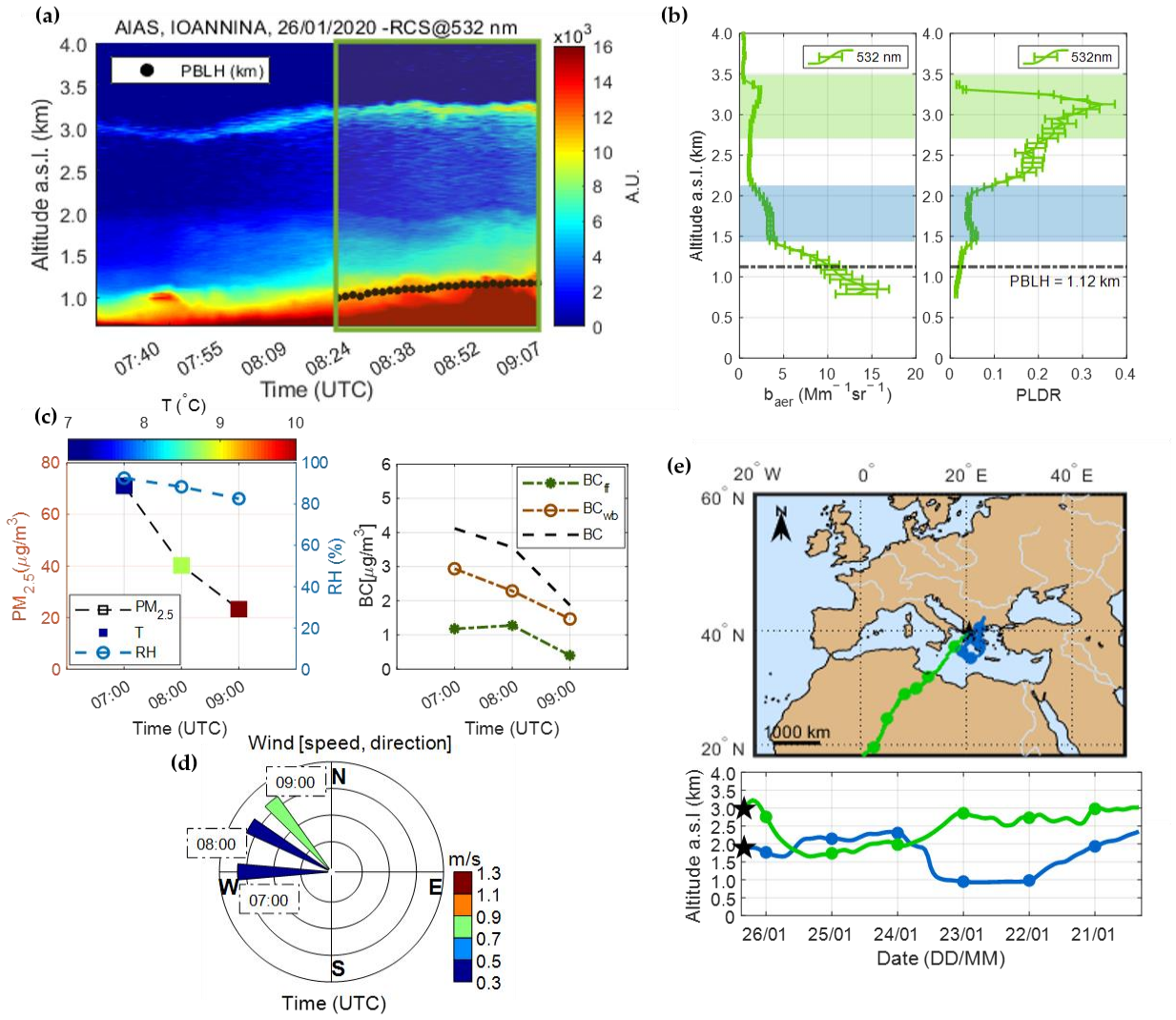

Figure 3. 17: (a) Spatio-temporal evolution of the range-corrected signal at 532 nm, (b) the vertical distribution of b_{aer} ($Mm^{-1}sr^{-1}$) and PLDR at 532 nm, as observed by the AIAS mobile lidar during the 26 of January 2020 between 08:29 and 09:04 UTC over the city of Ioannina, the 2-colored-shoadowed rectangles represent the geometrical boundaries of the studied aerosol layers. The black dashed line represents the PBLH. (c) the $PM_{2.5}$ concentration (μg/m³), the T (°C), RH (%) and the BC levels (μg/m³) along with the participation of the fossil fuel and wood burning to the total BC concentrations. (d) the wind speed and direction (hourly mean), during the measurement time. (e) The HYSPLIT air mass back trajectories for the 2 aerosol layers (Papanikolaou et al., 2022b).

In Figure 3.17e we present the backward air mass trajectories ending after 144 h over the city of Ioannina at 08:00 UTC on 26 January, at the two heights where the aerosol layers were observed. Based on the results of the HYSPLIT model (Figure 3.17e) we see that the air mass (green colored trajectory) left the African continent on 25 January, having remained over Libya, at 2–3 km height, for more than 112 h, and thus being enriched with dust particles, which finally arrived over Ioannina at the level of the second layer above the PBL. According to HYSPLIT, the

air mass (blue colored trajectory) arriving at the first layer above the PBL originated and travelled over not remotely located areas, i.e., Southern Greece and the Ionian Sea and thus being enriched with marine and local produced aerosols. Regarding the properties of that layer (blue colored) we measured a mean b_{aer} value of 2.59 ± 1.03 $Mm^{-1}sr^{-1}$ and a mean PLDR value of 0.08 ± 0.05. Inside the second layer we found a mean b_{aer} value of 1.50 ± 0.59 $Mm^{-1}sr^{-1}$ and a mean PLDR value of 0.20 ± 0.10. The PLDR value obtained between 2.71–3.48 km height amsl. can be attributed to dust aerosol mixtures that as indicated by HYSPLIT trajectories can enriched the air mass on the way to Greece. Such PLDR values are in accordance with previous studies on dust aerosols and dust mixtures (Müller *et al.*, 2009; Groß *et al.*, 2011; Burton *et al.*, 2012, 2013, 2014; Papayannis *et al.*, 2012; Groß *et al.*, 2015; Groß *et al.*, 2015; Soupiona *et al.*, 2019; Mylonaki *et al.*, 2021; Mylonaki *et al.*, 2021b).

During this case, the $PM_{2.5}$ concentrations were still high (between 23.3 and 71.1 $\mu g/m^3$) with temperature variations, at ground level, between 7.2–10.1°C, and RH values equal to 88 ± 5%. The wind speed for the measurement time ranged from 0.3 to 0.7 m/s, with North-Northwest direction. The BC levels were found ranging in much lower levers, from 1.9 to 4.1 μg/m3. In contrast to the previous case studies, the $PM_{2.5}$ and BC concentrations were decreasing from 07:00 to 09:00 UTC in line with the increasing T and the expanding PBL, leading to vertical mixing of particles accumulated within the surface and lower PBL. In this case, the BC_{wb} (1.5 to 2.9 $\mu g/m^3$) contribution to the total BC concentrations (~64.1-78.6%) was strongly differentiated from the previous two case studies. On the other hand, the BC_{ff} contribution to the total BC concentrations was much higher compared to other days (21.4– 35.9%), indicating a much more important presence of fossil fuel burning activity during that day.

3.2.4 Conclusions

During the PANACEA winter campaign (10 January–7 February 2020) the AIAS mobile depolarization lidar was placed in the city of Ioannina at 500 m amsl, which during cold winter days is characterized by extremely high (highest all over Greece) concentrations of fine carbonaceous aerosols from BB. The aim was to study the spatio-temporal evolution of the fresh BB aerosols within the PBL and LFT. In this study, we analyzed 17 cases as they have been observed by AIAS, complemented with in situ ($PM_{2.5}$, BC, BC_{ff}, and BC_{wb}) and meteorological (T, RH, wind speed, and direction) data.

In total, 33 out of 34 aerosol layers observed in the LFT were characterized as BB of local origin. These layers showed mean b_{aer} (532 nm) values of 1.45 ± 0.43 $Mm^{-1}sr^{-1}$ (from 0.37 ± 0.11 to 2.91 ± 0.91 $Mm^{-1}sr^{-1}$), with a mean PLDR (532 nm) value of 0.04 ± 0.02 (from 0.01 to 0.09), at altitudes between 1.21 and 2.23 km amsl. There was a single case observed on 26 January 2020, attributed to dust with a mean b_{aer} value equal to 1.50 ± 0.59 $Mm^{-1}sr^{-1}$, and a mean PLDR of 0.20 ± 0.10, in the altitude range from 2.71 to 3.49 km. The PBLH during the campaign ranged from 1.02 to 1.31 km, with a mean value of 1.13 ± 0.07 km, within it the mean b_{aer} value was found equal to 4.61 ± 2.88 $Mm^{-1}sr^{-1}$ (from 2.03 ± 0.74 to 12.19 ± 1.66 $Mm^{-1}sr^{-1}$), with the PLDR value ranging between 0.01 ± 0.01 and 0.03 ± 0.01, indicating a strong presence of fresh BB aerosols,

which is intensified within a shallow PBL by extensive residential heating during cold and calm conditions.

At ground level, the $PM_{2.5}$ mass concentrations ranged from 5.6 to 175.7 μg/m^3, while the T and RH ranged from 3.7 to 11.1 °C and 34 to 93%, respectively. Wind speed presented extremely low values (0.33 to 1.16 m/s), contributing to increased BC concentrations, due to air mass stagnant conditions. The BC presented a mean value of 6.6 ± 5.0 μg/m^3 (from 0.8 to 17.5 μg/m^3), while the wood burning emissions from residential heating, were increasing during the evening hours and decreasing temperatures. The BC_{wb} concentrations ranged from 0.5 to 17.5 μg/m^3, with an extremely high a mean BC_{wb} to BC contribution of 85.4%, which in some cases during night-time reached up to 100%. The diurnal pattern of the BC was following almost identically the variation of BC_{wb}. This could be attributed to the almost constant meteorological conditions prevailed during the campaign period and the high amount of wood burning activities which did not allow us to record significant fingerprints of any other anthropogenic-industrial activity. The only exception in the above statement is the small increase in BC_{ff} during North prevailing winds.

Overall, our study showed that the BC_{wb} to the BC values in Ioannina were very high, and exacerbated by the shallow PBL and the stagnant air conditions during cold winter days. The corresponding locally produced BB aerosol layers presented extremely low PLDR values inside the PBL (0.02 ± 0.01) and in the FT (0.04 ± 0.02). The results of this work can be used in different modelling schemes to forecast severe air pollution episodes in the city of Ioannina and to provide tools to the Greek authorities to reduce the air pollution levels at this city.

3.3 Australian Bushfires (2019–2020): Aerosol Optical Properties and Radiative Forcing

3.3.1 Introduction

Smoke aerosols affect the Earth's climate system in both direct and indirect ways, as they can highly absorb the sunlight due to their high content of BC, but they can also modify the cloud properties (i.e., cloud life-time, precipitation, and ice formation) (Yang et al., 2021b; Baars et al., 2019; Ohneiser et al., 2022, 2020b; Khaykin et al., 2020; Yang et al., 2021a). Freshly emitted soot particles are initially hydrophobic, but become hydrophilic as a result of aging. Additionally, they can undergo compaction upon humidification, thus increasing their ability to serve as CCN (Ansmann et al., 2021b).

The impact of smoke particles on the climate also depends on their horizontal and vertical distributions, as well as on their chemical composition (Ponczek et al., 2022; Zielinski et al., 2020). During long-range transport, there is evidence that the optical properties of smoke particles change (Ansmann et al., 2021b; Müller et al., 2007b), and different optical properties are commonly associated with the altitude range of the plumes (Haarig et al., 2018; Hu et al., 2019). Stratospheric smoke aerosols have significantly longer lifetimes than tropospheric ones, which increases the impact on Earth's atmosphere radiation budget. In general, smoke particles are one

of the key aerosol types in climate research, thus the study of their vertical stratification, both in the troposphere and stratosphere, along with their optical and radiative properties, has become an urgent need, especially regarding extreme biomass burning (BB) events.

Apart from a major source of particulate matter (PM), BB is also an important source of trace gases in the local, regional, and global atmosphere. The main gases produced during BB include carbon dioxide (CO_2), carbon monoxide (CO), methane (CH_4), and nitrogen oxides (NO_x). CO, CH_4, and NO_x lead to the photochemical production of ozone (O_3) in the troposphere that can be really harmful at high concentrations (Levine, 2013). Several studies have documented O_3 formation in smoke plumes (Akagi et al., 2013; Liu et al., 2016), while others have suggested that wildfires lead to an increased amount of ground-level O_3 (Liu et al., 2016; Brey and Fischer, 2016). For instance, wildfire emissions are reported to enhance the average summertime monthly mean of O_3 concentration by 2–8 ppb (Jaffe et al., 2013, 2018), while other studies have shown that the observed O_3 to CO enhancements in smoke plumes attributed 3.5% of the global tropospheric O_3 production to BB emissions (Bourgeois et al., 2021; Selimovic et al., 2020).

The record-breaking bushfires in Southeast Australia in the summer of 2019–2020 were the most devastating in the history of the country. According to Filkov *et al.* (2020), almost 19 million hectares were burned and more than 3 thousand houses were destroyed, while 33 people and more than 1 billion animals were killed, causing extreme damage to the wildlife and the ecosystem. The meteorological conditions were very favorable for the wildfire ignition and spread, increasing the severity of the event. The recorded temperatures were extremely high (+1.33 °C of the mean temperature and +1.59 °C of the local mean maximum) and the resulting drought was intense (annual mean precipitation of 277.6 mm) (Filkov et al., 2020).

These extreme wildfires occurred within the midlatitude cyclones belt (Hirsch and Koren, 2021), at relatively south latitudes where the tropopause height (TPPH) is relatively low. Along with the strong pyrocumulonimbus (pyroCB) convection (Kablick et al., 2020), the emitted BB aerosols managed to reach the higher troposphere and enter into the stratosphere. Compared to a similar extreme event of the North Hemisphere in 2017 (Pacific Northwest Wildfire Event) that injected about 0.1–0.3 Tg of smoke particles into the stratosphere (Hu et al., 2019; Peterson et al., 2018; Yu et al., 2021), the impact from the Australian brushfires (2019–2020) was much larger and injected the record amount of 0.4 ± 0.2 Tg in the stratosphere (Khaykin et al., 2020; Kablick et al., 2020; Li et al., 2021).

To date, an important number of studies have already investigated the event of the 2019–2020 Australian bushfires in terms of the aerosol optical, chemical, and radiative properties (Ohneiser et al., 2022; Khaykin et al., 2020; Yang et al., 2021a; Kloss et al., 2021; Nguyen et al., 2021; Tencé et al., 2022). These studies, either focus on specific regions/sites (Ohneiser *et al.*, 2020; Tencé *et al.*, 2022), or they utilize mostly passive remote-sensing techniques, without any information on the vertical distribution of aerosol properties. Here, we study this extreme event

over an extended time span (from 25 December 2019 to 12 February 2020), using range-resolved aerosol measurements by the CALIOP spaceborne lidar instrument.

Moreover, concentrations of CO and O_3 were also studied, as they are obtained by the Copernicus Atmosphere Monitoring Service (CAMS) at various pressure levels. In order to investigate the effect of the BB plume on a greater horizontal area, we recorded all the smoke layers and chemical concentrations extending from Australia (140° East) to the east coasts of South America (20° West), and within a latitude range of 20°–60° South. Dispersion simulations with a FLEXPART model were also used to support the aerosol observations and describe the atmospheric motions. The smoke layers were analyzed in terms of their geometrical and optical properties. To understand the radiative effect of the event, indicative cases of tropospheric and stratospheric smoke layers were used for analyzing the RF of BB particles.

3.3.2 Methods and Tools

Moderate-Resolution Imaging Spectroradiometer (MODIS): Active Fire Data and Burned Area Product

We used satellite products from the MODIS instrument, onboard the Terra and Aqua platforms, to analyze the distribution of active fires and burned area in Australia. The active fire data and MODIS burned area product are distributed through the FIRMS (https://firms.modaps.eosdis.nasa.gov) and through Land Processes Distributed Active Archive Center (LP DAAC) (https://lpdaac.usgs.gov/products/mcd64a1v006/ MCD64Al), respectively. The use of these data permitted us to locate and emphasize the exact area and period of fires.

Figure 3.18 shows the locations at which MODIS detected at least one fire event (Giglio *et al.*, 2016; Giglio *et al.*, 2018) during the compositing time period, with confidence greater than 70% (magenta crosses). The different colors of the burned area map correspond to different burn dates, starting from December 2019 to February 2020.

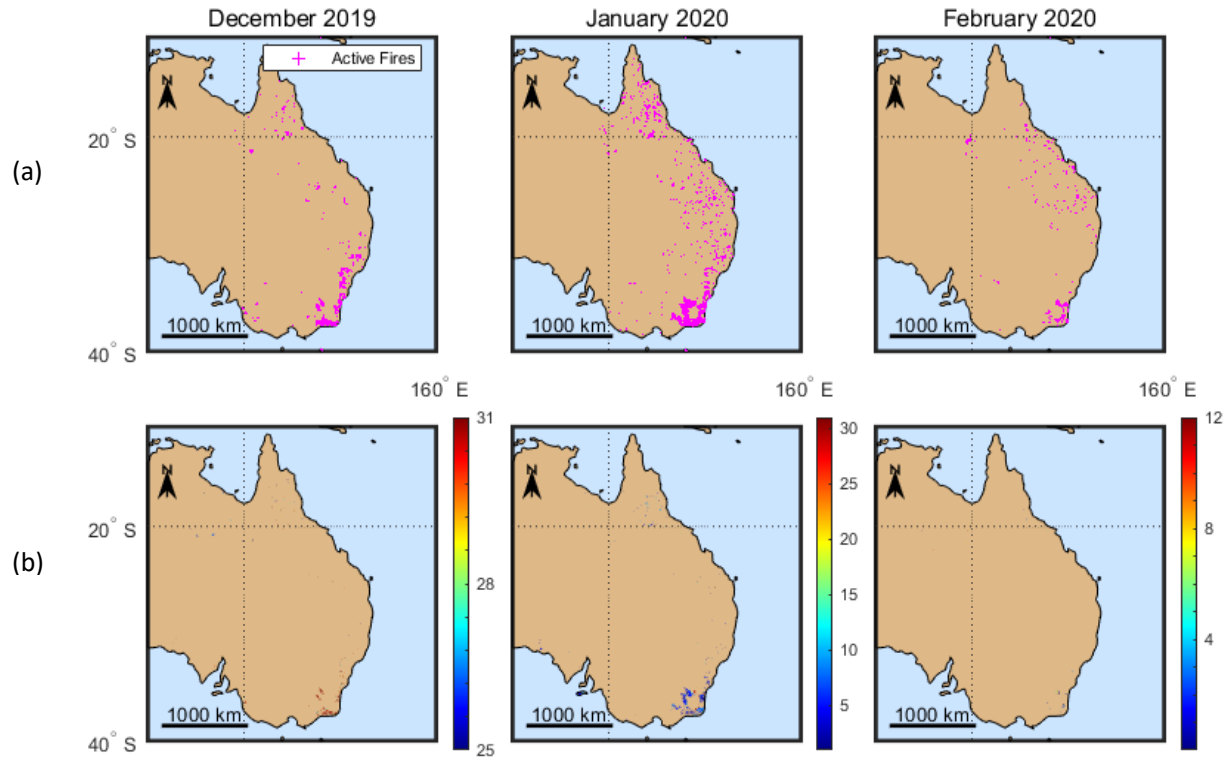

Figure 3. 18: (a) Active fires and (b) burned area according to burn date, as obtained by MODIS for the time period 25 December 2019- 12 February 2020 (Papanikolaou et al., 2022a).

As shown in Figure 3.18a, during the study period (25 December 2019–12 February 2020), the active fires spread all over the eastern coasts of Australia. Most of the active fires were located at the southeastern (New South Wales, NSW, and Victoria) and the northeastern (Queensland) parts of the country. The southeastern part, especially the area close to the borders of NSW and Victoria (~37° S, ~150° E), was highly affected by the fires. The areas burned from these bushfires (Figure 3.18b), were mostly burned during the last few days in December and the first few days in January, while a confined area was also burned during the first few days in February.

CAMS Reanalysis Data on Different Pressure Levels

The Copernicus Atmosphere Monitoring Service (CAMS; http://atmosphere.copernicus.eu is a component of the European Earth Observation program Copernicus. The CAMS global near-real-time service provides daily analyses and forecasts of reactive trace gases, greenhouse gases, and aerosol concentrations. CAMS reanalysis is the latest global reanalysis dataset of atmospheric composition produced by the European Centre for Medium-Range Weather Forecasts (ECMWF), consisting of three-dimensional time-consistent atmospheric composition fields, including aerosols and chemical species (Inness et al., 2019). The dataset covers the period 2003–2021. The atmospheric products can be found on single levels, total column, model levels, and pressure levels. Different pressure levels covered the vertical

range from 1000 to 1 hPa within 25 layers, with a horizontal resolution of 0.75° ± 0.75°, and a temporal resolution of 3 h. In this study, the mass mixing ratio of CO (kg/kg) and O_3 (kg/kg) was used on the pressure levels 950–200 hPa to find the enhancement of O_3 relative to CO in the smoke plumes.

FLEXPART Model

We used the Lagrangian transport model FLEXPART (FLEXible PARTicle) to simulate the forward dispersion of smoke particles from the wildfires (Stohl et al., 2005; Pisso et al., 2019). The simulations were initialized from the MODIS hot-spot detections and the meteorological driver was the 6-hourly final analysis dataset (FNL) from the National Centers for Environmental Prediction (NCEP) at 1° ± 1° resolution. The emitted particles were assumed to be black carbon (BC) and 1000 particles were attributed to each emission. Dry deposition as well as in-cloud and below-cloud scavenging were enabled for these runs. In order to limit our analysis only to the fires that actually contributed to the long-range transport of smoke, we excluded all hot spots with fire radiative power (FRP) less than 1000 MW, resulting in a total of 1611 emissions.

The injection height for each emission was parameterized based on the observed FRP as similar to (Solomos et al., 2019):

$$INJ_{\mathrm{HGT}}(\mathrm{m}) = 10^{0.39\times\log_{10}(\mathrm{FRP})+2)} \quad (3.1)$$

This approach is computationally efficient and provides a physically based distribution of injection heights for mid-latitude fires.

As it can be observed in Figure 3.19, the meteorological conditions during the study period result in a complex dispersion pattern for the simulated smoke particles over the entire southern hemisphere. The suspended particles are elevated to altitudes above 10 km as they travel eastwards from Australia towards South America, favored by the mesoscale circulation patterns in the South Pacific Ocean. After 17 January 2020, large portions of the plumes are found above a 15 km height, especially over the northeast parts of Australia. Until 10 February 2020, a distinct latitudinal belt of elevated smoke up to stratospheric levels is evident between the Equator and 30°.

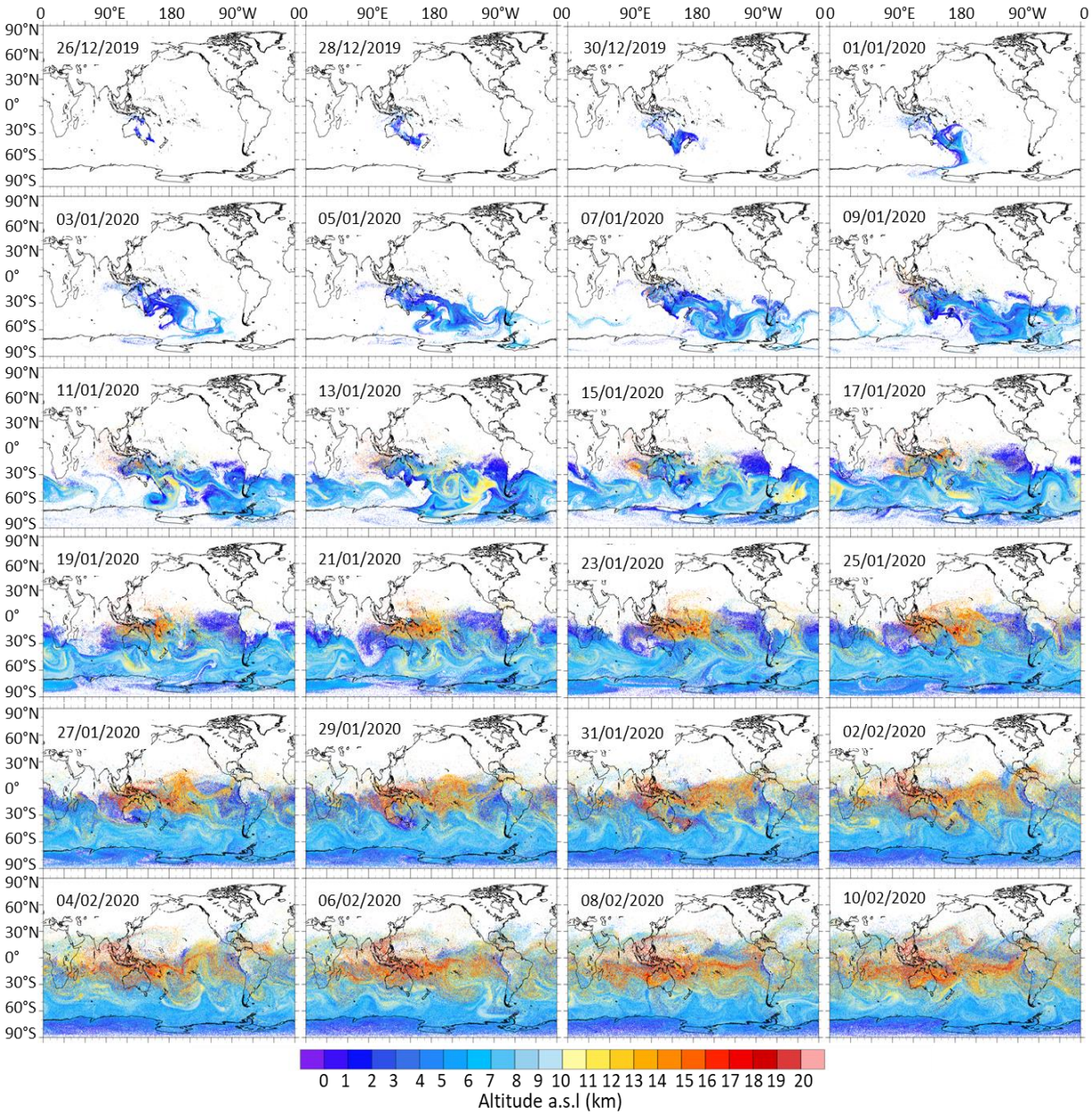

Figure 3. 19: Biomass burning aerosol's height, as calculated by the FLEXPART model for the under-study period (25 December 2019–12 February 2020 (Papanikolaou et al., 2022a).

The Cloud-Aerosol Lidar and Infrared Pathfinder Satellite Observation (CALIPSO) Satellite

In this work, the L2 version 4.20 CALIPSO APro and the VFM data products were used, provided with a 5 km horizontal resolution. From the Apro products, the extensive and intensive aerosol optical properties are derived, namely, the b_{aer}; the a_{aer}; the PLDR at 532 nm; $Å_b$, obtained by the pair of wavelengths 532 and 1064 nm; as well as the AOD, calculated by the integration of the a_{aer} over the smoke layers. The VFM products were used for separating aerosols from clouds, and further classifying aerosols in various types (Omar et al., 2009), in order to keep the ones

related to BB aerosols, namely, types 3 (polluted continental/smoke; top of the layer lower than 2.5 km) and 6 (smoke; top of the layer higher than 2.5 km), as classified by the CALIPSO algorithm.

Nevertheless, the CALIPSO satellite offers a unique opportunity to study such dynamic events, such as the one analyzed in this study, from their source region and across the intercontinental path that aerosols follow, where no ground-based lidars exist (Papanikolaou et al., 2020). Thus, in this study, it was used to track all the BB aerosol plumes as they were transported from Australia to South America. In order to detect any possible change in the geometrical and optical properties of the smoke layers, the main region of smoke's spatial distribution was limited from 20° S to 60° S. Within this latitude range, four study regions were created, the green (GR), yellow (YR), red (RR), and blue (BR) one, starting from the source of the fires in Australia (GR) and ending just after the South American continent (BR). All regions were located between 140° E and 20° W, with the exact same longitude range of 50° (Figure 3.20). The GR region surrounds the active fire area and the CALIPSO orbits closest to this area, containing freshly emitted smoke particles. Each one of the other regions was originated, so that the smoke layers in each transportation phase towards the South America would be captured.

All the nighttime and daytime CALIPSO orbits above each study region were used to obtain as much information as possible about the event. The retrievals were obtained per 2° latitude and longitude, along each CALIPSO orbit. Profiles that did not contain any smoke layers were excluded from our statistical analysis. However, most of them included more than one smoke layer at different altitude levels, both in the troposphere and stratosphere. A horizontal averaging of 105 km was applied to the CALIOP data to enhance the detection of the aerosol layers and increase the signal-to-noise ratio of the profiles. The data were screened using standard CALIPSO quality-assurance flags and cloud aerosol discrimination (CAD) scores (Wainker et al., 2013; Kim et al., 2018b). At this point, it is worth mentioning that, since September 2016, CALIOP has been experiencing low-laser-energy shots, which mostly occur over the South Atlantic Anomaly (SAA) region. As of March 2018, ~6% of all laser shots within the SAA have low energy, whereas the global frequency remains less than 1% (Noel et al., 2014). This fact may have affected the number of layers at the fourth study region (BR).

The smoke layers analyzed in this study were selected based on the aerosol typing algorithm, but also extra limitations were applied to them. More precisely, tropospheric aerosol layers had to be of thicknesses greater than 500 m, while no aerosol thickness limitation was applied to the stratospheric ones. Regarding the aerosol optical properties, only smoke layers with b_{aer} and PLDR values above 0.1 $Mm^{-1}sr^{-1}$ and 0.01 were kept, respectively. These two values were set as a threshold, in order to make sure that only valid aerosol layers were kept for further processing in our analysis. More precisely, the threshold value of 0.1 $Mm^{-1}sr^{-1}$ for the backscatter coefficient was set in accordance to the attenuated aerosol backscatter detectability limit of CALIOP, which has been reported to be of the order of 10^{-1} $Mm^{-1}sr^{-1}$ (Huang *et al.*, 2013; Zeng, 2021).

Additionally, the threshold value regarding PLDR observations was set to be 0.01, a value very close to the molecular depolarization values (~0.8%; E. W. Eloranta and P.Piironen (1994), depending on the wavelength and the atmospheric conditions (She, 2001; Behrendt and Nakamura, 2002), as PLDR values lower than that cannot be found in the literature concerning aerosol layers. Our approach, apart from ensuring that no misclassified aerosol layers were included in our analysis, due to their small backscatter coefficient or small PLDR values, also excluded any possible layers obtained over SAA, due to low-laser-energies.

The LibRadtran Radiative Transfer Model

For estimating the radiative effect of this BB event, a variety of cases was selected from each studied region based on the magnitude of the AOD. We ended up with five tropospheric and five stratospheric layers from each region. A total of 44 vertical levels were considered from the surface up to a 70 km height. Starting from the ground level (surface; SRF) and up to 20 km, the vertical resolution was 0.5 km, while the corresponding one from 20 to 70 km (top of the atmosphere; TOA) was 20 km. The a_{aer} profiles at 532 nm obtained from the CALIOP measurements for each smoke layer were used as inputs in the LibRadtran radiative transfer model version 2.0.2. (Emde et al., 2016). In our study, the uv_{spec} algorithm, which calculates the radiation field in the Earth's atmosphere, was implemented for the disort radiative transfer equation (1-D geometry) for the downwelling and upwelling SW (280–3000 nm) and LW (3000–30,000 nm) irradiances. Midlatitude summer conditions were used for a typical Air Force Geophysics Laboratory (AFGL) Atmospheric Constituent Profile (Anderson et al., 1986), along with a surface albedo value of 0.06 for the ocean areas and 0.20 for the land areas in the SW range that were considered.

For each case, two simulations (one for the SW and one for the LW range) referred to clear-sky atmosphere with background aerosol conditions and two simulations corresponded to the smoke loaded atmosphere, since SW and LW ranges were treated separately by LibRadtran. The aerosol RF depicts the perturbation in flux in the atmosphere caused by the presence of the aerosol layers in relation to that calculated under clear-sky conditions (Soupiona et al., 2020a; Kokkalis et al., 2021), and it is given by:

$$RF(z)=\Delta F_{smoke}(z)-\Delta F_{clear}(z) \quad (3.2)$$

where ΔF, at a level z, is calculated by:

$$\Delta F(z)=F\downarrow(z)-F\uparrow(z) \quad (3.3)$$

$F\downarrow(z)$ and $F\uparrow(z)$, is the downwelling and upwelling flux.

Therefore, the net RF, $RF_{NET}(z)$, is expressed by:

$$RF_{NET}(z)=RF_{SW}(z)+RF_{LW}(z) \quad (3.4)$$

It is important to notice that these estimations did not take into account the presence of clouds. For a typical average cloud coverage over the area, the surface all-sky RF can be reduced to ~50% and the TOA all-sky RF to ~30–50% of the clear-sky RF estimations (Khaykin et al., 2020). Finally, since the under-study cases referred to different days, times, and coordinates, the solar zenith angle (SZA) ranged between 24.65° and 46.86°.

3.3.3 Results

Aerosol Geometrical and Optical Properties per Study Region

For the time period from 25 December 2019 to 12 February 2020, the day and night CALIPSO orbits were used, and the aerosol vertical profiles were retrieved per 2° lat., covering the entire under-study region (20° to 60° S and 140° E to 20° W). As already mentioned, only the aerosol layers that were categorized as types 3 and 6 based on CALIPSO Level 2 v4.20 algorithm were kept and further analyzed. The total number of the selected BB aerosol layers, accumulated over time and space, was 3124 (GR: 1151, YR: 926, RR: 816, and BR: 231 BB layers). In order to study the vertical structure of the plumes in this admittedly large time–space scale, we divided the observed BB layers into 5 altitude range categories (3 tropospheric and 2 stratospheric), according to their mean height range extensions. The first tropospheric category contained layers below 2.5 km amsl., the second contained layers observed within 2.5 to 7.5 km amsl., while layers observed above 7.5 km amsl. and reaching up to the TPPH were finally grouped in the third tropospheric category.

On the other hand, the two stratospheric groups of layers were associated with aerosol layers observed between TPPH and 15 km amsl., and with layers above the 15 km amsl. The percentages of the layers found within each altitude category and region are extensively shown in the following diagrams (Figure 3.20).

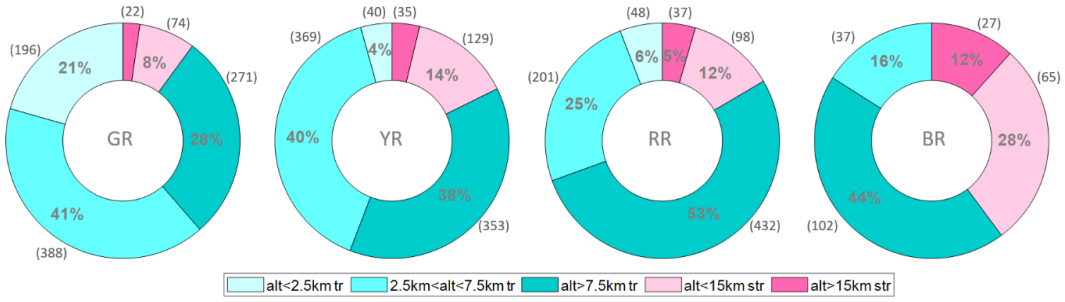

Figure 3. 20: Percentages of BB aerosol layers found in each under-study region (from left to right: GR, YR, RR, BR) and altitude category (chromatic scale). The numbers in the parenthesis next to the percentages refer to the accumulated number of observed layers (Papanikolaou et al., 2022a).

Furthermore, in order to obtain representative (for each region and for each altitude range category) values of the aerosol properties, namely, the b_{aer}, a_{aer}, PLDR (at 532 nm), $Å_b$ (532/1064 nm), and AOD (at 532 nm), we proceeded with the box-plot analysis presented in Figure 3.21. This analysis provides information about the distribution of the aerosol properties values previously mentioned, for all the smoke layers studied during the event. Boxes of cyan-color shades correspond to tropospheric and light and dark pink shades to stratospheric layers. The rhombus symbol, of different colors for each region, represent the mean value of each property. The horizontal line inside the boxes refers to the median values, while the min. and max. values are indicated at the end of the whiskers. The box limits correspond to the 75^{th} and 25^{th} percentile values of the dataset.

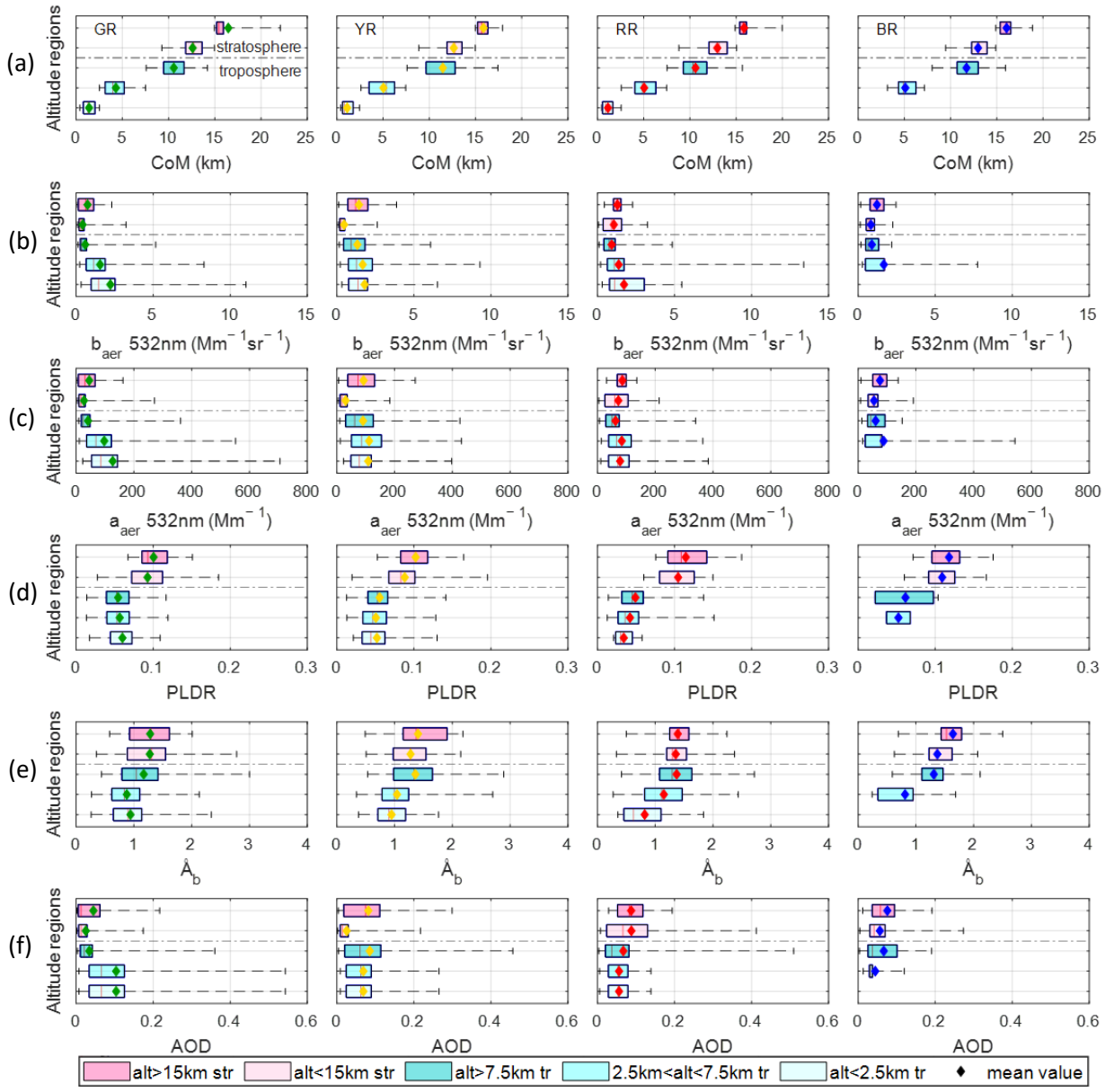

Figure 3. 21: BB aerosol layers according to (a) their CoM (amsl.), (b) b_{aer}, (c) a_{aer}, (d) PLDR at 532 nm, (e) $Å_b$ (532/1064 nm), (f) AOD at 532 nm. GR, YR, RR and BR (left to right) correspond to the four under-study regions, while the different colors indicate the different height-range categories (Papanikolaou et al., 2022a).

The center of mass (CoM) of the smoke layers was calculated according to Lucia *et al.* (2006) per study and altitude region (Figure 3.21a) to find the vertical spread of the aerosols in the atmosphere. Smoke layers were identified in all 4 regions, extending from the ground up to 22 km amsl., except for the BR, for which no smoke layers were found in the lower height-range group. This fact could possibly be connected to the SAA effect. Specifically, the tropospheric BB aerosol layers were found from near 0.5 km reaching altitudes up to 14.20 km in the GR, 17.42

km in the YR, 15.69 km in the RR, and from 3.18 to 15.94 km in the BR. The mean CoM of the stratospheric layers were found to be around 16 km in all the regions, with higher variabilities (9.29– 22.09 km) to be observed in the region containing the active.

In general, the b_{aer} and a_{aer} values, retrieved from each layer, decreased with the altitude, presenting higher values in the tropospheric altitude-range categories (Figure 3.21b, c). In the GR, mean values of b_{aer} ranged from 0.59 ± 0.63 to 2.23 ± 2.10 $Mm^{-1}sr^{-1}$. In YR, the corresponding mean values were found to be between 1.33 ± 1.16 and 1.81 ± 1.59 $Mm^{-1}sr^{-1}$, while, in RR, the b_{aer} values ranged from 0.93 ± 0.65 to 1.72 ± 1.31 $Mm^{-1}sr^{-1}$, even reaching the extreme value of 13.39 $Mm^{-1}sr^{-1}$ in the lower free troposphere (FT; alt. < 7.5 km). In BR, the b_{aer} values ranged from 0.89 ± 1.66 to 1.67 ± 1.86 $Mm^{-1}sr^{-1}$. The relatively low recorded values close to the fire region could be related to the fact that CALIOP is a nadir-only looking lidar, therefore the data were only collected along the satellite's orbit, and thus there is a possibility that some smoke plumes were not found at the exact overpass time and/or coordinates of the satellite track. However, considering the fact that, in our study, the statistical sample was very high, such uncertainties were probably eliminated and the main reason behind these decreased values was the high averaging areas over each grid that wiped out any detailed information that could be observed.

Additionally, we have to mention that the Andes mountain range could have played a role in this increase (FT b_{aer} values in the RR), as well as in the decrease in the number of layers in the BR. In particular, the narrow and steep Andes mountains act as a physical barrier to the Pacific Ocean FT (Campetella and Vera, 2002); they significantly disturb the atmospheric circulation resulting in a variety of synoptic and meso-scale phenomena, as well as climate conditions of sharp contrast between tropical and subtropical latitudes, along with a pressure-longitude cross section of the seasonal mean zonal wind summertime circulation (Garreaud, 2010), in which the aerosols are trapped within the RR. The aerosols uplift along the slopes of the mountains and then dive again into the Pacific Ocean, staying for longer time periods in the RR and possibly mix with other smoke layers not being able to move easterly, towards the BR.

The b_{aer} stratospheric values were found to be lower than the tropospheric ones, for all regions, ranging between 0.42 ± 0.40 and 1.44 ± 0.99 $Mm^{-1}sr^{-1}$. In contrast, the tropospheric a_{aer} values were greater than the stratospheric, in all regions, ranging from 41.26 ± 43.74 to 126.63 ± 117.88 Mm^{-1}, with a maximum recorded value of 705.78 Mm^{-1} observed at the lower tropospheric category (<2.5 km) in GR, apparently influenced by the emissions at the ground. In the rest of the regions, the values were found between 60.68 ± 34.21 and 111.52 ± 83.06 Mm^{-1}. The maximum recorded values of a_{aer} show a descending trend, except for the BR in which a maximum value of 542.94 Mm^{-1} appeared in the lower FT, which could also be related to smoke layers from the same event or even layers originating from fires in South America, active at the same time period (Figure C1), which may, additionally, have contributed to the smoke layers transported from Australia. In the stratosphere, the a_{aer} values ranged from 27.14 ± 32.41 to 92.59 ± 95.08 Mm^{-1}, while a maximum recorded value was 271.38 Mm^{-1}. In general, both a_{aer}

and b_{aer} seem to have a descending trend in the troposphere as the smoke moved westerly, passing over the four regions, while, for the stratospheric layers, it appears to be the exact opposite (Figure 3.21b, c). These b_{aer} and a_{aer} values, both in tropospheric and stratospheric heights, point out the significant impact of the event on the atmosphere at an almost hemispheric scale.

Moreover, the PLDR values increase with altitude in each region (Figure 3.21d). In the troposphere, the corresponding mean values were lower than 0.06, showing the presence of nearly spherical particles in the smoke layers, indicative of BB mixed with aerosols of sea-spray-origin (Burton *et al.*, 2013; Papanikolaou *et al.*, 2020; Mylonaki *et al.*, 2021). The maximum tropospheric PLDR values did not exceed 0.15, while, in the stratosphere, values as high as 0.20 were observed. Since high PLDR values suggest particles of irregular solid shapes, our stratospheric observations could possibly indicate that the smoke particles acquired an ice coating at the colder stratospheric temperatures, consistent with the ice-nucleating potential of smoke particles (Tan et al., 2014; Vaughan *et al.*, 2018).

Similar values of PLDR have been reported by two recent publications addressing the same event of BB aerosol plumes observed over Chile by a depolarization lidar (~0.20) (Ohneiser *et al.*, 2020) and over the French Antarctic Station (0.07–0.13) (Tencé et al., 2022). In good agreement with our results were, also, the PLDR values reported by studies concerning stratospheric smoke in the Northern Hemisphere originating from Canadian wildfires (Baars et al., 2019; Haarig et al., 2018; Hu et al., 2019). The presented PLDR values repeated the same pattern (lower values in the three tropospheric altitude-range categories and higher in the two stratospheric ones) over all regions. A slight decrease in tropospheric PLDR values was observed, as the smoke moved westerly, across the South Pacific Ocean, indicating that the tropospheric aerosols were becoming even more spherical, probably due to the increased relative humidity that affected them as they were transported over the ocean (Qin et al., 2021; Zhang et al., 2015). In contrast, the stratospheric aerosols tended to be less spherical (Figure 3.21d), probably because of their ice-nucleating potential already mentioned above.

Based on our findings, fine and ultrafine smoke particles were dominant in the stratosphere, since the observed $Å_b$ values were found to be relatively high, reaching even up to 3 in the first two regions (GR, YR). On the other hand, $Å_b$ values in the troposphere found to be below 1 (min. down to 0.27 in lower atmosphere), indicating coarser particles, possibly BB mixed with marine aerosol (Figure 3.21e). As the tropospheric aerosols moved towards North America, a slightly descending trend was observed, showing that they had probably grown in size as they fended off the source, while the stratospheric $Å_b$ values were slightly increased (Figure 3.21e).

Concerning the smoke load represented by the AOD values shown in Figure 3.21f, it is evident that higher loads are recorded in the lower troposphere, compared to those of the upper atmosphere, something that could be related both to the thickness of the tropospheric layers and their opacity. The maximum AOD value of 0.54 was recorded in the lower troposphere over

the fire spots (GR), while in the stratosphere AOD values reached up to 0.29, similar to the values (0.05–0.33) observed in the stratosphere over Chile (Ohneiser *et al.*, 2020).

Relevant studies addressing the same event by utilizing mostly passive remote-sensing techniques over Australia showed $Å_b$ values of ~1.5 (Kloss et al., 2021) and AOD values in a range of 0.15 to 2.76 (Kloss *et al.*, 2021; Nguyen *et al.*, 2021; Yang *et al.*, 2021). The measured values, as obtained by MODIS and/or AERONET over the fire region at wavelengths 440 and 550 nm, were in a good agreement with our results over GR, considering the lack of any information of the vertical distribution. Differences between the maximum observed AOD values (~2.76) could be explained by the fact that these values refer to the total atmospheric column, while our corresponding results (max 0.54) refer to distinct aerosol layers.

Chemical Properties: CO and O_3 Variations over the Study Area

Apart from a major source of atmospheric aerosols, BB events are also a great source of gases that can significantly impact atmospheric chemistry, climate forcing, as well as air quality and human health (Bourgeois et al., 2021). Wildfire smoke is an important source of CO, NO_x, and VOCs, emitted directly into the atmosphere, and may additionally contribute in tropospheric O_3 formation through photochemistry during fire seasons (Liu et al., 2016; Bourgeois et al., 2021; Selimovic et al., 2020). For that reason, we calculated the relative changes of the CO and O_3 for the entire time period of our study (25 December 2019–12 February 2020), with respect to the corresponding days of the months for December and January, but for the last 15 years (base period: 2004–2019).

This analysis was performed for the same region as of our aerosol optical properties study (20° to 60° S and 140° E to 20° W), and the results are shown in Figure 3.22a, b. During the above-mentioned time period, the CO concentration was found to increase up to 100%, compared to the base period, mostly in the higher-pressure levels (700–950 hPa) of the three last regions (YR, RR, BR). In the GR, the highest observed increase in CO was 92% at 950 hPa. Correspondingly, the O_3 enhancement presented values of 60–96% in the lower atmosphere and even 100% in the upper one (pressure levels 200–400 hPa). The mean values and standard deviations (std) of CO and O_3 concentrations relative change per region are presented in Table C.1.

In order to investigate the impact of emitted CO on the O_3 formation, we calculated the correlation coefficient (R^2) between the relative change concentrations of the aforementioned gases during the study period (6 h temporal resolution), with respect to the base period (Figure 3.22b). A significant correlation (R^2~0.8) was revealed between CO and O3 during the study period in most of the pressure levels, especially close to the fire source (GR). For the rest of the regions, moderate values of R^2 were found (0.4–0.6), suggesting that the CO variation did not play a key role in the observed O_3 enhancement. Some grids showed higher O_3 enhancement relative to CO (0.5–0.8), while others showed lower (0–0.4). However, increased chemical processes were expected to occur to an aerosol layer with a longer lifetime and wider transportation in the atmosphere, and hence a greater possibility of O_3 production (Baylon et al., 2015), although this may have been affected by various other parameters, such as shortwave

radiation and/or atmospheric temperature (Lu et al., 2019). When trying to study these changes with respect to the day- and night-time conditions (Figure C2), we found that the correlation coefficient did not vary significantly, indicating that the variation of shortwave radiation played a minor role in the presented anomalies, and the latter can be attributed mostly to the event itself.

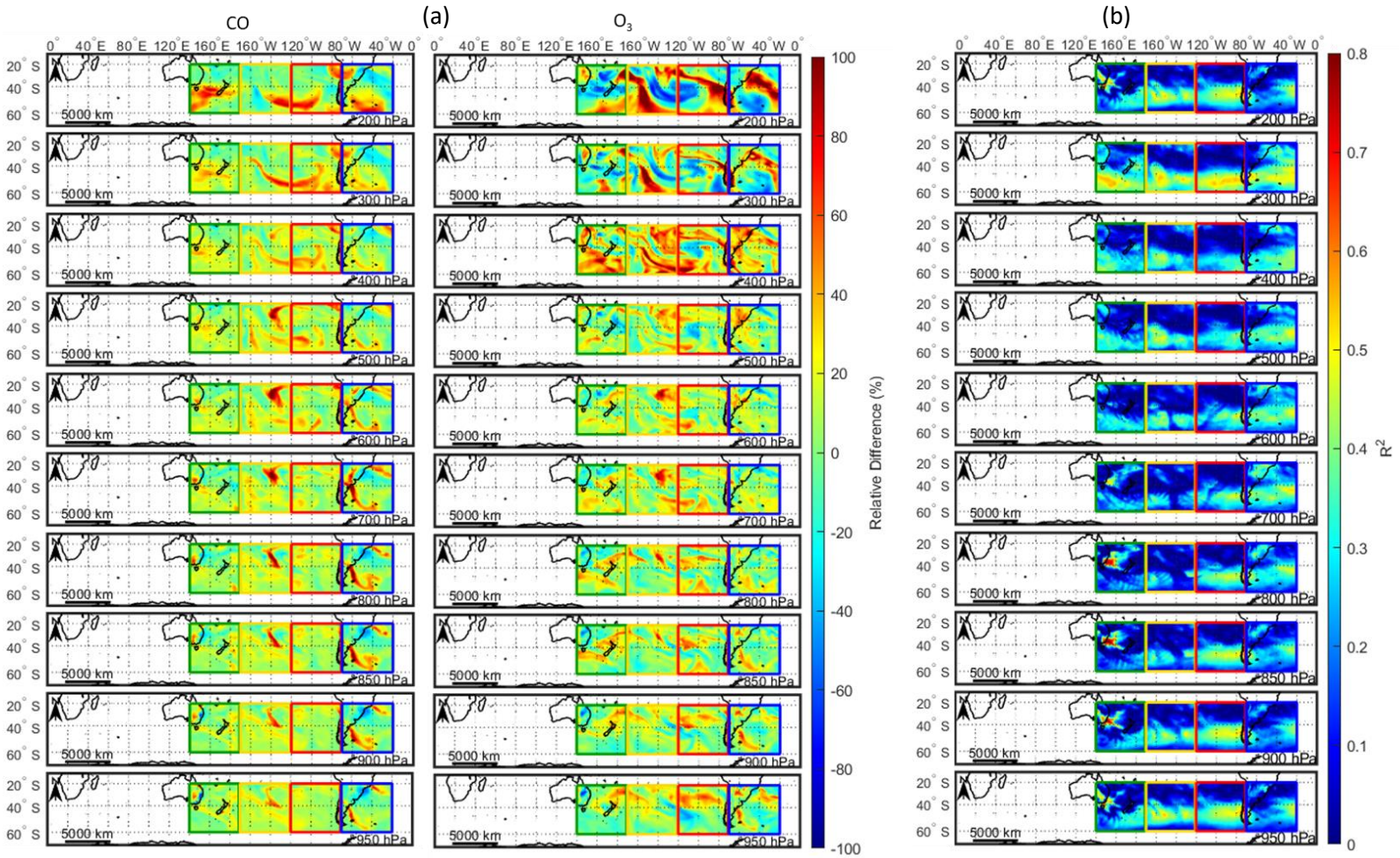

Figure 3. 22: (a) Relative differences of CO and O_3 calculated for the study period (25 December 2019 to 12 February 2020) over the study area (20° to 60° S and 140° E to 20° W) with respect to the same days through the years 2004–2019 (base period) (b) R^2 between CO and O_3 relative differences with respect to the base dataset, at various pressure levels (950–200 hPa) (Papanikolaou et al., 2022a).

Radiative Forcing of the Event

In order to estimate the role of the fire-emitted BB aerosols in the Earth's radiation budget, we performed simulations to quantify their impact on the radiative forcing. The mean RF_{NET} at the TOA, within the smoke layers and at the SRF-level was calculated during our simulations, using the LibRadtran radiation code twice: one for the index "clear", and one for the index "smoke" (Equation (3.2)). The latter includes the presence of the free tropospheric and stratospheric BB aerosol layers, so that the contribution of the BB load in the RF_{NET} (with respect to the "clear") could be found.

The RF_{NET} of each aerosol layer observed in the entire under-study region is presented in Figure 3.23. The calculated RF_{NET} values, for a range of the SZA between 24.65° and 46.86°, was found to vary from –87.10 to +13.18 W/m^2 (Figure 3.23I(a–c)), indicating cooling and heating, respectively. At the TOA, it ranged from –47.42 to +11.56 W/m^2 (mean value –12.83 ± 14.74 W/m^2) for the tropospheric aerosols, and from –25.96 to +13.18 W/m^2 (mean value +7.36 ± 11.98 W/m^2) for the stratospheric ones. Inside the tropospheric aerosol layers, the RF_{NET} was found between –74.47 and +8.30 W/m^2, with a mean value equal to –22.04 ± 22.62 W/m^2, while, inside the stratospheric layers, it was found between –38.99 and +7.40 W/m^2, with a corresponding mean value equal to –11.47 ± 13.21 W/m^2. At the SRF, the corresponding ranges were –87.10 to –4.53 W/m^2 for the tropospheric layers, and –42.79 to –3.80 W/m^2 for the stratospheric ones. The mean values were found to be equal to –32.22 ± 25.84 W/m^2 and –18.51 ± 14.73 W/m^2, respectively.

From (Figure 3.23I(a–c)), there is no evidence of SZA dependency with RF_{NET}, since the presented values do not follow any specific pattern concerning the SZA ranges, probably because of the SZA narrow range of variation. However, according to the slopes of the regression lines and the R^2 values, the RF_{NET} seem to have a good correlation with the aerosol load (Figure 3.23II(a–c)). More precisely, the correlation between RF_{NET} and AOD becomes stronger as we move from the TOA to the SRF. Regarding the stratospheric layers, R2 between RF_{NET} and AOD was found to be equal to 0.65 for the layers at the TOA, 0.76 for inside the AL, and 0.79 at SRF. Concerning the tropospheric layers, the corresponding R^2 values were found to be equal to 0.47, 0.57, and 0.84, revealing a very strong dependence near the ground. The layer observation height (CoM) seems not to be directly correlated with RF_{NET} (Figure 3.23III). However, the tropospheric layers presented a wide range of RF_{NET} values in all of the vertical levels, in contrast to the corresponding stratospheric layers' values, which showed less diversity.

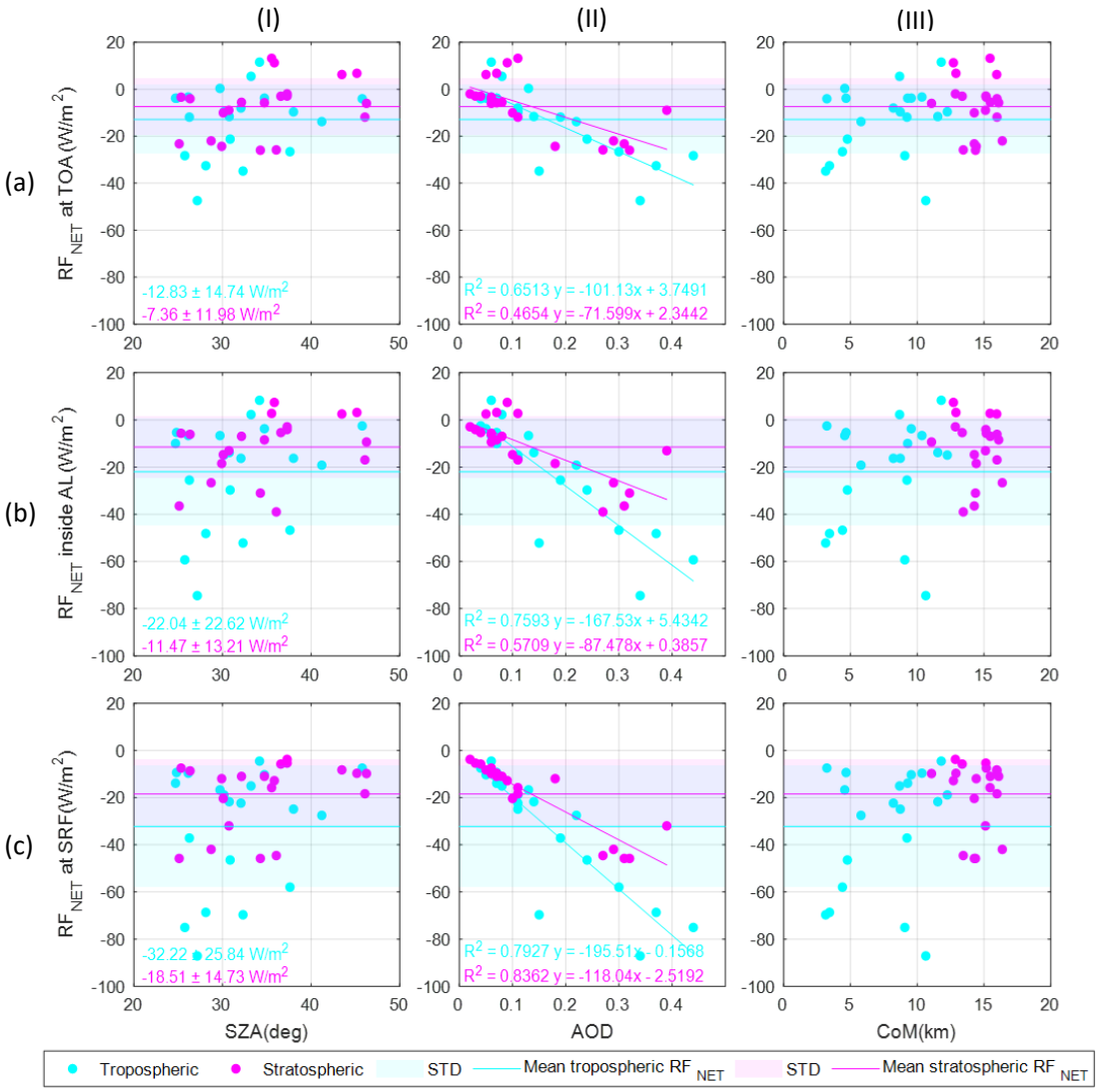

Figure 3. 23: Net radiative forcing values per case (illustrated by colored solid circles) at top of atmosphere (TOA) (a), inside the smoke layers (b), and at surface (SRF) (c), versus the SZA (I), the AOD (II), and the CoM (III) of the aerosol layers. The different colors correspond to the tropospheric (cyan) and stratospheric (magenta) BB aerosol layers, while the solid lines and shadowed areas correspond to the mean values and std of the RF_{NET} at TOA inside the layer and at the SRF (Papanikolaou et al., 2022a).

Heinold *et al.* (2021) found values up to +0.50 W/m^2 at the TOA and –0.81 W/m^2 at SRF direct radiative forcing averaged for the Southern Hemisphere during January 2020. Hirsch and Koren (2021) derived a value of +1.10 W/m^2 in the latitude belt between 20° S and 60° S. Yu *et al.* (2021) obtained an estimate for global annual average effective RF of –0.03 W/m^2 at TOA and –0.32 W/m^2 at the surface due to the smoke event. According to Chang *et al.* (2021) the wildfire event was associated with a strongly negative RF between –14.80 and –17.7 W/m^2, which decreased the surface air temperature by about 3.7–4.4 °C.

Khaykin *et al.* (2020) showed that, in the latitude band between 25° and 60° S, during February 2020, the RF was as large as about –1.00 W/m^2 at the TOA and –3.00 W/m^2 at the

surface. From the perspective of the stratospheric aerosol-layer perturbation, the global TOA RF produced by the Australian fires (2019–2020) was greater than the RF produced by all documented wildfire events and of the same order of magnitude of moderate volcanic eruptions during the last three decades (that have an integrated effect estimated at –0.19 ± 0.09 W/m^2, or smaller). We note here that the majority of the studies mentioned above present the RF as a mean value over a wide area and time period, in contrast to our study that focused on the forcing of each BB aerosol layer. Additionally, the average on the RF could have also affected the accuracy of the estimations, since the SZA information is lost, compared to this study in which the inclusion of the SZA provides a more precise approach.

3.3.4 Conclusions

The 2019–2020 extraordinary Australian bushfires injected large amounts of smoke particles into both the troposphere and stratosphere. This long-lasting BB event was studied within the time period ranging from 25 December 2019 to 12 February 2020, using range-resolved aerosol measurements performed by the CALIOP space-borne lidar instrument onboard the CALIPSO satellite. The smoke layers were analyzed in terms of their geometrical, optical, and radiative properties in different altitudes and regions, within the longitude range of 140° E to 20° W, in the latitude band of 20°–60° S, as they were transported from the Australian banks to the South American continent. In this transportation, the Andes mountain range possibly played an important role, acting similar to a physical barrier to the Pacific Ocean, forcing the aerosols to circulate, which resulted in them staying for longer time periods in the same longitude range.

The altitude of the smoke layers ranged from near ground and to the stratosphere, almost at the altitude of 22 km amsl. According to their main optical properties, the presented PLDR values replicated the same pattern over the regions, namely, lower values in the troposphere and higher in the stratosphere. More specifically, concerning the tropospheric altitude categories, the mean value of PLDR were lower than 0.06, while the maximum value did not exceed 0.15, indicating the presence of nearly spherical particles in the smoke layers, possibly affected by increased RH as they were transported over the ocean. In the stratosphere, PLDR values as high as 0.20 were observed, and values indicative of irregular solid shapes were possibly driven by the acquired ice coating obtained in the stratosphere. As the smoke moved westerly, a slight decrease in tropospheric PLDR values was observed, in contrary to the enhanced PLDR values of the stratospheric aerosols.

Fine and ultrafine smoke particles ($Å_b$ values up to 3) were dominant in the stratosphere, while, in the troposphere, $Å_b$ values were found to be even below 1, indicating coarser particles. As the aerosol plume moved towards North America, a slightly descending trend was observed in the tropospheric $Å_b$ values, while the stratospheric $Å_b$ values were lightly increased, showing that these particles probably grew in size in the troposphere and shrank in the stratosphere, respectively, as they fended off the source.

Concerning the smoke AOD values, higher BB aerosol loads were recorded in the lower troposphere, compared to the upper atmosphere. A maximum AOD value of 0.54 was found in the lower troposphere over the fire spots, while AOD values reached up to 0.29 in the stratosphere. In general, stratospheric layers showed less diversity in their properties compared to the tropospheric ones. During the same time period, the CO concertation increased up to 100%, compared to the same days of the event averaged over a base period (2004–2019), mostly in the 700–950 hPa pressure levels. The highest observed increase in CO was 92% at 950 hPa over the first study region. Likewise, the O_3 enhancement presented values of 60–96% in the higher atmospheric pressure levels and even 100% in the lower ones (200–400 hPa). R^2 values between the relative change in the concentrations of CO and O_3 showed that the impact of emitted CO on the O_3 formation was mostly significant close to the fire source (GR), while, for the rest of the regions, CO variation did not play a key role in the observed O_3 enhancement.

In regard to the RF_{NET}, it presented a good correlation with the AOD values, which tends to become stronger from the TOA to SRF. Both the tropospheric (–12.83 to –32.22 W/m^2) and stratospheric (–7.36 to –18.51 W/m^2) RF_{NET} of the smoke layers were negative in each vertical atmospheric level (TOA, inside the aerosol layer, SRF), despite the fact that the tropospheric layers showed a higher impact than the stratospheric ones, especially on the SRF.

Finally, it is crucial to point out that the range-resolved aerosol measurements, provided by our study, presented a new perspective on this unique smoke event in three different aspects (spatially, temporally, and vertically), as the aerosol properties were studied in a wide area of the South Hemisphere, during a long-lasting time period, from ground level to the stratosphere.

3.4 Long-range transported aerosols over Athens, Greece during Autumn 2020

3.4.1 Introduction

The long-range transport of atmospheric aerosols can influence the air quality worldwide in local, regional or even intercontinental level. It presents long residence times in the atmosphere and may contribute to the increase of air pollution (Martins et al., 2018).

For instance, aerosols produced in wildfires in North America once they are embedded in the FT or stratosphere, can travel over great distances and reach Europe (Papanikolaou et al., 2020; Baars et al., 2019; Ortiz-Amezcua et al., 2017). Under specific meteorological conditions their optical and chemical properties can be kept unaltered throughout their journey, or they can be changed through mixing processes with other aerosol types, for instance dessert dust, especially during lower free tropospheric transport (Papanikolaou et al., 2020).

Greece is an important cross-road of tropospheric aerosols originating from natural sources (desserts, volcanoes, wildfires, etc.) mostly within the European and the African continent (Soupiona et al., 2020a; Kokkalis et al., 2013; Mylonaki et al., 2021c), while the intercontinental transport (e.g. North America) of aerosols over our area has not been studied in a systematic way. In this work we present three cases of intercontinental transportation of

aerosols reaching Athens based on the DEPOLarization lidar systEm (DEPOLE) (Papayannis et al., 2020) located at the Laser Remote Sensing Unit (LRSU of National Technical University of Athens (NTUA, (37.97° N, 23.78° E, elev. 212 m amsl.), in terms of b_{aer} and PLDR at 355 nm.

3.4.2 Methodology

MODIS

In this study active fire data from MODIS (Berrick et al., 2009) Terra and Aqua were used to analyze the distribution of fires in U.S.A during the studied period. In Figure 4.1, with colored dots we present with colored dots the location where MODIS detected at least one fire event during the compositing time period, with confidence greater that 80% (the fire data are available from NASA's Earth Observing System Data and Information System (EOSDIS) (https://firms.modaps.eosdis.nasa.gov). The period covered by the shown fire map was set to 5 days, for each air mass trajectory ending over America.

Hybrid Single-Particle Lagrangian Integrated Trajectory

In order to determine the origin of the air masses carrying the aerosol plumes arriving over Athens' lidar station, an analysis of backward trajectories was performed by means of the HYSPLIT model (Stein et al., 2015; Rolph et al., 2017) developed by the NOAA (National Oceanographic and Atmospheric Administration) in collaboration with Australia's Bureau of Meteorology. All trajectories were calculated for a period of 144 to 264 h backward in time and were computed for arrival heights of approximately the center of the observed layers.

DEPOLarization lidar systEm (DEPOLE)

The DEPOLE is located at the LRSU of NTUA (37.97° N, 23.78° E, elev. 212 m amsl.). Based on a pulsed Nd: YAG laser with a third harmonic emission at 355 nm (polarization purity >99.5% achieved using a polarizing filter), DEPOLE emits a vertically polarized linear beam. A polarizing beam splitter cube optically separates the two polarization planes (parallel and perpendicular) of the elastically backscattered lidar signals at 355 nm, which are then collected by a 200 mm diameter (Dall-Kirkham Cassegrainian) telescope with a focal length of 1000 mm (at two polarization planes: parallel and perpendicular), which are optically separated by a polarizing beam splitter cube; the full overlap of DEPOLE is at ~500 m amsl. (Papayannis et al., 2020). The average (systematic and statistical) uncertainty of the vertical profile of the PLDR is less than 15% (D'Amico et al., 2016; Freudenthaler et al., 2009).

3.4.3 Results

The cases presented in this study refer to the long-range aerosol transport which occurred on 14 and 30 September and on 1 October 2020. The origin of the aerosols measured over the lidar station was found to be close to California, Western U.S state. In Figure 4.1 we present the air mass backward trajectories ending over the city of Athens for the corresponding dates. Based on the results of the HYSPLIT model, and along with the active fires spots obtained by MODIS, and the CALIPSO orbits passing over the areas that the backward trajectories started, we found that the studied air masses originated over the North America, between the time period 8 to 27 September, the same time that an extreme wildfire event was taking place in California state.

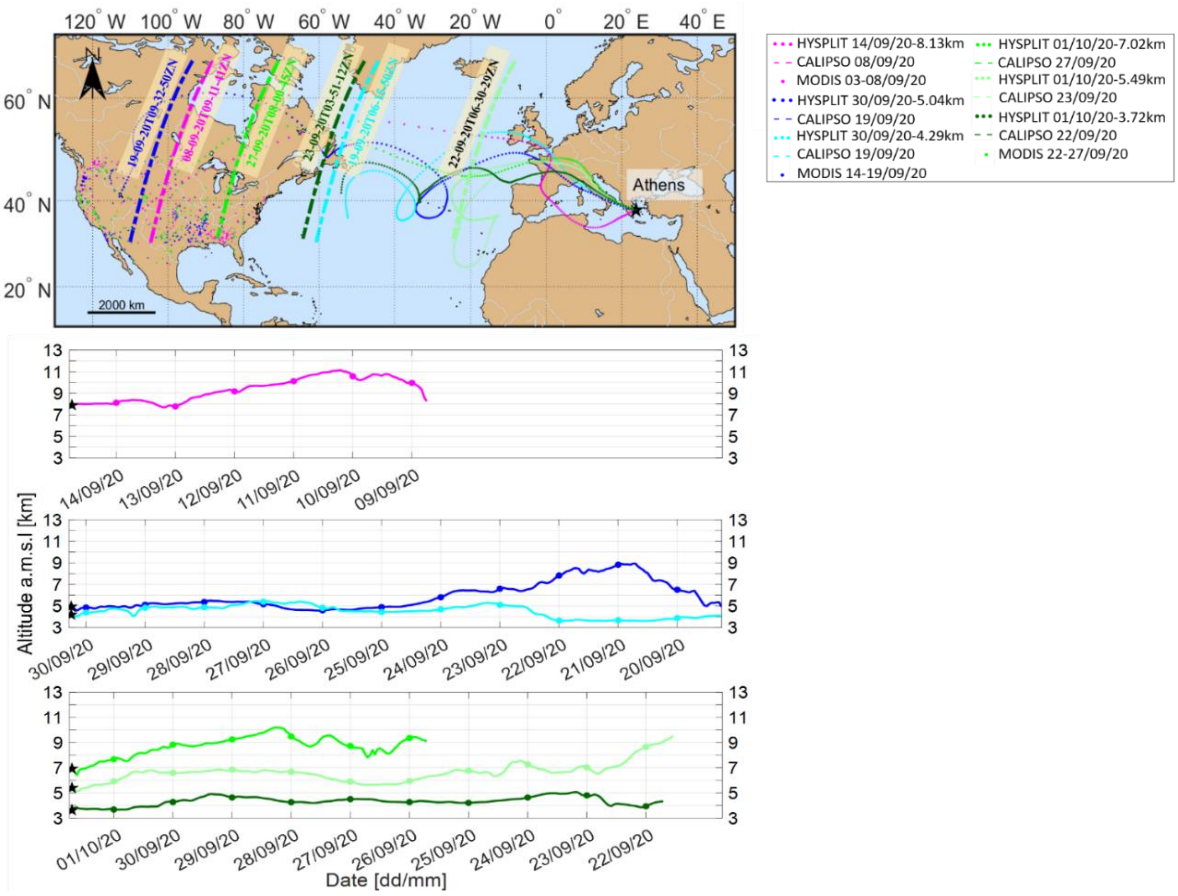

Figure 3. 24: The colored (magenta, blue and green) dots on the map represent the active fires retrieved by MODIS, with confidence greater than 80% and given for a 5-day period per case, respectively. The CALIPSO orbits (magenta, blue and green colored dashed lines) are provided for the corresponding dates over the source areas from where the air masses originated for each studied case according to HYSPLIT runs. The air mass backward trajectories for aerosols arriving over Athens on 14 September (magenta), 30 September (blue and cyan) and 01 October 2020 (dark green, light green and green) provided by the HYSPLIT model.

Figure 3.24 illustrates the aerosol subtype for some of the CALIPSO overpasses coinciding in space and time with the origin of the back-trajectories over the USA, confirming the smoke

(black color) and polluted dust (brown) content on the transported airmasses, that reached even up to 12 km along their path.

In Figure 3.25 we present the spatio-temporal evolution of the range-corrected lidar signal at 355 nm for each under study case, along with the vertical profiles of the aerosol optical properties (b_{aer}, PLDR at 355 nm), which were retrieved by using the SCC. The mean values of the properties along with the std are presented in Table 3.4.

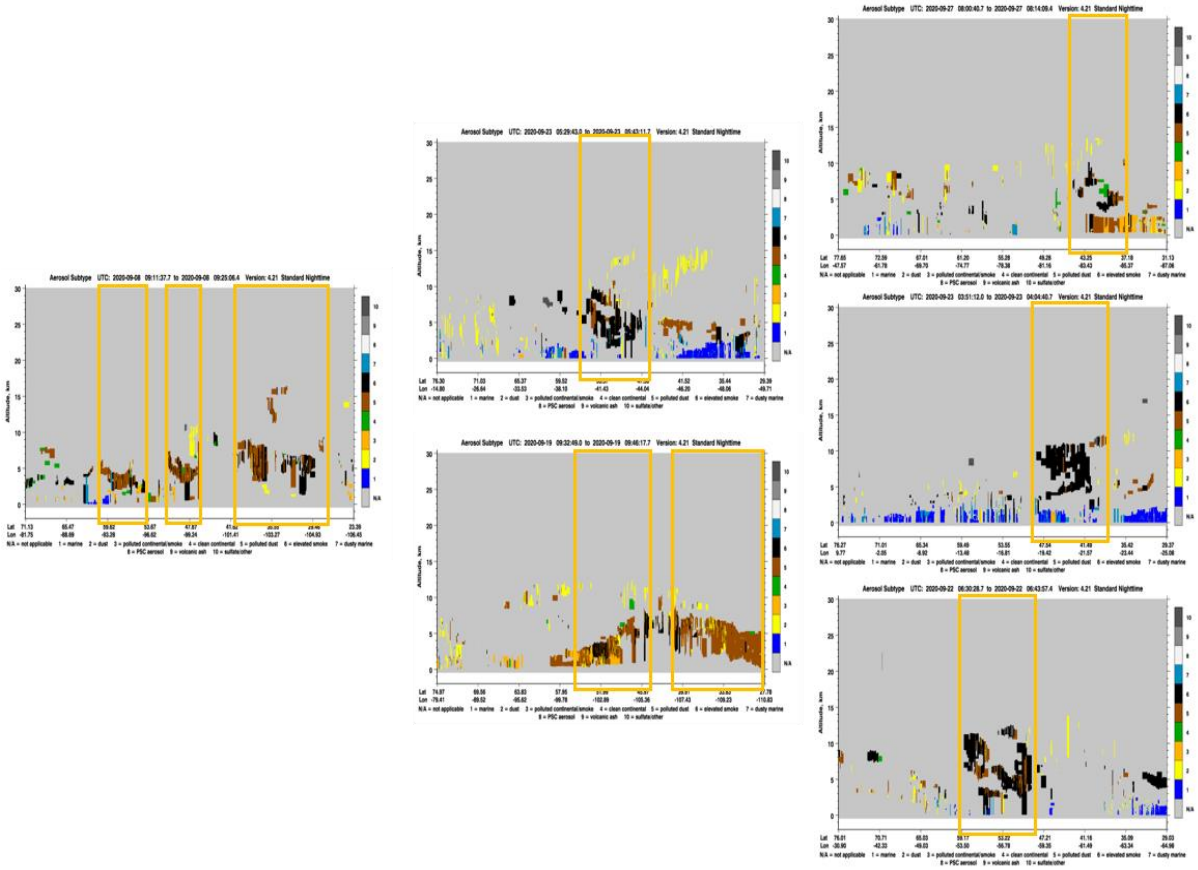

Figure 3. 25: CALIPSO aerosol subtypes for the 08 September 2020 (08-09-20T09-11-41ZN), 19 September 2020 (19-09-20T06-15-50ZN and 19-09-20T09-32-50ZN)and 22, 23 and 27 September 2020 (22-09-20T06-30-29ZN, 23-09-20T03-51-12ZNand 27-09-20T08-00-45ZN), close to the source of the airmass that reached Athens on 14 and 30 September and 01 October 2020, showing smoke and polluted dust aerosol layers in altitudes between 1 and 15 km close to the wildfire source.

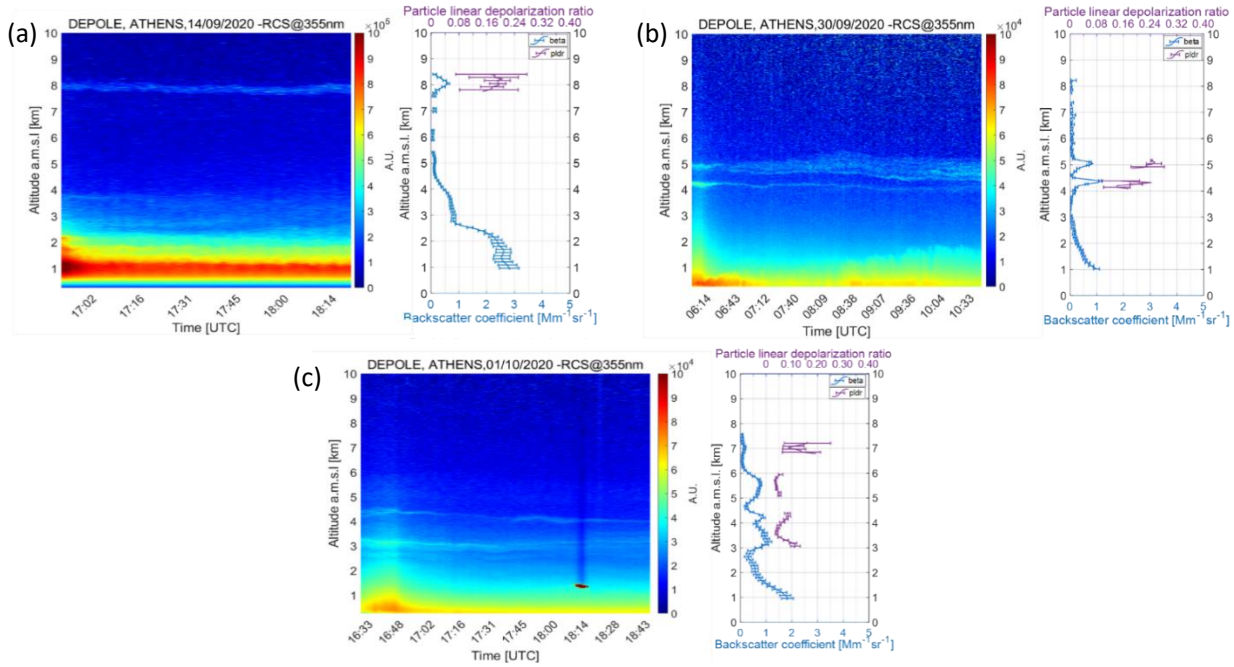

Figure 3. 26: (a) left graph: Spatio-temporal evolution of the range-corrected lidar signal at 355 nm; Right graph vertical distribution of b_{aer} ($Mm^{-1}sr^{-1}$) (blue line) and PLDR at 355 nm (purple line), as observed by the DEPOLE lidar system on 14 September 2020 (17:19 –18:19 UTC), (b) on 30 September 2020 (05:54-06:31 UTC) and (c) on 01 October 2020 2020 (17:09-17:08 UTC), over Athens, Greece.

Table 3. 4: Geometrical (top, bottom, mean altitude) and optical (mean b_{aer} and PLDR) properties of the studied aerosol layers, as observed by the DEPOLE lidar system at 355 nm over Athens on 14 and 30 September 2020 and 01 October 2020.

		Date (dd/mm/yy)	
Parameter	**14/09/20**	**30/09/20**	**01/10/20**
Bottom (km)	7.86	4.08	2.88
			3.96
		4.86	4.92
Top (km)	8.40	4.50	3.96
			4.50
		5.22	6.18
Mean altitude (km)	8.13±0.18	4.29±0.15	3.42±0.34
			4.23±0.18
		5.04±0.13	5.55±0.39
b_{aer} ($Mm^{-1}sr^{-1}$)	0.40±0.16	0.56±0.31	0.83±0.19
			0.66±0.19
		0.54±0.20	0.58±0.20
PLDR	0.19±0.01	0.16±0.05	0.07±0.03
			0.08±0.01
		0.22±0.02	0.06±0.01

In total 6 aerosol layers were observed, one layer on 14 September 2020, 2 layers on 30 September 2020 and 3 layers on 1 October 2020. The layers found to have a mean altitude that ranged from 3.72 ± 0.44 to 8.13 ± 0.18 km amsl. The corresponding b_{aer} values were found between 0.13 ± 0.03 and 0.82 ± 0.17 $Mm^{-1}sr^{-1}$, while the PLDR values were found ranging from 0.04 ± 0.01 to 0.22 ± 0.02, indicating that the aerosols were found to be in some cases spherical, while in others of irregular shape. According to studies of aged tropospheric aerosols from north or Western American and Canadian wildfires (Haarig *et al.*, 2018; Papanikolaou *et al.*, 2020) PLDR values are expected to be less than 0.11 in FT, thus PLDR values of 0.16 and 0.22 in our findings could be mixtures of smoke with dust, as was already indicated by CALIPSO observations close to the wildfires' source and along the path that aerosols traveled.

Finally, the profile of the backscatter coefficient at 355nm, that was obtained during the day-time measurement of 30 September 2020 (05:54-10:49), was the one used to estimate the RF_{NET}, both at TOA and SRF. The a_{aer} profile, used as input for the radiative transfer model, was initially at 355 nm and thus transformed with a spectral conversion factor (K_{δ}=1.34 ± 0.07;Abril-gago *et al.*, 2022) to 532 nm. Moreover, the SZA was equal to 64.38° and the surface albedo equal to 0.15 (Psiloglou and Kambezidis, 2009). In Figure 3.27 we present the net radiative effect at the SRF and at the TOA for this case.

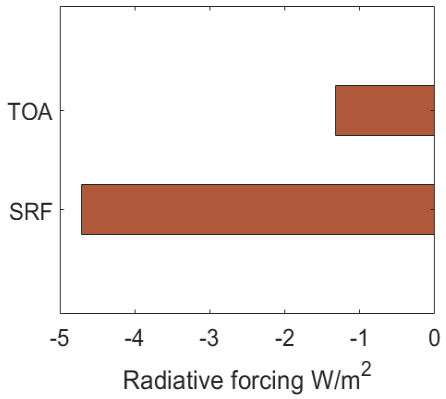

Figure 3. 27: Net radiative forcing at TOA and at SRF at 06:31 UTC on 30 September 2020, the SZA was equal to 64.38° over the NTUA lidar station.

The RF_{NET} of these two filaments, that traveled all the way from the Californian wildfires over Athens present small values at the TOA, equal to -1.33 W/m^2 and at SRF -4.71 W/m^2, indicating slight cooling effect both at SRF and TOA, respectively, at the current day and time over the station.

3.4.4 Conclusions

The long-range aerosol transport of BB aerosols originated from wildfires in California, Western U. S state, during the time period from 8 to 27 September, was studied in this work. The BB aerosol layers were observed over Athens on 14 and 30 September and on 1 October 2020. The HYSPLIT airmass back-trajectories ending over the city of Athens for the corresponding dates,

along with the active fires by MODIS, and the CALIPSO orbits passing over the areas that the backward trajectories started, showed that the studied air masses originated over the California, in Western U.S, between the time period from 8 to 27 September 2020, at the same time period that an extreme wildfire event was taking place in the state of California.

The free tropospheric filamented aerosol layers shown values of PLDR ranging from 0.04 ± 0.01 to 0.22 ± 0.02, indicating the presense of particles both of irregular shapes and spherical shape. The aerosol layers with PLDR values of 0.16 and 0.22 in our findings were probably polluted dust aerosol layers, namely mixtures of smoke with dust, as indicated also by CALIPSO. The filamented layers had a small radiative effect both at TOA and surface.

CHAPTER 4
EXTREME VOLCANIC AEROSOL EVENT

In Chapter 4 we present a discussion and evaluation of results regarding the extreme eruption of the Hunga Tonga-Ha'apai volcano (cf. Appendix D—Poster II).

4.1 Optical properties and radiative forcing of the Hunga Tonga-Ha'apai volcanic eruption in 2022

4.1.1 Introduction

Volcanic eruptions are a major source of natural pollution, as they emit enormous amounts of gases, volcanic ash and solid particles into the atmosphere. Depending on the particles' size, density, shape, and height in the atmosphere (tropospheric or stratospheric aerosols), the volcanic particles have different properties and lifetime. In general, coarse volcanic particles (radius > 100 μm) have a short lifetime (from minutes to hours), while fine volcanic aerosols (radius < 10 μm) can linger for days to weeks in the lower atmosphere, and even months to years if they reach the lower stratosphere (Gui et al., 2022; Hamill et al., 1997).

One of the strongest underwater volcanic eruptions ever recorded, was the eruption of the Hunga Tonga volcano on the island nation of Hunga Tonga-Hunga Ha'apai in the South Pacific Ocean (175.38°W, 20.57°S) that erupted violently on January 15, 2022 (Gui et al., 2022). The shock waves from this volcanic eruption encircled the world many times and pushed the plume of ash into the upper atmosphere. The explosion was powerful enough to penetrate the neutral atmosphere and even reach the ionized upper atmosphere, which begins between 80 and 90 kilometers above the surface of the planet (Rakesh et al., 2022). The volcano injected large amounts of particles in the stratosphere, found in this study within the latitude band of 5°–25° S, as they were transported from the source westerly, towards the Australian continent, between 15-19 January 2022. The 2022 Hunga Tonga eruption attracted a global attention because of its intensity (Adam, 2022; Zhao et al., 2022; Zhang et al., 2022; Zuo et al., 2022; Gui et al., 2022; Rakesh et al., 2022).

In this work we investigate the volcanic aerosol layers from the Hunga Tonga, that were observed with active and passive remote sensing sensors from space. Vertical profiles of aerosol optical properties, b_{aer}, a_{aer} coefficients, LR, $Å_b$, and PLDR, along with the geometrical properties, were obtained by the CALIPSO satellite. Moreover, the LibRadtran radiative transfer model was used in order to estimate the radiative forcing of volcanic particles.

4.1.2 Methodology

Ozone Monitoring Instrument (OMI)

The Ozone monitoring Instrument (OMI) is a spaceborne nadir-viewing imaging spectrometer with two separate channels that measure the shortwave radiation scattered back by the Earth's atmosphere and surface over the entire wavelength range from 270 to 500 nm with a spectral resolution of about 0.5 nm (Kleipool et al., 2022). OMI is measuring a number of trace gases in both the troposphere and the stratosphere in a high spectral and spatial resolution, and has been providing global observations of SO_2 pollution since 2004. The product files contain three estimates of the total SO_2 column in Dobson Units. These correspond to three vertical profiles selected to represent typical SO_2 vertical distributions for three SO_2 source regimes: SO_2 in the PBL (below 2 km) from anthropogenic sources, SO_2 distributed between 5 and 10 km from passive volcanic degassing in the free troposphere, and SO_2 distributed between 15 and 20 km representing injection from explosive volcanic eruptions (Li et al., 2020). In Figure 4.1 we present the SO_2 vertical column, over Australia on 18 January 2022, as emitted from Hunga-Tonga volcano.

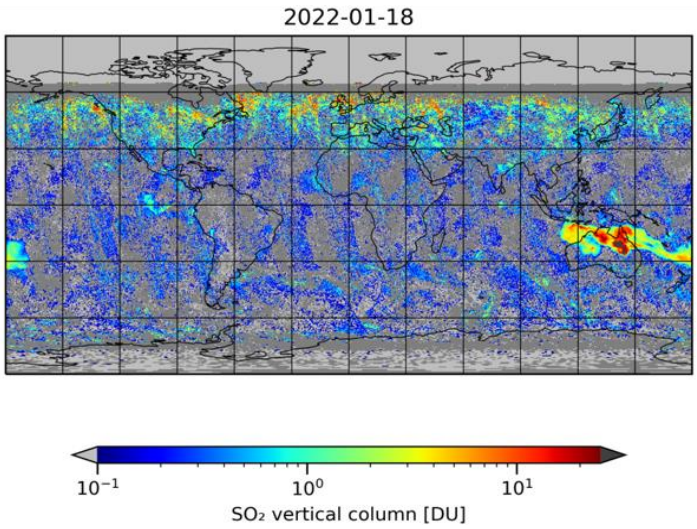

Figure 4. 1: OMI SO_2 vertical column over Australia on 18 January 2022, with SO_2 emission from Hunga-Tonga volcano.

The Cloud-Aerosol Lidar and Infrared Pathfinder Satellite Observation (CALIPSO) Satellite

The tracking of the volcanic plume, as it travelled towards Australia, was performed using the CALIOP observations. The CALIPSO orbits during the time period of 15–17 January 2022, were used during day and night time. To improve the identification of the aerosol layers, 105 km of horizontal averaging was applied to the CALIOP data. To obtain the atmospheric aerosol profiles, we used the AVD to filter out all other scatterers except the volcanic aerosols. In Figure 4.2 we present the area within the study of the volcanic aerosol layers was performed, based on the CALIPSO orbits. The "x" points correspond to the coordinates from which we retrieved the

aerosol optical depth. The magenta and green lines represent the night- and daytime CALIPSO orbits, respectively.

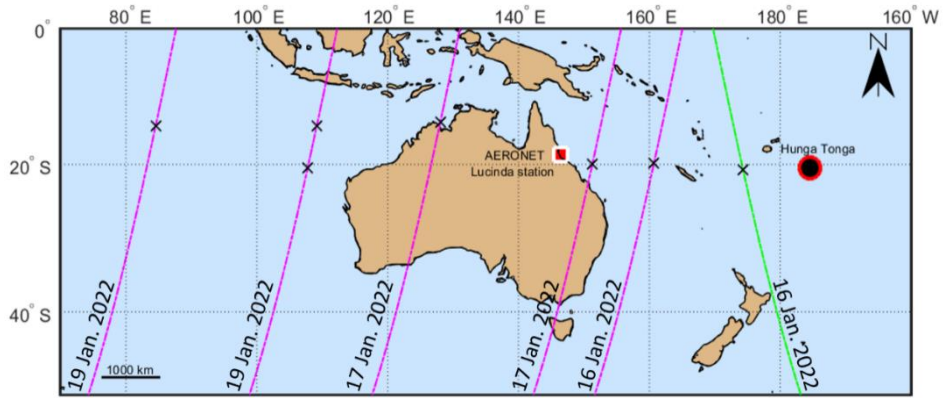

Figure 4. 2: The CALIPSO orbits (magenta and green colored lines) are provided for the corresponding dates after 1-4 days transport from the crater.

Aerosol Robotic Network (AERONET)

The AERONET (https://aeronet.gsfc.nasa.gov/) utilize hundreds of Sun/sky photometers (CIMEL) for direct sun and sky radiation measurements around the globe. For more than 25 years, the project provides a long-term, continuous and readily accessible public domain database of aerosol optical, microphysical and radiative properties. The network imposes standardization of instruments, calibration, processing and data distribution. These photometers perform direct solar irradiance measurements at 340, 380, 440, 500, 675, 870, 940 and 1020 nm and diffuse sky radiance at 440, 675, 870 and 1020 nm. The uncertainty of the aerosol size distribution retrieved by the sky radiance measurements is based on the calibration uncertainty of each wavelength, which is estimatedto be < ± 5%. More details can be found in Dubovik and King (2000) and Dubovik et al. (2006). The station considered in this study is the Lucinda (18.52°S, 146.39°E; 8.0 m amsl.; Figure 4.2) which is located in North-Eastern Australia. AERONET provided information about the AOD at 1020, 870, 667, 551, 532, 490, 443 and 412 nm and the Å of the volcanic plumes. The Å was obtained at 440- 675 nm and 440- 870 nm (Cuevas et al., 2019).

The LibRadtran Radiative Transfer Model

To estimate the radiative effect of this volcanic eruption, we used the a_{aer} profile at 532 nm obtained from the CALIOP measurement as input to the LibRadtran radiative transfer model version 2.0.2. (Emde *et al.*, 2016; Figure 4.3). A total of 44 vertical levels were considered from the surface up to a 70 km height. Starting from the ground level (surface; SRF) and up to 20 km, the vertical resolution was 0.5 km, while the corresponding one from 20 to 70 km (top of the atmosphere; TOA) was 20 km. Midlatitude summer conditions were used and the Atmospheric Constituent Profile (Anderson et al., 1986), was the one used to simulate the atmospheric conditions, along with a value of 0.06 for ocean surface albedo in the SW range. For each case, two simulations (one for the SW and one for the LW range) referred to clear-sky atmosphere with

background aerosol conditions and two simulations corresponded to the aerosol loaded atmosphere.

4.1.3 Results

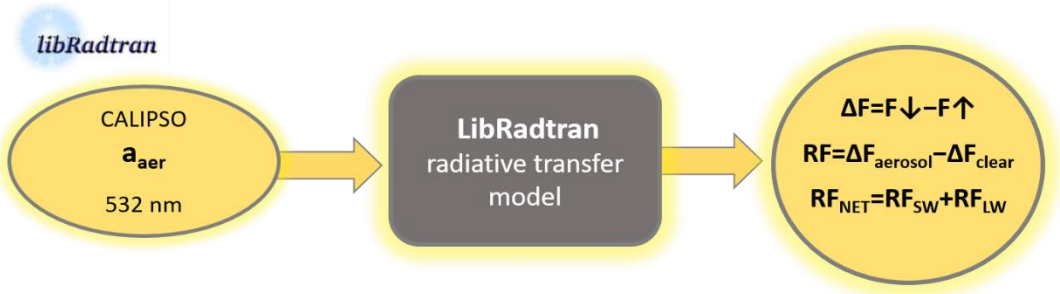

Figure 4. 3: The inputs used to estimate the volcanic eruption radiative forcing by LibRadtran model.

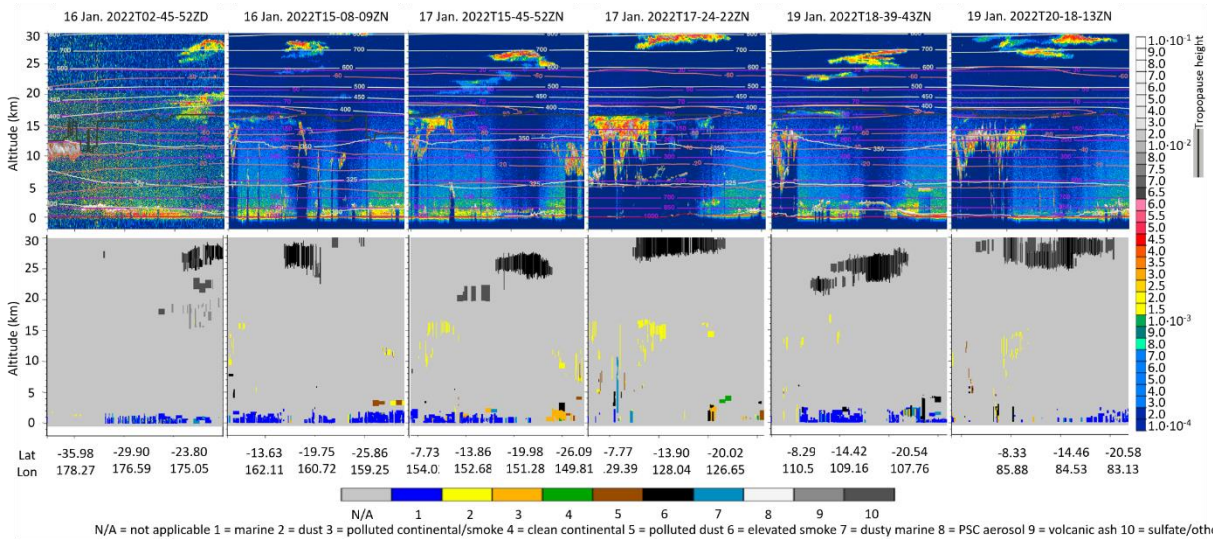

Figure 4. 4: CALIPSO total attenuated backscatter coefficient at 532 nm and aerosol subtypes versus altitude, latitude and longitude for nighttime and daytime orbits (16-19 January 2022).

The stratospheric volcanic layers were observed with CALIPSO satellite within an altitude range of 17 to 30 km. The identified layers and the aerosol types are presented in Figure 4.4 with black and grey colors. Black colors correspond to stratospheric smoke layers, while grey colors, light and dark, correspond to volcanic ash and sulfate aerosols respectively. However, since there was no evidence of extreme wildfires event at this time period and according to a recent publication of Tackett *et al.* (2022), there is strong evidence, that these layers identified partially as smoke are more luckily to be sulfate aerosols, or sulfate aerosols mixed with volcanic ash. The geometrical and optical properties of the stratospheric aerosol layers were retrieved by CALIPSO products.

The vertical distribution of the aerosol optical properties for the under-study period is presented in Figures 4.5.

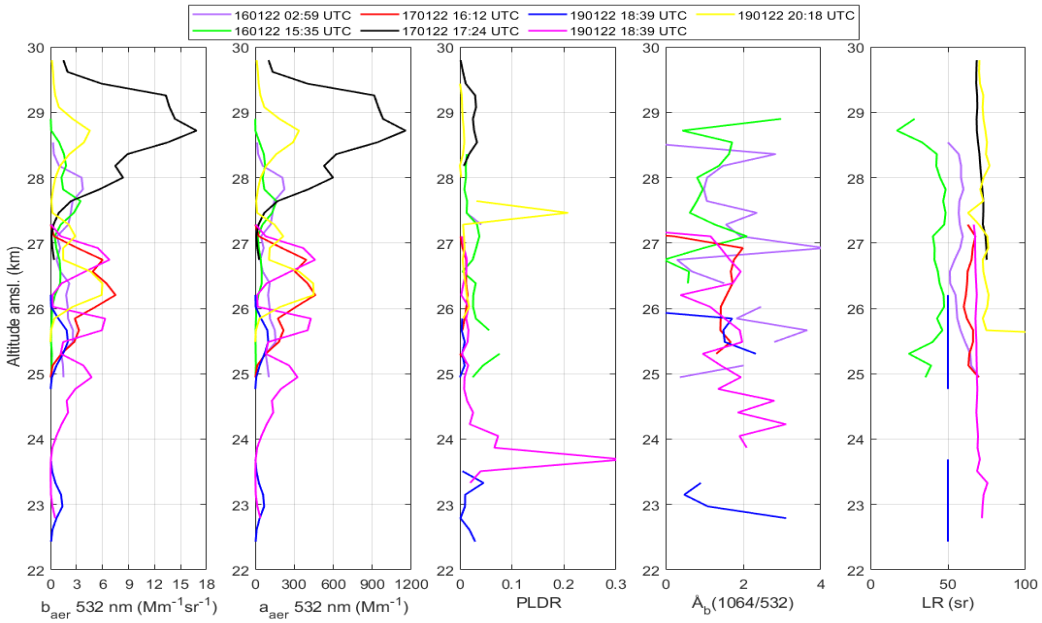

Figure 4. 5: Vertical distribution of the optical properties (b_{aer}, a_{aer}, PLDR $Å_b$ and LR at 532 nm), according to CALIPSO observation (16-19 January 2022).

Based on the layer analysis the CoM ranged from 23.05 and 28.67 km and layers' thickness was found between 1.08 and 2.69 km. The PLDR observations indicated mostly spherical (0.01 - 0.06) aerosols. Furthermore, the corresponding $Å_b$ values were found from 0.79 to 1.94. The LR values ranged from 42.43 to 74.03 sr, while the AOD, was found to vary from 0.04 to 1.40 for the aerosol layers, at 532 nm. The geometrical and optical properties' values are extensively shown Figure 4.6 and in Table 4.1.

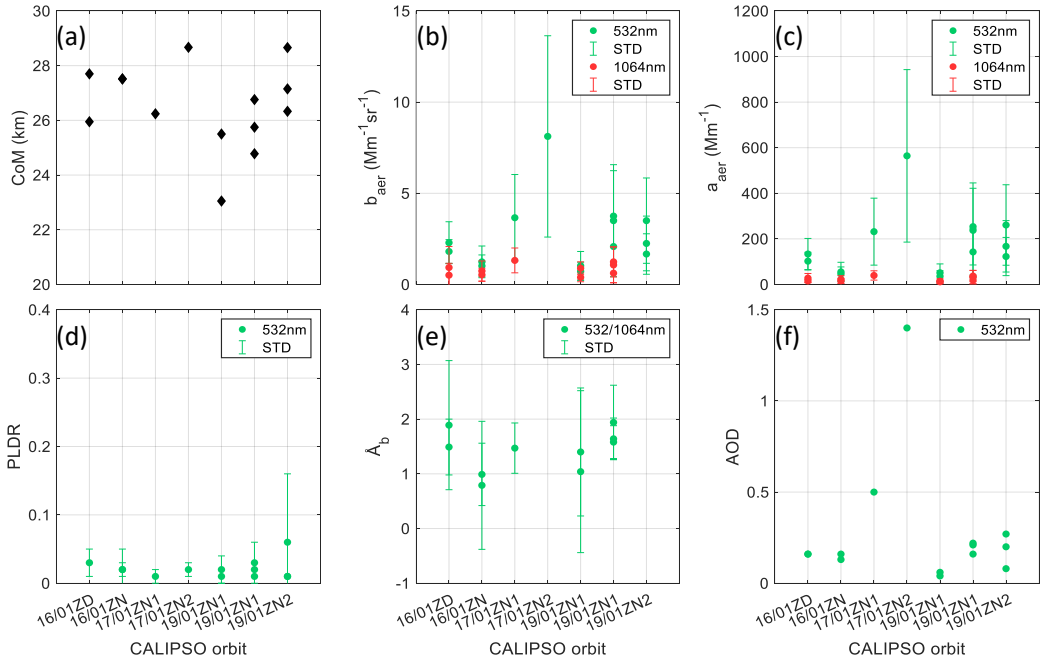

Figure 4. 6: (a) Geometrical and (b-f) mean optical properties of each aerosol layer observed by CALIPSO along with their std, for the time period of 16 – 19 January 2022.

Table 4. 1: Aerosol geometrical and optical properties of the volcanic ash plume, as obtained by CALIPSO during 16-19 January 2022.

Date (UTC)	CoM (km)	Thickness (km)	b_{aer} 532 nm ($Mm^{-1}sr^{-1}$)	b_{aer} 1064 nm ($Mm^{-1}sr^{-1}$)	a_{aer} 532 nm (Mm^{-1})	a_{aer} 1064 nm (Mm^{-1})	PLDR	$Å_b$	LR (sr)	AOD
16/01/22 02:45:52	27.70	1.08	2.29±1.15	0.93±1.15	133.68±68.30	27.98±20.29	0.03±0.02	1.49±0.51	56.3±24.29	0.16
	25.95	1.43	1.81±0.65	0.51±0.65	102.37±38.89	15.28±6.08	NaN±NaN	1.89±1.18	58.34±1.12	0.16
16/01/22 15:08:09	27.52	2.69	1.24±0.87	0.74±0.55	55.20±42.14	22.14±16.60	0.02±0.01	0.99±0.57	42.39±7.78	0.16
	27.51	2.69	1.02±0.60	0.53±0.36	46.21±30.78	15.97±10.88	0.02±0.03	0.79±1.17	42.43±7.3	0.13
17/01/22 15:45:52	26.24	1.98	3.66±2.37	1.32±0.681	231.74±146.90	39.59±20.43	0.01±0.01	1.47±0.46	63.94±2.29	0.50
17/01/22 17:24:22	28.67	2.34	8.12±5.52	NaN±NaN	564.26±378.35	NaN±NaN	0.02±0.01	NaN±NaN	70.25±1.79	1.40
19/01/22 18:39:43	25.50	1.08	1.03±0.78	0.39±0.24	51.41±38.79	11.61±7.31	0.01±0.00	1.04±1.48	50.00±0.00	0.06
	23.05	0.90	0.72±0.50	0.89±0.35	35.82±24.83	14.34±10.62	0.02±0.02	1.40±1.17	50.00±0.00	0.04
	26.76	0.72	3.75±2.49	1.24±0.83	253.81±168.22	37.09±24.88	0.01±0.00	1.58±0.30	67.73±0.28	0.21
	25.75	0.54	3.50±3.07	1.07±0.98	237.42±208.13	32.07±29.52	0.02±0.00	1.64±0.38	68.04±0.24	0.16
	24.78	1.44	2.08±1.48	0.62±0.52	142.71±101.51	18.67±15.46	0.03±0.03	1.94±0.68	68.75±0.35	0.22
19/01/22 20:18:13	28.66	1.08	2.25±1.5	NaN±NaN	167.41±112.81	NaN±NaN	0.01±0.00	NaN±NaN	74.03±1.57	0.20
	27.15	0.54	1.67±1.11	NaN±NaN	122.63±83.81	NaN±NaN	0.06±0.10	NaN±NaN	71.07±6.04	0.08
	26.33	0.90	3.50±2.34	NaN±NaN	260.95±176.56	NaN±NaN	0.01±0.00	NaN±NaN	73.95±1.61	0.27

The SO_2 observations obtained by OMI over the study region, revealed columnar concentrations varying from 2 and reaching the value of 13 DU on 16 January 2022, as can be seen in the following figure (Figure 4.7). Concerning other great volcanic eruptions, for instance the SO_2 columnar values from Eyjafjallajokull volcanic eruption ranged from 0.6–4.7 DU and a max value of 8 DU was recorded over Ireland, during the eruptions period (11 May) (Rix et al., 2012), while the North American Sarychev eruption on 19 and 20 June 2009 ejected columnar SO_2 concentrations of 8.6 DU and 3.7 DU, respectively (Zerefos et al., 2017). These indicative values reinforce the fact that Hunga Tonga underwater eruption was one of the strongest eruptions ever recorded.

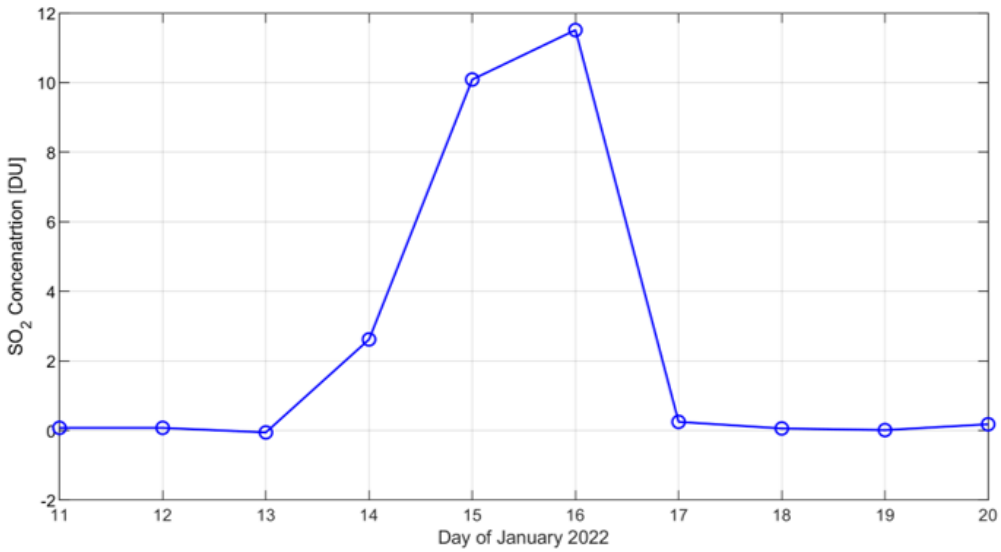

Figure 4. 7: SO_2 observations obtained by OMI over the study region, during the time period between 11 and 20 January 2022.

Moreover, along with the optical properties obtained by the CALIPSO satellite, the AOD and Å from the AERONET's ground based Lucinda station were also used. Aerosol optical depth values during 16 January 2022 were almost close to zero for the Lucinda station. However, between 21:00 UTC on 16 January and 03:00 UTC on 17 January 2022, the AOD values increased, reaching even up to 1.99 (1020 nm) and ranged between and 0.44 and 1.99, while at the same time the Å values ranged between 1.11 and 1.68, for the two pairs of wavelengths (indicating the presence of fine aerosols in the atmosphere (Figure 4.8).

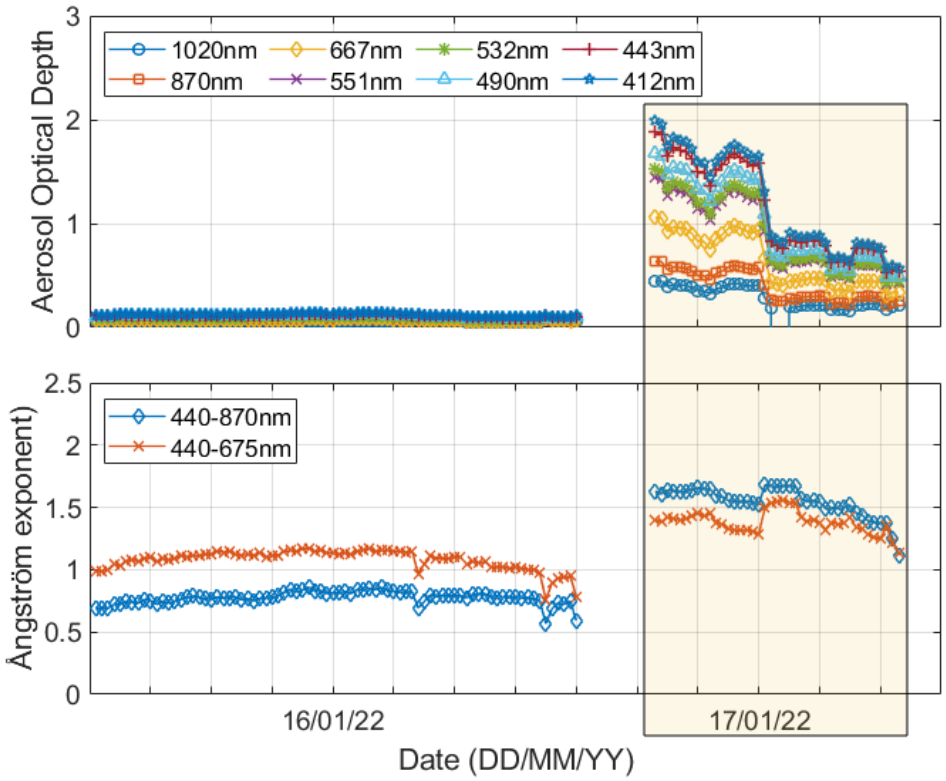

Figure 4. 8: Aerosol optical depth (1020, 870, 667, 551, 532, 490, 443 and 412 nm) and Ångström exponent (440- 675 nm and 440- 870 nm) as observed over the AERONET Lucinda station in Eastern Australia, when the volcanic plume reached the Australian banks on 17 January 2022.

On 16 January 2022 the RF_{NET} was calculated both at TOA and SRF using the a_{aer} profile at 532 nm obtained from the CALIOP measurement (02:59:20 UTC at 20.8° S, 174.3° E). Since this volcanic eruption event was characterized as one of the strongest underwater volcanic eruptions ever recorded (Adam, 2022; Zhao et al., 2022; Zhang et al., 2022; Zuo et al., 2022; Gui et al., 2022; Rakesh et al., 2022), and took place at the same region as the record-breaking Australian bushfires in the summer of 2019–2020 that were also described as the most devastating in the history of the country, a comparison between the two events was performed, in terms of radiative impact. The aerosol profile used for this comparison was obtained by CALIPSO on 01 January 2020 at 04:14:52 UTC, the coordinates of the profile were 36.0 ° S, 149.3° E, while the SZA was equal to 30.72°. In Figure 4.13 we present the net radiative effect at the SRF and at the TOA for the two cases, the biomass burning and the volcanic stratospheric aerosol layers obtained by LibRadtran model.

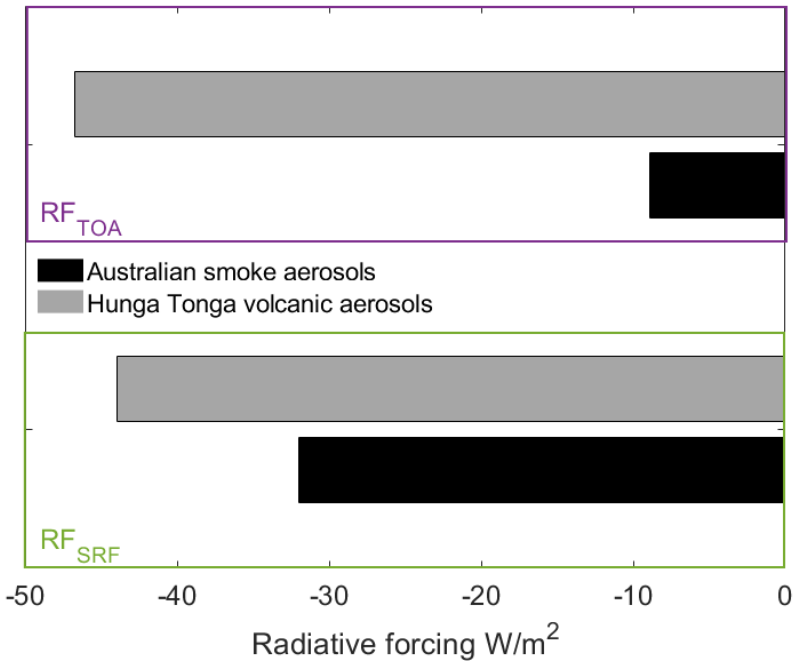

Figure 4. 9: Net radiative forcing values for each event (Hunga Tonga volcanic event is illustrated by grey-colored bars and Australian smoke event by black-colored ones) at TOA and SRF.

During 16 January 2022, one day after the eruption and before the volcanic plume reached the Australian banks (volcanic aerosol layers from 17 to 29 km) the calculated RF_{NET} over the ocean was −43.97 W/m^2 at SRF and −46.76 W/m^2 at TOA. The corresponding values for the Australian BB event were found equal to −31.98 W/m^2 at SRF and −8.94 W/m^2 at TOA. The volcanic RF_{NET} was higher compared to the smoke event, both at SRF and TOA. This can be attributed to the increased volcanic aerosol load, depicted in the extremely high AOD values, which boosted the cooling impact by reducing the quantity of shortwave radiation reaching the ground. The large difference of the RF_{NET} at TOA can be explained by the fact that the volcanic aerosol layer reached extremely high altitudes in the stratosphere (~ 30km) compared to the BB layers that were mostly found below 15 km.

Gui et al. (2022) showed that the aerosol plume produced an instantaneous direct aerosol radiative forcing (DARF) perturbation, at SRF and TOA, equal to −105.0 and −65.0 W/m^2, respectively. Values that can be largely attributed to enhanced stratospheric aerosol loading, with a stratospheric AOD of 0.6. However, Sellitto et al. (2022), included in the simulations the in-plume water vapor radio-sounding observations, apart from the aerosol extinction profile. Based on this approach he found values of −20 W/m^2 at TOA and −28 W/m^2 at SRF, values of RF that are possibly caused by the warming effect of excess H_2O in the stratosphere (Millán et al., 2022).

4.1.4 Conclusions

The major findings presented in this work concern the identification of the stratospheric volcanic layers, with high enough CoM reaching up to almost 29 km, according to the lidar

measurements. The corresponding $Å_b$ values were indicative of fine aerosols during the under-study region near the volcano. The PLDR values indicated the presence of mostly spherical (0.01-0.06) aerosols, probably sulfate particles, as was also indicated by the CALIPSO typing algorithm. The LR values ranged from 42.43 to 74.03, while the AOD, obtained by the lidar measurements, was found to vary from 0.04 to 1.40.

Concerning the SO_2 concentrations obtained by OMI over the study region, the measurements revealed a columnar SO_2 concentration of 13 DU on 16 January 2022. Moreover, the observations of the columnar AOD values, measured over the Lucinda station on 16 and 17 January 2022, as the volcanic plume moved towards Australia, showed a maximum AOD value of 1.99 along with Å values close to 1.5, showing that in this heavy aerosol load in the atmosphere the fine aerosols were dominant.

Finally, the calculated RF_{NET} of the aerosol profile obtained on 16 January 2022 was −43.97 W/m^2 at SRF and −46.76 W/m^2 at TOA. The radiative impact of the volcanic aerosols was higher compared to the BB aerosols studied during the Australian bushfires 2019-2020, a fact possibly attributed to the high reflectivity of the volcanic aerosols, the high AOD values and the extremely high altitude of the aerosol layers, that increased the cooling impact both at the SRF and TOA.

CHAPTER 5
EXTREME SAHARAN DUST EVENT

In Chapter 5, is presented a discussion and evaluation of results concerning the extreme Saharan dust event, that was observed over Athens, Greece (cf. Appendix D—Poster III).

5.1 Extreme Saharan dust event over Athens, Greece (March 2022): aerosol optical properties and radiative impact

5.1.1 Introduction

Saharan desert is one of the main global sources of dust particles, with more than 1–2 Tg of dust lofted in the atmosphere on an annual rate (Tanaka et al., 2006). Dust advection over the Mediterranean countries is driven by a rather regular seasonal pattern, in which spring and summer months are associated with high dust aerosol loads (Papayannis et al., 2009; Nisantzi et al., 2015; Soupiona et al., 2018).

A lot of studies have been published concerning the optical and radiative properties of Saharan dust layers, obtained by lidars, two recent ones over Athens (Soupiona *et al.*, 2020; Kokkalis *et al.*, 2021). However, the total direct radiative effect of mineral dust, that is estimated to be −0.11 ± 0.3 W/m^2 (Adebiyi and Kok, 2020), is still with a high uncertainty, thus Saharan dust events have to continue to be studied in all terms.

During March of 2022 the European continent was affected by one of the most extreme and long-lasting Saharan dust intrusions of the last decades. On 16 March 2022 the dust plume reached over Greece and the geometrical and optical properties of the dust aerosol layers were measured over Athens, by the elastic-Raman lidar system aErosol and Ozone Lidar systEm (EOLE) and the DEPOLE, both located at the LRSU of NTUA (37.97° N, 23.78° E, elev. 212 m amsl.). The aerosol geometrical and optical properties, along with a variety of models that were used to investigate the origin of the aerosols, along with the calculation of the dust radiative forcing, were all employed to imprint the overall impact of the event.

1.1.2 Methodology

Hybrid Single-Particle Lagrangian Integrated Trajectory

In order to determine the origin of the air masses carrying the aerosol plumes arriving over Athens' lidar station, an analysis of backward trajectories was performed by means of the HYSPLIT model (Stein et al., 2015; Rolph et al., 2017) All trajectories were calculated for a period of 120 h backward, for air masses arriving over Athens during 16 and 17 March, per hour of measurement (09:19 - 18:20 UTC and 08:24 – 11:00 UTC), for arrival heights of approximately the center of the main observed dust layer (2.54 – 5.40 km). Based on the results of the HYSPLIT model (Figure 5.1) we can see, that the air masses left the African continent having remained over Libya and Morocco, at 0–3 km height for several hours. The air masses followed a circular

path, passing from the Iberian Peninsula to France and through Germany, Italy and the Dalmatian Coasts, and reached Greece from the South.

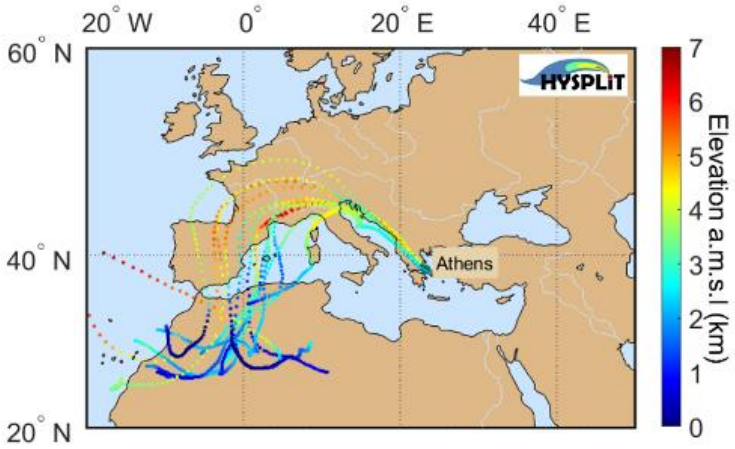

Figure 5. 1: 120 h backward trajectories for air masses arriving over Athens during 16 and 17 March, per hour of measurement (09:19 - 18:20 UTC and 08:24 – 11:00 UTC), for arrival heights of approximately the center of the main observed dust layer (2.54 – 5.40 km). The different colors in the trajectories represent the different altitudes that the air mass traveled until it reached the lidar station.

Navy Aerosol Analysis and Prediction System (NAAPS)

The global Navy Aerosol Analysis and Prediction System (NAAPS; http://www.nrlmry.navy.mil/aerosol/) model produces forecasts of three-dimensional aerosol concentrations on a global scale for four aerosol species including anthropogenic and biogenic fine (ABF) aerosols, smoke, sea salt, and dust (Lynch et al., 2016). The map of the aerosol optical depth during 16 and 17 March 2022 (Figure 4.14) shows that the dust plume (greenish color map areas) followed the same path, as indicated by the HYSPLIT model (Figure 5.2), and moreover that during the same period that we measured dust in Greece, the Saharan dust plume had even reached up to Scandinavian peninsula.

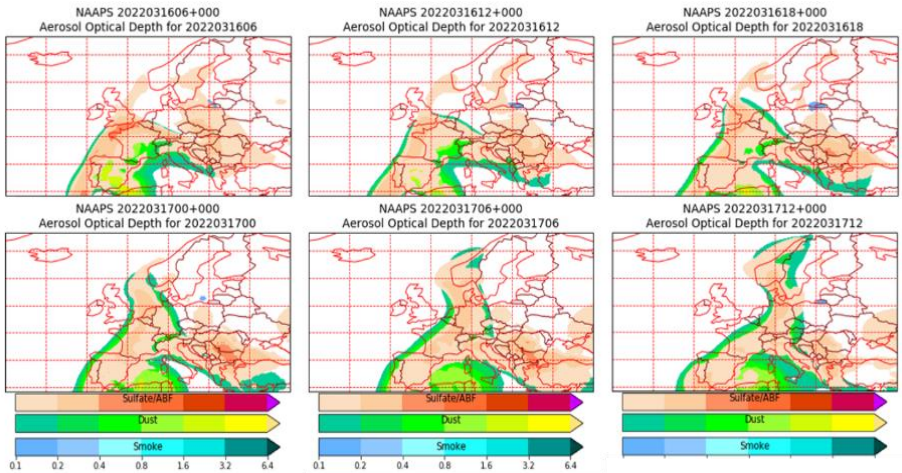

Figure 5. 2: Map of the aerosol optical depth calculated by NAAPS model during 16th and 17th March 2022, for three types of aerosols (http://www.nrlmry.navy.mil/aerosol/).

ATHENS NTUA AERONET station

The AERONET (https://aeronet.gsfc.nasa.gov/) has already been fully discussed in section 4.2.2. Within this study, data from the NTUA AERONET station (37.97°S, 23.78°E; 215 m amsl.) located inside the Athens Basin were used. NTUA station has been operating since July 2021 and among others provides information about the columnar AOD at 1640 1020, 870, 675, 500, 532, 440, 380 and 340 nm, Å at the pair of wavelengths 500-870, 440-870, 440-675, 380-500 and 340-440 nm and the fine and coarse mode of the aerosols measured.

Laser Remote Sensing Unit (LRSU) lidar systems

The campus of the NTUA is located inside the Athens Basin at 37.97 ° N, 23.78° E, with an elevation of 212 m amsl. The advanced multiwavelength elastic-Raman lidar system EOLE of the LRSU of NTUA (Papayannis et al., 2020) is based on a pulsed Nd:YAG laser system which emits, simultaneously, pulses at 355-532-1064 nm, with energies of 240-310-260 mJ, respectively, at a repetition rate of 10 Hz. The Cassegrainian telescope of the receiving unit is of 300 mm diameter (focal length 600 mm) and collects all elastically backscattered lidar signals, as well as the ones generated by the vibrational-rotational Raman effect (by atmospheric N_2 at 387 and 607nm, as well as by H_2O at 407 nm). EOLE lidar system is able to provide independent and simultaneous measurements of the vertical profiles of the aerosol backscatter b_{aer} (at 355, 532, and 1064 nm) and extinction a_{aer} (at 355 and 532 nm) coefficients, as well as the water vapor mixing ratio in the troposphere. Furthermore, EOLE provides the vertical profiles of the aerosol intensive parameters, namely the backscatter- and extinction-related Ångström exponents ($Å_{a355/532}$, $Å_{b355/532}$, $Å_{b532/1064}$), as well as the lidar ratio (LR) at 355 and 532 nm. The full overlap of EOLE is ~800 m amsl. (Kokkalis, 2017).

5.1.3 Results

The columnar AOD values (1640, 1020, 870, 675, 500, 440, 380 and 340 nm) and Å (500/870, 440/870, 440/675, 380/500, 340/440 nm) values, as observed over the AERONET NTUA station, on 16 March reached even up to 1.27 (0.87-1.27), while at the same time the Å values were close to zero (0.06 – 0.11) for all pairs of wavelengths, indicating the presence of coarse particles in the atmosphere. During the morning of 17 of March, the AOD values decreased and found ranging from 0.41 to 0.62. The Å values remained in relatively low values, from 0.31 to 0.61. It can be seen that when the highest AOD values ware registered, the Å values were at their lowest values. AERONET fine and coarse mode AOD at 500 nm for the same time period were equal to 74.93% during the first day of the event, while on the next day, this percentage was decreased to 57.96%. During the time periods that the event was more intense (red colored rectangles Figure 5.3), the coarse mode particles were equal to 85.08% and 67.39%, for the two days, respectively. This means that the coarse mode particles were dominant during the event, and especially on 16 March.

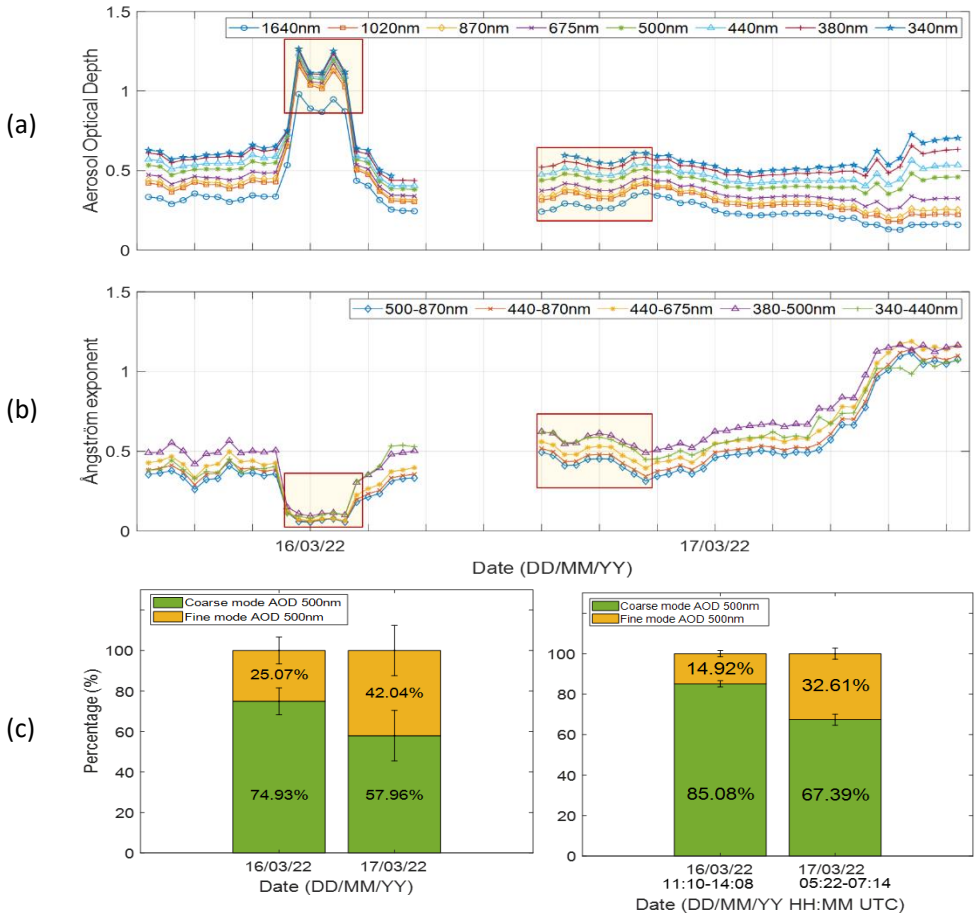

Figure 5. 3: Time series of mean hourly (a) AOD values at 1640, 1020, 870, 675, 500, 440, 380 and 340 nm and (b) Å at 500/870, 440/870, 440/675, 380/500, 340/440 nm and (c) fine- and coarse-mode fraction of aerosols, measured over Athens during 16-17 March 2022. Red colored rectangles frame the time periods when the values correspond to the measured dust event.

In Figure 5.4 we present the spatio-temporal evolution of the range-corrected lidar signal observed by DEPOLE at 532 nm, that indicates an extremely high aerosol load recorded (red-magenta and grey to white colors) between 4-6 km amsl., during the daytime of 16 March. After local noon, the dust layer followed a katabatic motion towards lower atmospheric heights (2-4.5 km). The acquired lidar data were processed to retrieve the vertical profiles of the aerosol optical properties per 1-hour of measurement.

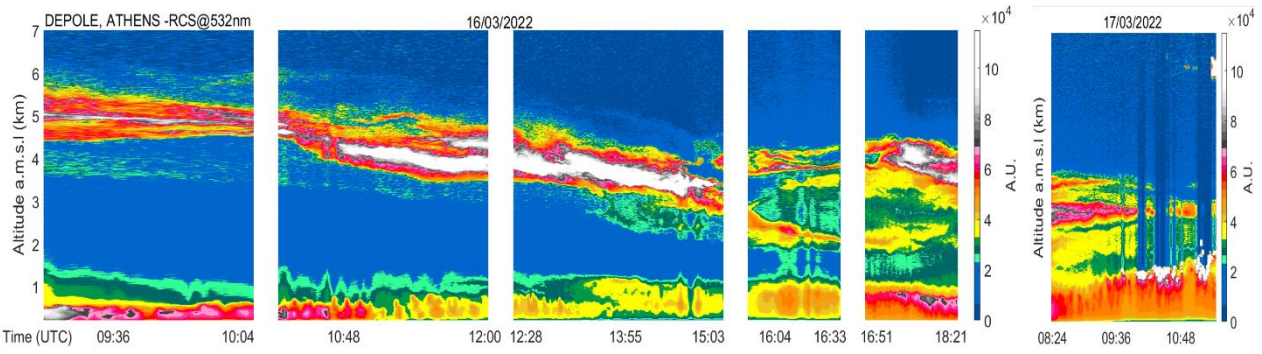

Figure 5. 5: Spatio-temporal evolution of the range-corrected lidar signal at 532 nm, as observed by DEPOLE lidar over Athens during 16-17 March 2022.

The vertical distribution of the optical properties, b_{aer} ($Mm^{-1}sr^{-1}$) and PLDR at 355 and 532 nm, as observed by the DEPOLE lidar during the dust event over the city of Athens are shown in Figure 5.5. Each profile, calculated per hour of measurement, is shown with different color. In total 10 profiles were obtained during the first day of measurement and one profile during the second.

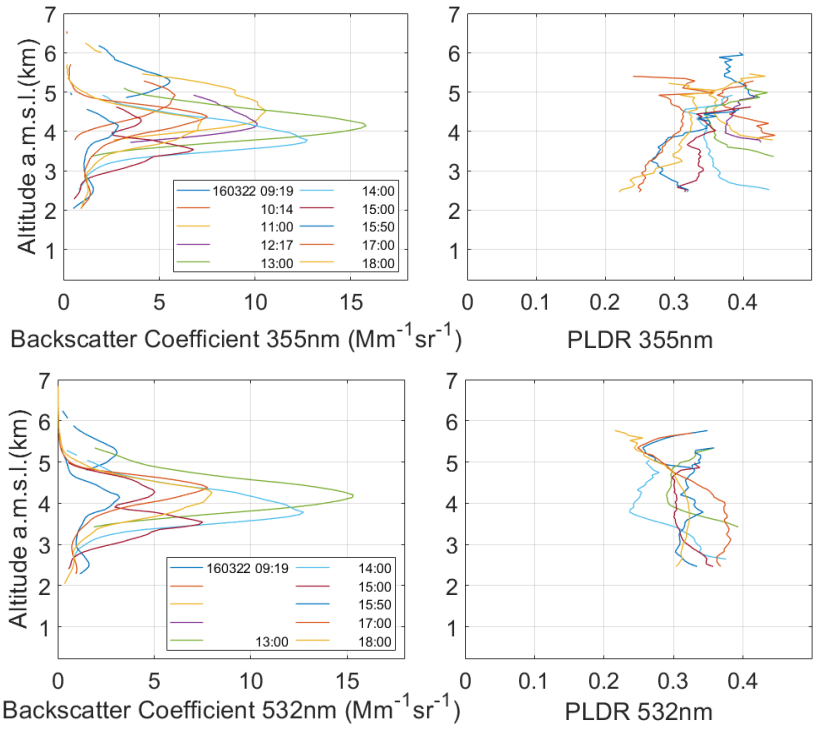

Figure 5. 4: Vertical distribution of the optical properties (b_{aer} and PLDR at 355 and 532 nm) of the aerosol layers observed over Athens on 16 March 2022 per hour of measurement (09:19 - 18:20 UTC), different colors correspond to different measurement hour.

During 16 March 2022 the vertical profiles of b_{aer} (Figure 5.5), at both wavelengths, revealed an extremely thick aerosol layer located during the measurement between 1.98 and 6.36 km, while the CoM ranged from 2.54 to 5.40 km amsl. Moreover, the b_{aer} shows almost

equal values at the two wavelengths (355 and 532 nm) inside the dust aerosol layers, while the extreme values of 7.64 ± 5.19 and 7.94 ± 5.38 $Mm^{-1}sr^{-1}$ was recorded at 532 and 355 nm, respectively. Concerning the vertical profiles of the PLDR, they show that inside the dust aerosol layers the values ranged from 0.29 ± 0.02 to 0.36 ± 0.05 (532 nm) and from 0.31 ± 0.04 to 0.40 ± 0.10 (355nm), corroborate the depolarizing ability of the dust aerosols and show that during the specific event the dust aerosols measured over the site were of unusually irregular shapes and thus presented these extreme values. PLDR values greater than 0.30 are representative for pure dust (Veselovskii et al., 2020, 2016; Groß et al., 2013; Ansmann et al., 2011).

Concerning the nighttime EOLE measurement (17:13-18:20 UTC) the corresponding a_{aer} (Mm^{-1}) at 355 and 532nm, along with the LR and the backscatter- and extinction-related Å ($Å_{b355/532}$, $Å_{a355/532}$), are presented in Figure 5.6

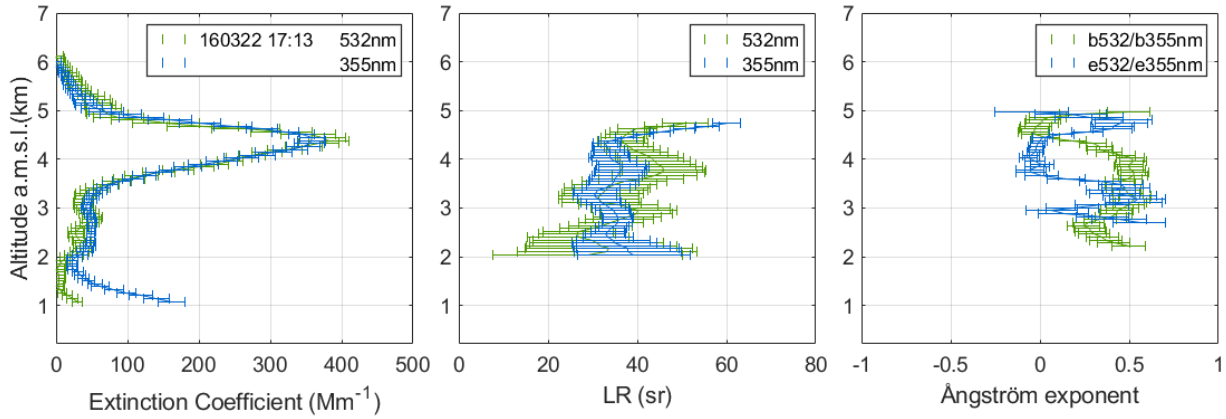

Figure 5. 6: Vertical distribution of the optical properties (a_{aer}, LR and $Å_b$, $Å_a$ at 355 and 532 nm) of the aerosol layer observed over Athens on 16 March 2022 during the nighttime EOLE measurement (17:13-18:20 UTC).

The a_{aer} values inside the layer were equal 168.93 ± 119.01 and 174.41 ± 114.67 Mm^{-1}. Concerning the LR inside the layers was equal to 53.22 ± 38.76 sr at 53 2nm and 44.82 ± 20.70 sr at 355nm, giving an indication of pure Saharan dust layers (Veselovskii et al., 2016). $Å_{a355/532}$ and $Å_{b355/532}$ on the same day and time, during the nighttime measurement show small values inside the dust aerosol layer equal to 0.16 ± 0.25 and 0.36 ± 0.19, respectively, that clearly indicate the dominance of coarser aerosols. Therefore, we could argue that the measured optical properties of the probed aerosols were representative of pure dust aerosols.

During the second day of this event (17 March 2022), the vertical distribution of the b_{aer} ($Mm^{-1}sr^{-1}$) and PLDR at 355 and 532 nm, was calculated at 08:30 UTC. The profiles of the optical properties for the pair of wavelengths 355 and 532 nm, are shown in Figure 5.7.

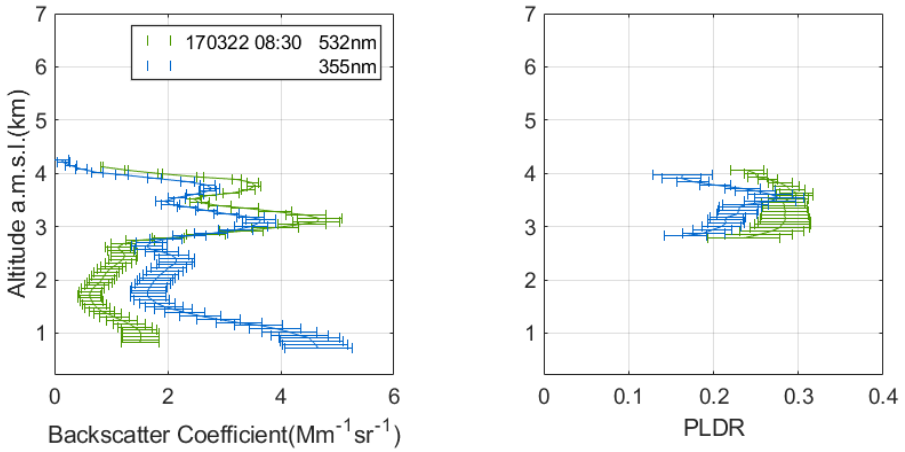

Figure 5. 8: Vertical distribution of the optical properties (b_{aer} and PLDR at 355 and 532 nm) of the aerosol layers observed over Athens on 17 March 2022 (08:30-09:30 UTC), the different colors correspond to different wavelength.

Finally, in order to estimate the RF_{NET} of the dust aerosols over Athens, we followed the procedure described in section 4.2.2. The simulation was performed at 09:20 UTC on 16 March 2022, the SZA was equal to 42.71°. The RF_{NET} was calculated at the TOA and at the SRF-level, using the LibRadtran model for the aerosol loaded atmosphere and for a typical atmosphere free of aerosols (Figure 5.8). The former includes the presence of the free tropospheric dust aerosol layer, so that the contribution of the dust load in the RF_{NET} could be found with respect to the clear atmosphere.

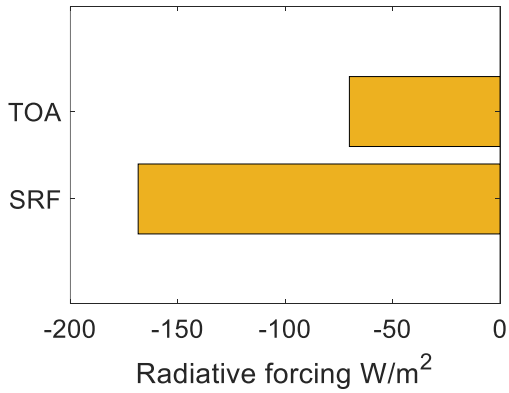

Figure 5. 7: Net radiative forcing at top of atmosphere (TOA) and at surface (SRF) at 09:20 UTC on 16 March 2022, the SZA was equal to 42.71° over the NTUA lidar station.

The RF_{NET} of the thick aerosol layer observed over Athens at the TOA was equal to −70.11 W/m^2 and at SRF −168.41 W/m^2, indicating cooling at SRF and TOA, respectively, at the current day and time over the station. Soupiona *et al.* (2020) showed that for SZA of 45°, the RF values at the SRF were high in absolute values with a cooling behavior and was found to decrease with increasing height of the layers. More specifically, the RF was found ranging from −150.0 to -1.9 W W/m^2 for the city of Granada, from −38.1 to −3.7 W/m^2 for Potenza, from −64.8 to −13.2

W/m^2 for Athens and from −90.3 to −28.4 W/m^2 for Limassol. Also, it was shown that peaks in a_{aer} at 532 nm that were observed between 2 and 6 km amsl. Indicated that the intrusion of dust decreases the shortwave radiation that reaches the SRF. These results, along with the intensity of the measured dust event explain the increased values at SRF.

5.1.4 Conclusions

In the period 16-17 March 2022, the meteorological conditions prevailing over the Eastern Mediterranean enabled the formation of an extreme (in terms of aerosol load) Saharan dust event over Greece. High AOD values, even up to 1.27, were observed by the AERONET NTUA station, on 16 March), while at the same time the Å values were close to zero (0.06 – 0.11), indicating the presence of coarse particles in the atmosphere. AERONET fine and coarse mode AOD at 500 nm for the same date and time period reached up to 85.08%.

During 16 March 2022 the b_{aer} values revealed an extremely thick aerosol layer located between 1.98 and 6.36 km, while the CoM was found between 2.54 and 5.40 km amsl. Concerning the PLDR aerosol values within the aerosol layer, t showed values ranging from 0.29 ± 0.02 to 0.36 ± 0.05 (532 nm) and from 0.31 ± 0.04 to 0.43 ± 0.27 (355nm), these values being representative of pure dust aerosols. The LR inside the layers was found equal to 53.22 ± 38.76 sr at 53 2nm and 44.82±20.70 sr at 355nm, providing indication of the presence of non-mixed layers of Saharan dust aerosols (Veselovskii et al., 2016). The $Å_{a355/532}$ and $Å_{b355/532}$ during the nighttime measurement showed small values inside the dust layer (0.16 ± 0.25 and 0.36 ± 0.19), that clearly indicate the dominance of coarser aerosols in the atmosphere over the lidar station.

Eventually, the thick aerosol layer observed over Athens on 16 March 2022 had a RF_{NET} of –70.11 W/m^2 at the TOA and –168.41 W/m^2 at SRF, both of which indicated cooling and demonstrated that less solar energy reaches the SRF as a result of dust infiltration.

CHAPTER 6
CONCUSIONS

In this Ph.D. Thesis a variety of extreme aerosol pollution events was studied, presented and analyzed. One of the cases concerns the local production of BB aerosols within the PBL and the LFT, over the small city of Ioannina, in Greece, while most of the studies, four in total, refer to the long-range transport of BB aerosols. Particularly interesting was the study of the volcanic aerosol's transport, emitted in the stratosphere by one of the strongest volcanic eruptions ever recorded. Finally, one of the most extreme Saharan dust events recorded during the last years, that affected Europe during March 2022 and specifically Athens (Greece), on 16-17 March 2022, was also studied. The aerosol properties were retrieved within the PBL, troposphere and stratosphere, while their radiative effect was also calculated, whenever possible.

At first, the extremely fresh BB aerosols from residential heating in the city of Ioannina, are measured inside the PBL (discussed in 3.2; Papanikolaou et al., 2022b). High b_{aer} (even up to 12.19 $Mm^{-1}sr^{-1}$) and extremely low PLDR values (0.01 - 0.03) were found, indicating a heavy load of spherical aerosols within the lowest atmosphere of the city. The lidar measurements were complemented by in situ fine aerosol ($PM_{2.5}$) mass concentration and BC measurements, revealing that the emissions in this middle-sized urban city was of the same order, and in some cases even greater, than the emissions in some of the biggest European cities (e.g., Granada, Lisbon, London, Madrid, Paris, Porto, Rome, or Zurich) (Herich et al., 2011; Titos et al., 2017; Fuller et al., 2014, 2013; Costabile et al., 2017; Borrego et al., 2010; Becerril-valle et al., 2017).

In the free troposphere , the freshly emitted BB aerosols measured in Ioannina (discussed in 3.2, along with the BB aerosols measured by CALIPSO satellite, close to the wildfires' sources, in Canada and Australia (discussed in 3.1 (Papanikolaou et al., 2020) and 3.3 (Papanikolaou et al., 2022a), respectively), confirmed that the aerosols in both cases were almost spherical (PLDR <0.06); while, according to $Å_b$ values (0.94 - 1.17), the fresh smoke particles were found to be of small size. Regarding the aged BB aerosols (taking into consideration only the results from the long-ranged events from: Canadian wildfires (Papanikolaou et al., 2020), Australian bushfires (Papanikolaou et al., 2022a) and Californian wildfires; discussed in 3.1, 3.3 and 3.4, respectively), the tropospheric aerosols' PLDR values were equal to 0.06 ± 0.04 for both Canadian and Australian smoke particles, after 3 to 10 days transport from the source, showing that the particles continue to be spherical during their long atmospheric journey.

The corresponding $Å_b$ values were found between 0.99 ± 0.95 and 1.02 ± 0.72 for the Canadian tropospheric BB aerosols, while the Australian BB aerosols presented a wider range, with values ranging from 0.81±0.39 (farther from the source region; BR) to 1.37 ± 0.46 (closer to the source region; YR). In the latter study, the aged tropospheric BB aerosols, seem to grow in size as they fend off the source. The tropospheric BB aerosols from the Californian wildfires, measured over Athens showed a wide range in the PLDR values (0.04 to 0.22). These tropospheric

PLDR values could be explained by the fact that throughout their path the aerosols were probably enriched with larger, more depolarizing particles (e.g. dust particles) (discussed in 5.1), also observed in the FT, the optical properties (b_{aer}, a_{aer}, AOD) revealed an extremely thick aerosol layer, with PLDR values greater than 0.29, values representative of pure dust aerosols, while Å values (0.16 ± 0.25 and 0.36 ± 0.19) clearly indicated the dominance of coarse aerosols in the atmosphere.

During the Australian bushfires time period, the CO concertation in the troposphere was increased up to 100% in the 700–950 hPa pressure levels, compared to the same days of the event averaged over a base period (2004–2019). The highest observed increase in CO was 92% at 950 hPa, while the O_3 enhancement presented values of 60–96% in the higher atmospheric pressure levels and even 100% in the lower ones (200–400 hPa). The impact of emitted CO on the O_3 formation was significant close to the fire source, while, for the rest of the regions, CO variation did not play a key role in the observed O_3 enhancement.

Furthermore, two of the events studied within this Ph.D. Thesis, are related to stratospheric aerosol properties: (i) Australian Bushfires (2019–2020): Aerosol Optical Properties and Radiative Forcing (discussed in 3.3; Papanikolaou et al., 2022a), and (ii) the Hunga Tonga-Ha'apai volcanic aerosols (discussed in 4.1). At first, the stratospheric BB aerosol layers were observed in the stratosphere up to 22 km height, while the volcanic aerosol layers were observed even at 30 km. During the Australian bushfires the mean PLDR values of the smoke particles in the stratosphere were found to be 0.11 ± 0.03, while the maximum observed values ranged from 0.15 to 0.20. These, higher PLDR values suggest particles of irregular solid shapes. The corresponding values of the volcanic aerosols were found ranging from 0.01 to 0.06, values indicative of the presence of sulphate spherical aerosols.

The corresponding $Å_b$ values, in the bushfire event, showed that the smoke particles' size was slightly decreased, as they drew away from source, while the maximum recorded $Å_b$ values (2.00 - 2.50) proved the presence of extremely small smoke particles in stratosphere. On the other hand, the volcanic $Å_b$ values were found from 0.79 to 1.94, indicating the existence of fine aerosols, that in some cases co-existed with coarser particles, possibly sulfur coated ash particles, that also exist within volcanic plumes and are larger than the sulfate aerosols. The maximum recorded AOD values of the two events was 0.40 for the Australian smoke and 1.40 for the volcanic aerosols.

To conclude, the radiative effect of three aerosol types (BB, volcanic and Saharan dust aerosols), studied during four unique aerosol pollution events, in different atmospheric altitudes and coordinates, was also estimated and presented in this Ph.D. Thesis. At SRF and TOA, the RF_{NET} of the stratospheric volcanic aerosols was –43.97 W/m^2 and –46.76 W/m^2, respectively. Regarding the Australian BB aerosols observed in the stratosphere, the corresponding values were estimated to be –31.98 W/m^2 and –8.94 W/m^2, respectively. The volcanic RF_{NET} was greater than the smokes', possibly due to the high reflectivity of the sulfate aerosols, which increased

the cooling effect by lowering the amount of shortwave radiation reaching the ground. Since the volcanic aerosol layer was much higher in the stratosphere, than the BB layer, the increased volcanic aerosol load had also a greater impact at the TOA. The aerosol profiles used to estimate the RF_{NET} were obtained in almost the same geographical region, time zone and hour, thus the results were comparable, with regard to the SZA.

Furthermore, the RF_{NET} of tropospheric BB aerosols, emitted by the Australian bushfires, at SRF was found from –87.10 to –4.53 W/m^2 (mean value –32.22 ± 25.84 W/m^2) ranged from –47.42 to +11.56 W/m^2 (mean value –12.83 ± 14.74 W/m^2) at TOA, for a range of the SZA between 24.65° and 46.86°. Regarding the aged Californian particles, observed over Athens, they presented a RF_{NET} both at SRF and TOA, that was equal to –1.33 W/m^2 and at SRF –4.71 W/m^2, indicating a slight cooling both at SRF and TOA. Finally, the thick aerosol layer detected over Athens had an estimated RF_{NET} of –168.41 W/m^2 at SRF and –70.11 W/m^2 at TOA, indicating cooling. The increased values at SRF could be explained by the magnitude of the observed dust event.

ΕΚΤΕΤΑΜΕΝΗ ΠΕΡΙΛΗΨΗ

Σκοπός της παρούσας διδακτορικής διατριβής είναι η μελέτη των γεωμετρικών και οπτικών ιδιοτήτων των τροποσφαιρικών και στρατοσφαιρικών αιωρούμενων σωματιδίων τόσο σε τοπική όσο και σε παγκόσμια κλίμακα, κατά τη διάρκεια έντονων επεισοδίων σωματιδιακής ρύπανσης, χρησιμοποιώντας επίγειες και δορυφορικές μεθόδους τηλεπισκόπησης. Εκτός από τις γεωμετρικές και οπτικές ιδιότητες των αιωρούμενων σωματιδίων των διαφόρων στρωματώσεων, όπως αυτές προκύπτουν από τις μετρήσεις lidar, χρησιμοποιούνται, επίσης, επιτόπια (in situ) δεδομένα στην επιφάνεια του εδάφους, καθώς και δεδομένα ολικής ατμοσφαρικής στήλης. Επιπλέον, γίνεται χρήση μετεωρολογικών μοντέλων, που συνεισφέρουν στην απόκτηση της πληροφορίας της πηγής των αερίων μαζών, ιδίως όταν παρατηρείται μεταφορά από άλλες χώρες ή διαφορετικές ηπείρους (π.χ. ερημική σκόνη). Το μοντέλο διάδοσης της ηλιακής ακτινοβολίας (LibRadtran) χρησιμοποιείται για να απεικονίσει την επίδραση που έχουν τα ατμοσφαιρικά αιωρούμενα σωματίδια στο ενεργειακό ισοζύγιο της ατμόσφαιρας.

Στο Κεφάλαιο 1 παρουσιάζεται συνοπτικά η δομή και η σύνθεση της ατμόσφαιρας. Επίσης, γίνεται αναφορά στα ατμοσφαιρικά αιωρούμενα σωματίδια και ο ρόλος τους στο ενεργειακό ισοζύγιο της ατμόσφαιρας. Οι διαφορετικοί τύποι των ατμοσφαιρικών αιωρούμενων σωματιδίων παρουσιάζουν μια ποικιλία γεωμετρικών και οπτικών ιδιοτήτων, καθώς σκεδάζουν ή/και απορροφούν την ακτινοβολία και έτσι επηρεάζουν το κλίμα της γης με διαφορετικούς τρόπους.

Στο Κεφάλαιο 2, αρχικά παρουσιάζεται το θεωρητικό υπόβαθρο των μεθόδων με τηλεπισκόπησης με εφαρμογές στην ατμόσφαιρα. Δεδομένου ότι τα ατμοσφαιρικά αιωρούμενα σωματίδια αλληλοεπιδρούν με την εισερχόμενη ηλιακή ακτινοβολία, καθώς και την εξερχόμενη γήινη ακτινοβολία, έμφαση δίνεται στους μηχανισμούς των αλληλεπιδράσεων των μορίων και των αιωρούμενων σωματιδίων της ατμόσφαιρας με το την ακτινοβολία. Οι θεμελιώδεις οπτικές διαδικασίες που λαμβάνουν χώρα στην ατμόσφαιρα και εξετάζονται εν συντομία, περιλαμβάνουν την απορρόφηση, τη σκέδαση, τον φθορισμό και την αποπόλωση του φωτός. Επιπλέον, παρουσιάζονται οι αρχές λειτουργίας της μεθόδου τηλεπισκόπησης lidar, με εφαρμογές στην ατμόσφαιρα. Τέλος, γίνεται εκτενής αναφορά στις μεθόδους επεξεργασίας δεδομένων lidar, τόσο από επίγεια, όσο και από δορυφορικά συστήματα, όπως το Cloud-Aerosol Lidar with Orthogonal Polarization (CALIOP) στον δορυφόρο Cloud-Aerosol Lidar and Infrared Pathfinder Satellite Observation (CALIPSO), καθώς και στις οπτικές ιδιότητες των αιωρούμενων σωματιδίων που ανακτώνται από αυτά.

Τα αποτελέσματα και η ανάλυση των δεδομένων της διατριβής παρουσιάζονται στα Κεφάλαια 3, 4 και 5. Αρχικά, στο Κεφάλαιο 3, παρουσιάζεται μια πλήρης ανάλυση τεσσάρων μελετών που αφορούν σε έντονα επεισόδια σωματιδιακής ρύπανσης από καύση βιομάζας. Η πρώτη από αυτές τις μελέτες αφορά σε ένα επεισόδιο πυρκαγιών στην περιοχή της Βρετανικής Κολομβίας (British Columbia) του Καναδά, το οποίο μελετήθηκε με δεδομένα από τον δορυφόρο

CALIPSO. Αυτό το μεγάλο επεισόδιο παρήγαγε τεράστιες ποσότητες σωματιδίων καπνού στην τροπόσφαιρα, τα οποία παρατηρήθηκαν κατά τη μεταφορά τους από τον Καναδά στην Ευρώπη, τον Αύγουστο του 2018, χρησιμοποιώντας δεδομένα ενεργούς τηλεπισκόπησης από τον δορυφόρο CALIPSO. Οι στρωματώσεις των αιωρούμενων σωματιδίων που ανιχνεύθηκαν, κατηγοριοποιήθηκαν σε αυτές του καπνού χωρίς προσμίξεις, καθώς και καπνού με προσμίξεις από άλλους τύπους αιωρούμενων σωματιδίων. Οι γεωμετρικές και οπτικές ιδιότητες των σωματιδίων καπνού, με ή χωρίς προσμίξεις, μελετήθηκαν εκτενώς στην πορεία τους προς την Ευρώπη.

Κάνοντας χρήση του μοντέλου Hybrid Single-Particle Lagrangian Integrated Trajectory (HYSPLIT) ensemble, καθώς και της χωρο-χρονικής μεταβολής του οπτικού βάθους των αιωρούμενων σωματιδίων (AOD) στα 550 nm, από το όργανο Moderate Resolution Imaging Spectroradiometer (MODIS), προσομοιώσαμε την εμπρόσθια κίνηση του καπνού από τον Καναδά προς την Ευρώπη (Εικόνα 1, α-β). Τα δεδομένα από τις τροχιές του δορυφόρου CALIPSO (Εικόνα 1, β), που παρακολουθούν τον καπνό καθ' όλη τη διάρκεια της μεταφοράς του, πρόσφεραν την κατακόρυφη κατανομή των οπτικών ιδιοτήτων τον αιωρούμενων σωματιδίων.

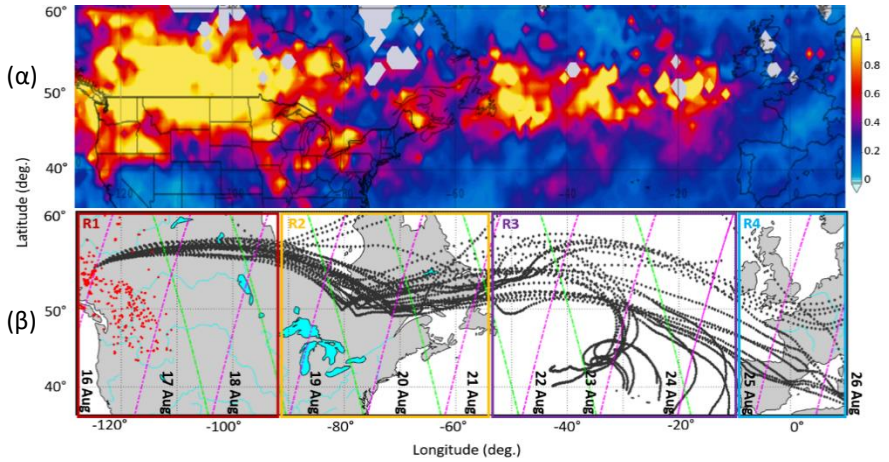

Εικόνα 1: (α) Χάρτης απεικόνισης της χωρο-χρονικής μεταβολής του AOD στα 550 nm (MODIS-Aqua MYD08_D3 v6.1) από τις 16 Αυγούστου 2018 και για περίοδο 10 ημερών. (β) Οι 10ήμερες εμπρόσθιες τροχιές HYSPLIT που ξεκινούν στις 16 Αυγούστου και λήγουν στις 25 Αυγούστου πάνω από την Ευρώπη. Οι κόκκινες κουκκίδες αντιστοιχούν σε ενεργές εστίες πυρκαγιών που παρατηρήθηκαν στο BC του Καναδά, από το MODIS. Οι γραμμές χρώματος ματζέντα και πράσινου, αντιστοιχούν σε τροχιές του CALIPSO κατά τη διάρκεια της νύχτας και της ημέρας, αντίστοιχα. Τα κόκκινα, κίτρινα, μοβ και κυανού χρώματος ορθογώνια αντιστοιχούν στις τέσσερεις υποπεριοχές (R1–R4) της κίνησης του καπνού (Papanikolaou et al., 2020).

Από τις 745 στρωματώσεις που ανιχνεύθηκαν, το 42% αναγνωρίστηκε ως καπνός χωρίς προσμίξεις. Το υπόλοιπο 58% αποδόθηκε σε στρωματώσεις καπνού αναμεμειγμένου με: ρυπασμένη σκόνη (34%), ηπειρωτικά (10%), ρυπασμένα ηπειρωτικά αιωρούμενα σωματίδια (5%), ερημική σκόνη (6%) και θαλάσσιας προέλευσης αιωρούμενα σωματίδια (3%). Οι

στρωματώσεις καπνού παρατηρήθηκαν σε ένα ευρύ φάσμα υψομέτρων από 0,8 km έως 10 km ύψος, ενώ οι πλειοψηφία των στρωματώσεων βρέθηκε μεταξύ 2.1 και 5.2 km amsl. (Εικόνα 2, α-β). Η μέση τιμή του b_{aer} στα 532 nm, για κάθε τύπο ανάμειξης καπνού κυμάνθηκε από 0.8 έως 2.6 $Mm^{-1}sr^{-1}$, ενώ η μέση τιμή του PLDR στα 532 nm βρέθηκε ίση με 0.04 ± 0.02 για σωματίδια καπνού χωρίς προσμίξεις, ενώ έφτασε μέχρι και 0.20 ± 0.04, για καπνό αναμεμειγμένο με ερημική σκόνη. Η μέση τιμή του $Å_b$ (532/1064 nm), ενδεικτική για το μέγεθος των σωματιδίων κυμάνθηκε για όλα τα στρώματα καπνού με προσμίξεις μεταξύ 0.8 και 1.6, σε κάθε υπο-περιοχή μελέτης.

Τέλος, διαπιστώθηκε ότι το σχήμα και το μέγεθος, όπως αυτά προκύπτουν από τις τιμές PLDR και $Å_b$, των αιωρούμενων σωματιδίων καπνού δεν αλλάζουν σημαντικά κατά τη μεταφορά των σωματιδίων καπνού. Το ίδιο ισχύει και για τις προσμίξεις του καπνού με άλλους τύπους σωματιδίων, με εξαίρεση την πρόσμιξη καπνού και ερημικής σκόνης, που έπαιξε τον κύριο ρόλο στις αλλαγές που παρατηρήθηκαν στις οπτικές ιδιότητες του αερολύματος.

Η δεύτερη δημοσίευση αφορά στην μελέτη της κατακόρυφης κατανομής των οπτικών ιδιοτήτων των αιωρούμενων σωματιδίων από καύση βιομάζας, που πραγματοποιήθηκε κατά τη διάρκεια της χειμερινής εκστρατείας μετρήσεων της ΠΑΝελλΑδικής υποδομής για τη μΕλέτη της ατμοσφαιρικής σύστασης και κλιματικής Αλλαγής (ΠΑΝΑΚΕΙΑ) το 2020 στην πόλη των

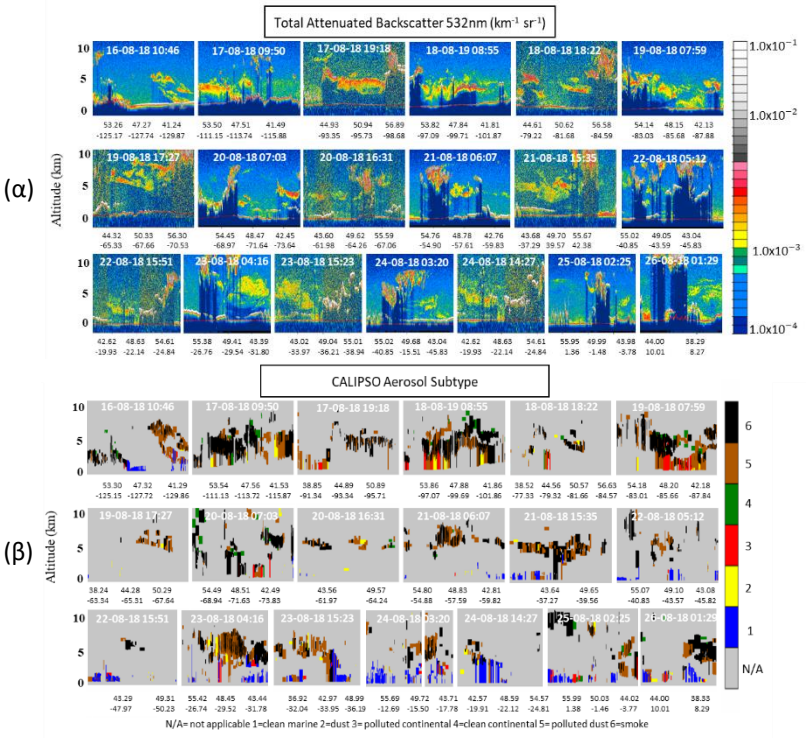

Εικόνα 2: (α) Ολικός συντελεστής οπισθοσκέδασης όπως παρατηρήθηκε από τον δορυφόρο CALIPSO στα 532 nm και (β) κατηγορίες αερολυμάτων αναφορικά με το ύψος, το γεωγραφικό πλάτος και μήκος για νυχτερινές και ημερήσιες τροχιές του δορυφόρου (16-26 Αυγούστου 2018) (Papanikolaou et al., 2020).

Ιωαννίνων. Τα Ιωάννινα είναι μία πόλη η οποία υποφέρει από επεισόδια ατμοσφαιρικής

ρύπανσης, κατά τη διάρκεια του χειμώνα, λόγω της καύσης βιομάζας για οικιακή θέρμανση. Η τεχνική lidar εφαρμόσθηκε, κατά τη διάρκεια της εκστρατείας αυτής, χρησιμοποιώντας το κινητό σύστημα lidar AIAS, που μετρά την αποπόλωση στα 532 nm. Στόχος της εκστρατείας ήταν η μέτρηση της χωρο-χρονικής εξέλιξης της κατακόρυφης κατανομής των πολύ «φρέσκων» σωματιδίων (χρόνος παραγωγής ~ ώρες) από καύση βιομάζας λόγω τοπικών δραστηριοτήτων οικιακής θέρμανσης. Ο συντελεστής οπισθοσκέδασης (b_{aer}) και ο γραμμικός λόγος αποπόλωσης (PLDR), στα 532 nm, σε συνδυασμό με σωματιδιακές συγκεντρώσεις ($PM_{2.5}$) και συγκεντρώσεις

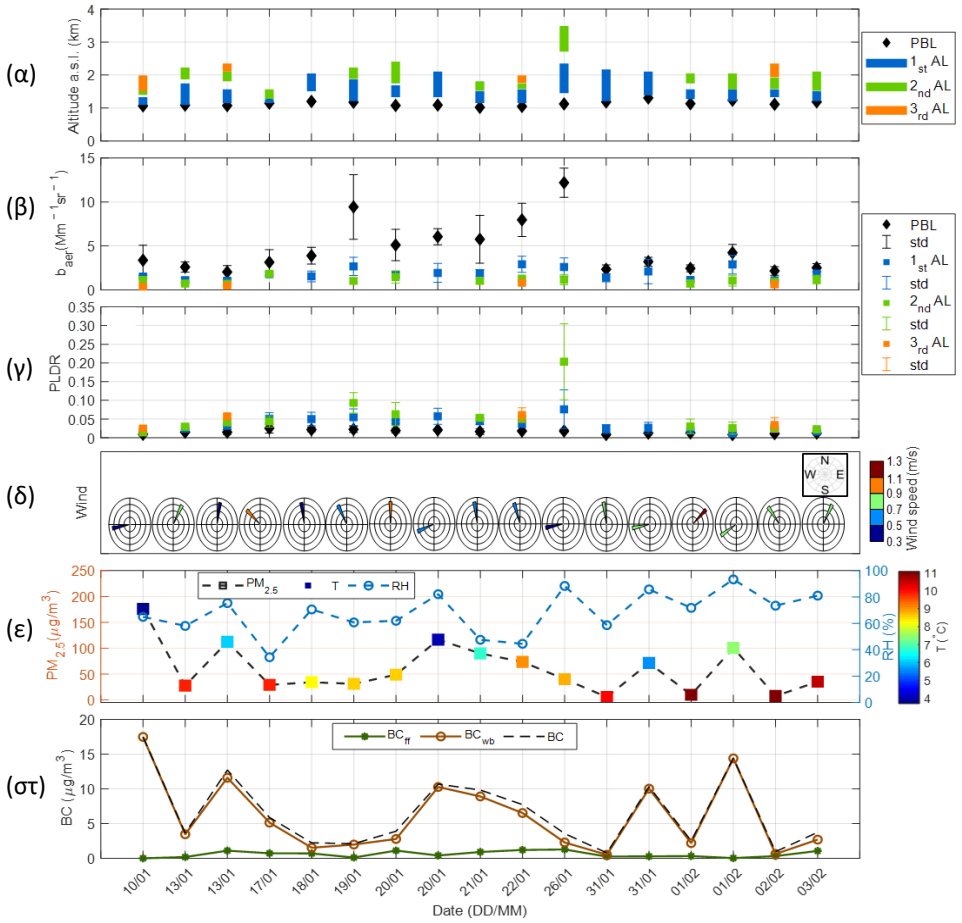

Εικόνα 3: Χρονική διακύμανση του (α) του ύψους του PBL (μαύρος ρόμβος) μαζί με τη βάση και την κορυφή κάθε στρωμάτωσης (AL, έγχρωμες ράβδοι) (km) και τις αντίστοιχες μέσες τιμές των (β) b_{aer} και std ($Mm^{-1}sr^{-1}$) και (γ) PLDR και std στα 532 nm, όπως ελήφθησαν από το κινητό σύστημα lidar AIAS, μαζί με (δ) την ταχύτητα του ανέμου (m/s) και την κατεύθυνση του (°), (ε) τις συγκεντρώσεις $PM_{2.5}$ ($\mu g/m^3$), θερμοκρασία (°C), σχετική υγρασία (%), (στ) οι συγκεντρώσεις BC ($\mu g/m^3$) μαζί με το ποσοστό συμβολής των ορυκτών καυσίμων και της καύσης βιομάζας, στη συνολική συγκέντρωση BC. Όλα τα δεδομένα που παρουσιάζονται υπολογίζονται κατά μέσο όρο για τις ίδιες χρονικές περιόδους κατά τις οποίες ανακτήθηκαν οι κατακόρυφες κατανομές των οπτικών ιδιοτήτων από το lidar (Papanikolaou et al., 2022b).

Μαύρου Άνθρακα (BC), χρησιμοποιήθηκαν για να δώσουν μία ολοκληρωμένη περιγραφή της ατμόσφαιρας πάνω από τα Ιωάννινα, κατά τη διάρκεια αυτών των έντονων επεισοδίων σωματιδιακής ρύπανσης, όπως φαίνεται και στην Εικόνα 3.

Συνολικά, 33 από τις 34 στρωματώσεις που παρατηρήθηκαν πάνω από το Ατμοσφαιρικό Οριακό Στρώμα (PBL), χαρακτηρίσθηκαν ως σωματίδια από καύση βιομάζας τοπικής προέλευσης. Οι μέση τιμή του b_{aer} για τις στρωματώσεις αυτές ήταν 1.45 ± 0.43 $Mm^{-1}sr^{-1}$ (από 0.37 ± 0.11 έως 2.91 ± 0.91 $Mm^{-1}sr^{-1}$), ενώ η μέση τιμή του PLDR ήταν ίση με 0.04 ± 0.01. Η 26 Ιανουαρίου 2020, αποτέλεσε εξαίρεση στην εκστρατεία μετρήσεων καθώς ήταν η μόνη ημέρα που δεν εντοπίστηκαν μόνο σωματίδια από καύση βιομάζας στην ατμόσφαιρα των Ιωαννίνων, αλλά σωματίδια ερημικής σκόνη, με μέση τιμή b_{aer} ίση με 1.50 ± 0.59 $Mm^{-1}sr^{-1}$, και μέση PLDR 0.20 ± 0.10, σε ύψος από 2.71 έως 3.49 km. Επιπρόσθετα, το ύψος του PBL (PBLH) κατά τη διάρκεια της εκστρατείας κυμάνθηκε από 1.02 έως 1.31 km, με μέση τιμή 1.13 ± 0.07 km, ενώ μέσα σε αυτό η μέση τιμή του b_{aer} βρέθηκε ίση με 4.61 ± 2.88 $Mm^{-1}sr^{-1}$ (από 2.03 ± 0.74 έως 12.69 ± 0.69 $Mm^{-1}sr^{-1}$), με την τιμή PLDR να κυμαίνεται μεταξύ 0.01 ± 0.01 και 0.03 ± 0.01, επιβεβαιώνοντας την παρουσία των φρέσκων σωματιδίων καύσης βιομάζας, η οποία φάνηκε να εντείνεται, παρουσία του ρηχού Ατμοσφαρικού Οριακού Στρώματος (ΑΟΣ), των χαμηλών θερμοκρασιών και των στάσιμων ατμοσφαιρικών συνθηκών που επικρατούσαν.

Στο επίπεδο του εδάφους, οι συγκεντρώσεις των $PM_{2.5}$ κυμαίνονταν από 5.6 έως 175.7 $\mu g/m^3$, ενώ η θερμοκρασία και η σχετική υγρασία κυμάνθηκαν από 3.7 έως 11.1 °C και 34 έως 93%, αντίστοιχα. Η ταχύτητα του ανέμου παρουσίασε εξαιρετικά χαμηλές τιμές (0.33 έως 1.16 m/s), συμβάλλοντας έτσι στις αυξημένες συγκεντρώσεις του BC. Η μέση τιμή των συγκεντρώσεων του BC ήταν 6.6 ± 5.0 $\mu g/m^3$ (από 0.8 σε 17.5 $\mu g/m^3$), ενώ οι εκπομπές καύσης βιομάζας από τη θέρμανση κατοικιών αυξάνονταν τις βραδινές ώρες, όταν μειωνόταν η θερμοκρασία. Το ποσοστό της συνεισφοράς της καύσης βιομάζας στις συγκεντρώσεις του BC ήταν εξαιρετικά υψηλό, με τη μέση συνεισφορά να είναι ίση με 85.4%, ενώ σε ορισμένες περιπτώσεις κατά τη διάρκεια της νύχτας έφτασε έως και το 100%. Τα αποτελέσματα αυτής της μελέτης μπορούν να χρησιμοποιηθούν σε μοντέλα πρόβλεψης σοβαρών επεισοδίων ατμοσφαιρικής ρύπανσης στην πόλη των Ιωαννίνων και όχι μόνο, καθώς και ως εργαλεία στις ελληνικές αρχές για τη μείωση των επιπέδων ατμοσφαιρικής ρύπανσης της πόλης.

Στην τρίτη κατά σειρά δημοσιευμένη μελέτη, παρουσιάζονται οι οπτικές ιδιότητες σωματιδίων καπνού, που παρατηρήθηκαν στην τροπόσφαιρα και την στρατόσφαιρα του νότιου ημισφαιρίου, από τον δορυφόρο CALIPSO, καθώς και η επίδραση τους στο ισοζύγιο ακτινοβολίας (RF). Τα σωματίδια καπνού εκπέμφθηκαν κατά τη διάρκεια ενός από τα πιο έντονα επεισόδια πυρκαγιών παγκοσμίως, το οποίο έλαβε χώρα στην Αυστραλία και μελετήθηκε από τις 25 Δεκεμβρίου 2019 έως τις 12 Φεβρουαρίου του 2020. Οι στρωματώσεις καπνού μελετήθηκαν ως προς τις γεωμετρικές και οπτικές τους ιδιότητες καθώς και την επίδραση τους στο ισοζύγιο ακτινοβολίας, από 140° Ανατολικά έως 20° Δυτικά, στη ζώνη γεωγραφικού πλάτους 20°–60° του νότιου ημισφαιρίου, καθώς τα σωματίδια μεταφέρθηκαν σταδιακά από τις όχθες της Αυστραλίας στη Νοτιοαμερικανική ήπειρο (Εικόνα 4).

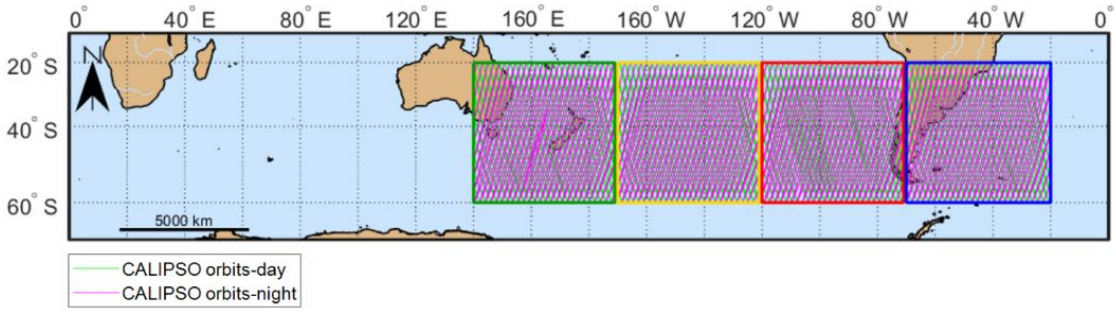

Εικόνα 4: CALIPSO ημερήσιες και νυχτερινές τροχιές ανά περιοχή μελέτης, για τη χρονική περίοδο 25 Δεκεμβρίου 2019–12 Φεβρουαρίου 2020 (Papanikolaou et al., 2022a).

Το υψόμετρο των στρωματώσεων καπνού κυμάνθηκε από την επιφάνεια του εδάφους μέχρι και τη στρατόσφαιρα, σχεδόν σε υψόμετρο 22 km amsl., ενώ οι κύριες οπτικές του ιδιότητες παρουσιάζονται στην Εικόνα 5.

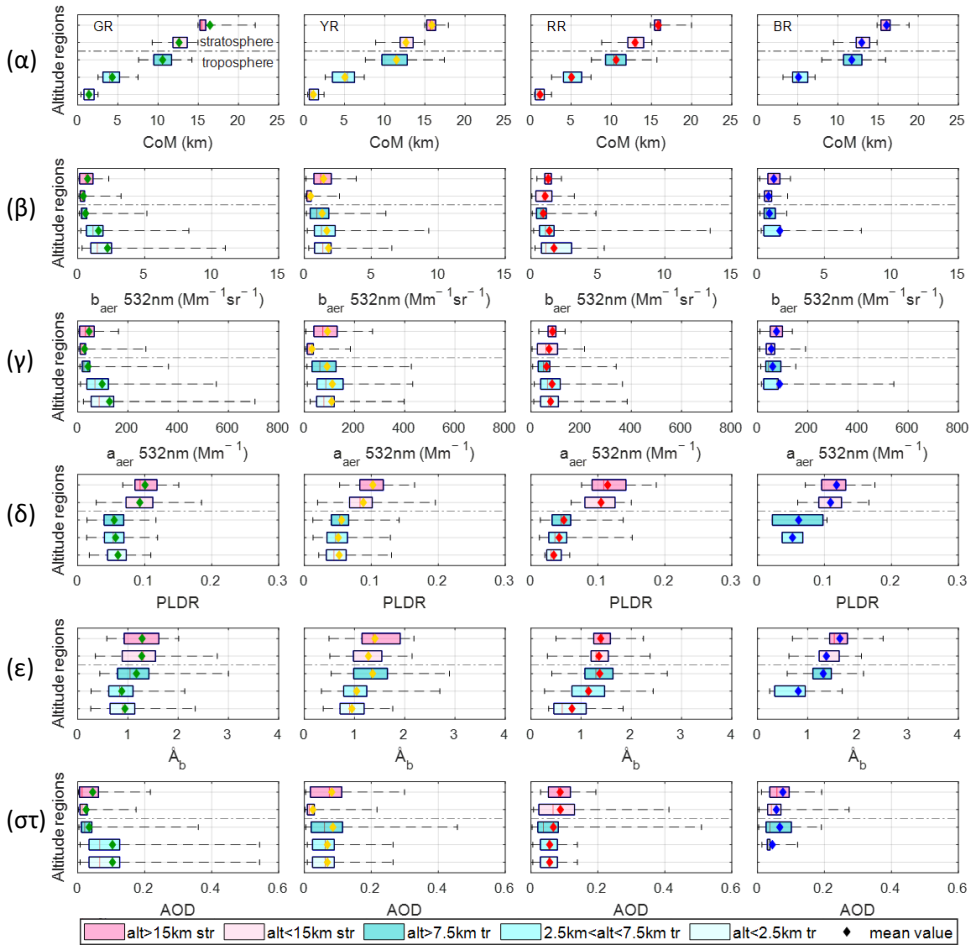

Εικόνα 5: (α) το CoM (amsl.), (β) το b_{aer}, (γ) το a_{aer}, (δ) το PLDR στα 532 nm, (ε) το $Å_b$ (532/1064 nm), (στ) το AOD στα 532 nm των στρωματώσεων καπνού που παρατηρήθηκαν. GR, YR, RR και BR (από αριστερά προς τα δεξιά) αντιστοιχούν στις τέσσερις υπό μελέτη περιοχές, ενώ τα διαφορετικά χρώματα υποδεικνύουν τις διαφορετικές κατηγορίες ύψους (Papanikolaou et al., 2022a).

Πιο συγκεκριμένα, όσον αφορά τα τροποσφαιρικά σωματίδια, η μέση τιμή του PLDR ήταν χαμηλότερη από 0.06, ενώ η μέγιστη τιμή τους δεν ξεπέρασε το 0.15, υποδηλώνοντας την παρουσία σχεδόν σφαιρικών σωματιδίων στα στρώματα καπνού. Στη στρατόσφαιρα, παρατηρήθηκαν τιμές PLDR έως και 0.20, τιμές ενδεικτικές για μη σφαιρικά σωματίδια. Οι στρατοσφαιρικές τιμές του PLDR πιθανώς οφείλονται στην επίστρωση πάγου που αποκτήθηκε στη στρατόσφαιρα, λόγω των πολύ χαμηλών θερμοκρασιών. Επιπρόσθετα, καθώς ο καπνός μετακινήθηκε προς τα δυτικά, παρατηρήθηκε μια ελαφρά μείωση στις τιμές PLDR της τροπόσφαιρας, σε αντίθεση με τις ενισχυμένες τιμές PLDR των αιωρούμενων σωματιδίων της στρατόσφαιρας.

Όσον αφορά τις τιμές του AOD, υψηλότερα σωματιδιακά φορτία καταγράφηκαν στην κατώτερη τροπόσφαιρα, σε σύγκριση με την ανώτερη τροπόσφαιρα και στρατόσφαιρα. Το AOD βρέθηκε ίσο με 0.54 πάνω από την ευρύτερη περιοχή των πυρκαγιών, ενώ οι τιμές AOD έφτασαν έως και 0.29 στη στρατόσφαιρα.

Κατά την ίδια χρονική περίοδο, η συγκεντρώσεις του CO αυξήθηκαν σε σύγκριση με την περίοδο αναφοράς (2004–2019), κυρίως στα επίπεδα πίεσης 700–950 hPa. Η υψηλότερη παρατηρούμενη αύξηση στη συγκέντρωση του CO ήταν 92% στα 950 hPa στην πρώτη περιοχή μελέτης, κοντά στις εστίες των πυρκαγιών. Ομοίως, το O_3 παρουσίασε αύξηση κατά 60–96%. Οι τιμές R^2 μεταξύ της σχετικής αλλαγής στις συγκεντρώσεις CO και O_3 έδειξαν ότι η επίδραση του εκπεμπόμενου CO στο σχηματισμό O_3 ήταν ως επί το πλείστων σημαντική κοντά στην πηγή των ενεργών εστιών, ενώ για τις υπόλοιπες περιοχές, η διακύμανση του CO δεν έπαιξε βασικό ρόλο στην παρατηρούμενη ενίσχυση του O_3.

Τέλος, όσον αφορά στην επίδραση των σωματιδίων καπνού στο ενεργειακό ισοζύγιο, τόσο τα τροποσφαιρικά (–12.83 έως –32.22 W/m^2) όσο και τα στρατοσφαιρικά (–7.36 έως –18.51 W/m^2) σωματίδια προκάλεσαν ψύξη, τόσο στην κορυφή της ατμόσφαιρας, όσο και στην επιφάνεια του εδάφους, ενώ φαίνεται τα πρώτα να έχουν μεγαλύτερο αντίκτυπο από τα δεύτερα, ιδίως στην επιφάνεια του εδάφους.

Η τελευταία μελέτη του κεφαλαίου, παρουσιάστηκε σε παγκόσμιο συνέδριο με τη μορφή έντυπης παρουσίασης και αφορά στην μεταφορά αιωρούμενων σωματιδίων μεγάλης εμβέλειας. Με βάση την ανάλυση των οπισθοτροχιών των αερίων μαζών οι οποίες κατέληξαν στην πόλη της Αθήνας, υποδεικνύεται ότι τα σωματίδια προήλθαν από την Καλιφόρνια, στην πολιτεία των Δυτικών ΗΠΑ. Πιο συγκεκριμένα, τη χρονική περίοδο 8 έως 27 Σεπτεμβρίου 2020 που οι αέριες μάζες φαίνεται να δημιουργήθηκαν, στην ευρύτερη περιοχή της Καλιφόρνια λάμβανε χώρα ένα ακραίο γεγονός δασικής πυρκαγιάς. Συμπερασματικά, σε συνδυασμό με τις ενεργές εστίες πυρκαγιών (MODIS) στην περιοχή και τις τροχιές του δορυφόρου CALIPSO, αποδείχθηκε ότι οι στρωματώσεις αιωρούμενων σωματιδίων που παρατηρήθηκαν πάνω από την Αθήνα στις 14 και 30 Σεπτεμβρίου και την 1 Οκτωβρίου 2020, προήλθαν από αυτές τις πυρκαγιές.

Οι νηματοειδείς στρωματώσεις των αιωρούμενων σωματιδίων στην ελεύθερη τροπόσφαιρα παρουσίασαν τιμές PLDR που κυμάνθηκαν από 0.04 ± 0.01 έως 0.22 ± 0.02. Οι τιμές του PLDR υποδεικνύουν την παρουσία σωματιδίων τόσο με ακανόνιστα σχήματα όσο και σφαιρικά, που πιθανώς οφείλονται στην παρουσία προσμείξεων των σωματιδίων καπνού με αυτά τις ερημικής σκόνης, όπως φαίνεται από τις υποκατηγορίες που δίνει ο δορυφόρος CALIPSO για την περιοχή μελέτης. Στην Εικόνα 6, παρουσιάζονται η χωροχρονική εξέλιξη του σήματος lidar στα 355 nm, όπως καταγράφθηκε από το σύστημα lidar DEPOLE πάνω από την Αθήνα, καθώς και η κατακόρυφη κατανομή των οπτικών ιδιοτήτων των αιωρούμενων

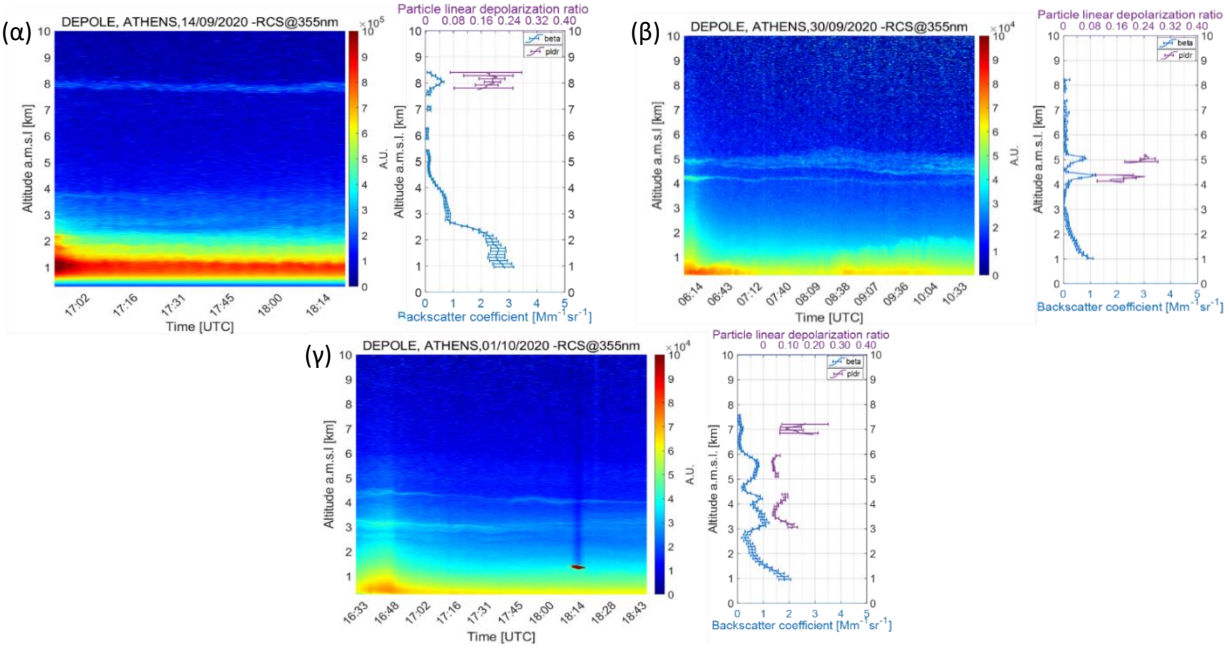

Εικόνα 6: (α) Αριστερό γράφημα: Η χωροχρονική εξέλιξη του σήματος lidar στα 355 nm; Δεξιό γράφημα: Η κατακόρυφη κατανομή των b_{aer} ($Mm^{-1}sr^{-1}$) (μπλε γραμμή) και PLDR στα 355 nm (μοβ γραμμή), όπως καταγράφθηκε από το σύστημα lidar DEPOLE στις 14 Σεπτεμβρίου 2020 (17:19 - 18:19 UTC), (β) στις 30 Σεπτεμβρίου 2020 (05:54 - 06:31 UTC) και (γ) την 01 Οκτωβρίου 2020 (17:09 - 17:08 UTC).πάνω από την Αθήνα, Ελλάδα,

σωματιδίων στις 14, 30 Σεπτεμβρίου και την 1 Οκτωβρίου 2020.

Στο Κεφάλαιο 4, παρουσιάζεται η μελέτη που αφορά στην αναγνώριση των ηφαιστειακών στρωμάτων στην στρατόσφαιρα του νότιου ημισφαιρίου, λόγω της ηφαιστειακής έκρηξης Hunga Tonga-Ha'apai, στις 15 Ιανουαρίου 2022. Μέρος των αποτελεσμάτων της μελέτης δημοσιεύθηκε σε παγκόσμιο συνέδριο, με τη μορφή έντυπης παρουσίασης. Τα στρατοσφαιρικά ηφαιστειακά αιωρούμενα σωματίδια παρατηρήθηκαν με τεχνικές ενεργητικής και παθητικής τηλεπισκόπησης, ενώ το μοντέλο μεταφοράς ακτινοβολίας libRadtran χρησιμοποιήθηκε προκειμένου να εκτιμηθεί η επίδραση των ηφαιστειακών σωματιδίων στο ενεργειακό ισοζύγιο (Εικόνα 7).

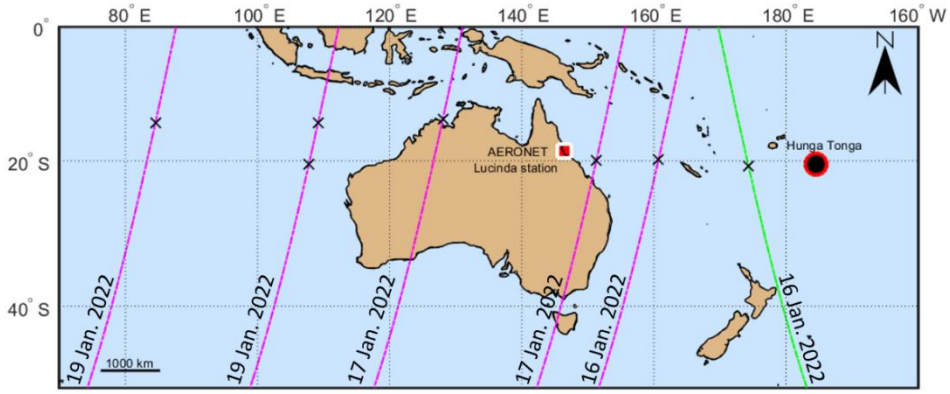

Εικόνα 7: Οι τροχιές του δορυφόρου CALIPSO (χρωματιστές γραμμές) παρέχονται για τις ημερομηνίες 17-19 Ιανουαρίου 2022, συνδυαστικά με την τοποθεσία του σταθμού AERONET Lucinda, στην βορειοδυτική Αυστραλία και θέση του ηφαιστείου Hunga Tonga-Ha'apai.

Με βάση την ανάλυση των γεωμετρικών και οπτικών ιδιοτήτων των ηφαιστειακών στρωματώσεων στην στρατόσφαιρα παρατηρήθηκε ότι το ύψος τους κυμάνθηκε από 23.05 έως 28.67 km και το οπτικό τους πάχος υπολογίσθηκε μεταξύ 1.08 και 2.69 km. Επιπλέον, οι τιμές $Å_b$ (0.79 - 1.94) έδειξαν ότι κατά την υπό μελέτη περίοδο τα αιωρούμενα σωματίδια που παρατηρήθηκαν στην ατμόσφαιρα ήταν μικρού μεγέθους και κυρίως σφαιρικά (PLDR: 0.01 - 0.06).

Επιπλέον, οι μετρήσεις ολικής στήλης AOD, όπως μετρήθηκαν από τον σταθμό AERONET Lucinda στις 17 Ιανουαρίου 2022, έδειξαν μέγιστη τιμή AOD 1.99, σε συνδυασμό με τιμές του εκθέτη Ångström κοντά στο 1.5, δείχνοντας ότι αυτό το τεράστιο σωματιδιακό φορτίο στην ατμόσφαιρα απαρτιζόταν κυρίως από μικρά σωματίδια. Τέλος, η επίδραση των ηφαιστειακών αιωρούμενων σωματιδίων στο ισοζύγιο ακτινοβολίας φαίνεται να είναι μεγαλύτερη σε

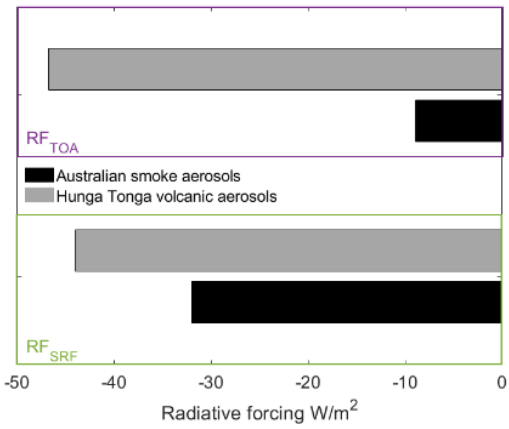

Εικόνα 8: Επίδραση αερολυμάτων στο ισοζύγιο ακτινοβολίας, με γκρι απεικονίζεται η επίδραση των σωματιδίων από την έκρηξη Hunga Tonga, ενώ με μαύρο η επίδραση των σωματιδίων καπνού που παράχθηκαν κατά τη διάρκεια των πυρκαγιών στην Αυστραλία (2019 - 2020), στην κορυφή της ατμόσφαιρας (TOA) και στην επιφάνεια του εδάφους (SRF).

σύγκριση με τα αιωρούμενα σωματίδια καπνού που μελετήθηκαν κατά τη διάρκεια των πυρκαγιών στην Αυστραλία (2019- 2020), όπως φαίνεται στην Εικόνα 8.

Τα αποτελέσματα της τελευταίας μελέτης, στο Κεφαλαίου 5, δημοσιεύθηκαν σε παγκόσμιο συνέδριο, με τη μορφή έντυπης παρουσίασης. Στην μελέτη αυτή παρουσιάζεται και αναλύεται ένα ακραίο (σε όρους φορτίου αερολύματος) επεισόδιο ερημικής σκόνης από την έρημο Σαχάρα πάνω από την Ελλάδα, όπως αυτό μετρήθηκε στην Αθήνα, στις 16 - 17 Μαρτίου 2022. Οι μετεωρολογικές συνθήκες που επικρατούσαν στη Μεσόγειο, κατά την χρονική περίοδο της μελέτης, επέτρεψαν στις αέριες μάζες να εισέλθουν στην Ευρωπαϊκή ήπειρο και οδήγησαν στον σχηματισμό πολύ μεγάλου σωματιδιακού φορτίου στην ατμόσφαιρα της πόλης (Εικόνα 9).

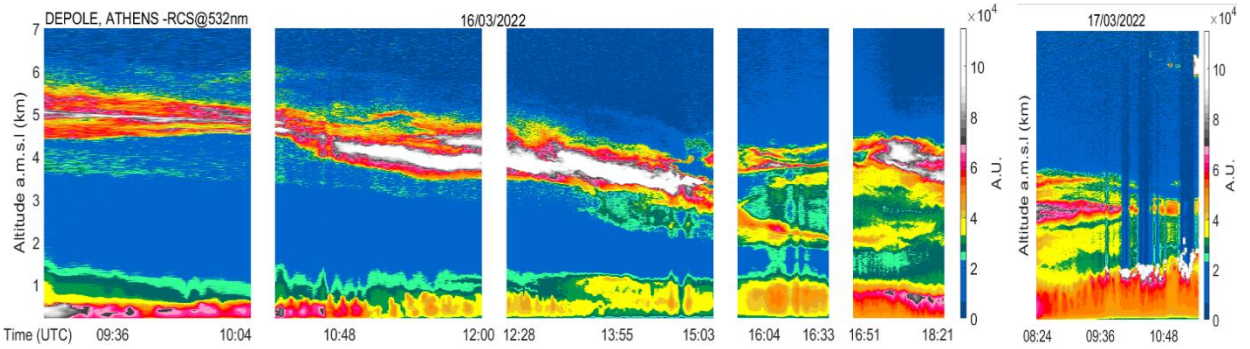

Εικόνα 9: Χωρο-χρονική εξέλιξη του διορθωμένου εύρους σήματος lidar στα 532 nm, όπως παρατηρήθηκε από το DEPOLE lidar πάνω από την Αθήνα κατά τις 16-17 Μαρτίου 2022.

Πιο συγκεκριμένα, στις 16 Μαρτίου 2022 οι τιμές b_{aer} υπέδειξαν μία εξαιρετικά πυκνή στρωμάτωση μεταξύ 1.98 και 6.36 km, πάνω από τον σταθμό της Αθήνας. Όσον αφορά τις τιμές PLDR εντός του στρώματος, αυτές βρέθηκαν μεταξύ 0.29 ± 0.02 έως 0.36 ± 0.05 (532 nm) και από 0.31 ± 0.04 έως 0.40 ± 0.10 (355 nm), τιμές αντιπροσωπευτικές σωματιδίων ερημικής σκόνης χωρίς προσμίξεις. Το LR μέσα στα στρώματα ήταν ίσο με 53.22 ± 38.76 sr στα 532 nm και 44.82 ± 20.70 sr στα 355 nm δίνοντας ακόμη μία ένδειξη ότι τα σωματίδια δεν υπέστησαν προσμίξεις κατά τη διάρκεια της μεταφορά τους (Veselovskii et al., 2016). Οι συντελεστές $Å_{a,355/532}$ και $Å_{b,355/532}$ κατά τη νυχτερινή μέτρηση δείχνουν μικρές τιμές στο εσωτερικό του στρώματος σκόνης (0.16 ± 0.25 και 0.36 ± 0.19), που υποδηλώνουν ξεκάθαρα την κυριαρχία των μεγάλου μεγέθους σωματιδίων στην ατμόσφαιρα πάνω από τον σταθμό lidar της Αθήνας. Επιπρόσθετα, η επίδραση του επεισοδίου στο ενεργειακό ισοζύγιο ακτινοβολίας για τις 16 Μαρτίου του 2022 βρέθηκε ίση με –70.11 W/m^2 στην TOA και –168.41 W/m^2 στην SRF, υποδεικνύοντας πως η ύπαρξη αυτού του μεγάλου φορτίου σκόνης στην ατμόσφαιρα έχει ως αποτέλεσμα λιγότερη ηλιακή ακτινοβολία να φτάνει στην SRF.

Συμπερασματικά, σε αυτήν τη διδακτορική διατριβή μελετήθηκε, παρουσιάσθηκε και αναλύθηκε μια ποικιλία ακραίων επεισοδίων σωματιδιακής ρύπανσης. Μία από τις υπό μελέτη περιπτώσεις αφορά στην τοπική παραγωγή σωματιδίων BB εντός του PBL και της LFT, πάνω από την πόλη των Ιωαννίνων, στην Ελλάδα, ενώ οι περισσότερες από τις μελέτες, τέσσερις συνολικά, αφορούν στη μεταφορά σωματιδίων καπνού, σε μεγάλη κλίμακα. Ιδιαίτερα ενδιαφέρουσα ήταν

η μελέτη μιας από τις ισχυρότερες ηφαιστειακές εκρήξεις που έχουν καταγραφεί, ενώ μελετήθηκε και ένα από τα πιο έντονα επεισόδια εισροής αφρικανικής σκόνης, που έχει καταγραφεί τα τελευταία χρόνια, και επηρέασε την Ευρώπη τον Μάρτιο του 2022. Οι γεωμετρικές και οπτικές ιδιότητες των αιωρούμενων σωματιδίων μελετήθηκαν εντός του PBL, της τροπόσφαιρας και της στρατόσφαιρας, ενώ υπολογίστηκε και η επίδραση της ακτινοβολίας, όποτε αυτό ήταν εφικτό.

Η μελέτη των εξαιρετικά φρέσκων σωματιδίων BB στην πόλη των Ιωαννίνων, ανέδειξε πολύ μεγάλες τιμές του b_{aer} εντός του PBL, και κατ' επέκταση μεγάλες συγκεντρώσεις σωματιδίων τα οποία βρέθηκαν εγκλωβισμένα μέσα στο PBL. Τα σωματίδια παρουσίασαν εξαιρετικά χαμηλές τιμές PLDR, υποδεικνύοντας ότι το σχήμα τους ήταν σχεδόν σφαιρικό. Τα συμπληρωματικά δεδομένα στην επιφάνεια του εδάφους ($PM_{2.5}$, BC) υπέδειξαν ότι οι εκπομπές BC, σε αυτή τη μεσαίου μεγέθους πόλη, ήταν της ίδιας τάξης και σε ορισμένες περιπτώσεις ακόμη μεγαλύτερη, με τις εκπομπές BC στις μεγαλύτερες ευρωπαϊκές πόλεις.

Στην ελεύθερη τροπόσφαιρα, τα σωματίδια BB που μετρήθηκαν στα Ιωάννινα παρουσιάζουν ομοιότητες, όσον αφορά τις οπτικές τους τις ιδιότητες, με τα σωματίδια BB, που μετρήθηκαν από τον δορυφόρο CALIPSO, κοντά στις πηγές των πυρκαγιών, τόσο στον Καναδά, όσο και στην Αυστραλία. Και στις τρεις μελέτες, τα σωματίδια ήταν σχεδόν σφαιρικά (PLDR <0.06), ωστόσο οι τιμές του PLDR ήταν μεγαλύτερες αυτών που παρατηρήθηκαν μέσα στο PBL. Σύμφωνα με τις τιμές $Å_b$ (0.94 - 1.17), τα σωματίδια φρέσκου καπνού στην τροπόσφαιρα βρέθηκαν να είναι σχετικά μικρού μεγέθους. Όσον αφορά τα επεισόδια μεγάλης εμβέλειας, εκτός από φρέσκα σωματίδια καπνού, παρατηρήθηκαν σε αυτά και γηρασμένα σωματίδια (3-10 ημέρες μεταφοράς από την πηγή). Τόσο τα σωματίδια BB από τις πυρκαγιές στον Καναδά όσο και αυτά από την Αυστραλία, παρέμειναν σχεδόν σφαιρικά καθ' όλη τη διάρκεια της μεταφοράς τους, με μικρές διακυμάνσεις στις τιμές του PLDR. Ο $Å_b$ βρέθηκε μεταξύ 0.99 ± 0.95 και 1.02 ± 0.72 για τα τροποσφαιρικά σωματίδια από Καναδά, ενώ τα αυστραλιανά σωματίδια BB παρουσίασαν ένα μεγαλύτερο εύρος τιμών, καθώς κυμάνθηκαν από 0.81 ± 0.39 (περιοχή πιο μακριά από την πηγή) έως και 1.37 ± 0.46 (πιο κοντά στην περιοχή πηγής).

Στην τελευταία μελέτη, τα γηρασμένα τροποσφαιρικά σωματίδια καπνού, φαίνεται να αυξάνονται σε μέγεθος καθώς απομακρύνονται από την πηγή. Τα σωματίδια από τις πυρκαγιές στην Καλιφόρνια, τα οποία παρατηρήθηκαν πάνω από την Αθήνα, έδειξαν ακόμη μεγάλο εύρος τιμών PLDR (0.04 έως 0.22), που θα μπορούσε να αιτιολογηθεί από το γεγονός ότι κατά τη διαδρομή τους τα αιωρούμενα σωματίδια πιθανόν να εμπλουτίστηκαν με μεγαλύτερα και ακανόνιστου σχήματος σωματίδια, όπως αυτά της ερημικής σκόνης, καταλήγοντας έτσι στην αύξηση των PLDR τιμών τους. Τέλος, όσον αφορά το επεισόδιο σκόνης από την έρημο Σαχάρα, το οποίο παρατηρήθηκε επίσης στην FT, οι οπτικές ιδιότητες (b_{aer}, a_{er}, AOD) αποκάλυψαν ένα εξαιρετικά παχύ στρώμα σωματιδίων, με τιμές PLDR μεγαλύτερες από 0.29, τιμές αντιπροσωπευτικές σωματιδίων ερημικής σκόνης χωρίς προσμίξεις, ενώ οι τιμές Å (0.16 ± 0.25 και 0.36 ± 0.19) υποδεικνύουν σαφέστατα την κυριαρχία των χονδρόκοκκων σωματιδίων.

Όσον αφορά τις οπτικές ιδιότητες των στρατοσφαιρικών σωματιδίων, κατά τη διάρκεια των πυρκαγιών στην Αυστραλία, οι μέσες τιμές PLDR των σωματιδίων καπνού στη στρατόσφαιρα βρέθηκαν να είναι 0.11 ± 0.03, ενώ οι μέγιστες παρατηρούμενες τιμές κυμανθηκαν από 0.15 έως 0.20. Οι υψηλότερες στρατοσφαιρικές τιμές PLDR (συγκριτικά με τις τροποσφαιρικές τιμές) υποδηλώνουν σωματίδια ακανόνιστου σχήματος, που πιθανώς αποκτήθηκε λόγω των ψυχρότερων θερμοκρασιών στην στρατόσφαιρα. Οι αντίστοιχες τιμές των ηφαιστειακών αιωρούμενων σωματιδίων βρέθηκαν να κυμαίνονται μεταξύ 0.01 και 0.06, υποδηλώνοντας την ύπαρξη θειικών σωματιδίων στην στρατσόδφαιρα. Οι τιμές $Å_b$, όσον αφορά τα σωματίδια καπνού παρουσίασαν μια μικρή αύξηση, υποδεικνύοντας ότι τα σωματίδια καπνού στην στρατόσφαιρα γίνονται μικρότερα σε μέγεθος, καθώς απομακρύνονται από την πηγή, ενώ οι μέγιστες τιμές $Å_b$ που καταγράφηκαν (2.00 - 2.50) επιβεβαιώνουν την ύπαρξη πολύ μικρών σωματιδίων. Από την άλλη, οι τιμές $Å_b$ των ηφαιστειακών σωματιδίων βρέθηκαν από 0.79 έως 1.94, υποδηλώνοντας την ύπαρξη κυρίως μικρών σωματιδίων, και σε ορισμένες περιπτώσεις λίγο μεγαλύτερων. Οι μέγιστες καταγεγραμμένες τιμές AOD των δύο συμβάντων ήταν 0.40 για τον στρατοσφαιρικό καπνό και 1.40 για τα ηφαιστειακά αιωρούμενα σωματίδια.

Τέλος, η επίδραση στην ακτινοβολία για τους τρείς αυτούς διαφορετικούς τύπους σωματιδίων (σωματίδια BB, ηφαιστειακά αιωρούμενα σωματίδια και σκόνη από τη Σαχάρα), που μελετήθηκαν κατά τη διάρκεια τεσσάρων επεισοδίων σωματιδιακής ρύπανσης, έδειξε ότι στην SRF και στην TOA, το εκτιμώμενο RF_{NET} των ηφαιστειακών αιωρούμενων σωματιδίων ήταν –43.97 W/m^2 και –46.76 W/m^2, αντίστοιχα. Όσον αφορά τα σωματίδια BB από τις αυστραλιανές πυρκαγιές, οι αντίστοιχες τιμές ήταν –31.98 W/m^2 και –8.94 W/m^2. Το RF_{NET} όπως υπολογίστηκε για τα ηφαιστειακά αιωρούμενα σωματίδια ήταν μεγαλύτερο από αυτό των σωματιδίων καπνού, πιθανόν λόγω της υψηλής ανακλαστικότητας των ηφαιστειακών αιωρούμενων σωματιδίων, που μείωσαν αισθητά την ποσότητα της ηλιακής ακτινοβολίας που φθάνει στο έδαφος, και έτσι προκάλεσαν ψύξη στο έδαφος. Επίσης, καθώς τα σωματίδια μετά την ηφαιστειακή έκρηξη βρέθηκαν σε πολύ μεγαλύτερο ύψος στη στρατόσφαιρα από ό,τι τα σωματίδια BB, τα πρώτα προκάλεσαν μεγαλύτερη ψύξη και στην TOA.

Επιπλέον, το RF_{NET} των τροποσφαιρικών σωματιδίων BB, που παράχθηκαν από τις πυρκαγιές της Αυστραλίας, ήταν ίσο με –87.10 έως –4.53 W/m^2 (μέση τιμή –32.22 ± 25.84 W/m^2) στην SRF κυμαινόταν από –47.42 έως +11.5 W/m^2 μέση τιμή –12.83 ± 14.74 W/m^2) στην TOA, για τιμές του SZA μεταξύ 24.65° και 46.86°. Όσον αφορά τα γηρασμένα σωματίδια από τις πυρκαγιές στην Καλιφόρνια, παρουσίασαν ένα RF_{NET} τόσο στη SRF όσο και στην TOA, ίσο με –4.71 W/m^2 και –1.33 W/m^2, αντίστοιχα υποδηλώνοντας μια ελαφρά ψύξη τόσο και στα δύο ύψη. Τέλος, όσον αφορά το ανιχνεύθηκε πάνω από την Αθήνα είχε εκτιμώμενο RFNET –168.41 W/m^2 στην SRF και –70.11 W/m^2 στην TOA, και τα δύο υποδεικνύουν ψύξη, δείχνοντας ότι λιγότερη ηλιακή ακτινοβολία φτάνει στην SRF, ως αποτέλεσμα της ύπαρξης ερημικής σκόνης στην ατμόσφαιρα.

BIBLIOGRAPHY

Abril-gago, J., Ortiz-amezcua, P., Bermejo-pantaleón, D., Andújar-maqueda, J., Bravo-aranda, J. A., Granados-muñoz, M. J., Navas-guzmán, F., Foyo-moreno, I., and Guerrero-rascado, J. L.: Validation Activities of Aeolus Wind Products in the Southeastern Iberian Peninsula, 1–32, 2022.

Adam, D.: Tonga volcano created puzzling atmospheric ripples, Nature, 602, 497–498, 2022.

Adebiyi, A. A. and Kok, J. F.: Climate models miss most of the coarse dust in the atmosphere, Sci. Adv., 6, 1–10, https://doi.org/10.1126/sciadv.aaz9507, 2020.

Akagi, S. K., Yokelson, R. J., Burling, I. R., Meinardi, S., Simpson, I., Blake, D. R., McMeeking, G. R., Sullivan, A., Lee, T., Kreidenweis, S., Urbanski, S., Reardon, J., Griffith, D. W. T., Johnson, T. J., and Weise, D. R.: Measurements of reactive trace gases and variable O3 formation rates in some South Carolina biomass burning plumes, Atmos. Chem. Phys., 13, 1141–1165, https://doi.org/10.5194/acp-13-1141-2013, 2013.

Alados-Arboledas, L., Müller, D., Guerrero-Rascado, J. L., Navas-Guzmán, F., Pérez-Ramírez, D., and Olmo, F. J.: Optical and microphysical properties of fresh biomass burning aerosol retrieved by Raman lidar, and star-and sun-photometry, Geophys. Res. Lett., 38, 1–5, https://doi.org/10.1029/2010GL045999, 2011.

Albani, S., Mahowald, N. M., Winckler, G., Anderson, R. F., Bradtmiller, L. I., Delmonte, B., François, R., Goman, M., Heavens, N. G., Hesse, P. P., Hovan, S. A., Kohfeld, K. E., Lu, H., Maggi, V., Mason, J. A., Mayewski, P. A., McGee, D., Miao, X., Otto-Bliesner, B. L., Perry, A. T., Pourmand, A., Roberts, H. M., Rosenbloom, N., Stevens, T., and Sun, J.: Twelve thousand years of dust: the Holocene global dust cycle constrained by natural archives, Clim. Past Discuss., 10, 4277–4363, https://doi.org/10.5194/cpd-10-4277-2014, 2014.

Allaerts, D.: Large-eddy Simulation of Wind Farms in Conventionally Neutral and Stable Atmospheric Boundary Layers, 2016.

Allen, R. J., Amiri-Farahani, A., Lamarque, J. F., Smith, C., Shindell, D., Hassan, T., and Chung, C. E.: Observationally constrained aerosol–cloud semi-direct effects, npj Clim. Atmos. Sci., 2, 1–12, https://doi.org/10.1038/s41612-019-0073-9, 2019.

Amiridis, V., Balis, D., Giannakaki, E., Stohl, A., Kazadzis, S., Koukouli, M., and Zanis, P.: Optical characteristics of biomass burning aerosols over Southeastern Europe determined from UV-Raman lidar measurements, Atmos. Chem. Phys. Discuss., 9, https://doi.org/10.5194/acp-9-2431-2009, 2008.

Amiridis, V., Giannakaki, E., Balis, D. S., Gerasopoulos, E., Pytharoulis, I., Zanis, P., Kazadzis, S., Melas, D., Zerefos, C., and Sensing, R.: and Physics Smoke injection heights from agricultural burning in Eastern Europe as seen by CALIPSO, 11567–11576, https://doi.org/10.5194/acp-10-11567-2010, 2010.

Ancellet, G., Pelon, J., Totems, J., Chazette, P., Bazureau, A., Sicard, M., Di Iorio, T., Dulac, F., and Mallet, M.: Long-range transport and mixing of aerosol sources during the 2013 North American biomass burning episode: Analysis of multiple lidar observations in the western Mediterranean basin, Atmos. Chem. Phys., 16, 4725–4742, https://doi.org/10.5194/acp-16-4725-2016, 2016.

Anderson, G., Clough, S., and Kneizys, F.: AFGL atmospheric constituent profiles, Tech. Rep. AFGL-TR-86- 0110, 46, 1986.

Ansmann, A., Riebesell, M., Wandinger, U., Weitkamp, C., Voss, E., Lahmann, W., and Michaelis, W.: Combined raman elastic-backscatter LIDAR for vertical profiling of moisture, aerosol extinction, backscatter, and LIDAR ratio, Appl. Phys. B Photophysics Laser Chem., 55, 18–28, https://doi.org/10.1007/BF00348608, 1992.

Ansmann, A., Bösenberg, J., Chiakovsky, A., Comerón, A., Eckhardt, S., Eixmann, R., Freudenthaler, V., Ginoux, P., Komguem, L., Linné, H., Lopez Marquez, M. Á., Matthias, V., Mattis, I., Mitev, V., Müller, D., Music, S., Nickovic, S., Pelon, J., Sauvage, L., Sobolewsky, P., Srivastava, M. K., Stohl, A., Torres, O., Vaughan, G., Wandinger, U., and Wiegner, M.: Long-range transport of Saharan dust to northern Europe: The 11-16 October 2001 outbreak observed with EARLINET, J. Geophys. Res. D Atmos., 108, 1–15, https://doi.org/10.1029/2003JD003757, 2003.

Ansmann, A., Petzold, A., Kandler, K., Tegen, I., Wendisch, M., Müller, D., Weinzierl, B., Müller, T., and Heintzenberg, J.: Saharan Mineral Dust Experiments SAMUM-1 and SAMUM-2: What have we learned?, Tellus, Ser. B Chem. Phys. Meteorol., 63, 403–429, https://doi.org/10.1111/j.1600-0889.2011.00555.x, 2011.

Ansmann, A., Ohneiser, K., Mamouri, R., Knopf, D. A., Veselovskii, I., Baars, H., Engelmann, R., Foth, A., Jimenez, C., Seifert, P., and Barja, B.: Tropospheric and stratospheric wildfire smoke profiling with lidar : Mass , surface area , CCN and INP retrieval, 1–45, 2020.

Ansmann, A., Ohneiser, K., Chudnovsky, A., Baars, H., and Engelmann, R.: CALIPSO Aerosol-Typing Scheme Misclassified Stratospheric Fire Smoke: Case Study From the 2019 Siberian Wildfire Season, Front. Environ. Sci., 9, 1–14, https://doi.org/10.3389/fenvs.2021.769852, 2021a.

Ansmann, A., Ohneiser, K., Mamouri, R. E., Knopf, D. A., Veselovskii, I., Baars, H., Engelmann, R., Foth, A., Jimenez, C., Seifert, P., and Barja, B.: Tropospheric and stratospheric wildfire smoke profiling with lidar: Mass, surface area, CCN, and INP retrieval, Atmos. Chem. Phys., 21, 9779–9807, https://doi.org/10.5194/acp-21-9779-2021, 2021b.

Aubry, T. J., Staunton-Sykes, J., Marshall, L. R., Haywood, J., Abraham, N. L., and Schmidt, A.: Climate change modulates the stratospheric volcanic sulfate aerosol lifecycle and radiative forcing from tropical eruptions, Nat. Commun., 12, https://doi.org/10.1038/s41467-021-24943-7, 2021.

Baars, H., Ansmann, A., Ohneiser, K., Haarig, M., Engelmann, R., Althausen, D., Hanssen, I., Gausa, M., Pietruczuk, A., Szkop, A., Stachlewska, I. S., Wang, D., Reichardt, J., Skupin, A., Mattis, I., Trickl, T., Vogelmann, H., and Navas-guzmán, F.: The unprecedented 2017 – 2018 stratospheric smoke event : decay phase and aerosol properties observed with the EARLINET, 15183–15198, 2019.

Balis, D. S., Amiridis, V., Zerefos, C., Gerasopoulos, E., Andreae, M., Zanis, P., Kazantzidis, A., Kazadzis, S., and Papayannis, A.: Raman lidar and sunphotometric measurements of aerosol optical properties over Thessaloniki, Greece during a biomass burning episode, https://doi.org/10.1016/S1352-2310(03)00581-8, 2003.

Baumgardner, D., Newton, R., Krämer, M., Meyer, J., Beyer, A., Wendisch, M., and Vochezer, P.: The Cloud Particle Spectrometer with Polarization Detection (CPSPD): A next generation open-

path cloud probe for distinguishing liquid cloud droplets from ice crystals, Atmos. Res., 142, 2–14, https://doi.org/10.1016/j.atmosres.2013.12.010, 2014.

Baylon, P., Jaffe, D. A., Wigder, N. L., Gao, H., and Hee, J.: Ozone enhancement in western US wildfire plumes at the Mt. Bachelor Observatory: The role of NOx, Atmos. Environ., 109, 297–304, https://doi.org/10.1016/j.atmosenv.2014.09.013, 2015.

Becerril-valle, M., Coz, E., Pr, A. S. H., and S, A. M.: Characterization of atmospheric black carbon and co-pollutants in urban and rural areas of Spain v o, 169, 36–53, https://doi.org/10.1016/j.atmosenv.2017.09.014, 2017.

Behrendt, A. and Nakamura, T.: Calculation of the calibration constant of polarization lidar and its dependency on atmospheric temperature, Opt. Express, 10, 805, https://doi.org/10.1364/oe.10.000805, 2002.

Belegante, L., Antonio Bravo-Aranda, J., Freudenthaler, V., Nicolae, D., Nemuc, A., Ene, D., Alados-Arboledas, L., Amodeo, A., Pappalardo, G., D'Amico, G., Amato, F., Engelmann, R., Baars, H., Wandinger, U., Papayannis, A., Kokkalis, P., and Pereira, S. N.: Experimental techniques for the calibration of lidar depolarization channels in EARLINET, Atmos. Meas. Tech., 11, 1119–1141, https://doi.org/10.5194/amt-11-1119-2018, 2018.

Berrick, S., Leptoukh, G., Farley, J., and Rui, H.: Giovanni: A Web Service Workflow-Based Data Visualization and Analysis System, Geosci. Remote Sensing, IEEE Trans., 47, 106–113, https://doi.org/10.1109/TGRS.2008.2003183, 2009.

Borrego, C., Valente, J., Carvalho, A., Sá, E., Lopes, M., and Miranda, A. I.: Contribution of residential wood combustion to PM10 levels in Portugal, Atmos. Environ., 44, 642–651, https://doi.org/https://doi.org/10.1016/j.atmosenv.2009.11.020, 2010.

Boselli, A., Scollo, S., Leto, G., Sanchez, R. Z., Sannino, A., Wang, X., Coltelli, M., and Spinelli, N.: First Volcanic Plume Measurements by an Elastic/Raman Lidar Close to the Etna Summit Craters, Front. Earth Sci., 6, 1–12, https://doi.org/10.3389/feart.2018.00125, 2018.

Bougiatioti, A., Bezantakos, S., Stavroulas, I., Kalivitis, N., Kokkalis, P., Biskos, G., Mihalopoulos, N., Papayannis, A., and Nenes, A.: Biomass-burning impact on CCN number, hygroscopicity and cloud formation during summertime in the eastern Mediterranean, Atmos. Chem. Phys., 16, 7389–7409, https://doi.org/10.5194/acp-16-7389-2016, 2016.

Bourgeois, I., Peischl, J., Andrew Neuman, J., Brown, S. S., Thompson, C. R., Aikin, K. C., Allen, H. M., Angot, H., Apel, E. C., Baublitz, C. B., Brewer, J. F., Campuzano-Jost, P., Commane, R., Crounse, J. D., Daube, B. C., DiGangi, J. P., Diskin, G. S., Emmons, L. K., Fiore, A. M., Gkatzelis, G. I., Hills, A., Hornbrook, R. S., Gregory Huey, L., Jimenez, J. L., Kim, M., Lacey, F., McKain, K., Murray, L. T., Nault, B. A., Parrish, D. D., Ray, E., Sweeney, C., Tanner, D., Wofsy, S. C., and Ryerson, T. B.: Large contribution of biomass burning emissions to ozone throughout the global remote troposphere, Proc. Natl. Acad. Sci. U. S. A., 118, 1–10, https://doi.org/10.1073/pnas.2109628118, 2021.

Brey, S. J. and Fischer, E. V.: Smoke in the City: How Often and Where Does Smoke Impact Summertime Ozone in the United States?, Environ. Sci. Technol., 50, 1288–1294, https://doi.org/10.1021/acs.est.5b05218, 2016.

Bui, V. K. H., Moon, J. Y., Chae, M., Park, D., and Lee, Y. C.: Prediction of aerosol deposition in the human respiratory tract via computational models: A review with recent updates, Atmosphere (Basel)., 11, https://doi.org/10.3390/atmos11020137, 2020.

Burton, S. P., Ferrare, R. A., Hostetler, C. A., Hair, J. W., Rogers, R. R., Obland, M. D., Butler, C. F., Cook, A. L., Harper, D. B., and Froyd, K. D.: Aerosol classification using airborne High Spectral Resolution Lidar measurements-methodology and examples, Atmos. Meas. Tech., 5, 73–98, https://doi.org/10.5194/amt-5-73-2012, 2012.

Burton, S. P., Ferrare, R. A., Vaughan, M. A., Omar, A. H., Rogers, R. R., Hostetler, C. A., and Hair, J. W.: Aerosol classification from airborne HSRL and comparisons with the CALIPSO vertical feature mask, Atmos. Meas. Tech., 6, 1397–1412, https://doi.org/10.5194/amt-6-1397-2013, 2013.

Burton, S. P., Vaughan, M. A., Ferrare, R. A., and Hostetler, C. A.: Separating mixtures of aerosol types in airborne High Spectral Resolution Lidar data, Atmos. Meas. Tech., 7, 419–436, https://doi.org/10.5194/amt-7-419-2014, 2014.

Burton, S. P., Hair, J. W., Kahnert, M., Ferrare, R. A., Hostetler, C. A., Cook, A. L., Harper, D. B., and Berkoff, T. A.: Observations of the spectral dependence of linear particle depolarization ratio of aerosols using NASA Langley airborne High, 13453–13473, https://doi.org/10.5194/acp-15-13453-2015, 2015.

Campetella, C. M. and Vera, C. S.: The influence of the Andes mountains on the South American low-level flow, Geophys. Res. Lett., 29, 6–9, https://doi.org/10.1029/2002GL015451, 2002.

Chalvatzaki, E., Chatoutsidou, S. E., Mammi-Galani, E., Almeida, S. M., Gini, M. I., Eleftheriadis, K., Diapouli, E., and Lazaridis, M.: Estimation of the personal deposited dose of particulate matter and particle-bound metals using data from selected European cities, Atmosphere (Basel)., 9, 18–20, https://doi.org/10.3390/atmos9070248, 2018.

Chang, D. Y., Yoon, J., Lelieveld, J., Park, S. K., Yum, S. S., Kim, J., and Jeong, S.: Direct radiative forcing of biomass burning aerosols from the extensive Australian wildfires in 2019-2020, Environ. Res. Lett., 16, https://doi.org/10.1088/1748-9326/abecfe, 2021.

Chen, J., Li, Z., Lv, M., Wang, Y., Wang, W., Zhang, Y., Wang, H., Yan, X., Sun, Y., and Cribb, M.: Aerosol hygroscopic growth, contributing factors and impact on haze events in a severely polluted region in northern China, Atmos. Chem. Phys. Discuss., 1–42, https://doi.org/10.5194/acp-2018-753, 2018.

Colbeck, I. and Lazaridis, M.: Aerosol Science: Technology and Applications, https://doi.org/10.1002/9781118682555.ch1, 2014.

Costabile, F., Alas, H., Aufderheide, M., Avino, P., Amato, F., Argentini, S., Id, F. B., Berico, M., Bernardoni, V., Biondi, R., Calzolai, G., Canepari, S., Casasanta, G., Ciampichetti, S., Conidi, A., Cordelli, E., Ianni, A. Di, Liberto, L. Di, Facchini, M. C., Facci, A., Id, D. F., Gilardoni, S., Grollino, M. G., Id, M. G., Lucarelli, F., Malaguti, A., Manigrasso, M., Montagnoli, M., Nava, S., Padoan, E., Perrino, C., Petralia, E., Petenko, I., Querol, X., Simonetti, G., Tranfo, G., Ubertini, S., Valli, G., Valentini, S., Vecchi, R., Volpi, F., Weinhold, K., Wiedensohler, A., Zanini, G., and Gobbi, G. P.: First Results of the " Carbonaceous Aerosol in Rome and Environs (CARE)" Experiment : Beyond

Current Standards for PM 10, https://doi.org/10.3390/atmos8120249, 2017.

Cuevas, E., Romero-Campos, P. M., Kouremeti, N., Kazadzis, S., Räisänen, P., García, R. D., Barreto, A., Guirado-Fuentes, C., Ramos, R., Toledano, C., Almansa, F., and Gröbner, J.: Aerosol optical depth comparison between GAW-PFR and AERONET-Cimel radiometers from long-term (2005-2015) 1 min synchronous measurements, Atmos. Meas. Tech., 12, 4309–4337, https://doi.org/10.5194/amt-12-4309-2019, 2019.

D'Amico, G., Amodeo, A., Baars, H., Binietoglou, I., Freudenthaler, V., Mattis, I., Wandinger, U., and Pappalardo, G.: EARLINET Single Calculus Chain-overview on methodology and strategy, Atmos. Meas. Tech., 8, 4891–4916, https://doi.org/10.5194/amt-8-4891-2015, 2015.

D'Amico, G., Amodeo, A., Mattis, I., Freudenthaler, V., and Pappalardo, G.: EARLINET Single Calculus Chain-technical andndash; Part 1: Pre-processing of raw lidar data, Atmos. Meas. Tech., 9, 491–507, https://doi.org/10.5194/amt-9-491-2016, 2016.

D 'amico, G., Amodeo, A., Baars, H., Binietoglou, I., Freudenthaler, V., Mattis, I., Wandinger, U., and Pappalardo, G.: EARLINET Single Calculus Chain – overview on methodology and strategy, Atmos. Meas. Tech, 8, 4891–4916, https://doi.org/10.5194/amt-8-4891-2015, 2015.

Diapouli, E., Kalogridis, A. C., Markantonaki, C., Vratolis, S., Fetfatzis, P., Colombi, C., and Eleftheriadis, K.: Annual variability of black carbon concentrations originating from biomass and fossil fuel combustion for the suburban aerosol in Athens, Greece, Atmosphere (Basel)., 8, https://doi.org/10.3390/atmos8120234, 2017.

Drinovec, L., Močnik, G., Zotter, P., Prévôt, A. S. H., Ruckstuhl, C., Coz, E., Rupakheti, M., Sciare, J., Müller, T., Wiedensohler, A., and Hansen, A. D. A.: The "dual-spot" Aethalometer: an improved measurement of aerosol black carbon with real-time loading compensation, Atmos. Meas. Tech., 8, 1965–1979, https://doi.org/10.5194/amt-8-1965-2015, 2015.

Dubovik, O., Holben, B., Eck, T. F., Smirnov, A., Kaufman, Y. J., King, M. D., Tanré, D., and Slutsker, I.: Variability of Absorption and Optical Properties of Key Aerosol Types Observed in Worldwide Locations, J. Atmos. Sci., 59, 590–608, https://doi.org/10.1175/1520-0469(2002)059<0590:VOAAOP>2.0.CO;2, 2002.

E. W. Eloranta and P.Piironen: О Наилучшем L_1-Приближении Алгебраическими Многочленами Усеченных Степеней И Классов Функций С Ограниченной В L_1 Производной, Proc. 17th ILRC, July 25-29 1994, 63, 147–168, https://doi.org/10.4213/im246, 1994.

Emde, C., Buras-Schnell, R., Kylling, A., Mayer, B., Gasteiger, J., Hamann, U., Kylling, J., Richter, B., Pause, C., Dowling, T., and Bugliaro, L.: The libRadtran software package for radiative transfer calculations (version 2.0.1), Geosci. Model Dev., 9, 1647–1672, https://doi.org/10.5194/gmd-9-1647-2016, 2016.

Emeis, S.: Surface-Based Remote Sensing of the Atmospheric Boundary Layer, 2010.

Emeis, S. and Schäfer, K.: Remote sensing methods to investigate boundary-layer structures relevant to air pollution in cities, 377–385, https://doi.org/10.1007/s10546-006-9068-2, 2006.

Fameli, K.-M. and Assimakopoulos, V. D.: The new open Flexible Emission Inventory for Greece

and the Greater Athens Area (FEI-GREGAA): Account of pollutant sources and their importance from 2006 to 2012, Atmos. Environ., 137, 17–37, https://doi.org/https://doi.org/10.1016/j.atmosenv.2016.04.004, 2016.

Ferrare, R. A. and Feltz, W. F.: CART Raman Lidar Retrievals of Aerosol Extinction and Relative Humidity Profiles, 1–6, 1999.

Filkov, A. I., Ngo, T., Matthews, S., Telfer, S., and Penman, T. D.: Impact of Australia's catastrophic 2019/20 bushfire season on communities and environment. Retrospective analysis and current trends, J. Saf. Sci. Resil., 1, 44–56, https://doi.org/10.1016/j.jnlssr.2020.06.009, 2020.

Finlayson-Pitts, B. J. and Pitts, J. N.: Tropospheric air pollution: Ozone, airborne toxics, polycyclic aromatic hydrocarbons, and particles, Science (80-.)., 276, 1045–1052, https://doi.org/10.1126/science.276.5315.1045, 1997.

Flemming, J., Benedetti, A., Inness, A., Engelen J, R., Jones, L., Huijnen, V., Remy, S., Parrington, M., Suttie, M., Bozzo, A., Peuch, V. H., Akritidis, D., and Katragkou, E.: The CAMS interim Reanalysis of Carbon Monoxide, Ozone and Aerosol for 2003-2015, Atmos. Chem. Phys., 17, 1945–1983, https://doi.org/10.5194/acp-17-1945-2017, 2017.

Floutsi, A. A., Baars, H., Radenz, M., Haarig, M., Yin, Z., Seifert, P., Jimenez, C., Wandinger, U., Engelmann, R., Barja, B., Zamorano, F., and Ansmann, A.: Biomass burning aerosols in the southern hemispheric midlatitudes as observed with a multiwavelength polarization Raman lidar, 2020.

Fourtziou, L., Liakakou, E., Stavroulas, I., Theodosi, C., Zarmpas, P., Psiloglou, B., Sciare, J., Maggos, T., Bairachtari, K., Bougiatioti, A., Gerasopoulos, E., Sarda-Estève, R., Bonnaire, N., and Mihalopoulos, N.: Multi-tracer approach to characterize domestic wood burning in Athens (Greece) during wintertime, Atmos. Environ., 148, 89–101, https://doi.org/https://doi.org/10.1016/j.atmosenv.2016.10.011, 2017.

Freitas, S. R., Longo, K. M., Silva Dias, M. A. F., Silva Dias, P. L., Chatfield, R., Prins, E., Artaxo, P., Grell, G. A., and Recuero, F. S.: Monitoring the transport of biomass burning emissions in South America, Environ. Fluid Mech., 5, 135–167, https://doi.org/10.1007/s10652-005-0243-7, 2005.

Freudenthaler, V.: About the effects of polarising optics on lidar signals and the Δ90 calibration, Atmos. Meas. Tech., 9, 4181–4255, https://doi.org/10.5194/amt-9-4181-2016, 2016.

Freudenthaler, V., Esselborn, M., Wiegner, M., Heese, B., Tesche, M., Ansmann, A., Müller, D., Althausen, D., Wirth, M., Fix, A., Ehret, G., Knippertz, P., Toledano, C., Gasteiger, J., Garhammer, M., and Seefeldner, M.: Depolarization ratio profiling at several wavelengths in pure Saharan dust during SAMUM 2006, Tellus, Ser. B Chem. Phys. Meteorol., 61, 165–179, https://doi.org/10.1111/j.1600-0889.2008.00396.x, 2009.

Fröhlich-Nowoisky, J., Kampf, C. J., Weber, B., Huffman, J. A., Pöhlker, C., Andreae, M. O., Lang-Yona, N., Burrows, S. M., Gunthe, S. S., Elbert, W., Su, H., Hoor, P., Thines, E., Hoffmann, T., Després, V. R., and Pöschl, U.: Bioaerosols in the Earth system: Climate, health, and ecosystem interactions, Atmos. Res., 182, 346–376, https://doi.org/10.1016/j.atmosres.2016.07.018, 2016.

Fuller, G. W., Sciare, J., Lutz, M., Moukhtar, S., and Wagener, S.: New Directions: Time to tackle

urban wood burning?, Atmos. Environ., 68, 295–296, https://doi.org/https://doi.org/10.1016/j.atmosenv.2012.11.045, 2013.

Fuller, G. W., Tremper, A. H., Baker, T. D., Espen, K., and Butter, D.: Contribution of wood burning to PM 10 in London, 87, 87–94, https://doi.org/10.1016/j.atmosenv.2013.12.037, 2014.

Garreaud, R. D., Molina, A., and Farias, M.: Andean uplift, ocean cooling and Atacama hyperaridity: A climate modeling perspective, Earth Planet. Sci. Lett., 292, 39–50, https://doi.org/10.1016/j.epsl.2010.01.017, 2010.

Generoso, S., Bréon, F. M., Balkanski, Y., Boucher, O., and Schulz, M.: Improving the seasonal cycle and interannual variations of biomass burning aerosol sources, Atmos. Chem. Phys., 3, 1211–1222, https://doi.org/10.5194/acp-3-1211-2003, 2003.

Georgakaki, P., Bougiatioti, A., Wieder, J., Mignani, C., Ramelli, F., Kanji, Z. A., Henneberger, J., Hervo, M., Berne, A., Lohmann, U., and Nenes, A.: On the drivers of droplet variability in alpine mixed-phase clouds, Atmos. Chem. Phys., 21, 10993–11012, https://doi.org/10.5194/acp-21-10993-2021, 2021.

Giannakaki, E., Balis, D. S., Amiridis, V., and Zerefos, C.: Optical properties of different aerosol types: Seven years of combined Raman-elastic backscatter lidar measurements in Thessaloniki, Greece, Atmos. Meas. Tech., 3, 569–578, https://doi.org/10.5194/amt-3-569-2010, 2010.

Giannakaki, E., Pfüller, A., Korhonen, K., Mielonen, T., Laakso, L., Vakkari, V., Baars, H., Engelmann, R., Beukes, J. P., Van Zyl, P. G., Josipovic, M., Tiitta, P., Chiloane, K., Piketh, S., Lihavainen, H., Lehtinen, K. E. J., and Komppula, M.: One year of Raman lidar observations of free-tropospheric aerosol layers over South Africa, Atmos. Chem. Phys., 15, 5429–5442, https://doi.org/10.5194/acp-15-5429-2015, 2015.

Giglio, L., Schroeder, W., and Justice, C. O.: The collection 6 MODIS active fire detection algorithm and fire products, Remote Sens. Environ., 178, 31–41, https://doi.org/10.1016/j.rse.2016.02.054, 2016.

Giglio, L., Boschetti, L., Roy, D. P., Humber, M. L., and Justice, C. O.: The Collection 6 MODIS burned area mapping algorithm and product, Remote Sens. Environ., 217, 72–85, https://doi.org/10.1016/j.rse.2018.08.005, 2018.

Gioda, A., Mayol-Bracero, O. L., Scatena, F. N., Weathers, K. C., Mateus, V. L., and McDowell, W. H.: Chemical constituents in clouds and rainwater in the Puerto Rican rainforest: Potential sources and seasonal drivers, Atmos. Environ., 68, 208–220, https://doi.org/10.1016/J.ATMOSENV.2012.11.017, 2013.

Glasse, B., Zerwas, A., Guardani, R., and Fritsching, U.: Refractive indices of metal working fluid emulsion components, Meas. Sci. Technol., 25, https://doi.org/10.1088/0957-0233/25/3/035205, 2014.

Gratsea, M., Liakakou, E., Mihalopoulos, N., Adamopoulos, A., Tsilibari, E., and Gerasopoulos, E.: The combined effect of reduced fossil fuel consumption and increasing biomass combustion on Athens' air quality, as inferred from long term CO measurements, Sci. Total Environ., 592, 115–123, https://doi.org/10.1016/j.scitotenv.2017.03.045, 2017.

Groß, S., Tesche, M., Freudenthaler, V., Toledano, C., Wiegner, M., Ansmann, A., Althausen, D., and Seefeldner, M.: Characterization of Saharan dust, marine aerosols and mixtures of biomass-burning aerosols and dust by means of multi-wavelength depolarization and Raman lidar measurements during SAMUM 2, Tellus, Ser. B Chem. Phys. Meteorol., 63, 706–724, https://doi.org/10.1111/j.1600-0889.2011.00556.x, 2011a.

Groß, S., Tesche, M., Freudenthaler, V., Toledano, C., Wiegner, M., Ansmann, A., Althausen, D., and Seefeldner, M.: Characterization of Saharan dust, marine aerosols and mixtures of biomass-burning aerosols and dust by means of multi-wavelength depolarization and Raman lidar measurements during SAMUM 2, Tellus, Ser. B Chem. Phys. Meteorol., 63, 706–724, https://doi.org/10.1111/j.1600-0889.2011.00556.x, 2011b.

Groß, S., Esselborn, M., Weinzierl, B., Wirth, M., Fix, A., and Petzold, A.: Aerosol classification by airborne high spectral resolution lidar observations, Atmos. Chem. Phys., 13, 2487–2505, https://doi.org/10.5194/acp-13-2487-2013, 2013.

Groß, S., Freudenthaler, V., Schepanski, K., Toledano, C., Schäfler, A., Ansmann, A., and Weinzierl, B.: Optical properties of long-range transported Saharan dust over Barbados as measured by dual-wavelength depolarization Raman lidar measurements, Atmos. Chem. Phys., 15, 11067–11080, https://doi.org/10.5194/acp-15-11067-2015, 2015a.

Groß, S., Freudenthaler, V., Wirth, M., and Weinzierl, B.: Towards an aerosol classification scheme for future EarthCARE lidar observations and implications for research needs, Atmos. Sci. Lett., 16, 77–82, https://doi.org/10.1002/asl2.524, 2015b.

Gui, K., Che, H., Tian, L., Wang, Y., Shi, C., Yao, W., Liang, Y., Li, L., Zheng, Y., Zhang, L., Zeng, Z., Zhong, J., Wang, Z., and Zhang, X.: Columnar optical, microphysical and radiative properties of the 2022 Hunga Tonga volcanic ash plumes, Sci. Bull., 67, 2013–2021, https://doi.org/10.1016/j.scib.2022.08.018, 2022.

H.-O. Pörtner, D.C. Roberts, M. Tignor, E.S. Poloczanska, K. Mintenbeck, A. Alegría, M. Craig, S. Langsdorf, S. Löschke, V. Möller, A. Okem, B. R.: IPCC, 2022: Climate Change 2022: Impacts, Adaptation, and Vulnerability. Contribution of Working Group II to the Sixth Assessment Report of the Intergovernmental Panel on Climate Change, 3949 pp., https://doi.org/10.1017/9781009325844.Front, 2022.

Haarig, M., Ansmann, A., Baars, H., Jimenez, C., Veselovskii, I., Engelmann, R., and Althausen, D.: Depolarization and lidar ratios at 355, 532, and 1064 nm and microphysical properties of aged tropospheric and stratospheric Canadian wildfire smoke, Atmos. Chem. Phys., 18, 11847–11861, https://doi.org/10.5194/acp-18-11847-2018, 2018.

Hamill, P., Jensen, E. J., Russeii, P. B., and Bauman, J. J.: The Life Cycle of Stratospheric Aerosol Particles, Bull. Am. Meteorol. Soc., 78, 1395–1410, https://doi.org/10.1175/1520-0477(1997)078<1395:TLCOSA>2.0.CO;2, 1997.

Harris, A. J. L., Gurioli, L., Hughes, E. E., and Lagreulet, S.: Impact of the Eyjafjallajökull ash cloud: A newspaper perspective, J. Geophys. Res. Solid Earth, 117, https://doi.org/10.1029/2011JB008735, 2012.

Heinold, B., Baars, H., Barja, B., Christensen, M., Kubin, A., Ohneiser, K., Schepanski, K.,

Schutgens, N., Senf, F., Schrödner, R., Villanueva, D., and Tegen, I.: Important role of stratospheric injection height for the distribution and radiative forcing of smoke aerosol from the 2019/2020 Australian wildfires, Atmos. Chem. Phys. Discuss., 1–20, 2021.

Heintzenberg, J., Covert, D. C., and Van Dingenen, R.: Size distribution and chemical composition of marine aerosols: A compilation and review, Tellus, Ser. B Chem. Phys. Meteorol., 52, 1104–1122, https://doi.org/10.3402/tellusb.v52i4.17090, 2000.

Herich, H., Hueglin, C., and Buchmann, B.: Techniques A 2 . 5 year ' s source apportionment study of black carbon from wood burning and fossil fuel combustion at urban and rural sites in Switzerland, 1409–1420, https://doi.org/10.5194/amt-4-1409-2011, 2011.

Hinds, W. C.: Aerosol technology: properties, behavior, and measurement of airborne particles, John Wiley \& Sons, 1998.

Hirsch, E. and Koren, I.: Record-breaking aerosol levels explained by smoke injection into the stratosphere, Science (80-.)., 371, 1269–1274, https://doi.org/10.1126/science.abe1415, 2021.

Ho, S. P., Peng, L., Anthes, R. A., Kuo, Y. H., and Lin, H. C.: Marine boundary layer heights and their longitudinal, diurnal, and interseasonal variability in the southeastern Pacific using COSMIC, CALIOP, and radiosonde data, J. Clim., 28, 2856–2872, https://doi.org/10.1175/JCLI-D-14-00238.1, 2015.

Hoppel, W. A. and Frick, G. M.: Submicron aerosol size distributions measured over the tropical and South Pacific, Atmos. Environ. Part A, Gen. Top., 24, 645–659, https://doi.org/10.1016/0960-1686(90)90020-N, 1990.

Hu, Q., Goloub, P., Veselovskii, I., Bravo-Aranda, J. A., Elisabeta Popovici, I., Podvin, T., Haeffelin, M., Lopatin, A., Dubovik, O., Pietras, C., Huang, X., Torres, B., and Chen, C.: Long-range-transported Canadian smoke plumes in the lower stratosphere over northern France, Atmos. Chem. Phys., 19, 1173–1193, https://doi.org/10.5194/acp-19-1173-2019, 2019.

Huang, L., Jiang, J. H., Tackett, J. L., Su, H., and Fu, R.: Seasonal and diurnal variations of aerosol extinction profile and type distribution from CALIPSO 5-year observations, J. Geophys. Res. Atmos., 118, 4572–4596, https://doi.org/10.1002/jgrd.50407, 2013.

Inness, A., Ades, M., Agustí-Panareda, A., Barr, J., Benedictow, A., Blechschmidt, A. M., Jose Dominguez, J., Engelen, R., Eskes, H., Flemming, J., Huijnen, V., Jones, L., Kipling, Z., Massart, S., Parrington, M., Peuch, V. H., Razinger, M., Remy, S., Schulz, M., and Suttie, M.: The CAMS reanalysis of atmospheric composition, Atmos. Chem. Phys., 19, 3515–3556, https://doi.org/10.5194/acp-19-3515-2019, 2019.

IPCC: Future Climate Changes, Risks and Impacts, 60–62 pp., https://doi.org/10.1017/CBO9781107415324, 2014.

Jaffe, D. A., Wigder, N., Downey, N., Pfister, G., Boynard, A., and Reid, S. B.: Impact of wildfires on ozone exceptional events in the western U.S., Environ. Sci. Technol., 47, 11065–11072, https://doi.org/10.1021/es402164f, 2013.

Jaffe, D. A., Cooper, O. R., Fiore, A. M., Henderson, B. H., Tonnesen, G. S., Russell, A. G., Henze, D. K., Langford, A. O., Lin, M., and Moore, T.: Scientific assessment of background ozone over the

U.S.: Implications for air quality management, 6, https://doi.org/10.1525/elementa.309, 2018.

Kablick, G. P., Allen, D. R., Fromm, M. D., and Nedoluha, G. E.: Australian PyroCb Smoke Generates Synoptic-Scale Stratospheric Anticyclones, Geophys. Res. Lett., 47, https://doi.org/10.1029/2020GL088101, 2020.

Kahnert, M. and Kanngießer, F.: Journal of Quantitative Spectroscopy & Radiative Transfer Optical properties of marine aerosol : modelling the transition from dry , irregularly shaped crystals to brine-coated , dissolving salt particles, J. Quant. Spectrosc. Radiat. Transf., 295, 108408, https://doi.org/10.1016/j.jqsrt.2022.108408, 2023.

Kalogridis, A., Vratolis, S., Liakakou, E., Gerasopoulos, E., and Mihalopoulos, N.: Assessment of wood burning versus fossil fuel contribution to wintertime black carbon and carbon monoxide concentrations in Athens , Greece, 10219–10236, 2018.

Kaskaoutis, D. G., Grivas, G., Theodosi, C., Tsagkaraki, M., Paraskevopoulou, D., Stavroulas, I., Liakakou, E., Gkikas, A., Hatzianastassiou, N., Wu, C., Gerasopoulos, E., and Mihalopoulos, N.: Carbonaceous aerosols in contrasting atmospheric environments in Greek cities: Evaluation of the EC-tracer methods for secondary organic carbon estimation, Atmosphere (Basel)., 11, https://doi.org/10.3390/atmos11020161, 2020.

Kassomenos, P. A., Sindosi, O. A., Lolis, C. J., and Chaloulakou, A.: On the relation between seasonal synoptic circulation types and spatial air quality characteristics in Athens, Greece, J. Air Waste Manag. Assoc., 53, 309–324, https://doi.org/10.1080/10473289.2003.10466154, 2003.

Khaykin, S., Legras, B., Bucci, S., Sellitto, P., Isaksen, L., Tencé, F., Bekki, S., Bourassa, A., Rieger, L., Zawada, D., Jumelet, J., and Godin-Beekmann, S.: The 2019/20 Australian wildfires generated a persistent smoke-charged vortex rising up to 35 km altitude, Commun. Earth Environ., 1, 1–12, https://doi.org/10.1038/s43247-020-00022-5, 2020.

Kim, J. S., Kug, J. S., Jeong, S. J., Park, H., and Schaepman-Strub, G.: Extensive fires in southeastern Siberian permafrost linked to preceding Arctic Oscillation, Sci. Adv., 6, 1–8, https://doi.org/10.1126/sciadv.aax3308, 2020.

Kim, K.-H., Kabir, E., and Jahan, S. A.: Airborne bioaerosols and their impact on human health, J. Environ. Sci., 67, 23–35, https://doi.org/https://doi.org/10.1016/j.jes.2017.08.027, 2018a.

Kim, M. H., Omar, A. H., Tackett, J. L., Vaughan, M. A., Winker, D. M., Trepte, C. R., Hu, Y., Liu, Z., Poole, L. R., Pitts, M. C., Kar, J., and Magill, B. E.: The CALIPSO version 4 automated aerosol classification and lidar ratio selection algorithm, Atmos. Meas. Tech., 11, 6107–6135, https://doi.org/10.5194/amt-11-6107-2018, 2018b.

Kleipool, Q., Rozemeijer, N., Van Hoek, M., Leloux, J., Loots, E., Ludewig, A., Van Der Plas, E., Adrichem, D., Harel, R., Spronk, S., Ter Linden, M., Jaross, G., Haffner, D., Veefkind, P., and Levelt, P. F.: Ozone Monitoring Instrument (OMI) collection 4: Establishing a 17-year-long series of detrended level-1b data, Atmos. Meas. Tech., 15, 3527–3553, https://doi.org/10.5194/amt-15-3527-2022, 2022.

Klett, J. D.: Stable analytical inversion solution for processing lidar returns, Appl. Opt., 20, 211, https://doi.org/10.1364/ao.20.000211, 1981.

Klett, J. D.: Lidar inversion with variable backscatter/extinction ratios, Appl. Opt., 24, 1638–1643, https://doi.org/10.1364/AO.24.001638, 1985.

Klimont, Z., Kupiainen, K., Heyes, C., Purohit, P., Cofala, J., Rafaj, P., Borken-Kleefeld, J., and Schöpp, W.: Global anthropogenic emissions of particulate matter including black carbon, Atmos. Chem. Phys., 17, 8681–8723, https://doi.org/10.5194/acp-17-8681-2017, 2017.

Kloss, C., Sellitto, P., von Hobe, M., Berthet, G., Smale, D., Krysztofiak, G., Xue, C., Qiu, C., Jégou, F., Ouerghemmi, I., and Legras, B.: Australian Fires 2019–2020: Tropospheric and Stratospheric Pollution Throughout the Whole Fire Season, Front. Environ. Sci., 9, 1–11, https://doi.org/10.3389/fenvs.2021.652024, 2021.

Kokkalis, P.: Using paraxial approximation to describe the optical setup of a typical EARLINET lidar system, 10, 3103–3115, https://doi.org/10.5194/amt-10-3103-2017, 2017.

Kokkalis, P., Papayannis, A., Amiridis, V., Mamouri, R. E., Veselovskii, I., Kolgotin, A., Tsaknakis, G., Kristiansen, N. I., Stohl, A., and Mona, L.: Optical, microphysical, mass and geometrical properties of aged volcanic particles observed over Athens, Greece, during the Eyjafjallajökull eruption in April 2010 through synergy of Raman lidar and sunphotometer measurements, Atmos. Chem. Phys., 13, 9303–9320, https://doi.org/10.5194/acp-13-9303-2013, 2013.

Kokkalis, P., Alexiou, D., Papayannis, A., Rocadenbosch, F., Soupiona, O., Raptis, P. I., Mylonaki, M., Tzanis, C. G., and Christodoulakis, J.: Application and Testing of the Extended-Kalman-Filtering Technique for Determining the Planetary Boundary-Layer Height over Athens, Greece, Boundary-Layer Meteorol., 176, 125–147, https://doi.org/10.1007/s10546-020-00514-z, 2020.

Kokkalis, P., Soupiona, O., Papanikolaou, C. A., Foskinis, R., Mylonaki, M., Solomos, S., Vratolis, S., Vasilatou, V., Kralli, E., Anagnou, D., and Papayannis, A.: Radiative effect and mixing processes of a long-lasting dust event over athens, greece, during the COVID-19 period, Atmosphere (Basel)., 12, 1–26, https://doi.org/10.3390/atmos12030318, 2021.

Kosmopoulos, G., Salamalikis, V., Pandis, S. N., Yannopoulos, P., Bloutsos, A. A., and Kazantzidis, A.: Low-cost sensors for measuring airborne particulate matter: Field evaluation and calibration at a South-Eastern European site, Sci. Total Environ., 748, 141396, https://doi.org/10.1016/j.scitotenv.2020.141396, 2020.

Kovalev, V. A. and Eichinger, W. E.: Elastic lidar: theory, practice, and analysis methods, John Wiley \& Sons, 2004.

Labonne, M., Bréon, F. M., and Chevallier, F.: Injection height of biomass burning aerosols as seen from a spaceborne lidar, Geophys. Res. Lett., 34, https://doi.org/10.1029/2007GL029311, 2007.

Lazaridis, M.: Bacteria as Cloud Condensation Nuclei (CCN) in the Atmosphere, Atmosphere (Basel)., 10, https://doi.org/10.3390/atmos10120786, 2019.

Levine, J. S.: Biomass Burning: The Cycling of Gases and Particulates from the Biosphere to the Atmosphere, Treatise Geochemistry Second Ed., 5, 139–150, https://doi.org/10.1016/B978-0-08-095975-7.00405-8, 2013.

Li, C., Krotkov, N. A., Leonard, P. J. T., Carn, S., Joiner, J., Spurr, R. J. D., and Vasilkov, A.: Version 2 Ozone Monitoring Instrument SO2 product (OMSO2 V2): New anthropogenic SO2 vertical

column density dataset, Atmos. Meas. Tech., 13, 6175–6191, https://doi.org/10.5194/amt-13-6175-2020, 2020.

Li, M., Shen, F., and Sun, X.: 2019–2020 Australian bushfire air particulate pollution and impact on the South Pacific Ocean, Sci. Rep., 11, 1–13, https://doi.org/10.1038/s41598-021-91547-y, 2021.

Liakakou, E., Stavroulas, I., Kaskaoutis, D. G., Grivas, G., and Paraskevopoulou, D.: Long-term variability , source apportionment and spectral properties of black carbon at an urban background site in Athens , Greece, Atmos. Environ., 222, 117137, https://doi.org/10.1016/j.atmosenv.2019.117137, 2020.

Lin, W., Chen, L., Yu, W., Ma, H., Zeng, Z., Lin, J., and Zeng, S.: Radioactivity impacts of the Fukushima Nuclear Accident on the atmosphere, Atmos. Environ., 102, 311–322, https://doi.org/10.1016/j.atmosenv.2014.11.047, 2015.

Liou, K. N. (Ed.): Chapter 1 - Fundamentals of Radiation for Atmospheric Applications, in: An Introduction to Atmospheric Radiation, vol. 84, Academic Press, 1–36, https://doi.org/https://doi.org/10.1016/S0074-6142(02)80016-X, 2002.

Liu, J. C., Mickley, L. J., Sulprizio, M. P., Dominici, F., Yue, X., Ebisu, K., Anderson, G. B., Khan, R. F. A., Bravo, M. A., and Bell, M. L.: Particulate air pollution from wildfires in the Western US under climate change, Clim. Change, 138, 655–666, https://doi.org/10.1007/s10584-016-1762-6, 2016.

Liu, S., Yang, L., Zhang, C., Xiang, Y. T., Liu, Z., Hu, S., and Zhang, B.: Online mental health services in China during the COVID-19 outbreak, 7, e17–e18, https://doi.org/10.1016/S2215-0366(20)30077-8, 2020.

Liu, Z., Kar, J., Zeng, S., Tackett, J., Vaughan, M., Avery, M., Pelon, J., Getzewich, B., Lee, K. P., Magill, B., Omar, A., Lucker, P., Trepte, C., and Winker, D.: Discriminating between clouds and aerosols in the CALIOP version 4.1 data products, Atmos. Meas. Tech., 12, 703–734, https://doi.org/10.5194/amt-12-703-2019, 2019.

Lu, X., Zhang, L., and Shen, L.: Meteorology and Climate Influences on Tropospheric Ozone: a Review of Natural Sources, Chemistry, and Transport Patterns, Curr. Pollut. Reports, 5, 238–260, https://doi.org/10.1007/s40726-019-00118-3, 2019.

Lucia, M., Amodeo, A., Pandolfi, M., and Pappalardo, G.: Saharan dust intrusions in the Mediterranean area: Three years of Raman lidar measurements, J. Geophys. Res., 111, https://doi.org/10.1029/2005JD006569, 2006.

Lynch, P., Reid, J. S., Westphal, D. L., Zhang, J., Hogan, T. F., Hyer, E. J., Curtis, C. A., Hegg, D. A., Shi, Y., Campbell, J. R., Rubin, J. I., Sessions, W. R., Turk, F. J., and Walker, A. L.: An 11-year global gridded aerosol optical thickness reanalysis (v1.0) for atmospheric and climate sciences, Geosci. Model Dev., 9, 1489–1522, https://doi.org/10.5194/gmd-9-1489-2016, 2016.

Mahowald, N., Albani, S., Kok, J. F., Engelstaeder, S., Scanza, R., Ward, D. S., and Flanner, M. G.: The size distribution of desert dust aerosols and its impact on the Earth system, Aeolian Res., 15, 53–71, https://doi.org/10.1016/j.aeolia.2013.09.002, 2014.

Martins, L. D., Hallak, R., Alves, R. C., Almeida, D. S. De, Squizzato, R., Moreira, C. A. B., Beal, A.,

Silva, I., Rudke, A., and Martins, J. A.: Long-range Transport of Aerosols from Biomass Burning over Southeastern South America and their Implications on Air Quality, 1734–1745, https://doi.org/10.4209/aaqr.2017.11.0545, 2018.

Mattis, I., Ansmann, A., Mu, D., Wandinger, U., and Althausen, D.: Multiyear aerosol observations with dual-wavelength Raman lidar in the framework of EARLINET, 109, 1–15, https://doi.org/10.1029/2004JD004600, 2004.

Mattis, I., Siefert, P., Müller, D., Tesche, M., Hiebsch, A., Kanitz, T., Schmidt, J., Finger, F., Wandinger, U., and Ansmann, A.: Volcanic aerosol layers observed with multiwavelength Raman lidar over central Europe in 2008-2009, J. Geophys. Res. Atmos., 115, 1–9, https://doi.org/10.1029/2009JD013472, 2010.

Mattis, I., D'Amico, G., Baars, H., Amodeo, A., Madonna, F., and Iarlori, M.: EARLINET Single Calculus Chain - Technical - Part 2: Calculation of optical products, Atmos. Meas. Tech., 9, 3009–3029, https://doi.org/10.5194/amt-9-3009-2016, 2016.

McKendry, I., Strawbridge, K., Karumudi, M. L., O'Neill, N., MacDonald, A. M., Leaitch, R., Jaffe, D., Cottle, P., Sharma, S., Sheridan, P., and Ogren, J.: Californian forest fire plumes over southwestern British Columbia: Lidar, sunphotometry, and mountaintop chemistry observations, Atmos. Chem. Phys., 11, 465–477, https://doi.org/10.5194/acp-11-465-2011, 2011.

Millán, L., Santee, M. L., Lambert, A., Livesey, N. J., Werner, F., Schwartz, M. J., Pumphrey, H. C., Manney, G. L., Wang, Y., Su, H., Wu, L., Read, W. G., and Froidevaux, L.: The Hunga Tonga-Hunga Ha'apai Hydration of the Stratosphere, Geophys. Res. Lett., 49, 1–10, https://doi.org/10.1029/2022GL099381, 2022.

Minnis, P., Harrison, E. F., Stowe, L. L., Gibson, G. G., Denn, F. M., Doelling, D. R., and Smith, W. L.: Radiative Climate Forcing, 1993.

Mona, L., Amodeo, A., Pandolfi, M., and Pappalardo, G.: Saharan dust intrusions in the Mediterranean area: Three years of Raman lidar measurements, J. Geophys. Res. Atmos., 111, 1–13, https://doi.org/10.1029/2005JD006569, 2006.

Mosca, S., Conti, C., Stone, N., and Matousek, P.: Spatially offset Raman spectroscopy, Nat. Rev. Methods Prim., 1, 21, https://doi.org/10.1038/s43586-021-00019-0, 2021.

Müller, D.: Indo-Asian pollution during INDOEX: Microphysical particle properties and single-scattering albedo inferred from multiwavelength lidar observations, J. Geophys. Res., 108, 4600, https://doi.org/10.1029/2003JD003538, 2003.

Müller, D., Mattis, I., Wandinger, U., Ansmann, A., Althausen, D., and Stohl, A.: Raman lidar observations of aged Siberian and Canadian forest fire smoke in the free troposphere over Germany in 2003: Microphysical particle characterization, J. Geophys. Res. D Atmos., 110, 75–90, https://doi.org/10.1029/2004JD005756, 2005.

Müller, D., Ansmann, A., Mattis, I., Tesche, M., Wandinger, U., Althausen, D., and Pisani, G.: Aerosol-type-dependent lidar ratios observed with Raman lidar, J. Geophys. Res. Atmos., 112, https://doi.org/10.1029/2006JD008292, 2007a.

Müller, D., Mattis, I., Ansmann, A., Wandinger, U., Ritter, C., and Kaiser, D.: Multiwavelength

Raman lidar observations of particle growth during long-range transport of forest-fire smoke in the free troposphere, Geophys. Res. Lett., 34, https://doi.org/10.1029/2006GL027936, 2007b.

Müller, D., Heinold, B., Tesche, M., Tegen, I., Althausen, D., Arboledas, L. A., Amiridis, V., Amodeo, A., Ansmann, A., Balis, D., Comeron, A., D'amico, G., Gerasopoulos, E., Guerrero-rascado, J. L., Freudenthaler, V., Giannakaki, E., Heese, B., Iarlori, M., Knippertz, P., Mamouri, R. E., Mona, L., Papayannis, A., Pappalardo, G., Perrone, R. M., Pisani, G., Rizi, V., Sicard, M., Spinelli, N., Tafuro, A., and Wiegner, M.: EARLINET observations of the 14-22-May long-range dust transport event during SAMUM 2006: Validation of results from dust transport modelling, Tellus, Ser. B Chem. Phys. Meteorol., 61, 325–339, https://doi.org/10.1111/j.1600-0889.2008.00400.x, 2009.

Murayama, T., Okamoto, H., Kaneyasu, N., and Kamataki, H.: Application of lidar depolarization measurement in the atmospheric boundary layer : Effects of dust and sea-salt particles, 104, 781–792, 1999.

Murayama, T., Müller, D., Wada, K., Shimizu, A., Sekiguchi, M., and Tsukamoto, T.: Characterization of Asian dust and Siberian smoke with multi-wavelength Raman lidar over Tokyo, Japan in spring 2003, Geophys. Res. Lett., 31, 1–5, https://doi.org/10.1029/2004GL021105, 2004.

Mylonaki, M., Giannakaki, E., Papayannis, A., Papanikolaou, C., and Komppula, M.: Aerosol type classification analysis using EARLINET multiwavelength and depolarization lidar observations, 2211–2227, 2021a.

Mylonaki, M., Papayannis, A., Anagnou, D., Veselovskii, I., Papanikolaou, C. A., Kokkalis, P., Soupiona, O., Foskinis, R., Gidarakou, M., and Kralli, E.: Optical and microphysical properties of aged biomass burning aerosols and mixtures, based on 9-year multiwavelength raman lidar observations in athens, greece, Remote Sens., 13, https://doi.org/10.3390/rs13193877, 2021b.

Mylonaki, M., Papayannis, A., Papanikolaou, C.-A., Foskinis, R., Soupiona, O., Maroufidis, G., Anagnou, D., and Kralli, E.: Tropospheric vertical profiling of the aerosol backscatter coefficient and the particle linear depolarization ratio for different aerosol mixtures during the PANACEA campaign in July 2019 at Volos, Greece, Atmos. Environ., 247, 118184, https://doi.org/https://doi.org/10.1016/j.atmosenv.2021.118184, 2021c.

Nepomuceno Pereira, S., Preißler, J., Guerrero-Rascado, J. L., Silva, A. M., and Wagner, F.: Forest fire smoke layers observed in the free troposphere over Portugal with a multiwavelength Raman lidar: Optical and microphysical properties, Sci. World J., 2014, https://doi.org/10.1155/2014/421838, 2014a.

Nepomuceno Pereira, S., Preißler, J., Guerrero-Rascado, J. L., Silva, A. M., and Wagner, F.: Forest fire smoke layers observed in the free troposphere over Portugal with a multiwavelength Raman lidar: Optical and microphysical properties, Sci. World J., 2014, https://doi.org/10.1155/2014/421838, 2014b.

Nguyen, H. D., Azzi, M., White, S., Salter, D., Trieu, T., Morgan, G., Rahman, M., Watt, S., Riley, M., Chang, L. T. C., Barthelemy, X., Fuchs, D., Lieschke, K., and Nguyen, H.: The summer 2019–2020 wildfires in east coast australia and their impacts on air quality and health in new south wales, australia, Int. J. Environ. Res. Public Health, 18, 1–27,

https://doi.org/10.3390/ijerph18073538, 2021.

Nicolae, D., Nemuc, A., Müller, D., Talianu, C., Vasilescu, J., Belegante, L., and Kolgotin, A.: Characterization of fresh and aged biomass burning events using multiwavelength Raman lidar and mass spectrometry, J. Geophys. Res. Atmos., 118, 2956–2965, https://doi.org/10.1002/jgrd.50324, 2013.

Nisantzi, A., Mamouri, R. E., Ansmann, A., and Hadjimitsis, D.: Injection of mineral dust into the free troposphere during fire events observed with polarization lidar at Limassol, Cyprus, Atmos. Chem. Phys., 14, 12155–12165, https://doi.org/10.5194/acp-14-12155-2014, 2014.

Noel, V., Chepfer, H., Hoareau, C., Reverdy, M., and Cesana, G.: Effects of solar activity on noise in CALIOP profiles above the South Atlantic Anomaly, Atmos. Meas. Tech., 7, 1597–1603, https://doi.org/10.5194/amt-7-1597-2014, 2014.

Ohneiser, K., Ansmann, A., Baars, H., Seifert, P., Barja, B., Jimenez, C., Radenz, M., Teisseire, A., Floutsi, A., Haarig, M., Engelmann, R., Zamorano, F., Bühl, J., and Wandinger, U.: Smoke of extreme Australian bushfires observed in the stratosphere over Punta Arenas, Chile, in January 2020: optical thickness, lidar ratios, and depolarization ratios at 355 and 532 nm, Atmos. Chem. Phys., 1–16, https://doi.org/10.5194/acp-2020-96, 2020a.

Ohneiser, K., Ansmann, A., Baars, H., Seifert, P., Barja, B., Jimenez, C., Radenz, M., Teisseire, A., Floutsi, A., Haarig, M., Foth, A., Chudnovsky, A., Engelmann, R., Zamorano, F., Bühl, J., and Wandinger, U.: Smoke of extreme Australian bushfires observed in the stratosphere over Punta Arenas, Chile, in January 2020: Optical thickness, lidar ratios, and depolarization ratios at 355 and 532 nm, Atmos. Chem. Phys., 20, 8003–8015, https://doi.org/10.5194/acp-20-8003-2020, 2020b.

Ohneiser, K., Ansmann, A., Kaifler, B., Chudnovsky, A., Barja, B., Knopf, D. A., Kaifler, N., Baars, H., Seifert, P., Villanueva, D., Jimenez, C., Radenz, M., Engelmann, R., Veselovskii, I., and Zamorano, F.: Australian wildfire smoke in the stratosphere: the decay phase in 2020/21 and impact on ozone depletion, Atmos. Chem. Phys. Discuss., 1–41, 2022.

Omar, A. H., Winker, D. M., Kittaka, C., Vaughan, M. A., Liu, Z., Hu, Y., Trepte, C. R., Rogers, R. R., Ferrare, R. A., Lee, K. P., Kuehn, R. E., and Hostetler, C. A.: The CALIPSO automated aerosol classification and lidar ratio selection algorithm, J. Atmos. Ocean. Technol., 26, 1994–2014, https://doi.org/10.1175/2009JTECHA1231.1, 2009.

Ortiz-Amezcua, P., Luis Guerrero-Rascado, J., Granados-Munõz, M. J., Benavent-Oltra, J. A., Böckmann, C., Samaras, S., Stachlewska, I. S., Janicka, L., Baars, H., Bohlmann, S., and Alados-Arboledas, L.: Microphysical characterization of long-range transported biomass burning particles from North America at three EARLINET stations, Atmos. Chem. Phys., 17, 5931–5946, https://doi.org/10.5194/acp-17-5931-2017, 2017.

Pan, Y., Pinnick, R. G., Hill, S. C., Rosen, J. M., and Chang, R. K.: Single-particle laser-induced-fluorescence spectra of biological and other organic-carbon aerosols in the atmosphere : Measurements at New Haven , Connecticut , and Las Cruces , New Mexico, 112, 1–15, https://doi.org/10.1029/2007JD008741, 2007.

Papagiannopoulos, N., Mona, L., Alados-Arboledas, L., Amiridis, V., Baars, H., Binietoglou, I.,

Bortoli, D., D'Amico, G., Giunta, A., Luis Guerrero-Rascado, J., Schwarz, A., Pereira, S., Spinelli, N., Wandinger, U., Wang, X., and Pappalardo, G.: CALIPSO climatological products: Evaluation and suggestions from EARLINET, Atmos. Chem. Phys., 16, 2341–2357, https://doi.org/10.5194/acp-16-2341-2016, 2016.

Papagiannopoulos, N., Mona, L., Amodeo, A., D'Amico, G., Gumà Claramunt, P., Pappalardo, G., Alados-Arboledas, L., Luís Guerrero-Rascado, J., Amiridis, V., Kokkalis, P., Apituley, A., Baars, H., Schwarz, A., Wandinger, U., Binietoglou, I., Nicolae, D., Bortoli, D., Comerón, A., Rodríguez-Gómez, A., Sicard, M., Papayannis, A., and Wiegner, M.: An automatic observation-based aerosol typing method for EARLINET, Atmos. Chem. Phys., 18, 15879–15901, https://doi.org/10.5194/acp-18-15879-2018, 2018.

Papanastasiou, D. K. and Melas, D.: Statistical characteristics of ozone and PM 10 levels in a medium-sized Mediterranean city, 36, 127–138, 2009.

Papanikolaou, C., Kokkalis, P., Soupiona, O., Solomos, S., Papayannis, A., Mylonaki, M., Anagnou, D., Foskinis, R., and Gidarakou, M.: Australian Bushfires (2019 – 2020): Aerosol Optical Properties and Radiative Forcing, 2022a.

Papanikolaou, C. A., Giannakaki, E., Papayannis, A., Mylonaki, M., and Soupiona, O.: Canadian biomass burning aerosol properties modification during a long-ranged event on August 2018, 20, 1–19, https://doi.org/10.3390/s20185442, 2020.

Papanikolaou, C. A., Papayannis, A., Mylonaki, M., Foskinis, R., Kokkalis, P., Liakakou, E., Stavroulas, I., Soupiona, O., Hatzianastassiou, N., Gavrouzou, M., Kralli, E., and Anagnou, D.: Vertical Profiling of Fresh Biomass Burning Aerosol Optical Properties over the Greek Urban City of Ioannina, during the PANACEA Winter Campaign, Atmosphere (Basel)., 13, https://doi.org/10.3390/atmos13010094, 2022b.

Papayannis, A., Ancellet, G., Pelon, J., and Mégie, G.: Multiwavelength lidar for ozone measurements in the troposphere and the lower stratosphere, Appl. Opt., 29, 467–476, https://doi.org/10.1364/AO.29.000467, 1990.

Papayannis, A., Mamouri, R.-E., Amiridis, V., Kazadzis, S., Pérez García-Pando, C., Tsaknakis, G., Kokkalis, P., and Baldasano, J.: Systematic lidar observations of Saharan dust layers over Athens, Greece in the frame of EARLINET project (2004-2006), Ann. Geophys., 27, 3611–3620, https://doi.org/10.5194/angeo-27-3611-2009, 2009.

Papayannis, A., Mamouri, R. E., Amiridis, V., Remoundaki, E., Tsaknakis, G., Kokkalis, P., Veselovskii, I., Kolgotin, A., Nenes, A., and Fountoukis, C.: Optical-microphysical properties of Saharan dust aerosols and composition relationship using a multi-wavelength Raman lidar, in situ sensors and modelling: A case study analysis, Atmos. Chem. Phys., 12, 4011–4032, https://doi.org/10.5194/acp-12-4011-2012, 2012a.

Papayannis, A., Mamouri, R. E., Amiridis, V., Giannakaki, E., Veselovskii, I., Kokkalis, P., Tsaknakis, G., Balis, D., Kristiansen, N. I., Stohl, A., Korenskiy, M., Allakhverdiev, K., Huseyinoglu, M. F., and Baykara, T.: Optical properties and vertical extension of aged ash layers over the Eastern Mediterranean as observed by Raman lidars during the Eyjafjallajökull eruption in May 2010, Atmos. Environ., 48, 56–65, https://doi.org/10.1016/j.atmosenv.2011.08.037, 2012b.

Papayannis, A., Kokkalis, P., Mylonaki, M., Soupiona, R., Papanikolaou, C. A., and Foskinis, R.: Recent upgrades of the EOLE and AIAS lidar systems of the National Technical University of Athens operating since 2000 in Athens , Greece, 02030, 4–7, 2020.

Pappalardo, G., Amodeo, A., Mona, L., Pandolfi, M., Pergola, N., and Cuomo, V.: Raman lidar observations of aerosol emitted during the 2002 Etna eruption, Geophys. Res. Lett., 31, 4–7, https://doi.org/10.1029/2003gl019073, 2004.

Perlwitz, J. and Miller, R. L.: Cloud cover increase with increasing aerosol absorptivity: A counterexample to the conventional semidirect aerosol effect, J. Geophys. Res. Atmos., 115, https://doi.org/10.1029/2009JD012637, 2010.

Peterson, D. A., Campbell, J. R., Hyer, E. J., Fromm, M. D., Kablick, G. P., Cossuth, J. H., and DeLand, M. T.: Wildfire-driven thunderstorms cause a volcano-like stratospheric injection of smoke, npj Clim. Atmos. Sci., 1, 1–8, https://doi.org/10.1038/s41612-018-0039-3, 2018.

Pisso, I., Sollum, E., Grythe, H., Kristiansen, N. I., Cassiani, M., Eckhardt, S., Arnold, D., Morton, D., Thompson, R. L., Groot Zwaaftink, C. D., Evangeliou, N., Sodemann, H., Haimberger, L., Henne, S., Brunner, D., Burkhart, J. F., Fouilloux, A., Brioude, J., Philipp, A., Seibert, P., and Stohl, A.: The Lagrangian particle dispersion model FLEXPART version 10.4, Geosci. Model Dev., 12, 4955–4997, https://doi.org/10.5194/gmd-12-4955-2019, 2019.

Ponczek, M., Franco, M. A., Carbone, S., Rizzo, L. V, Monteiro, D., Morais, F. G., Duarte, A., Barbosa, H. M. J., and Artaxo, P.: Environmental Science : Linking the chemical composition and optical properties of biomass burning aerosols in, 252–269, https://doi.org/10.1039/d1ea00055a, 2022.

Powell, K. A., Hostetler, C. A., Liu, Z., Vaughan, M. A., Kuehn, R. E., Hunt, W. H., Lee, K. P., Trepte, C. R., Rogers, R. R., Young, S. A., and Winker, D. M.: Calipso lidar calibration algorithms. Part I: Nighttime 532-nm parallel channel and 532-nm perpendicular channel, J. Atmos. Ocean. Technol., 26, 2015–2033, https://doi.org/10.1175/2009JTECHA1242.1, 2009.

Preißler, J., Wagner, F., Guerrero-Rascado, J. L., and Silva, A. M.: Two years of free-tropospheric aerosol layers observed over Portugal by lidar, J. Geophys. Res. Atmos., 118, 3676–3686, https://doi.org/10.1002/jgrd.50350, 2013a.

Preißler, J., Pereira, S., Silva, A. M., and Wagner, F.: Vertically resolved optical and microphysical properties of Portuguese forest fire smoke observed in February 2012, Lidar Technol. Tech. Meas. Atmos. Remote Sens. IX, 8894, 88940Y, https://doi.org/10.1117/12.2029184, 2013b.

Prospero, J. M.: Long-range transport of mineral dust in the global atmosphere: Impact of African dust on the environment of the southeastern United States, Proc. Natl. Acad. Sci. U. S. A., 96, 3396–3403, https://doi.org/10.1073/pnas.96.7.3396, 1999.

Prospero, J. M., Ginoux, P., Torres, O., Nicholson, S. E., and Gill, T. E.: Environmental characterization of global sources of atmospheric soil dust identified with the Nimbus 7 Total Ozone Mapping Spectrometer (TOMS) absorbing aerosol product, Rev. Geophys., 40, https://doi.org/10.1029/2000RG000095, 2002.

Proud, S. R., Prata, A. T., and Schmauß, S.: The January 2022 eruption of Hunga Tonga-Hunga

Ha\&\#x2019;apai volcano reached the mesosphere, Science (80-.)., 378, 554–557, https://doi.org/10.1126/science.abo4076, 2022.

Psiloglou, B. E. and Kambezidis, H. D.: Estimation of the ground albedo for the Athens area, Greece, J. Atmos. Solar-Terrestrial Phys., 71, 943–954, https://doi.org/10.1016/j.jastp.2009.03.017, 2009.

Qin, Y., Ye, J., Ohno, P., Zhai, J., Han, Y., Liu, P., Wang, J., Zaveri, R. A., and Martin, S. T.: Humidity Dependence of the Condensational Growth of α-Pinene Secondary Organic Aerosol Particles, Environ. Sci. Technol., 55, 14360–14369, https://doi.org/10.1021/acs.est.1c01738, 2021.

Rakesh, V., Haridas, S., Sivan, C., Manoj, M. G., Abhilash, S., Paul, B., Unnikrishnan, K., Mohanakumar, K., and Sumesh Chandran, R.: Impact of the Hunga Tonga-Hunga Ha'apai volcanic eruption on the changes observed over the Indian near-equatorial ionosphere, Adv. Sp. Res., 70, 2480–2493, https://doi.org/10.1016/j.asr.2022.07.004, 2022.

Remer, L. A., Kaufman, Y. J., Tanré, D., Mattoo, S., Chu, D. A., Martins, J. V., Li, R. R., Ichoku, C., Levy, R. C., Kleidman, R. G., Eck, T. F., Vermote, E., and Holben, B. N.: The MODIS aerosol algorithm, products, and validation, J. Atmos. Sci., 62, 947–973, https://doi.org/10.1175/JAS3385.1, 2005.

Richardson, S. C., Mytilinaios, M., Foskinis, R., Kyrou, C., Papayannis, A., and Pyrri, I.: Science of the Total Environment Bioaerosol detection over Athens , Greece using the laser induced fl uorescence technique, Sci. Total Environ., 696, 133906, https://doi.org/10.1016/j.scitotenv.2019.133906, 2019.

Rix, M., Valks, P., Hao, N., Loyola, D., Schlager, H., Huntrieser, H., Flemming, J., Koehler, U., Schumann, U., and Inness, A.: Volcanic SO2, BrO and plume height estimations using GOME-2 satellite measurements during the eruption of Eyjafjallajökull in May 2010, J. Geophys. Res. Atmos., 117, https://doi.org/10.1029/2011JD016718, 2012.

Rolph, G., Stein, A., and Stunder, B.: Real-time Environmental Applications and Display sYstem: READY, Environ. Model. Softw., 95, 210–228, https://doi.org/10.1016/j.envsoft.2017.06.025, 2017.

Saltzman, E. S.: Marine Aerosols, Surf. Ocean. Atmos. Process., 17–35, https://doi.org/10.1029/2008GM000769, 2013.

Sandradewi, J., Prévôt, A. S. H., Szidat, S., Perron, N., Alfarra, M. R., Lanz, V. A., Weingartner, E., and Baltensperger, U.: Using aerosol light absorption measurements for the quantitative determination of wood burning and traffic emission contributions to particulate matter., Environ. Sci. Technol., 42, 3316–3323, https://doi.org/10.1021/es702253m, 2008.

Sarigiannis, D. A., Karakitsios, S. P., Kermenidou, M., Nikolaki, S., Zikopoulos, D., Semelidis, S., Papagiannakis, A., and Tzimou, R.: Total exposure to airborne particulate matter in cities: The effect of biomass combustion, Sci. Total Environ., 493, 795–805, https://doi.org/https://doi.org/10.1016/j.scitotenv.2014.06.055, 2014.

Seinfeld, J. H. and Pandis, S. N.: Atmospheric Chemistry and Physics, Atmos. Chem. Phys., 5, 139–152, 2006.

Selimovic, V., Yokelson, R. J., McMeeking, G. R., and Coefield, S.: Aerosol Mass and Optical Properties, Smoke Influence on O3, and High NO3 Production Rates in a Western U.S. City Impacted by Wildfires, J. Geophys. Res. Atmos., 125, 1–22, https://doi.org/10.1029/2020JD032791, 2020.

Sellitto, P., Podglajen, A., Belhadji, R., Boichu, M., Carboni, E., Cuesta, J., Duchamp, C., Kloss, C., Siddans, R., Begue, N., Blarel, L., Jegou, F., Khaykin, S., Renard, J., and Legras, B.: The unexpected radiative impact of the Hunga Tonga eruption of January 15th , 2022, Res. Prepr. / Nat. Portf. - Rev. Process., 1–10, https://doi.org/10.1038/s43247-022-00618-z, 2022.

Sharma, A., Sivakumar, V., Bollig, C., Van Der Westhuizen, C., and Moema, D.: System description of the mobile LIDAR of the CSIR, South Africa, S. Afr. J. Sci., 105, 456–462, https://doi.org/10.4102/sajs.v105i11/12.140, 2009.

Sharma Ghimire, P., Tripathee, L., Chen, P., and Kang, S.: Linking the conventional and emerging detection techniques for ambient bioaerosols: a review, Rev. Environ. Sci. Biotechnol., 18, 495–523, https://doi.org/10.1007/s11157-019-09506-z, 2019.

She, C.-Y.: Spectral structure of laser light scattering revisited: bandwidths of nonresonant scattering lidars, Appl. Opt., 40, 4875, https://doi.org/10.1364/ao.40.004875, 2001.

Shin, S. K., Tesche, M., Noh, Y., and Müller, D.: Aerosol-type classification based on AERONET version 3 inversion products, Atmos. Meas. Tech., 12, 3789–3803, https://doi.org/10.5194/amt-12-3789-2019, 2019.

Sicard, M., Barragan, R., Dulac, F., Alados-Arboledas, L., and Mallet, M.: Aerosol optical, microphysical and radiative properties at regional background insular sites in the western Mediterranean, Atmos. Chem. Phys., 16, 12177–12203, https://doi.org/10.5194/acp-16-12177-2016, 2016.

Sindosi, O., Markozannes, G., Rizos, E., and Ntzani, E.: Effects of economic crisis on air quality in Ioannina, Greece, J. Environ. Sci. Heal. - Part A Toxic/Hazardous Subst. Environ. Eng., 54, 768–781, https://doi.org/10.1080/10934529.2019.1592534, 2019.

Sindosi, O. A., Katsoulis, B. D., and Bartzokas, A.: An objective definition of air mass types affecting athens, greece; The corresponding atmospheric pressure patterns and air pollution levels, Environ. Technol., 24, 947–962, https://doi.org/10.1080/09593330309385633, 2003.

Sindosi, O. A. and Hatzianastassiou, N.: PM 10 Concentrations in a Provincial City of Inland Greece in the Times of Austerity and Their Relationship with Meteorological and Socioeconomic Conditions, 2021.

Smirnov, A., Holben, B. N., Dubovik, O., Frouin, R., Eck, T. F., and Slutsker, I.: Maritime component in aerosol optical models derived from Aerosol Robotic Network data, J. Geophys. Res. Atmos., 108, 1–11, https://doi.org/10.1029/2002jd002701, 2003.

Solomos, S., Gialitaki, A., Marinou, E., Proestakis, E., Amiridis, V., Baars, H., Komppula, M., and Ansmann, A.: Modeling and remote sensing of an indirect Pyro-Cb formation and biomass transport from Portugal wildfires towards Europe, Atmos. Environ., 206, 303–315, https://doi.org/10.1016/j.atmosenv.2019.03.009, 2019.

Soupiona, O., Samaras, S., Ortiz-Amezcua, P., Böckmann, C., Papayannis, A., Moreira, G. A., Benavent-Oltra, J. A., Guerrero-Rascado, J. L., Bedoya-Velásquez, A. E., Olmo, F. J., Román, R., Kokkalis, P., Mylonaki, M., Alados-Arboledas, L., Papanikolaou, C. A., and Foskinis, R.: Retrieval of optical and microphysical properties of transported Saharan dust over Athens and Granada based on multi-wavelength Raman lidar measurements: Study of the mixing processes, Atmos. Environ., 214, 116824, https://doi.org/10.1016/j.atmosenv.2019.116824, 2019a.

Soupiona, O., Samaras, S., Ortiz-Amezcua, P., Böckmann, C., Papayannis, A., Moreira, G. A., Benavent-Oltra, J. A., Guerrero-Rascado, J. L., Bedoya-Velásquez, A. E., Olmo, F. J., Román, R., Kokkalis, P., Mylonaki, M., Alados-Arboledas, L., Papanikolaou, C. A., and Foskinis, R.: Retrieval of optical and microphysical properties of transported Saharan dust over Athens and Granada based on multi-wavelength Raman lidar measurements: Study of the mixing processes, Atmos. Environ., 214, https://doi.org/10.1016/j.atmosenv.2019.116824, 2019b.

Soupiona, O., Papayannis, A., Kokkalis, P., Foskinis, R., Sánchez Hernández, G., Ortiz-Amezcua, P., Mylonaki, M., Papanikolaou, C. A., Papagiannopoulos, N., Samaras, S., Groß, S., Mamouri, R. E., Alados-Arboledas, L., Amodeo, A., and Psiloglou, B.: EARLINET observations of Saharan dust intrusions over the northern Mediterranean region (2014-2017): Properties and impact on radiative forcing, Atmos. Chem. Phys., 20, 15147–15166, https://doi.org/10.5194/acp-20-15147-2020, 2020a.

Soupiona, O., Papayannis, A., Kokkalis, P., Foskinis, R., Sánchez Hernández, G., Ortiz-Amezcua, P., Mylonaki, M., Papanikolaou, C.-A., Papagiannopoulos, N., Samaras, S., Groß, S., Mamouri, R.-E., Alados-Arboledas, L., Amodeo, A., and Psiloglou, B.: Saharan dust intrusions over the northern Mediterranean region in the frame of EARLINET (2014-2017): Properties and impact in radiative forcing, 2020, 1–22, https://doi.org/10.5194/acp-2020-611, 2020b.

Speight, J. G.: Water systems, 1–51 pp., https://doi.org/10.1016/b978-0-12-803810-9.00001-2, 2020.

Stachlewska, I. S., Samson, M., Zawadzka, O., Harenda, K. M., Janicka, L., Poczta, P., Szczepanik, D., Heese, B., Wang, D., Borek, K., Tetoni, E., Proestakis, E., Siomos, N., Nemuc, A., Chojnicki, B. H., Markowicz, K. M., Pietruczuk, A., Szkop, A., Althausen, D., Stebel, K., Schuettemeyer, D., and Zehner, C.: Modification of local urban aerosol properties by long-range transport of biomass burning aerosol, Remote Sens., 10, 1–28, https://doi.org/10.3390/rs10030412, 2018.

Stavroulas, I., Grivas, G., Michalopoulos, P., Liakakou, E., Bougiatioti, A., Kalkavouras, P., Fameli, K. M., Hatzianastassiou, N., Mihalopoulos, N., and Gerasopoulos, E.: Field evaluation of low-cost PM sensors (Purple Air PA-II) Under variable urban air quality conditions, in Greece, Atmosphere (Basel)., 11, https://doi.org/10.3390/atmos11090926, 2020.

Stein, A. F., Draxler, R. R., Rolph, G. D., Stunder, B. J. B., Cohen, M. D., and Ngan, F.: Noaa's hysplit atmospheric transport and dispersion modeling system, Bull. Am. Meteorol. Soc., 96, 2059–2077, https://doi.org/10.1175/BAMS-D-14-00110.1, 2015.

Stohl, A., Forster, C., Frank, A., Seibert, P., and Wotawa, G.: Technical note: The Lagrangian particle dispersion model FLEXPART version 6.2, Atmos. Chem. Phys., 5, 2461–2474, https://doi.org/10.5194/acp-5-2461-2005, 2005.

Stull, R.: An Introduction to Boundary Layer Meteorology, 1988.

Su, T., Li, Z., and Kahn, R.: Relationships between the planetary boundary layer height and surface pollutants derived from lidar observations over China : regional pattern and influencing factors, 15921–15935, 2018.

Tackett, J. L., Kar, J., Vaughan, M. A., Getzewich, B. J., Kim, M., Omar, A. H., Magill, B. E., Pitts, M. C., and Winker, D. M.: The CALIPSO version 4 . 5 stratospheric aerosol subtyping algorithm, 1–42, 2022.

Takle, E. S.: Agricultural Meteorology and Climatology, 92–97 pp., https://doi.org/10.1016/B978-0-12-382225-3.00009-8, 2015.

Tan, I., Storelvmo, T., and Choi, Y. S.: Spaceborne lidar observations of the ice-nucleating potential of dust, polluted dust, and smoke aerosols in mixed-phase clouds, J. Geophys. Res., 119, 6653–6665, https://doi.org/10.1002/2013JD021333, 2014.

Tencé, F., Jumelet, J., Sarkissian, A., Bekki, S., and Khaykin, S.: Optical properties of smoke particules from Australian 2019-20 wildfires derived from lidar measurements at the French Antarctic station Dumont d ' Urville, 12466, 2022.

Tesche, M., Ansmann, A., Müller, D., Althausen, D., Engelmann, R., Freudenthaler, V., and Groß, S.: Vertically resolved separation of dust and smoke over Cape Verde using multiwavelength Raman and polarization lidars during Saharan Mineral Dust Experiment 2008, J. Geophys. Res. Atmos., 114, 1–14, https://doi.org/10.1029/2009JD011862, 2009.

Tesche, M., Müller, D., Gross, S., Ansmann, A., Althausen, D., Freudenthaler, V., Weinzierl, B., Veira, A., and Petzold, A.: Optical and microphysical properties of smoke over Cape Verde inferred from multiwavelength lidar measurements, Tellus, Ser. B Chem. Phys. Meteorol., 63, 677–694, https://doi.org/10.1111/j.1600-0889.2011.00549.x, 2011a.

Tesche, M., Gross, S., Ansmann, A., Müller, D., Althausen, D., Freudenthaler, V., and Esselborn, M.: Profiling of Saharan dust and biomass-burning smoke with multiwavelength polarization Raman lidar at Cape Verde, Tellus, Ser. B Chem. Phys. Meteorol., 63, 649–676, https://doi.org/10.1111/j.1600-0889.2011.00548.x, 2011b.

Tesche, M., Wandinger, U., Ansmann, A., Althausen, D., Müller, D., and Omar, A. H.: Ground-based validation of CALIPSO observations of dust and smoke in the Cape Verde region, J. Geophys. Res. Atmos., 118, 2889–2902, https://doi.org/10.1002/jgrd.50248, 2013.

Titos, G., Águila, A., Cazorla, A., Lyamani, H., Casquero-vera, J. A., Colombi, C., Cuccia, E., Gianelle, V., Mo, G., Alastuey, A., Olmo, F. J., and Alados-arboledas, L.: Science of the Total Environment Spatial and temporal variability of carbonaceous aerosols : Assessing the impact of biomass burning in the urban environment, 578, 613–625, https://doi.org/10.1016/j.scitotenv.2016.11.007, 2017.

Torres, O., Bhartia, P. K., Taha, G., Jethva, H., Das, S., Colarco, P., Krotkov, N., Omar, A., and Ahn, C.: Stratospheric Injection of Massive Smoke Plume From Canadian Boreal Fires in 2017 as Seen by DSCOVR-EPIC, CALIOP, and OMPS-LP Observations, J. Geophys. Res. Atmos., 125, 1–25, https://doi.org/10.1029/2020JD032579, 2020.

Union, E. G., Immler, F., Engelbart, D., Schrems, O., Service, W., and Lindenberg, M. O.: and Physics Fluorescence from atmospheric aerosol detected by a lidar indicates biogenic particles in the lowermost stratosphere, 345–355, 2005.

Vakkari, V.: Geophysical Research Letters, Vakkari, V. Geophys. Res. Lett. , 2644–2651, doi10.1002/2014GL059396.Received, 2014., 2644–2651, https://doi.org/10.1002/2014GL059396.Received, 2014.

Vaughan, G., Draude, A. P., Ricketts, H. M. A., Schultz, D. M., Adam, M., Sugier, J., and Wareing, D. P.: Transport of Canadian forest fire smoke over the UK as observed by lidar, Atmos. Chem. Phys., 18, 11375–11388, https://doi.org/10.5194/acp-18-11375-2018, 2018.

Vaughan, M. A., Young, S. A., Winker, D. M., Powell, K. A., Omar, A. H., Liu, Z., Hu, Y., and Hostetler, C. A.: Fully automated analysis of space-based lidar data: an overview of the CALIPSO retrieval algorithms and data products, Laser Radar Tech. Atmos. Sens., 5575, 16, https://doi.org/10.1117/12.572024, 2004.

Veselovskii, I., Whiteman, D. N., Korenskiy, M., Suvorina, A., and Perez-Ramirez, D.: Use of rotational Raman measurements in multiwavelength aerosol lidar for evaluation of particle backscattering and extinction, Atmos. Meas. Tech., 8, 4111–4122, https://doi.org/10.5194/amt-8-4111-2015, 2015.

Veselovskii, I., Goloub, P., Podvin, T., Bovchaliuk, V., Derimian, Y., Augustin, P., Fourmentin, M., Tanre, D., Korenskiy, M., Whiteman, D. N., Diallo, A., Ndiaye, T., Kolgotin, A., and Dubovik, O.: Retrieval of optical and physical properties of African dust from multiwavelength Raman lidar measurements during the SHADOW campaign in Senegal, Atmos. Chem. Phys., 16, 7013–7028, https://doi.org/10.5194/acp-16-7013-2016, 2016.

Veselovskii, I., Hu, Q., Goloub, P., Podvin, T., Korenskiy, M., Derimian, Y., Legrand, M., and Castellanos, P.: Variability in lidar-derived particle properties over West Africa due to changes in absorption: Towards an understanding, Atmos. Chem. Phys., 20, 6563–6581, https://doi.org/10.5194/acp-20-6563-2020, 2020.

Veselovskii, I., Hu, Q., Ansmann, A., Goloub, P., Podvin, T., and Korenskiy, M.: Fluorescence lidar observations of wildfire smoke inside cirrus: a contribution to smoke-cirrus interaction research, Atmos. Chem. Phys., 22, 5209–5221, https://doi.org/10.5194/acp-22-5209-2022, 2022.

Wainker, D. M., Tackett, J. L., Getzewich, B. J., Liu, Z., Vaughan, M. A., and Rogers, R. R.: The global 3-D distribution of tropospheric aerosols as characterized by CALIOP, Atmos. Chem. Phys., 13, 3345–3361, https://doi.org/10.5194/acp-13-3345-2013, 2013.

Wallace, J. M., & Hobbs, P. V.: Introduction and Overview 1 1.1, Atmos. Sci., 1–23, https://doi.org/10.1016/B978-0-12-732951-2.50006-5, n.d.

Wandinger, U.: Introduction to Lidar BT - Lidar: Range-Resolved Optical Remote Sensing of the Atmosphere, edited by: Weitkamp, C., Springer New York, New York, NY, 1–18, https://doi.org/10.1007/0-387-25101-4_1, 2005.

Wandinger, U., Müller, D., Böckmann, C., Althausen, D., Matthias, V., Bösenberg, J., Weiß, V., Fiebig, M., Wendisch, M., Stohl, A., and Ansmann, A.: Optical and microphysical characterization

of biomass-burning and industrial-pollution aerosols from multiwavelength lidar and aircraft measurements, J. Geophys. Res. Atmos., 107, https://doi.org/10.1029/2000JD000202, 2002.

Wang, X., Boselli, A., D'Avino, L., Pisani, G., Spinelli, N., Amodeo, A., Chaikovsky, A., Wiegner, M., Nickovic, S., Papayannis, A., Perrone, M. R., Rizi, V., Sauvage, L., and Stohl, A.: Volcanic dust characterization by EARLINET during Etna's eruptions in 2001-2002, Atmos. Environ., 42, 893–905, https://doi.org/10.1016/j.atmosenv.2007.10.020, 2008.

Weitkamp, C.: Lidar, Range-Resolved Optical Remote Sensing of the Atmosphere, Lidar, Range-Resolved Opt. Remote Sens. Atmos. Ed. by Claus Weitkamp. Berlin Springer, 2005., 102, https://doi.org/10.1007/b106786, 2005.

Winker, D. M., Vaughan, M. A., Omar, A., Hu, Y., Powell, K. A., Liu, Z., Hunt, W. H., and Young, S. A.: Overview of the CALIPSO mission and CALIOP data processing algorithms, J. Atmos. Ocean. Technol., 26, 2310–2323, https://doi.org/10.1175/2009JTECHA1281.1, 2009.

Yang, X., Zhao, C., Yang, Y., and Fan, H.: Long-term multi-source data analysis about the characteristics of aerosol optical properties and types over Australia, Atmos. Chem. Phys., 21, 3803–3825, https://doi.org/10.5194/acp-21-3803-2021, 2021a.

Yang, X., Zhao, C., Yang, Y., Yan, X., and Fan, H.: Statistical aerosol properties associated with fire events from 2002 to 2019 and a case analysis in 2019 over Australia, Atmos. Chem. Phys., 21, 3833–3853, https://doi.org/10.5194/acp-21-3833-2021, 2021b.

Yu, P., Davis, S. M., Toon, O. B., Portmann, R. W., Bardeen, C. G., Barnes, J. E., Telg, H., Maloney, C., and Rosenlof, K. H.: Persistent Stratospheric Warming Due to 2019–2020 Australian Wildfire Smoke, Geophys. Res. Lett., 48, https://doi.org/10.1029/2021GL092609, 2021.

Zeng, Z., Wang, Z., and Zhang, B.: An adjustment approach for aerosol optical depth inferred from calipso, Remote Sens., 13, https://doi.org/10.3390/rs13163085, 2021.

Zerefos, C., Nastos, P., Balis, D., Papayannis, A., Kelepertsis, A., Kannelopoulou, E., Nikolakis, D., Eleftheratos, C., Thomas, W., and Varotsos, C.: A complex study of Etna's volcanic plume from ground-based, in situ and space-borne observations, Int. J. Remote Sens., 27, 1855–1864, https://doi.org/10.1080/01431160500462154, 2006.

Zerefos, C. S., Eleftheratos, K., Kapsomenakis, J., Solomos, S., Inness, A., Balis, D., Redondas, A., Eskes, H., Allaart, M., Amiridis, V., Dahlback, A., De Bock, V., Diémoz, H., Engelmann, R., Eriksen, P., Fioletov, V., Gröbner, J., Heikkilä, A., Petropavlovskikh, I., JarosÅawski, J., Josefsson, W., Karppinen, T., Köhler, U., Meleti, C., Repapis, C., Rimmer, J., Savinykh, V., Shirotov, V., Siani, A. M., Smedley, A. R. D., Stanek, M., and Stübi, R.: Detecting volcanic sulfur dioxide plumes in the Northern Hemisphere using the Brewer spectrophotometers, other networks, and satellite observations, Atmos. Chem. Phys., 17, 551–574, https://doi.org/10.5194/acp-17-551-2017, 2017.

Zhang, H., Wang, F., Li, J., Duan, Y., Zhu, C., and He, J.: Potential Impact of Tonga Volcano Eruption on Global Mean Surface Air Temperature, J. Meteorol. Res., 36, 1–5, https://doi.org/10.1007/s13351-022-2013-6, 2022.

Zhang, L., Sun, J. Y., Shen, X. J., Zhang, Y. M., Che, H., Ma, Q. L., Zhang, Y. W., Zhang, X. Y., and

Ogren, J. A.: Observations of relative humidity effects on aerosol light scattering in the Yangtze River Delta of China, Atmos. Chem. Phys., 15, 8439–8454, https://doi.org/10.5194/acp-15-8439-2015, 2015.

Zhao, W., Sun, C., and Guo, Z.: Reawaking of Tonga volcano, Innov., 3, 100218, https://doi.org/10.1016/j.xinn.2022.100218, 2022.

Zhu, S. and Sartelet, K. N.: Modelling of externally-mixed particles in the atmosphere, Springer Proc. Complex., 43–48, https://doi.org/10.1007/978-3-319-24478-5_7, 2016.

Zielinski, T., Bolzacchini, E., Cataldi, M., Ferrero, L., Graßl, S., Hansen, G., Mateos, D., Mazzola, M., Neuber, R., Pakszys, P., Posyniak, M., Ritter, C., Severi, M., Sobolewski, P., Traversi, R., and Velasco-merino, C.: Study of Chemical and Optical Properties of Biomass Burning Aerosols during Long-Range Transport Events toward the Arctic in Summer 2017, 2020.

Zuo, M., Zhou, T., Man, W., Chen, X., Liu, J., Liu, F., and Gao, C.: Volcanoes and Climate: Sizing up the Impact of the Recent Hunga Tonga-Hunga Ha'apai Volcanic Eruption from a Historical Perspective, Adv. Atmos. Sci., 39, 1986–1993, https://doi.org/10.1007/s00376-022-2034-1, 2022.

APPENDICES

APPENDIX A: Paper I

sensors

MDPI

Article

Canadian Biomass Burning Aerosol Properties Modification during a Long-Ranged Event on August 2018

Christina-Anna Papanikolaou [1,*], Elina Giannakaki [2,3], Alexandros Papayannis [1], Maria Mylonaki [1] and Ourania Soupiona [1]

1 Laser Remote Sensing Unit, Physics Department, School of Applied Mathematics and Physical Sciences, National Technical University of Athens, 157 80 Zografou, Greece; apdlidar@central.ntua.gr (A.P.); mylonaki.mari@gmail.com (M.M.); soupiona.rania@gmail.com (O.S.)

2 Department of Environmental Physics and Meteorology, Faculty of Physics, National and Kapodistrian University of Athens, 157-72 Zografou, Greece; elina@phys.uoa.gr

3 Finnish Meteorological Institute, P.O Box 1627, 70211 Kuopio, Finland

* Correspondence: papanikolaou.ca@gmail.com

Received: 28 July 2020; Accepted: 16 September 2020; Published: 22 September 2020

check for updates

Abstract: The aim of this paper is to study the spatio-temporal evolution of a long-lasting Canadian biomass burning event that affected Europe in August 2018. The event produced biomass burning aerosol layers which were observed during their transport from Canada to Europe from the 16 to the 26 August 2018 using active remote sensing data from the space-borne system Cloud-Aerosol Lidar and Infrared Pathfinder Satellite Observation (CALIPSO). The total number of aerosol layers detected was 745 of which 42% were identified as pure biomass burning. The remaining 58% were attributed to smoke mixed with: polluted dust (34%), clean continental (10%), polluted continental (5%), desert dust (6%) or marine aerosols (3%). In this study, smoke layers, pure and mixed ones, were observed by the CALIPSO satellite from 0.8 and up to 9.6 km height above mean sea level (amsl.). The mean altitude of these layers was found between 2.1 and 5.2 km amsl. The Ångström exponent, relevant to the aerosol backscatter coefficient (532/1064 nm), ranged between 0.9 and 1.5, indicating aerosols of different sizes. The mean linear particle depolarization ratio at 532 nm for pure biomass burning aerosols was found equal to 0.05 ± 0.04, indicating near spherical aerosols. We also observed that, in case of no aerosol mixing, the sphericity of pure smoke aerosols does not change during the air mass transportation (0.05–0.06). On the contrary, when the smoke is mixed with dessert dust the mean linear particle depolarization ratio may reach values up to 0.20 ± 0.04, especially close to the African continent (Region 4).

Keywords: CALIPSO; Lidar; biomass burning aerosol; Canadian smoke; Canadian wildfires 2018

Table A. 1: Descriptive Statistics for different aerosol types for Region 1 (R1): mean, standard deviation (std), median, maximum value (max), minimum value (min), 75th and 25th percentile for all variables.

	Type	Parameter	Mean	Std	Median	Max	Min	75th perc	25th perc
Pure	**S**	Alt (km)	4.81	2.02	4.93	9.59	1.15	5.88	3.36
		b_{aer} ($Mm^{-1}sr^{-1}$)	1.65	1.60	1.14	8.01	0.18	1.97	0.66
		PLDR	0.05	0.04	0.05	0.19	0.01	0.07	0.03
		Å$_b$	1.05	0.74	1.12	3.20	-1.00	1.43	0.66
Smoke mixed with	**PD**	Alt (km)	4.59	1.43	4.86	8.24	0.91	5.52	3.69
		b_{aer} ($Mm^{-1}sr^{-1}$)	1.71	0.61	1.37	6.64	0.20	2.07	0.93
		PLDR	0.09	0.05	0.08	0.20	0.01	0.11	0.06
		Å$_b$	1.26	0.59	1.33	2.79	-0.89	1.60	0.95
	D	Alt (km)	3.87	1.80	3.09	7.52	1.21	5.04	2.04
		b_{aer} ($Mm^{-1}sr^{-1}$)	2.24	0.93	2.25	4.50	0.65	2.88	1.59
		PLDR	0.15	0.06	0.13	0.25	0.07	0.21	0.09
		Å$_b$	1.31	0.45	1.20	2.33	0.42	1.61	1.00
	CC	Alt (km)	5.19	1.59	5.19	9.50	2.22	6.32	3.96
		b_{aer} ($Mm^{-1}sr^{-1}$)	0.80	0.50	0.65	2.90	0.23	0.94	0.53
		PLDR	0.05	0.03	0.04	0.13	0.00	0.06	0.03
		Å$_b$	0.89	0.55	0.92	1.86	-0.75	1.28	0.66
	CP	Alt (km)	2.08	0.96	2.01	3.90	0.70	2.63	1.25
		b_{aer} ($Mm^{-1}sr^{-1}$)	2.05	1.35	1.67	4.52	0.36	3.25	0.83
		PLDR	0.07	0.04	0.07	0.15	0.00	0.09	0.03
		Å$_b$	1.04	0.44	1.72	1.72	-0.39	1.36	0.75
	M	Alt (km)	2.99	0.25	2.93	3.66	2.76	3.18	2.82
		b_{aer} ($Mm^{-1}sr^{-1}$)	2.60	1.00	2.69	4.12	0.57	3.31	2.25
		PLDR	0.06	0.04	0.13	0.13	0.00	0.12	0.03
		Å$_b$	1.45	0.42	1.59	1.94	0.55	1.78	1.16

Table A. 2: Descriptive Statistics for different aerosol types for Region 2 (R2): (std), median, maximum value (max), minimum value (min), 75th and 25th percentile for all variables.

	Type	Parameter	Mean	Std	Median	Max	Min	75th perc	25th perc
Pure	**S**	Alt (km)	4.81	2.02	4.93	9.59	1.15	5.88	3.36
		b_{aer}($Mm^{-1}sr^{-1}$)	1.65	1.60	1.14	8.01	0.18	1.97	0.66
		PLDR	0.05	0.04	0.05	0.19	0.01	0.07	0.03
		Å$_b$	1.05	0.74	1.12	3.20	-1.00	1.43	0.66
	PD	Alt (km)	4.59	1.43	4.86	8.24	0.91	5.52	3.69
		b_{aer}($Mm^{-1}sr^{-1}$)	1.71	0.61	1.37	6.64	0.20	2.07	0.93
		PLDR	0.09	0.05	0.08	0.20	0.01	0.11	0.06
		Å$_b$	1.26	0.59	1.33	2.79	-0.89	1.60	0.95
	D	Alt (km)	3.87	1.80	3.09	7.52	1.21	5.04	2.04
		b_{aer}($Mm^{-1}sr^{-1}$)	2.24	0.93	2.25	4.50	0.65	2.88	1.59
		PLDR	0.15	0.06	0.13	0.25	0.07	0.21	0.09
		Å$_b$	1.31	0.45	1.20	2.33	0.42	1.61	1.00

Smoke mixed with	**CC**	Alt (km)	5.19	1.59	5.19	9.50	2.22	6.32	3.96
		$b_{aer}(Mm^{-1}sr^{-1})$	0.80	0.50	0.65	2.90	0.23	0.94	0.53
		PLDR	0.05	0.03	0.04	0.13	0.00	0.06	0.03
		Åb	0.89	0.55	0.92	1.86	-0.75	1.28	0.66
	CP	Alt (km)	2.08	0.96	2.01	3.90	0.70	2.63	1.25
		$b_{aer}(Mm^{-1}sr^{-1})$	2.05	1.35	1.67	4.52	0.36	3.25	0.83
		PLDR	0.07	0.04	0.07	0.15	0.00	0.09	0.03
		Åb	1.04	0.44	1.72	1.72	-0.39	1.36	0.75
	M	Alt (km)	2.99	0.25	2.93	3.66	2.76	3.18	2.82
		$b_{aer}(Mm^{-1}sr^{-1})$	2.60	1.00	2.69	4.12	0.57	3.31	2.25
		PLDR	0.06	0.04	0.13	0.13	0.00	0.12	0.03
		Åb	1.45	0.42	1.59	1.94	0.55	1.78	1.16

Table A. 3: Descriptive Statistics for different aerosol types for Region 3 (R3): mean, standard deviation (std), median, maximum value (max), minimum value (min), 75th and 25th percentile for all variables.

	Type	Parameter	Mean	Std	Median	Max	Min	75^{th} perc	25^{th} perc
Pure	**S**	Alt (km)	4.81	2.02	4.93	9.59	1.15	5.88	3.36
		b_{aer} ($Mm^{-1}sr^{-1}$)	1.65	1.60	1.14	8.01	0.18	1.97	0.66
		PLDR	0.05	0.04	0.05	0.19	0.01	0.07	0.03
		Åb	1.05	0.74	1.12	3.20	-1.00	1.43	0.66
Smoke mixed with	**PD**	Alt (km)	4.59	1.43	4.86	8.24	0.91	5.52	3.69
		b_{aer} ($Mm^{-1}sr^{-1}$)	1.71	0.61	1.37	6.64	0.20	2.07	0.93
		PLDR	0.09	0.05	0.08	0.20	0.01	0.11	0.06
		Åb	1.26	0.59	1.33	2.79	-0.89	1.60	0.95
	D	Alt (km)	3.87	1.80	3.09	7.52	1.21	5.04	2.04
		b_{aer} ($Mm^{-1}sr^{-1}$)	2.24	0.93	2.25	4.50	0.65	2.88	1.59
		PLDR	0.15	0.06	0.13	0.25	0.07	0.21	0.09
		Åb	1.31	0.45	1.20	2.33	0.42	1.61	1.00
	CC	Alt (km)	5.19	1.59	5.19	9.50	2.22	6.32	3.96
		b_{aer} ($Mm^{-1}sr^{-1}$)	0.80	0.50	0.65	2.90	0.23	0.94	0.53
		PLDR	0.05	0.03	0.04	0.13	0.00	0.06	0.03
		Åb	0.89	0.55	0.92	1.86	-0.75	1.28	0.66
	CP	Alt (km)	2.08	0.96	2.01	3.90	0.70	2.63	1.25
		b_{aer} ($Mm^{-1}sr^{-1}$)	2.05	1.35	1.67	4.52	0.36	3.25	0.83
		PLDR	0.07	0.04	0.07	0.15	0.00	0.09	0.03
		Åb	1.04	0.44	1.72	1.72	-0.39	1.36	0.75
	M	Alt (km)	2.99	0.25	2.93	3.66	2.76	3.18	2.82
		b_{aer} ($Mm^{-1}sr^{-1}$)	2.60	1.00	2.69	4.12	0.57	3.31	2.25
		PLDR	0.06	0.04	0.13	0.13	0.00	0.12	0.03
		Åb	1.45	0.42	1.59	1.94	0.55	1.78	1.16

Table A. 4: Descriptive Statistics for pure smoke aerosols in all four regions: mean, standard deviation (std), median, maximum value (max), minimum value (min), 75th and 25th percentile for all variables.

Region	Parameter	Mean	Std	Median	Max	Min	75th perc	25th perc
Region 1	Alt (km)	3.95	1.86	3.99	7.82	1.15	5.76	2.10
	b_{aer} ($Mm^{-1}sr^{-1}$)	2.11	2.03	1.24	8.00	0.20	2.63	0.77
	PLDR	0.05	0.04	0.04	0.17	0.01	0.06	0.03
	$Å_b$	0.96	0.66	1.12	2.22	-0.89	1.32	0.73
Region 2	Alt (km)	5.10	2.22	5.16	9.59	1.30	6.35	3.27
	b_{aer} ($Mm^{-1}sr^{-1}$)	1.75	1.69	0.97	8.00	0.97	2.81	0.55
	PLDR	0.06	0.04	0.04	0.18	0.01	0.09	0.03
	$Å_b$	0.99	0.95	1.14	2.99	-0.90	1.59	0.37
Region 3	Alt (km)	5.33	1.52	5.22	9.26	1.83	5.85	4.36
	b_{aer} ($Mm^{-1}sr^{-1}$)	1.08	0.71	0.91	2.93	0.20	1.57	0.57
	PLDR	0.06	0.04	0.05	0.19	0.01	0.79	0.03
	$Å_b$	1.02	0.72	1.16	3.20	-0.91	1.60	0.79
Region 4	Alt (km)	5.47	1.98	5.22	8.84	1.71	6.89	4.28
	b_{aer} ($Mm^{-1}sr^{-1}$)	1.26	0.74	1.21	3.33	0.22	1.72	0.67
	PLDR	0.05	0.03	0.05	0.14	0.01	0.06	0.03
	$Å_b$	1.01	0.51	1.02	2.24	-0.11	1.37	0.60

APPENDIX B: Paper II

atmosphere

MDPI

Article

Vertical Profiling of Fresh Biomass Burning Aerosol Optical Properties over the Greek Urban City of Ioannina, during the PANACEA Winter Campaign

Christina-Anna Papanikolaou [1,*], Alexandros Papayannis [1,*], Maria Mylonaki [1], Romanos Foskinis [1], Panagiotis Kokkalis [2], Eleni Liakakou [3], Iasonas Stavroulas [3,4], Ourania Soupiona [1], Nikolaos Hatzianastassiou [5], Maria Gavrouzou [5], Eleni Kralli [1] and Dimitra Anagnou [1]

[1] Laser Remote Sensing Unit, Department of Physics, National and Technical University of Athens, 15780 Zografou, Greece; mylonakimari@mail.ntua.gr (M.M.); foskinis@mail.ntua.gr (R.F.); raniaphd@mail.ntua.gr (O.S.); elkralli@survey.ntua.gr (E.K.); dimiana@phys.uoa.gr (D.A.)
[2] Physics Department, Kuwait University, P.O. Box 5969, Safat 13060, Kuwait; panagiotis.kokkalis@ku.edu.kw
[3] Institute for Environmental Research and Sustainable Development, National Observatory of Athens, Palaia Penteli, 15236 Athens, Greece; liakakou@noa.gr (E.L.); istavroulas@noa.gr (I.S.)
[4] Environmental Chemical Processes Laboratory, Department of Chemistry, University of Crete, 71003 Crete, Greece
[5] Department of Physics, University of Ioannina, 54110 Ioannina, Greece; nhatzian@uoi.gr (N.H.); m.gavrouzou@uoi.gr (M.G.)
* Correspondence: papanikolaouca@mail.ntua.gr (C.-A.P.); apdlidar@mail.ntua.gr (A.P.)

Abstract: Vertical profiling of aerosol particles was performed during the PANhellenic infrastructure for Atmospheric Composition and climatE chAnge (PANACEA) winter campaign (10 January 2020–7 February 2020) over the city of Ioannina, Greece (39.65° N, 20.85° E, 500 m a.s.l.). The middle-sized city of Ioannina suffers from wintertime air pollution episodes due to biomass burning (BB) domestic heating activities. The lidar technique was applied during the PANACEA winter campaign on Ioannina city, to fill the gap of knowledge of the spatio-temporal evolution of the vertical mixing of the particles occurring during these winter-time air pollution episodes. During this campaign the mobile single-wavelength (532 nm) depolarization Aerosol lIdAr System (AIAS) was used to measure the spatio-temporal evolution of the aerosols' vertical profiles within the Planetary Boundary Layer (PBL) and the lower free troposphere (LFT; up to 4 km height a.s.l.). AIAS performed almost continuous lidar measurements from morning to late evening hours (typically from 07:00 to 19:00 UTC), under cloud-free conditions, to provide the vertical profiles of the aerosol backscatter coefficient (b_{aer}) and the particle linear depolarization ratio (PLDR), both at 532 nm. In this study we emphasized on the vertical profiling of very fresh (~hours) biomass burning (BB) particles originating from local domestic heating activities in the area. In total, 33 out of 34 aerosol layers in the lower free troposphere were characterized as fresh biomass burning ones of local origin, showing a mean particle linear depolarization value of 0.04 ± 0.02 with a range of 0.01 to 0.09 (532 nm) in a height region 1.21–2.23 km a.s.l. To corroborate our findings, we used in situ data, particulate matter (PM) concentrations ($PM_{2.5}$) from a particulate sensor located close to our station, and the total black carbon (BC) concentrations along with the respective contribution of the fossil fuel (BC_{ff}) and biomass/wood burning (BC_{wb}) from the Aethalometer. The $PM_{2.5}$ mass concentrations ranged from 5.6 to 175.7 μg/m^3, while the wood burning emissions from residential heating were increasing during the evening hours, with decreasing temperatures. The BC_{wb} concentrations ranged from 0.5 to 17.5 μg/m^3, with an extremely high mean contribution of BC_{wb} equal to 85.4%, which in some cases during night-time reached up to 100% during the studied period.

Keywords: lidar; depolarization ratio; fresh biomass burning aerosols; domestic heating; black carbon; $PM_{2.5}$

check for updates

Citation: Papanikolaou, C.-A.; Papayannis, A.; Mylonaki, M.; Foskinis, R.; Kokkalis, P.; Liakakou, E.; Stavroulas, I.; Soupiona, O.; Hatzianastassiou, N.; Gavrouzou, M.; et al. Vertical Profiling of Fresh Biomass Burning Aerosol Optical Properties over the Greek Urban City of Ioannina, during the PANACEA Winter Campaign. *Atmosphere* **2022**, *13*, 94. https://doi.org/10.3390/atmos13010094

Academic Editor: Sergey Nizkorodov

Received: 8 December 2021
Accepted: 5 January 2022
Published: 7 January 2022

Publisher's Note: MDPI stays neutral with regard to jurisdictional claims in published maps and institutional affiliations.

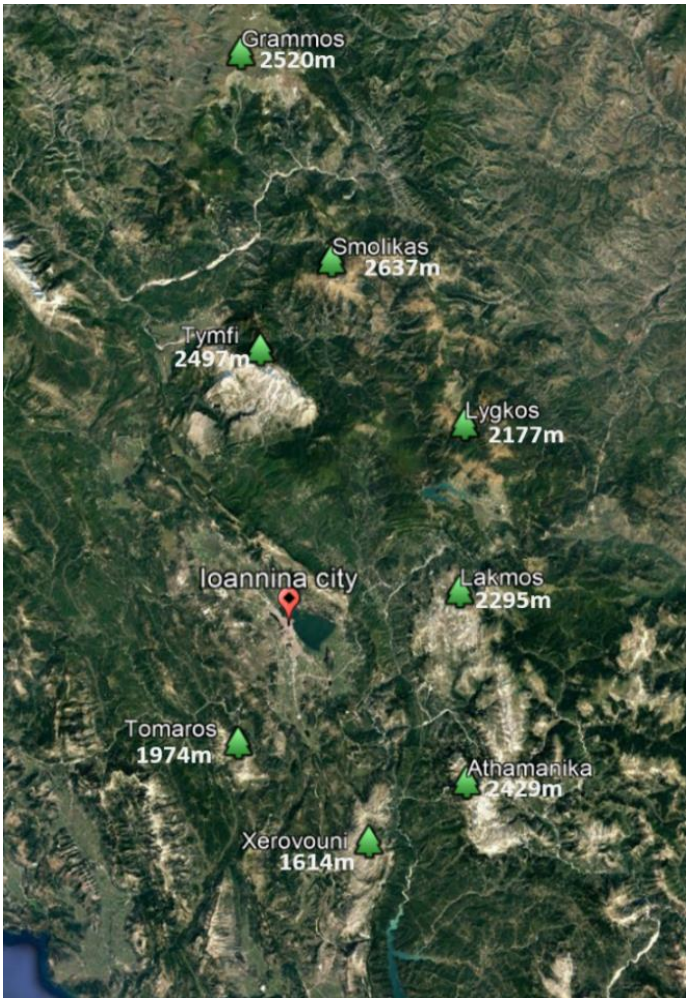

Figure B. 1: The terrain Google Earth map of the Ioannina basin showing the city and the and the surrounding mountains, along with their names and top's height (Papanikolaou et al., 2022b).

Table B. 1: Date, time, and mean height of the aerosol layers (ALH; grey shadowed cells represent the PBLH and mean values inside the PBL), mean b_{aer}, and PLDR at 532 nm inside the aerosol layers, as observed by the AIAS lidar system, during the PANACEA winter campaign.

Date	Time	ALH	b_{aer}	PLDR
(DD/MM)	(UTC)	(km)	($Mm^{-1}sr^{-1}$)	
10/01	19:00–19:30	1.07	3.38 ± 1.70	0.01 ± 0.01
		1.21 ± 0.12	1.52 ± 0.16	0.02 ± 0.01
		1.36 ± 0.15	1.12 ± 0.31	0.01 ± 0.01
		1.75 ± 0.24	0.37 ± 0.11	0.02 ± 0.01
13/01	14:27–15:04	1.09	2.59 ± 0.57	0.01 ± 0.01
		1.42 ± 0.33	1.12 ± 0.30	0.02 ± 0.01
		2.05 ± 0.18	0.73 ± 0.18	0.03 ± 0.01
13/01	16:59–17:31	1.07	2.03 ± 0.74	0.01 ± 0.01
		1.36 ± 0.21	1.02 ± 0.09	0.03 ± 0.01
		1.96 ± 0.15	0.69 ± 0.08	0.04 ± 0.01
		2.23 ± 0.12	0.48 ± 0.04	0.06 ± 0.01

17/01	16:14–16:47	1.15	3.14 ± 1.44	0.03 ± 0.01
		1.21 ± 0.06	1.77 ± 0.22	0.05 ± 0.02
		1.42 ± 0.15	1.82 ± 0.31	0.04 ± 0.01
18/01	15:00–15:40	1.20	3.88 ± 0.96	0.02 ± 0.01
		1.78 ± 0.27	1.53 ± 0.62	0.05 ± 0.02
19/01	13:03–13:40	1.18	9.43 ± 3.67	0.02 ± 0.01
		1.54 ± 0.33	2.68 ± 1.04	0.05 ± 0.02
		2.05 ± 0.18	1.02 ± 0.30	0.09 ± 0.03
20/01	15:04–15:37	1.08	5.11 ± 1.78	0.02 ± 0.01
		1.51 ± 0.18	1.71 ± 0.26	0.04 ± 0.01
		2.08 ± 0.33	1.46 ± 0.71	0.06 ± 0.03
20/01	18:49–19:19	1.09	6.05 ± 0.91	0.02 ± 0.01
		1.72 ± 0.39	1.93 ± 1.07	0.06 ± 0.02
21/01	15:29–16:02	1.02	5.76 ± 2/72	0.02 ± 0.01
		1.33 ± 0.18	1.91 ± 0.40	0.04 ± 0.01
		1.66 ± 0.15	1.02 ± 0.23	0.05 ± 0.01
22/01	14:39–15:41	1.05	7.96 ± 1.89	0.02 ± 0.01
		1.36 ± 0.21	2.91 ± 0.91	0.04 ± 0.01
		1.66 ± 0.09	1.29 ± 0.18	0.05 ± 0.01
		1.87 ± 0.12	0.80 ± 0.25	0.06 ± 0.02
26/01	08:29–09:04	1.12	12.19 ± 1.66	0.02 ± 0.01
		1.89 ± 0.28	2.59 ± 1.03	0.08 ± 0.05
		3.10 ± 0.25	1.50 ± 0.59	0.20 ± 0.10
31/01	13:30–14:05	1.18	2.34 ± 0.50	0.01 ± 0.01
		1.69 ± 0.48	1.38 ± 0.46	0.02 ± 0.01
31/01	18:39–19:21	1.31	3.20 ± 0.50	0.01 ± 0.01
		1.75 ± 0.36	2.09 ± 1.39	0.03 ± 0.01
01/02	15:28–16:02	1.13	2.44 ± 0.40	0.01 ± 0.01
		1.42 ± 0.15	1.13 ± 0.17	0.02 ± 0.01
		1.90 ± 0.15	0.72 ± 0.39	0.03 ± 0.02
01/02	18:29–19:31	1.24	4.23 ± 0.94	0.01 ± 0.01
		1.39 ± 0.18	2.87 ± 1.06	0.01 ± 0.01
		1.81 ± 0.24	1.05 ± 0.61	0.03 ± 0.02
02/02	15:19–15:45	1.11	2.16 ± 0.49	0.01 ± 0.01
		1.45 ± 0.12	1.09 ± 0.07	0.02 ± 0.01
		1.75 ± 0.18	0.92 ± 0.09	0.02 ± 0.01
		2.14 ± 0.21	0.62 ± 0.28	0.03 ± 0.02
03/02	16:00–16:36	1.19	2.52 ± 0.46	0.01 ± 0.01
		1.36 ± 0.15	1.86 ± 0.25	0.02 ± 0.01
		1.81 ± 0.30	1.18 ± 0.48	0.02 ± 0.01

Table B. 2: Hourly averaged data of PM2.5 and BC, along with the meteorological parameters (T, RH, wind speed, and direction), during the PANACEA winter campaign in Ioannina. All data presented are averaged for the same time periods during which the lidar profiles were retrieved.

Date	Time	$PM_{2.5}$	BC	BC_{wb}	BC_{ff}	T	RH	Wind Speed	Wind Direction
(DD/MM)	(UTC)	($\mu g/m^3$)	($\mu g/m^3$)	($\mu g/m^3$)	($\mu g/m^3$)	(°C)	(%)	(m/s)	(°)
10/01	19:00–20:00	205.9	17.5	17.5	0.0	3.7	65	0.3	187.8
13/01	14:00–15:00	41.6	3.7	3.5	0.2	9.8	58	0.9	56.4
13/01	17:00–18:00	140.4	12.7	11.6	1.1	6.0	75	0.3	78.3
17/01	16:00–17:00	63.3	5.9	5.2	0.7	9.8	34	0.9	141.2
18/01	15:00–16:00	50.4	2.2	1.5	0.7	8.3	71	0.5	104.1
19/01	13:00–14:00	46.6	2.1	2.0	0.1	8.6	61	0.5	116.0
20/01	15:00–16:00	65.5	3.9	2.8	1.1	8.6	62	0.9	94.1
20/01	18:00–20:00	137.1	10.7	10.3	0.4	4.0	82	0.6	202.1
21/01	15:00–16:00	96.7	9.8	8.9	0.9	6.8	48	0.6	101.2
22/01	14:00–16:00	106.7	7.7	6.5	1.2	9.1	45	0.7	106.7
26/01	08:00–09:00	55.4	3.6	2.3	1.3	8.8	88	0.3	194.8
31/01	13:00–14:00	6.7	0.8	0.5	0.3	10.1	59	0.8	97.9
31/01	18:00–19:00	104.5	10.3	10.0	0.3	5.6	86	0.8	185.2
01/02	15:00–16:00	16.1	2.5	2.2	0.3	11.1	72	1.2	36.3
01/02	18:00–20:00	145.5	14.4	14.4	0.0	7.5	93	0.7	213.1
02/02	16:00–17:00	11.1	1.0	0.6	0.3	11.1	73	0.8	125.5
03/02	16:00–17:00	52.1	3.8	2.7	1.1	10.6	81	0.8	64.5

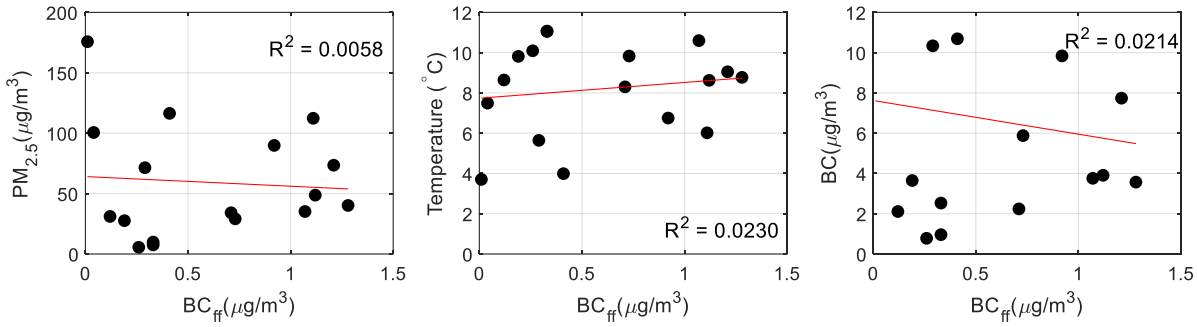

Figure B. 2: Correlation graphs between BC_{ff}, $PM_{2.5}$, BC_{ff} and T, and, finally, BC_{ff} and BC (Papanikolaou et al., 2022b).

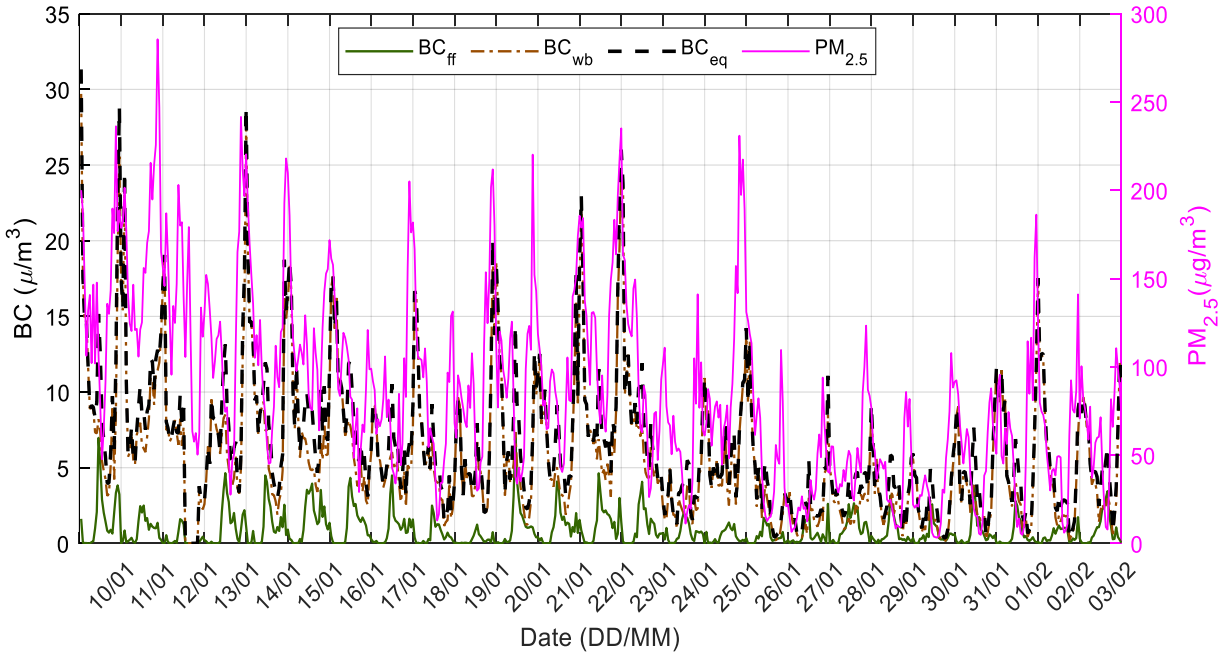

Figure B. 3: Time series analysis of BC, BC_{wb}, BC_{ff}, and $PM_{2.5}$ concentration (μg/m^3) for the period 10 January 2020–3 February 2020 in Ioannina city (Papanikolaou et al., 2022b).

Appendix C: Paper III

atmosphere

MDPI

Article

Australian Bushfires (2019–2020): Aerosol Optical Properties and Radiative Forcing

Christina-Anna Papanikolaou [1,*], Panagiotis Kokkalis [2], Ourania Soupiona [1,3], Stavros Solomos [4], Alexandros Papayannis [1,5], Maria Mylonaki [1], Dimitra Anagnou [1], Romanos Foskinis [1] and Marilena Gidarakou [1]

[1] Laser Remote Sensing Unit, Department of Physics, National and Technical University of Athens, 15780 Zografou, Greece; raniaphd@mail.ntua.gr (O.S.); apdlidar@mail.ntua.gr (A.P.); mylonakimari@mail.ntua.gr (M.M.); dimiana@phys.uoa.gr (D.A.); foskinis@mail.ntua.gr (R.F.); ge16082@central.ntua.gr (M.G.)
[2] Physics Department, Kuwait University, P.O. Box 5969, Safat 13060, Kuwait; panagiotis.kokkalis@ku.edu.kw
[3] Raymetrics S.A., Spartis 32, 14452 Athens, Greece
[4] Research Centre for Atmospheric Physics and Climatology, Academy of Athens, 10680 Athens, Greece; ssolomos@academyofathens.gr
[5] LAPI, École Polytechnique Fédérale de Lausanne, 1015 Lausanne, Switzerland
* Correspondence: papanikolaouca@mail.ntua.gr

Abstract: In the present study, we present the aerosol optical properties and radiative forcing (RF) of the tropospheric and stratospheric smoke layers, observed by the Cloud-Aerosol Lidar and Infrared Pathfinder Satellite Observation (CALIPSO) satellite, during the extraordinary Australian biomass burning (BB) event in 2019–2020. These BB layers were studied and analyzed within the longitude range 140° E–20° W and the latitude band 20°–60° S, as they were gradually transported from the Australian banks to the South American continent. These layers were found to be trapped within the Andes circulation, staying for longer time periods in the same longitude region. The BB aerosols reached altitudes even up to 22 km amsl., and regarding their optical properties, they were found to be nearly spherical (particle linear depolarization ratio (PLDR) < 0.10) in the troposphere; while, in the stratosphere, they were more depolarizing with PLDR values reaching up to 0.20. Fine and ultrafine smoke particles were dominant in the stratosphere, according to the observed Ångström exponent, related to the backscatter coefficients obtained by the pair of wavelengths 532 and 1064 nm ($Å_b$ up to 3), in contrast to the $Å_b$ values in the troposphere ($Å_b$ < 1) indicative of the presence of coarser particles. As the aerosols fend off the source, towards North America, a slightly descending trend was observed in the tropospheric $Å_b$ values, while the stratospheric ones were lightly increased. A maximum aerosol optical depth (AOD) value of 0.54 was recorded in the lower troposphere over the fire spots, while, in the stratosphere, AOD values up to 0.29 were observed. Sharp changes of carbon monoxide (CO) and ozone (O_3) concentrations were also recorded by the Copernicus Atmosphere Monitoring Service (CAMS) in various atmospheric heights over the study region, associated with fire smoke emissions. The tropospheric smoke layers were found to have a negative mean radiative effect, ranging from −12.83 W/m^2 at the top of the atmosphere (TOA), to −32.22 W/m^2 on the surface (SRF), while the radiative effect of the stratospheric smoke was estimated between −7.36 at the TOA to −18.51 W/m^2 at the SRF.

Keywords: Australian bushfires; biomass burning aerosols; tropospheric aerosols; stratospheric aerosols; CALIPSO; optical properties; ozone; carbon monoxide; radiative forcing

check for updates

Citation: Papanikolaou, C.-A.; Kokkalis, P.; Soupiona, O.; Solomos, S.; Papayannis, A.; Mylonaki, M.; Anagnou, D.; Foskinis, R.; Gidarakou, M. Australian Bushfires (2019–2020): Aerosol Optical Properties and Radiative Forcing. *Atmosphere* **2022**, *13*, 867. https://doi.org/10.3390/atmos13060867

Academic Editor: Sergey Nizkorodov

Received: 14 April 2022
Accepted: 24 May 2022
Published: 25 May 2022

Publisher's Note: MDPI stays neutral with regard to jurisdictional claims in published maps and institutional affiliations.

1. Introduction

Smoke aerosols affect the Earth's climate system in both direct and indirect ways, as they can highly absorb the sunlight due to their high content of black carbon (BC), but they can also modify the cloud properties (i.e., cloud life-time, precipitation, and ice formation) [1–6]. Freshly emitted soot particles are initially hydrophobic, but become hydrophilic

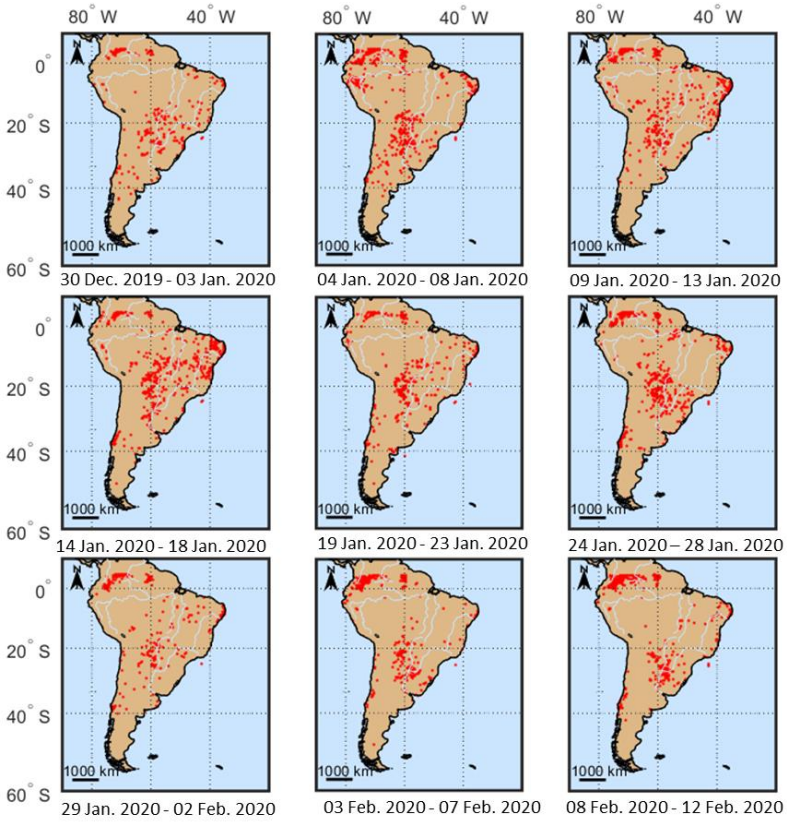

Figure C. 1: Active fires in South America, as obtained by MODIS for the time period December 2019-February 2020, the confidence of the fire spots was set to be above 70% (Papanikolaou et al., 2022a).

Table C. 1: Mean values and std of the relative change of CO and O_3 as they were calculated per region and pressure level of the study area.

Pressure level (hPa)	950	900	850	800	700	600	500	400	300	200
					CO (%)					
GR	8±14	8±13	7±14	6±14	6±14	9±11	11±10	12±12	12±14	14±24
YR	14±12	14±13	14±16	14±18	15±20	18±22	18±20	13±14	8±18	4±21
RR	10±9	10±10	10±11	12±12	11±10	13±14	15±15	17±15	18±19	12±24
BR	3±19	5±22	7±24	9±24	13±24	11±20	8±16	7±16	7±20	10±27
					O_3 (%)					
GR	3±20	5±19	9±22	9±21	8±19	9±17	7±20	26±28	2±29	2±36
YR	10±17	8±16	5±17	7±20	15±21	14±21	12±21	32±30	10±38	18±51
RR	9±23	9±19	8±19	10±20	11±16	10±16	7±19	19±31	2±34	13±44
BR	5±21	6±19	5±17	6±17	7±17	8±18	11±20	26±24	9±35	12±44

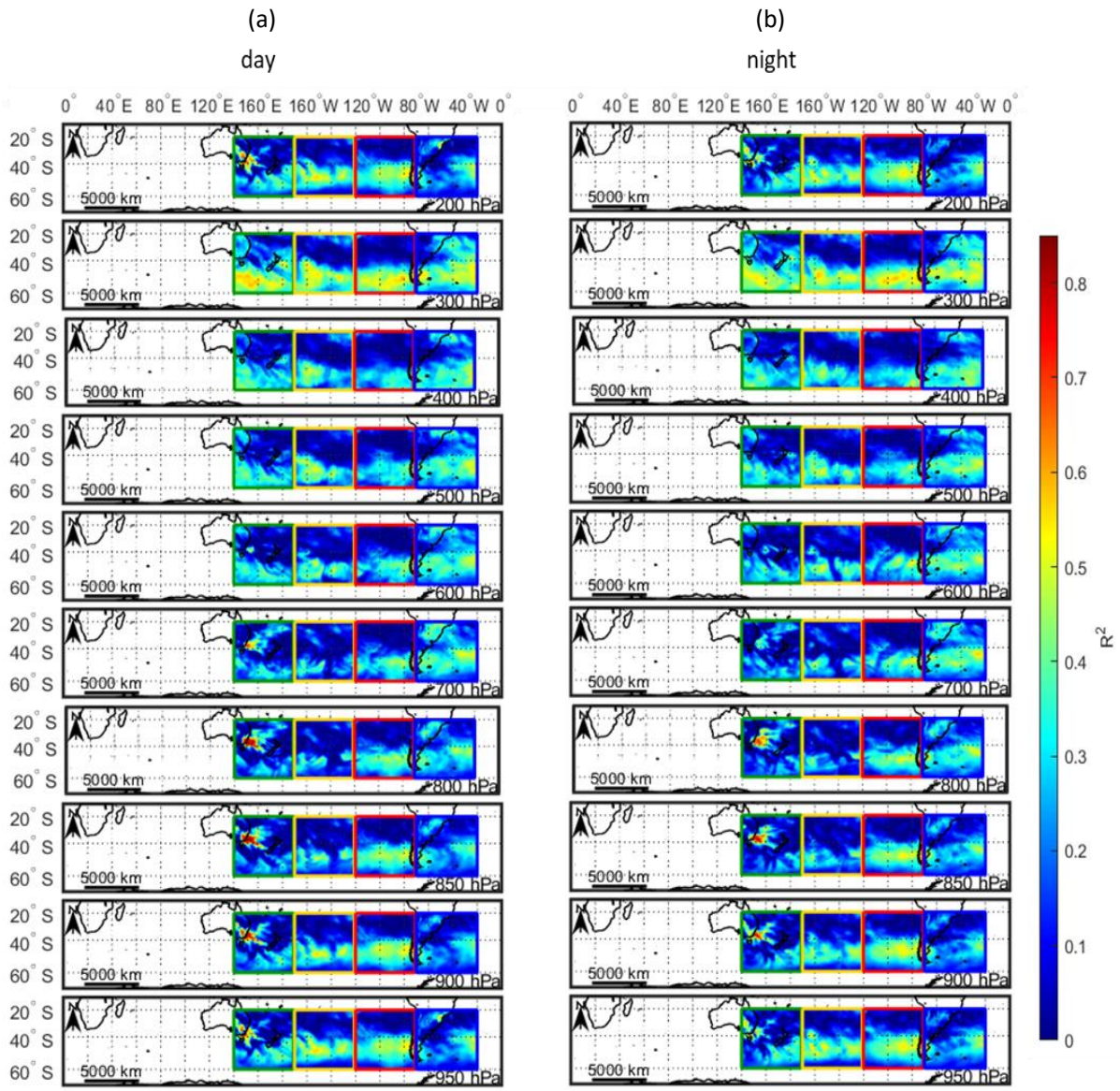

Figure C. 2: R^2 between CO and O_3 relative differences with respect to the base dataset, at various pressure levels (950–200 hPa) (a) during day and (b) night (Papanikolaou et al., 2022a).

Appendix D

Poster I

[Reserved field]

Long-range transport of aerosols over Athens, Greece during Autumn 2020

C. A. Papanikolaou[1], A. Papayannis[1], M. Mylonaki[1], O. Soupiona[1], E. Kralli[1], P. Kokkalis[2], R. Foskinis[1], D. Anagnou[1], M. Gidarakou[1]
papanikolaouca@mail.ntua.gr
(1) Laser Remote Sensing Unit, Department of Physics, National and Technical University of Athens, Zografou, 15780, Greece
(2) Physics Department, Kuwait University, P.O. Box 5969, 13060 Safat, Kuwait

Poster II

Optical properties and radiative forcing of the Hunga Tonga-Ha'apai volcanic eruption in 2022

Panagiotis Kokkalis[1], Christina-Anna Papanikolaou[2], Ourania Soupiona[2], Alexandros Papayannis[2]

[(1)] Physics Department, Kuwait University, P.O. Box 5969, 13060 Safat, Kuwait, E-mail: panagiotis.kokkalis@ku.edu.kw

[(2)] Laser Remote Sensing Unit, Department of Physics, National and Technical University of Athens, Zografou| 15780, Greece, E-mail: papanikolaouca@mail.ntua.gr; raniaphd@mail.ntua.gr; apdlidar@mail.ntua.gr;

Poster III

Extreme Saharan dust event over Athens, Greece (March 2022): aerosol optical properties and radiative impact

C.-A. Papanikolaou[1], A. Papayannis[1,2], D. Anagnou[1], O. Soupiona[1], P. Kokkalis[3], M. Mylonaki[1], M. Gidarakou[1], and R. Foskinis[1,4]

[1]Laser Remote Sensing Unit, Department of Physics, National and Technical University of Athens, Zografou, 15780, Greece
[2]Laboratory of Atmospheric Processes and their Impacts (LAPI), Ecole Polytechnique Fédérale de Lausanne (EPFL), Lausanne, CH-1015, Switzerland
[3]Physics Department, Kuwait University, 5969, 13060 Safat, Kuwait
[4]Environmental Radioactivity Laboratory, N.C.S.R. "Demokritos", Ag. Paraskevi, 15310, Greece
Keywords: lidar, Saharan dust, aerosol optical properties
Presenting author's email: papanikolaouca@mail.ntua.gr

Table D. 1: Mean geometrical and optical properties of the dust layers along with their std during 16/03/22 of the long-lasting dust episode, as observed over Athens by DEPOLE lidar system.

Date-hour	**09:19**	**10:14**	**11:00**	**12:17**	**13:00**	**14:00**	**15:00**		**15:50**		**17:00**	**18:00**
Bottom (km)	4.50	3.84	3.60	3.48	3.36	2.88	2.70	1.98	3.18	3.00	3.90	3.72
Top (km)	6.36	5.94	6.30	5.52	5.40	4.92	3.30	3.00	5.16	5.10	4.86	4.80
CoM (km)	5.40	4.85	4.74	4.32	4.26	4.26	3.41	4.34	2.54	4.16	4.21	4.06
properties@532nm												
$\mathbf{b_{aer}\ (Mm^{-1}sr^{-1})}$	1.67±1.06	-	-	-	7.64±5.19	6.81±3.67	4.10±3.24	3.68±1.79	1.10±0.53	2.06±1.18	3.31±2.76	4.11±2.77
PLDR	0.35±0.14	-	-	-	0.32±0.04	0.29±0.02	0.31±0.01	0.30±0.01	0.36±0.05	0.32±0.03	0.34±0.04	0.31±0.02
properties@355nm												
$\mathbf{b_{ae\ r}(Mm^{-1}sr^{-1})}$	3.39±1.60	3.28±2.03	5.82±3.84	6.17±3.45	7.94±5.38	6.59±3.74	3.78±2.88	2.92±1.48	1.17±0.42	1.90±1.06	3.41±2.58	3.89±2.48
PLDR	0.40±0.10	-	-	-	-	0.35±0.06	0.33±0.02	-	0.31±0.04	0.38±0.16	0.31±0.10	0.31±0.04

Table D. 2: Mean optical properties (a_{aer}, LR, $Å_b$, $Å_a$) of the dust layer along with their std during 16/03/22 nighttime measurement of the Saharan dust episode, as observed over Athens by the EOLE lidar system.

Date-hour /properties@532nm	**16/03/22 17:15 UTC**
a_{aer} (Mm^{-1})	168.93±119.01
LR (sr)	53.22±38.76
properties@355nm	
a_{aer} (Mm^{-1})	174.41±114.67
LR (sr)	44.82±20.70
$Å_b$	0.36±0.19
$Å_a$	0.16±0.25

Table D. 3: Mean geometrical and optical properties of the dust layers along with their std during 17/03/22 of the Saharan dust episode, as observed over Athens by DEPOLE lidar systems.

Date-hour	**17/03/22 08:30 UTC**	
Bottom (km)	2.64	3.54
Top (km)	3.54	4.26
CoM (km)	3.08	3.77
properties@532nm		
b_{aer} ($Mm^{-1}sr^{-1}$)	3.11±1.32	2.19±1.52
PLDR	0.27±0.03	0.24±0.06
properties@355nm		
$b_{ae\,r}$($Mm^{-1}sr^{-1}$)	2.54±0.90	1.53±1.22
PLDR	0.20±0.06	0.28±0.11

LIST OF ABBREVIATIONS

Abbreviation	Description
agl.	Above ground level
amsl.	Above mean sea level
AD	Analog Detection mode
AERONET	AErosol RObotic NETwork
AIAS	Aerosol lidar system
AOD	Aerosol Optical Depth
BB	Biomass Burning
BC	Black Carbon
BC_{ff}	Black carbon from fossil fuel
BC_{wb}	Black Carbon from wood burning
CALIPSO	Cloud-Aerosol Lidar and Infrared Pathfinder Satellite Observation
CALIOP	Cloud-Aerosol Lidar with Orthogonal Polarization
CCN	Cloud Condensation Nuclei
DEPOLE	DEPOLarization lidar systEm
EZ	entrainment zone
EOLE	aErosol and Ozone Lidar systEm
FIRMS	Fire Information for Resource Management System
FT	Free Troposphere
HYSPLIT	Hybrid Single Particle Langrangian Integrated Trajectory Model
IN	Ice Nuclei
IPCC	Intergovernmental Panel on Climate Change
Laser	Light Amplification by Stimulated Emission of Radiation
LibRadtran	Library for Radiative transfer
Lidar	Light Detection and Ranging
LR	Lidar ratio
LRSU	Laser Remote Sensing Unit
LW	Longwave
ML	Mixed Layer
MODIS	Moderate Resolution Imaging Spectroradiometer
NTUA	National Technical University of Athens
OPAC	Optical Properties of Aerosol and Clouds
PANACEA	PANhellenic infrastructure for Atmospheric Composition and climatE change
PBL	Planetary Boundary Layer
PLDR	particle linear depolarization ratio

PMT	Photomultiplier tube
PSC	Polar stratospheric cloud
PC	Photon Counting mode
RCS	Range corrected signal
RL	residual layer
SBL	stable boundary layer
SL	Surface layer
SW	Shortwave
TOA	Top of Atmosphere
VLDR	Volume linear depolarization ratio

LIST OF FIGURES

Figure 1. 1: (left) The vertical structure of the atmosphere, (right) including the planetary boundary layer (Figures from Wallace and Hobbs (2006), modified by Lin *et al.* (2015). 2
Figure 1. 2: Planetary boundary layer structure during a diurnal cycle in a high-pressure region over land. Adapted with permission of Springer, from "An introduction to Boundary Layer Meteorology", Stull (1988). modified by Allaerts et al., (2016). 3
Figure 1. 3: (a) Sources of aerosol, both of anthropogenic and natural origin. Credit: CCSP Strategic Plan (illustrated by P. Rekacewicz), (b) main aerosol sources observed in a global scale (https://svs.gsfc.nasa.gov). 4
Figure 1. 4: Aerosol size distribution and morphology of various aerosol types (Colbeck and Lazaridis, 2014). 5
Figure 1. 5: Desert dust storm (left) and Saharan Dust Outbreak over Northwestern Africa (right) (earthobservatory.nasa.gov)..... 6
Figure 1. 6: (a) Wildfires burning across Australia, along with the smoke cascading off the edge of Australia on 01 January 2020, as captured by NOAA-NASA's Suomi NPP (https://www.nasa.gov), (b) smoke between 15 and 19 km in the stratosphere on 06 January 2020, as measured by CALIPSO, after the most explosive fire activity in Australia (https://earthobservatory.nasa.gov).7
Figure 1. 7: (a) Sea-spray aerosols (https://source.colostate.edu/) and (b) shipborne aerosol measurements in Arctic (https://www.meteorologicaltechnologyinternational.com). 8
Figure 1. 8: (a) India obscured by air pollution in 2017 image and (b) the corresponding aerosol optical depth map, both acquired by MODIS (nasa.org). 9
Figure 1. 9: Eruption of the under-sea volcano Hunga Tonga-Hunga Ha'apai as observed by GOES-17 and Himawari-8 (earthobservatory. nasa.gov). 10
Figure 1. 10: Major bioaerosol components present in the atmosphere, (a) bioaerosol aerodynamic diameter and (b) images of different types of bioaerosol microorganisms view from an electron microscope. (Sharma Ghimire et al., 2019). 11
Figure 1. 11: (a) The change in effective radiative forcing from 1750 to 2019, (b) the effective radiative forcing for specific greenhouse gases and aerosol components (IPCC, 2022)..... 13

Figure 2. 1: Absorption spectra of the most important trace gases in the atmosphere (Takle, 2015). 14
Figure 2. 2: Potential interaction between an incident light beam and a spherical particle (Glasse et al., 2014). 15
Figure 2. 3: Atmospheric scattering as a function of particle radius and incident radiation wavelength (Wallace and Hobbs, 2006). 16
Figure 2. 4: (a) Energy level diagram of Rayleigh scattering, Raman scattering and fluorescence (Mosca et al., 2021), (b) Atmospheric Raman backscatter spectrum for a stimulation wavelength of 355 nm (Wandinger, 2005). 17

Figure 2. 5: Diagram illustrating the interaction between linearly polarized light with spherical and non-spherical particles (Baumgardner et al., 2014). 17
Figure 2. 6: Typical lidar system layout showing the transmission, receiver and data acquisition sub-systems (Sharma et al., 2009). 19
Figure 2. 7: Flowchart of the CALIPSO aerosol subtype selection scheme for tropospheric and stratospheric aerosols, in V3 and V4 of CALIPSO products (Kim et al., 2018b). 27
Figure 2. 8: CALIPSO algorithm used in processing the Level 2 APro data, from version 3.01 and on, developed in MATLAB environment. 28

Figure 3. 1: (a) Time Averaged Map of Combined Dark Target and Deep Blue AOD at 550 nm for land and ocean: Mean daily 1° (MODIS-Aqua MYD08_D3 v6.1) from 16 August 2018 and for a 10-day period. (b) The 10-day forward HYSPLIT trajectories starting on 16 August and ending on 10 August. The red dots correspond to active fires observed in BC, Canada, by MODIS with confidence greater than 80%. Magenta and green lines correspond to nighttime and daytime CALIPSO orbits, respectively. Red, yellow, purple and cyan boxes correspond to the four subregions (R1–R4) of the smoke motion (Papanikolaou et al., 2020). 31
Figure 3. 2: (a) 10-day forward ensemble air mass trajectories starting on 16 August (11:00 UTC), as provided by HYSPLIT. Different color-lines of the forward trajectories correspond to trajectories for all-possible offsets in longitude, latitude and altitude according to the ensemble analysis). (b) 10-day-forward ensemble air mass trajectories, along with selected CALIPSO curtains (Papanikolaou et al., 2020). 33
Figure 3. 3: Vertically resolved aerosol optical properties: (a) b_{aer} 532 nm, (b) $Å_b$ 532/1064 nm, (c) PLDR at 532 nm and (d) aerosol typing according to the CALIPSO algorithm (M: marine, D: Dust, PC: Polluted Continental, CC: Clean Continental, PD: Polluted Dust, S: Smoke), as retrieved from the nighttime CALIOP orbit on 20 August. The coordinates used to derive these properties were 42.5° N and 73.8° W. Green shadowed lines correspond to the standard deviation for each aerosol property (Papanikolaou et al., 2020). 34
Figure 3. 4: CALIPSO total attenuated backscatter coefficient at 532 nm and aerosol subtypes versus altitude, latitude and longitude for nighttime and daytime orbits (16^{th}-26^{th} of August 2018) (Papanikolaou et al., 2020). 36
Figure 3. 5: Percentages of aerosol layers mixing types for the total event, types found in percentages less than 3%, are not presented with numbers in the figure (Papanikolaou et al., 2020). 37
Figure 3. 6: Aerosol layers mixtures according to (a) their altitude (amsl.), (b) b_{aer} at 532 nm, (c) PLDR at 532 nm, (d) $Å_b$ at 532/1064 nm, for the total event (S: pure smoke layers, PD: smoke mixed with polluted dust layers, CC: smoke mixed with clean continental layers, PC: smoke mixed with polluted continental layers, D: smoke mixed with dust layers and M: smoke mixed with marine layers) (Papanikolaou et al., 2020). 37

Figure 3. 7: Percentages of the aerosol layers mixing types for the subregions (R1–R4). Aerosol types found in percentages less than 3%, are not presented with numbers in the figure (Papanikolaou et al., 2020). 40
Figure 3. 8: Aerosol layers mixtures according to (a) their altitude (amsl.), (b) b_{aer} at 532 nm, (c) PLDR at 532 nm, (d) $Å_b$ (532/1064 nm). R1–R4 (left to right) correspond to the four subregions (S: pure smoke layers, PD: smoke mixed with polluted dust layers, CC: smoke mixed with clean continental layers, PC: smoke mixed with polluted continental layers, D: smoke mixed with dust layers and M: smoke mixed with marine layers) (Papanikolaou et al., 2020)..... 42
Figure 3. 9: Pure smoke aerosol layers according to (a) their altitude (amsl.) and relevant optical properties: (b) b_{aer} at 532 nm, (**c**) PLDR at 532 nm, (**d**) AE related to β (532/1064 nm). R1–R4 correspond to the four subregions (Papanikolaou et al., 2020)..... 44
Figure 3. 10: (a) PANACEA sites during the winter campaign 2020; (b) AIAS mobile lidar system location (39.65° N, 20.85° E) inside the Ioannina basin. The map shows the Ioannina city, the Pamvotis lake and the surrounding area (Google Earth Pro v7.1.5. Epirus Region, Greece) (Papanikolaou et al., 2022b). 48
Figure 3. 11: Spatio-temporal evolution of the range-corrected lidar signal at 532 nm, for the days used in this study, during the PANACEA campaign, in Ioannina city (Papanikolaou et al., 2022b). 50
Figure 3. 12: Vertical distribution of b_{aer} ($Mm^{-1}sr^{-1}$) and PLDR at 532 nm, as observed by the AIAS mobile depolarization system (Papanikolaou et al., 2022b). 54
Figure 3. 13: Temporal variation of (a) the PBL altitude (amsl.; black rhombus) along with the base and top of each aerosol layer (AL; colored bars) (km) and the corresponding mean values of (b) b_{aer} and std ($Mm^{-1}sr^{-1}$) and (c) PLDR and std at 532 nm, as obtained by the AIAS mobile depolarization lidar, along with the (d) wind speed (m/s) and direction (°), (e) $PM_{2.5}$ mass concentrations (μg/m³), T (°C), RH (%), (f) the BC mass concentrations (μg/m³) along with the contribution of the fossil fuel and wood burning to the total BC mass concentrations, during the PANACEA winter campaign in Ioannina. All data presented are averaged for the same time periods during which the lidar profiles were retrieved (Papanikolaou et al., 2022b). 55
Figure 3. 14: Correlation graphs between: (a) BC_{wb} and $PM_{2.5}$, (b) BC_{wb} and T and finally, (c) $PM_{2.5}$ and T, along with the linear fit (red solid line) and the corresponding coefficients of determination R^2 (Papanikolaou et al., 2022b)..... 58
Figure 3. 15: (a) Spatio-temporal evolution of the range-corrected lidar signal at 532 nm, and (b) the vertical distribution of b_{aer} ($Mm^{-1}sr^{-1}$) and PLDR at 532 nm, as observed by the AIAS mobile lidar on 22 January 2020 between 14:39 – 15:41 UTC over the city of Ioannina. The 3-colored-shadowed rectangles represent the geometrical boundaries of the studied aerosol layers. The black dashed line represents the mean PBLH. (c) upper graph: Temporal evolution of the $PM_{2.5}$ mass concentration (μg/m³), versus T (°C) and RH (%); lower graph: BC mass concentrations (μg/m³) at ground level, along with the contribution of the fossil fuel (BC_{ff}) and wood burning (BC_{wb}) to the total BC concentrations. (d) the wind speed and direction (hourly mean), during the measurement time (Papanikolaou et al., 2022b). 60

Figure 3. 16: (a) Spatio-temporal evolution of the range-corrected signal at 532 nm, (b) the vertical distribution of b_{aer} ($Mm^{-1}sr^{-1}$) and PLDR at 532 nm, as observed by the AIAS mobile lidar on 01 February 2020 between 14:32 and 19:31 UTC over the city of Ioannina. The 2-colored-shadowed rectangle represent the geometrical boundaries of the studied aerosol layers. The black dashed line represents the mean PBLH. (c) upper graph: Temporal evolution of the $PM_{2.5}$ mass concentration (μg/m³), versus T (°C) and RH (%); lower graph: BC mass concentrations (μg/m³) at ground level, along with the contribution of the fossil fuel (BC_{ff}) and wood burning (BC_{wb}) activities to the total BC concentrations. (d) the wind speed and direction (hourly mean), during the measurement time (Papanikolaou et al., 2022b). 62
Figure 3. 17: (a) Spatio-temporal evolution of the range-corrected signal at 532 nm, (b) the vertical distribution of b_{aer} ($Mm^{-1}sr^{-1}$) and PLDR at 532 nm, as observed by the AIAS mobile lidar during the 26 of January 2020 between 08:29 and 09:04 UTC over the city of Ioannina, the 2-colored-shoadowed rectangles represent the geometrical boundaries of the studied aerosol layers. The black dashed line represents the PBLH. (c) the $PM_{2.5}$ concentration (μg/m³), the T (°C), RH (%) and the BC levels (μg/m³) along with the participation of the fossil fuel and wood burning to the total BC concentrations. (d) the wind speed and direction (hourly mean), during the measurement time. (e) The HYSPLIT air mass back trajectories for the 2 aerosol layers (Papanikolaou et al., 2022b). 64
Figure 3. 18: (a) Active fires and (b) burned area according to burn date, as obtained by MODIS for the time period 25 December 2019- 12 February 2020 (Papanikolaou et al., 2022a). 69
Figure 3. 19: Biomass burning aerosol's height, as calculated by the FLEXPART model for the under-study period (25 December 2019–12 February 2020 (Papanikolaou et al., 2022a). 71
Figure 3. 20: Percentages of BB aerosol layers found in each under-study region (from left to right: GR, YR, RR, BR) and altitude category (chromatic scale). The numbers in the parenthesis next to the percentages refer to the accumulated number of observed layers (Papanikolaou et al., 2022a)..... 74
Figure 3. 21: BB aerosol layers according to (a) their CoM (amsl.), (b) b_{aer}, (c) a_{aer}, (d) PLDR at 532 nm, (e) $Å_b$ (532/1064 nm), (f) AOD at 532 nm. GR, YR, RR and BR (left to right) correspond to the four under-study regions, while the different colors indicate the different height-range categories (Papanikolaou et al., 2022a). 76
Figure 3. 22: (a) Relative differences of CO and O_3 calculated for the study period (25 December 2019 to 12 February 2020) over the study area (20° to 60° S and 140° E to 20° W) with respect to the same days through the years 2004–2019 (base period) (b) R^2 between CO and O_3 relative differences with respect to the base dataset, at various pressure levels (950–200 hPa) (Papanikolaou et al., 2022a). 81
Figure 3. 23: Net radiative forcing values per case (illustrated by colored solid circles) at top of atmosphere (TOA) (a), inside the smoke layers (b), and at surface (SRF) (c), versus the SZA (I), the AOD (II), and the CoM (III) of the aerosol layers. The different colors correspond to the tropospheric (cyan) and stratospheric (magenta) BB aerosol layers, while the solid lines and

shadowed areas correspond to the mean values and std of the RF_{NET} at TOA inside the layer and at the SRF (Papanikolaou et al., 2022a). 83
Figure 3. 24: The colored (magenta, blue and green) dots on the map represent the active fires retrieved by MODIS, with confidence greater than 80% and given for a 5-day period per case, respectively. The CALIPSO orbits (magenta, blue and green colored dashed lines) are provided for the corresponding dates over the source areas from where the air masses originated for each studied case according to HYSPLIT runs. The air mass backward trajectories for aerosols arriving over Athens on 14 September (magenta), 30 September (blue and cyan) and 01 October 2020 (dark green, light green and green) provided by the HYSPLIT model. 87
Figure 3. 25: CALIPSO aerosol subtypes for the 08 September 2020 (08-09-20T09-11-41ZN), 19 September 2020 (19-09-20T06-15-50ZN and 19-09-20T09-32-50ZN)and 22, 23 and 27 September 2020 (22-09-20T06-30-29ZN, 23-09-20T03-51-12ZNand 27-09-20T08-00-45ZN), close to the source of the airmass that reached Athens on 14 and 30 September and 01 October 2020, showing smoke and polluted dust aerosol layers in altitudes between 1 and 15 km close to the wildfire source. 88
Figure 3. 26: (a) left graph: Spatio-temporal evolution of the range-corrected lidar signal at 355 nm; Right graph vertical distribution of b_{aer} ($Mm^{-1}sr^{-1}$) (blue line) and PLDR at 355 nm (purple line), as observed by the DEPOLE lidar system on 14 September 2020 (17:19 –18:19 UTC), (b) on 30 September 2020 (05:54-06:31 UTC) and (c) on 01 October 2020 2020 (17:09-17:08 UTC), over Athens, Greece. 89
Figure 3. 27: Net radiative forcing at TOA and at SRF at 06:31 UTC on 30 September 2020, the sza was equal to 64.38° over the NTUA lidar station. 90

Figure 4. 1: OMI SO_2 vertical column over Australia on 18 January 2022, with SO_2 emission from Hunga-Tonga volcano. 93
Figure 4. 2: The CALIPSO orbits (magenta and green colored lines) are provided for the corresponding dates after 1-4 days transport from the crater. 94
Figure 4. 3: The inputs used to estimate the volcanic eruption radiative forcing by LibRadtran model. 95
Figure 4. 4: CALIPSO total attenuated backscatter coefficient at 532 nm and aerosol subtypes versus altitude, latitude and longitude for nighttime and daytime orbits (16-19 January 2022).95
Figure 4. 5: Vertical distribution of the optical properties (b_{aer}, a_{aer}, PLDR $Å_b$ and LR at 532 nm), according to CALIPSO observation (16-19 January 2022). 96
Figure 4. 6: (a) Geometrical and (b-f) mean optical properties of each aerosol layer observed by CALIPSO along with their std, for the time period of 16 – 19 January 2022. 96
Figure 4. 7: SO_2 observations obtained by OMI over the study region, during the time period between 11 and 20 January 2022. 98
Figure 4. 8: Aerosol optical depth (1020, 870, 667, 551, 532, 490, 443 and 412 nm) and Ångström exponent (440- 675 nm and 440- 870 nm) as observed over the AERONET Lucinda station in Eastern Australia, when the volcanic plume reached the Australian banks on 17 January 2022.99

Figure 4. 9: Net radiative forcing values for each event (Hunga Tonga volcanic event is illustrated by grey-colored bars and Australian smoke event by black-colored ones) at TOA and SRF..... 100

Figure 5. 1: 120 h backward trajectories for air masses arriving over Athens during 16 and 17 March, per hour of measurement (09:19 - 18:20 UTC and 08:24 – 11:00 UTC), for arrival heights of approximately the center of the main observed dust layer (2.54 – 5.40 km). The different colors in the trajectories represent the different altitudes that the air mass traveled until it reached the lidar station. 103
Figure 5. 2: Map of the aerosol optical depth calculated by NAAPS model during 16th and 17th March 2022, for three types of aerosols (http://www.nrlmry.navy.mil/aerosol/)..... 103
Figure 5. 3: Time series of mean hourly (a) AOD values at 1640, 1020, 870, 675, 500, 440, 380 and 340 nm and (b) Å at 500/870, 440/870, 440/675, 380/500, 340/440 nm and (c) fine- and coarse-mode fraction of aerosols, measured over Athens during 16-17 March 2022. Red colored rectangles frame the time periods when the values correspond to the measured dust event. 105
Figure 5. 4: Vertical distribution of the optical properties (b_{aer} and PLDR at 355 and 532 nm) of the aerosol layers observed over Athens on 16 March 2022 per hour of measurement (09:19 - 18:20 UTC), different colors correspond to different measurement hour. 106
Figure 5. 5: Spatio-temporal evolution of the range-corrected lidar signal at 532 nm, as observed by DEPOLE lidar over Athens during 16-17 March 2022. 106
Figure 5. 6: Vertical distribution of the optical properties (a_{aer}, LR and $Å_b$, $Å_a$ at 355 and 532 nm) of the aerosol layer observed over Athens on 16 March 2022 during the nighttime EOLE measurement (17:13-18:20 UTC). 107
Figure 5. 7: Vertical distribution of the optical properties (b_{aer} and PLDR at 355 and 532 nm) of the aerosol layers observed over Athens on 17 March 2022 (08:30-09:30 UTC), the different colors correspond to different wavelength. 108
Figure 5. 8: Net radiative forcing at top of atmosphere (TOA) and at surface (SRF) at 09:20 UTC on 16 March 2022, the SZA was equal to 42.71° over the NTUA lidar station..... 108

Figure B. 1: The terrain Google Earth map of the Ioannina basin showing the city and the and the surrounding mountains, along with their names and top's height (Papanikolaou et al., 2022b). 155

Figure B. 2: Correlation graphs between $BC_{ff,}$ $PM_{2.5}$, BC_{ff} and T, and, finally, BC_{ff} and BC (Papanikolaou et al., 2022b). 158
Figure B. 3: Time series analysis of BC, BC_{wb}, BC_{ff}, and $PM_{2.5}$ concentration ($\mu g/m^3$) for the period 10 January 2020–3 February 2020 in Ioannina city (Papanikolaou et al., 2022b). 158

Figure C. 1: Active fires in South America, as obtained by MODIS for the time period December 2019-February 2020, the confidence of the fire spots was set to be above 70% (Papanikolaou et al., 2022a)..... 160

Figure C. 2: R^2 between CO and O_3 relative differences with respect to the base dataset, at various pressure levels (950–200 hPa) (a) during day and (b) night (Papanikolaou et al., 2022a)..... 161

LIST OF TABLES

Table 3. 1: Descriptive statistics of the altitude, b_{aer}, PLDR and $\mathring{A}_b$ values for different aerosol types for the total event: mean, standard deviation (std), median, maximum value (max), minimum value (min), 75^{th} and 25^{th} percentile for all variables. 39
Table 3. 2: Optical properties of smoke aerosols measured during Canadian and North American biomass burning events, as cited in the relevant literature (2002–today). 45
Table 3. 3: PLDR (532 nm) values of fresh BB aerosols as cited in the relevant literature (2012–today). 56
Table 3. 4: Geometrical (top, bottom, mean altitude) and optical (mean b_{aer} and PLDR) properties of the studied aerosol layers, as observed by the DEPOLE lidar system at 355 nm over Athens on 14 and 30 September 2020 and 01 October 2020. 89

Table 4. 1: Aerosol geometrical and optical properties of the volcanic ash plume, as obtained by CALIPSO during 16-19 January 2022. 97

Table A 1: Descriptive Statistics for different aerosol types for Region 1 (R1): mean, standard deviation (std), median, maximum value (max), minimum value (min), 75th and 25th percentile for all variables. 151
Table A 2: Descriptive Statistics for different aerosol types for Region 2 (R2): (std), median, maximum value (max), minimum value (min), 75th and 25th percentile for all variables. 151
Table A 3: Descriptive Statistics for different aerosol types for Region 3 (R3): mean, standard deviation (std), median, maximum value (max), minimum value (min), 75th and 25th percentile for all variables. 152
Table A 4: Descriptive Statistics for pure smoke aerosols in all four regions: mean, standard deviation (std), median, maximum value (max), minimum value (min), 75th and 25th percentile for all variables. 153

Table B. 1: Date, time, and mean height of the aerosol layers (ALH; grey shadowed cells represent the PBLH and mean values inside the PBL), mean b_{aer}, and PLDR at 532 nm inside the aerosol layers, as observed by the AIAS lidar system, during the PANACEA winter campaign. 155
Table B. 2: Hourly averaged data of PM2.5 and BC, along with the meteorological parameters (T, RH, wind speed, and direction), during the PANACEA winter campaign in Ioannina. All data presented are averaged for the same time periods during which the lidar profiles were retrieved. 157

Table C. 1: Mean values and std of the relative change of CO and O_3 as they were calculated per region and pressure level of the study area. 160

Table D. 1: Mean geometrical and optical properties of the dust layers along with their std during 16/03/22 of the long-lasting dust episode, as observed over Athens by DEPOLE lidar system. 163
Table D. 2: Mean optical properties (a_{aer}, LR, $Å_b$, $Å_a$) of the dust layer along with their std during 16/03/22 nighttime measurement of the Saharan dust episode, as observed over Athens by the EOLE lidar system. 164
Table D. 3: Mean geometrical and optical properties of the dust layers along with their std during 17/03/22 of the Saharan dust episode, as observed over Athens by DEPOLE lidar systems. ... 164

CURICULUM VITAE

Education

Ph.D. in Atmospheric Physics
Nov 2019 – Feb 2023

National Technical University of Athens
Advisor: Prof. Alexandros Papayannis
Dissertation: *Study of aerosol properties at local and global scale during extreme aerosol events using ground – based and spaceborne remote sensing techniques*

M.Sc. in Environmental Physics
Oct 2017 – Jun 2019

National and Kapodistrian University of Athens
Advisor: Assistant Prof. Eleni Giannakaki
Dissertation: *Optical properties of Canadian biomass burning particles over Europe observed with CALIPSO and ground – based lidar systems*
Degree 8.53/10

B.A. in Physics
Sep 2010 – Mar 2016

University of Crete
Degree 7.13/10

Participation in Research Programs

03.06.2019 – 31.04.2022: National Technical University of Athens, Athens, Greece, (research program PANACEA).

01.08.2018 – 28.02.2019: National Observatory of Athens, Penteli, Athens, Greece (European Program HORIZON 2020 "ACTRIS – 2: Aerosols Clouds and Trace gases Research Infrastructure".

Participation in Measurement Campaigns

03.06.2019 – 31.04.2022: National Technical University of Athens, Athens, Greece, (research program PANACEA).

23.09.2021–30.11.2021: Cloud - AerosoL InteractionS in the Helmos background TropOsphere (CALISHTO).

08.05.2020 – 31.05.2020: EARLINET/ACTRIS near real time (NRT) campaign during COVID – 19 crises

10.01.2020 – 10.02.2020: 2nd PANACEA measurement campaign winter 2020 (Greece)

10.07.2019 – 10.08.2019: 1st PANACEA measurement campaign summer 2019 (Greece)

Participation in Conferences/Schools/Workshops

22.09.2022 – 24.09.2022: 10th Conference of Metsovion Research Center (Metsovo, Greece)

04.09.2022 – 09.09.2022: 11th *International Aerosol Conference* (Athens, Greece)

26.06.2022 – 01.07.2022: 30th International Laser Radar Conference (Montana, USA, virtual)

16.11.2021 – 18.11.2021: European Lidar Conference (Granada, Spain)

13.10.2021 – 14.10.2021: ACTRIS: Aerosol Remote Sensing workshop (ARS; virtual)

18.11.2020 – 20.11.2020: 2nd European Lidar Conference (virtual)

26.10.2020 – 28.10.2020: ACTRIS: Aerosol Lidar (ARS – ARES) Workshop

29.09.2020 – 01.10.2020: 2nd Scientific Conference PANACEA

30.06.2020 – 02.07.2020: Aerosol lidar workshop (ACTRIS)

23.09.2019 – 24.09.2019: 1st cientific Conference PANACEA (Heraklion, Greece)

24.06.2019 – 28.06.2019: 29th International Laser Radar Conference (Hefei, China)

04.12.2018 – 06.12.2018: Actris – 2 WP2 SCC Winter School (Potenza, Italy)

03.07.2019 – 05.07.2018: 1st uropean Lidar Conference (Thessaloniki, Greece)

Informal Thesis Supervision

03.2022 – 02.2023: National Technical University of Athens (Greece), Applied Mathematics and Physical Sciences, Physics Department.

Title: "Geometrical and optical properties of aerosols and clouds using active and passive remote sensing".

03.2022 – 03.2023: National Technical University of Athens (Greece), Applied Mathematics and Physical Sciences, Physics Department and University of Patras (Greece), Engineering School, Department of Chemical Engineering.

Title: "Study of atmospheric aerosols with the lidar technique".

Skills

Experimental skills: Operation and Quality control of lidar measurements

Software skills: MATLAB, IDL (beginner level), Python (beginner level), Single Calculus Chain (SCC), retrieval and processing of Cloud-Aerosol Lidar with Orthogonal Polarization (CALIOP) measurements

Languages

Greek, English, German

Presentations in Conferences

"Extreme Saharan dust event over Athens, Greece (March 2022): aerosol optical properties and radiative impact" | 2022
11th International Aerosol Conference, 5-9 September 2022, Athens, Greece | poster presentation

"Australian bushfires 2019-2020: aerosol optical and radiative properties" | 2022
30th International Laser Radar Conference, 26 June-1July 2022, Athens, Greece | oral presentation

"Long-range transported aerosols over Athens, Greece during Autumn 2020" | 2021
3rd European Lidar Conference, 16-18 November 2021, Granada, Spain | poster presentation

"Biomass burning aerosol properties retrieved from satellite observations" |2020
2nd European Lidar Conference, 18-20 November 2020, Web Conference| poster presentation

"The impact of biomass burning for heating on Ioannina city's air quality during winter time" |2020
2nd PANACEA Conference, 29 September – 1 October 2020 | oral presentation

"Aerosol detection in the FT over the city of Volos, Greece, during the 1st PANACEA campaign (July 2019)" |2019
1st PANACEA Conference, 23-24 September 2019, Heraklion, Greece| poster presentation

"Optical properties of Canadian biomass burning aerosols observed with CALIPSO and ground-based lidar systems" |2019
29th International Laser Radar Conference, 24-28 June 2019, Hefei, China| poster presentation

Participation in Conferences, Schools and Workshops

22.09.2022 – 24.09.2022: 10th Conference of Metsovion Research Center (Metsovo, Greece)

04.09.2022 – 09.09.2022: 11th International Aerosol Conference (Athens, Greece)

26.06.2022 – 01.07.2022: 30th International Laser Radar Conference (Montana, USA, virtual)

16.11.2021 – 18.11.2021: European Lidar Conference (Granada, Spain)

13.10.2021 – 14.10.2021: ACTRIS: Aerosol Remote Sensing workshop (ARS; virtual)

18.11.2020 – 20.11.2020: 2nd European Lidar Conference (virtual)

26.10.2020 – 28.10.2020: ACTRIS: Aerosol Lidar (ARS – ARES) Workshop

29.09.2020 – 01.10.2020: 2nd Scientific Conference PANACEA

30.06.2020 – 02.07.2020: Aerosol lidar workshop (ACTRIS)

23.09.2019 – 24.09.2019: 1st Scientific Conference PANACEA (Heraklion, Greece)

24.06.2019 – 28.06.2019: 29th International Laser Radar Conference (Hefei, China)

04.12.2018 – 06.12.2018: Actris – 2 WP2 SCC Winter School (Potenza, Italy)

03.07.2019 – 05.07.2018: 1st European Lidar Conference (Thessaloniki, Greece)

Publications

1. Gkikas, A., Gialitaki, A., Binietoglou, I., Marinou, E., Tsichla, M., Siomos, N., Paschou, P., Kampouri, A., Voudouri, K. A., Proestakis, E., Mylonaki, M., **Papanikolaou, C.-A.**, Michailidis, K., Baars, H., Straume, A. G., Balis, D., Papayannis, A., Parrinello, T., and Amiridis, V.: **First assessment of Aeolus L2A particle backscatter coefficient retrievals in the Eastern Mediterranean,** Atmospheric Measurement Techniques Discussion, [preprint], in review, 2022.
2. **Papanikolaou, C.-A.**, Kokkalis, P., Soupiona, O., Solomos, S., Papayannis, A., Mylonaki, M., Anagnou, D., Foskinis, Gidarakou, M.-E.: **Australian bushfires 2019-2020: aerosol optical properties and radiative forcing,** Atmosphere, 2022.
3. **Papanikolaou, C.-A.**, Papayannis, A., Maria Mylonaki, M., Foskinis, R., Kokkalis, P., Liakakou, E., Stavroulas, I., Soupiona, O., Hatzianastassiou, N., Gavrouzou, M., Kralli, E., Anagnou, D.: **Vertical profiling of fresh biomass burning aerosol optical properties over the Greek urban city of Ioannina, during the PANACEA winter campaign,** Atmosphere, 2022.
4. Mylonaki, M., Papayannis, A., Anagnou, D., Veselovskii, I., **Papanikolaou, C.-A.**, Kokkalis, P., Soupiona, O., Foskinis, R., Gidarakou, M., Kralli, E.: **Optical and Microphysical Properties of Aged Biomass Burning Aerosols and Mixtures, Based on 9-Year Multiwavelength Raman Lidar Observations in Athens, Greece,** Remote Sensing, 2021.
5. Kokkalis, P., Soupiona, O., **Papanikolaou, C.-A.**, Foskinis, R., Mylonaki, M., Solomos, S., Vratolis, S., Vasilatou, V., Kralli, E., Anagnou, D., Papayannis, A**.: Radiative Effect and Mixing Processes of a Long-Lasting Dust Event over Athens, Greece, during the COVID-19 Period,** Atmosphere, 2021.
6. Mylonaki, M., Giannakaki, E., Papayannis, A., **Papanikolaou, C.-A.**, Komppula, M., Nicolae, D., Papagiannopoulos, N., Amodeo, A., Baars, H., and Soupiona, O.: **Aerosol type classification analysis using EARLINET multiwavelength and depolarization lidar observations,** Atmospheric Chemistry and Physics, 2021.
7. Mylonaki, M., Giannakaki, E., Papayannis, A., **Papanikolaou, C.-A.**, Komppula, M., Nicolae, D., Papagiannopoulos, N., Amodeo, A., Baars, H., and Soupiona, O.: **Aerosol type classification analysis using EARLINET multiwavelength and depolarization lidar observations,** Atmospheric Chemistry and Physics, 2021.
8. Mylonaki, M., Papayannis, A., **Papanikolaou, C.-A.**, Foskinis, R., Soupiona, O., Maroufidis, I., Anagnou, D., Kralli, E.: **Tropospheric vertical profiling of the aerosol backscatter coefficient and the particle linear depolarization ratio for different aerosol mixtures during the PANACEA campaign on July 2019 at Volos, Greece,** Atmospheric Environment, 2021.
9. Soupiona, O., Papayannis, A., Kokkalis, P., Foskinis, R., Sánchez Hernández, G., Ortiz-Amezcua, P., Mylonaki, M., **Papanikolaou, C.-A.**, Papagiannopoulos, N., Samaras, S., Groß, S., Mamouri, R.-E., Alados-Arboledas, L., Amodeo, A., and Psiloglou, B., **EARLINET observations of Saharan dust intrusions over the northern Mediterranean region (2014–2017): properties and impact on radiative forcing**, Atmospheric Chemistry and Physics, 20, 15147–15166, 2020.

10. **Papanikolaou, C.-A.**, Giannakaki, E., Papayannis, A., Mylonaki, M., Soupiona, O.: **Canadian Biomass Burning Aerosol Properties Modification during a Long-Ranged Event on August 2018**, Sensors, 2020.
11. Soupiona, O., S. Samaras, P. Ortiz Amezcua, C. Böckmann, A. Papayannis, G. Moreira, J. Benavent-Oltra, J.L. Rascado, Bedoya-Velásquez A.E., Olmo F.J., Román R., Kokkalis P., Mylonaki M., Arboledas L., **Papanikolaou C.-A.**, Foskinis R.: **Retrieval of optical and microphysical properties of transported Saharan dust over Athens and Granada based on multi-wavelength Raman lidar measurements: Study of the mixing processes,** Atmospheric Environment, 2019.
12. Solomos, S., Bougiatioti, A., Soupiona, O., Papayannis, A., Mylonaki M., **Papanikolaou, C.-A.**, Argyrouli, A., Nenes, A.: **Effects of regional and local atmospheric dynamics on the aerosol and CCN load over Athens,** Atmospheric Environment, 2019.

Proceedings of International Conferences

1. **Papanikolaou, C.-A.**, Papayannis, A., Anagnou, D., Soupiona, O., Kokkalis, P., Mylonaki, M., Gidarakou, M., and Foskinis, R.:"Extreme Saharan dust event over Athens, Greece (March 2022): aerosol optical properties and radiative impact", Proc. 11th International Aerosol Conference, 5-9 September 2022, Athens, Greece.
2. Papayannis, A., **Papanikolaou, C.-A.**, Anagnou, D., Foskinis, R., Moutafidou, A., Aktypis, A., Eleftheriadis, K., Nenes, A., Gini, M., Motos, G., Fetfatzis, P., Gidarakou, M., Granakis, K., Zografou, O., Spitieri, C., Diapouli, E., Komppula, M., Vakkari, Berne, A., Vogel, F., Möhler, O., Kokkalis, P., Mylonaki, M., Soupiona, O., Solomos, S., Podvin, T., Goloub, P., Kaltsonoudis, C., Pandis, S.: "Highlights of tropospheric aerosol transport from a coastal to a high-altitude station based on *in situ* and remote sensing measurements during the CALISHTO-HELMOS Campaign", Proc. 11th International Aerosol Conference, 5-9 September 2022, Athens, Greece.
3. Papayannis, A., **Papanikolaou, C.-A.**, Anagnou, D., Foskinis, Soupiona, O., Mylonaki, M., Gidarakou, M.: "Optical properties and radiative forcing estimations of high-altitude aerosol transport based on laser remote sensing techniques: Highlights from the CLIMPACT Campaign at the Helmos mountain (September 2021)", Proc. 11th International Aerosol Conference, 5-9 September 2022, Athens, Greece.
4. **Papanikolaou, C.-A.**, Papayannis, A., Mylonaki, M., Soupiona, O., Kralli, E., Kokkalis, P., Foskinis, R., Anagnou, D., M. Gidarakou, M.," Long-range transported aerosols over Athens, Greece during Autumn 2020", Proc. 3rd European Lidar Conference, 16-18 November 2021, Granada, Spain.
5. **Papanikolaou, C.-A.**, Papayannis, A., Mylonaki, M., Soupiona, O., Giannakaki, E., Foskinis, R.,"Australian bushfires during January 2020: biomass burning aerosol properties retrieved from satellite observations", Proc. 2nd European Lidar Conference, 18-20 November 2020, Web Conference.
6. Mylonaki, M., Papayannis, A., **Papanikolaou, C.-A.**, Foskinis, R., Soupiona, O., Maroufidis, I.,"Aerosol Typong from AIAS Depolarization Lidar Data, Observed over Volos City, during PANACEA Campaign, July 2019", Proc. 2nd European Lidar Conference, 18-20 November 2020, Web Conference.
7. Papayannis, A., **Papanikolaou, C.-A.**, Foskinis, R., Mylonaki, M., Soupiona, O., Kralli, E., Tombrou, M., Bossioli, E., Maroufidis, I.,"Saharan Dust Particles Observed by Elastic-Raman Depolarization Lidars over Three Greek Urban Sites (Volos, Ioannina and Athens) during the PANACEA campaigns 2019-2020", Proc. 2nd European Lidar Conference, 18-20 November 2020, Web Conference.

8. Soupiona, O., Foskinis, R., Papayannis, A., Sánchez Hernández, G., Ortiz-Amezcua, P., Mylonaki, M., **Papanikolaou, C.-A.**, Alados-Arboledas, L., Psiloglou, B.,"Radiative effects of Saharan dust spheroidal aerosols over the Northern Meditettanean using lidar retrieved signals as inputs in LibRadtran model", Proc. 2nd European Lidar Conference, 18-20 November 2020, Web Conference.
9. **Papanikolaou, C.-A.**, "The impact of biomass burning for heating on Ioannina city's air quality during winter time" (oral presentation), Proc. 2nd PANACEA Conference, 29 September – 1 October 2020, Web Conference.
10. Papayannis, A., Mylonaki, M., **Papanikolaou, C.-A.**, Kokkalis, P., Soupiona, O., Foskinis, R., Kralli, E., Anagnou, D., "Intercomparison of three collocated multi-wavelength aerosol lidar systems at the National Technical University of Athens' Campus during 2020", Proc. 2nd PANACEA Conference, 29 September – 1 October 2020, Web Conference.
11. Foskinis, R., Papayannis, A., Kokkalis, P., Soupiona, O., Mylonaki, M., **Papanikolaou, C.-A.**, Kralli, E., and Anagnou, D., "Study of the Planetary Boundary Layer Height over selected sites in Greece during Panacea Campaigns (2019-2020) using multi-wavelength aerosol lidar systems", Proc. 2nd PANACEA Conference, 29 September – 1 October 2020, Web Conference.
12. Soupiona, O., Papayannis, A., Bossioli, E., Methymaki, G., Tombrou, M., Romanos, F., Mylonaki, M., **Papanikolaou, C.-A.**, Anagnou, D., and Kralli, E.," Aerosol optical, chemical and radiative properties of a 3-day dust event observed over Athens, Greece using laser remote sensing and modelling", Proc. 2nd PANACEA Conference, 29 September – 1 October 2020, Web Conference.
13. **Papanikolaou, C.-A.**, M. Mylonaki, O. Soupiona, A. Papayannis, R. Foskinis and E.Kralli, "Aerosol detection in the free troposphere over the city of Volos, Greece, during the 1st PANACEA campaign (July 2019)", Proc. 1st PANACEA Conference, 23-24 September 2019, Heraklion, Greece.
14. **Papanikolaou, C.-A.**, E. Gianakaki, A. Papayannis, M. Mylonaki, and O. Soupiona, "Optical properties of Canadian biomass burning particles over Europe observed with CALIPSO and ground-based lidar systems", Proc. 29th International Laser Radar Conference, 24-28 June 2019, Hefei, China.
15. Papayannis, A., M. Mylonaki, O. Soupiona, P. Kokkalis, G. Tsaknakis, **C.-A. Papanikolaou**, and R. Foskinis, "Highlights of Biomass Burning Events from 10-year Profiling over Athens, Greece in the Frame of EARLINET (2007-2017)", Proc. 1st European Lidar Conference, 3-5 July 2018, Thessaloniki, Greece.
16. Soupiona, O., C. Böckmann, A. Papayannis, M. Mylonaki, and P. Kokkalis, **C.-A. Papanikolaou**, and R. Foskinis, "Lidar-based Inversions of Aerosol Microphysical Parameters from Long-range Transported Events over Athens", Proc. 1st European Lidar Conference, 3-5 July 2018, Thessaloniki, Greece.

DATA SOURCE ACKNOWLEDGEMENTS

Papanikolaou C.-A gratefully acknowledges the NOAA Air Resources Laboratory (ARL) for the provision of the HYSPLIT transport and dispersion model and/or READY website (**https://www.ready.noaa.gov**) used in this Thesis. She also acknowledges MODIS for the active fire and burned area products that were distributed through the Fire Information for Resource Management System (FIRMS: **https://firms.modaps.eosdis.nasa.gov**) and through the Land Processes Distributed Active Archive Center (LP DAAC; **https://lpdaac.usgs.gov/products/mcd64a1v006**), respectively. Moreover, she acknowledges the Cloud-Aerosol Lidar and Infrared Pathfinder Satellite Observation (CALIPSO) satellite for the Cloud-Aerosol Lidar with Orthogonal Polarization (CALIOP) for the Aerosol Profile (APro) and the Vertical Feature Mask (VFM) data products obtained from the NASA Langley Research Center Atmospheric Science Data Center (**https://www-calipso.larc.nasa.gov/**). The author acknowledges the Copernicus Atmosphere Monitoring Service (CAMS) for the carbon monoxide and ozone concentrations data in various atmospheric pressure levels. Author acknowledges AERONET-Europe for providing calibration service. AERONET-Europe is part of ACTRIS-IMP project that received funding from the European Union (H2020-INFRADEV-2018-2020) under Grant Agreement No 871115. Finally, author gratefully acknowledges support of this work by the project "PANhellenic infrastructure for Atmospheric Composition and climatE change" (MIS 5021516), which is implemented under the Action "Reinforcement of the Research and Innovation Infrastructure", funded by the Operational Programme "Competitiveness, Entrepreneurship and Innovation" (NSRF 2014–2020) and co-financed by Greece and the European Union (European Regional Development Fund).